MULTIPHYSICS ELECTROCHEMICAL SIMULATIONS OF LITHIUM-ION BATTERY ELECTRODE MICROSTRUCTURES

By

Affan Malik

A DISSERTATION

Submitted to
Michigan State University
in partial fulfillment of the requirements
for the degree of

Chemical Engineering – Doctor of Philosophy
Computational Mathematics, Science and Engineering – Dual Major

2024

ABSTRACT

Energy storage technologies are key to a future of less reliance on fossil fuels and cleaner energy. Rechargeable batteries, particularly lithium-ion batteries have become a mainstay in energy storage, notably in electric vehicles and mobile applications. However, optimizing their performance to achieve faster charging, increased capacity, and higher utilization remains a challenge. Accomplishing these goals requires a microscopic-level understanding of battery electrodes, which is hindered by their complex morphologies. Computer simulations can bridge this gap by providing insights into microstructure phenomena. A framework combining smoothed boundary method (SBM) and adaptive mesh refinement (AMR) is introduced to model and study electrode microstructures. This framework is implemented with finite difference methods (FDM) and parametrized with material properties from literature. We demonstrate the framework's usage and effectiveness with half-cell simulations of $Li_xNi_{1/3}Mn_{1/3}Co_{1/3}O_2$ (NMC-333) cathode through one-dimensional and three-dimensional simulations on synthetically generated microstructures. A crucial goal of our work is studying lithium plating on electrodes which is a major obstacle in realizing an electrode's true theoretical capacity and fast charging. Graphite, the predominant anode material in lithium-ion batteries, is particularly prone to lithium plating, especially at fast charging conditions. Thus, modeling graphite is critical to grasp the dynamics of li-ion batteries and lithium plating. Graphite anode undergoes phase transformations under lithiation. Incorporating the Cahn-Hilliard phase-field equation into the framework allows for detailed and more accurate simulations of these phase transformations in graphite anodes. Using the developed framework for graphite, we identified overcharging conditions, the influence of particle size, and the importance of pore tortuosity on real reconstructed electrodes. The framework can facilitate the design of thick electrodes, promising higher capacity without experimental construction. Furthermore, the framework allowed us to examine two different approaches to delay lithium plating in graphite. A thermodynamic approach of hybrid anodes where we mix graphite with hard carbon and a kinetic approach of tunnels where we introduce synthetic channels in the electrode. Through our simulations, we identify that hard carbon particles act as a buffer for lithiation in hybrid anodes, delaying the surface saturation of

graphite particles and thus delaying the lithium plating on graphite. On the other hand, creating tunnels generates easier paths for ion diffusion and therefore leads to better utilization of the electrode. Such channels in thick electrodes can generate high-capacity and efficient electrodes. Finally, the development of this framework culminates with a demonstration of full-cell simulations. In summary, simulating electrochemical processes in complex electrode microstructures is streamlined by the presented framework and offers a fast and robust tool for designing and studying microstructures.

This thesis is dedicated to my parents and my brother.

ACKNOWLEDGEMENTS

I would like to take this opportunity to express my deepest gratitude to all those who have provided their invaluable support and assistance throughout my Ph.D. journey and the completion of this thesis. Firstly, I extend my heartfelt thanks to my advisor, Dr. Hui-Chia Yu, for his continued guidance and unwavering support. His expertise and encouragement have been instrumental in my growth as a researcher and academic. Beyond being a mentor and providing invaluable feedback, he has taught me the importance of articulating and refining my ideas with clarity and confidence, lessons I will carry forward in my career. I am also deeply grateful to my committee members, Dr. Scott Calabrese Barton, Dr. Philip Eisenlohr, and Dr. Huan Lei, for their valuable insights, constructive feedback, and continuous support. Their assistance at crucial junctures has been pivotal in shaping the trajectory of my research and Ph.D. career. A special thanks goes to my research group members, Danqi Qu and Robert Termuhlen, for their help, insightful opinions, and generous advice over the years.

I would like to acknowledge FORD Motor Company for its financial support through the FORD-MSU alliance project, which helped make this research possible. I am also indebted to the High-Performance Computing Center (HPCC) resources provided by the Institute for Cyber-Enabled Research (ICER) at Michigan State University.

I am greatly thankful to my friend, Chauncey Splichal, who has been a constant source of encouragement throughout my Ph.D. journey. His support has pushed me beyond what I ever imagined I could achieve. To my family away from home—Aditya, Apoorva, Gouree, Shalin, Sushanta, Renu, and Sneha—thank you for the warmth, love, and companionship you brought into my life in a new and unfamiliar place. Through good times, bad times, and the strange times (looking at you, COVID), your presence made all the difference. Any expression of gratitude would be incomplete without acknowledging my newfound brothers—Surya, Vinai, Neil, and Bhaskar. They have stood by me through thick and thin, and their camaraderie and the sense of home they provided have been crucial to my well-being. I would also like to show my appreciation for the rest of the 'Squirtle squad'—Alan, Bryan, Jimmy, Chris, and so many more "volleyball" friends—who

provided me a much-needed balance in my life. The time spent with them has been a wonderful outlet and a great source of joy and relaxation. To my 'forever friends'—Samrat, Saurabh, Ajay, Pratik, Hima, and Richik—who I have been fortunate to know for over a decade, thank you for the constant affection, support, and inspiration you have provided. Your belief in me long before this journey began has been one of the greatest sources of strength and motivation throughout the years.

Finally, and definitely most importantly, a special thanks and all my love go to my family—my parents and my brother—for their unconditional love, encouragement, and understanding during the challenging phases of this journey. Their support has been the source of my strength and motivation. To everyone mentioned above, and to anyone I may have inadvertently missed, I express my deepest gratitude. Without your support and encouragement, this work would not have been possible. Thank you!!

TABLE OF CONTENTS

CHAPTER 1

INTRODUCTION

1.1 Motivation

Energy storage technologies have become increasingly indispensable in modern times, significantly impacting the efficiency and environmental footprint of electrical power networks. They serve a crucial role in enhancing overall effectiveness while mitigating environmental impact throughout energy generation and distribution [1, 2]. Among these technologies, rechargeable batteries stand out as a versatile solution for storing energy sourced from various outlets for later usage as required. Notably, they have gained traction in powering electric vehicles, contributing to the conservation of fossil fuels and the reduction of carbon emissions in recent years. Lithium-ion batteries have one of the highest energy densities and have seen widespread adoption across diverse applications, from everyday devices like cell phones, and computers, to more far-reaching applications like drones, remote surveillance, and electric vehicles. Other popular energy storage technologies include pumped hydro, compressed air energy storage (CAES), and flywheel. Newer technologies like hydrogen and supercapacitors are also being explored [3–9]. Pumped hydro and CAES are large-scale and long-discharge duration technologies making them desirable for bulk energy applications including load management. On the other hand, high initial costs and slower response times render them less suitable for any applications requiring immediate power supply. Flywheels store kinetic energy in a rotating mass and have long life cycles, high energy density, low maintenance costs, and quick response speeds. High initial costs and limited capacity restrict their usage for any long-duration energy delivery leaving them ideal for short-term applications like load-leveling and load-shifting. Supercapacitors or electrochemical capacitors utilize a thin layer of conducting electrolyte as the dielectric between two solid conductors. Fast response times and long lifetimes make them potentially a decent alternative to batteries. Their power density is generally higher than that of batteries, while their energy density is typically lower. The relatively low energy density and high self-discharge limit their current usage in practice. Fuel cells, similar to batteries, convert stored chemical energy directly into electrical energy through electrochemical reactions using hydrogen and oxygen. They are typically lightweight, highly scalable, and versatile in their usage. The lack of hydrogen infrastructure and high capital investment requirements must be addressed to fully realize their potential. Hydrogen energy storage complements fuel cells, typically, acting as the external fuel supply. Hydrogen is environmentally clean and offers high energy density but faces the same problems of high costs and limited possibilities for hydrogen production. Overall, energy storage needs to be technologically improved to meet the demands of the power system, expedite the transition away from over-reliance on fossil fuels, and facilitate the integration of renewable energy sources. [3–9] Lithium-ion batteries stand as the technology that offers the best balance of versatile applications, low cost, high energy density, long cycle life, and relatively low self-discharge rates.

Lithium-ion batteries, despite their prevalent use, have ample room for optimizing battery performance which necessitates a deep and comprehensive understanding of battery electrodes' mechanism and behavior [10–12]. Key areas of improvement include faster charging, increased capacity, higher utilization, and improved temperature control [13–16]. A significant barrier to gaining such an understanding is the non-uniform nature of Li-ion battery electrode microstructures, which elicit irregular particle-electrolyte interfaces and convoluted electrolyte pathways. The intricacy of these complex microstructure configurations dictates the macroscopic properties and

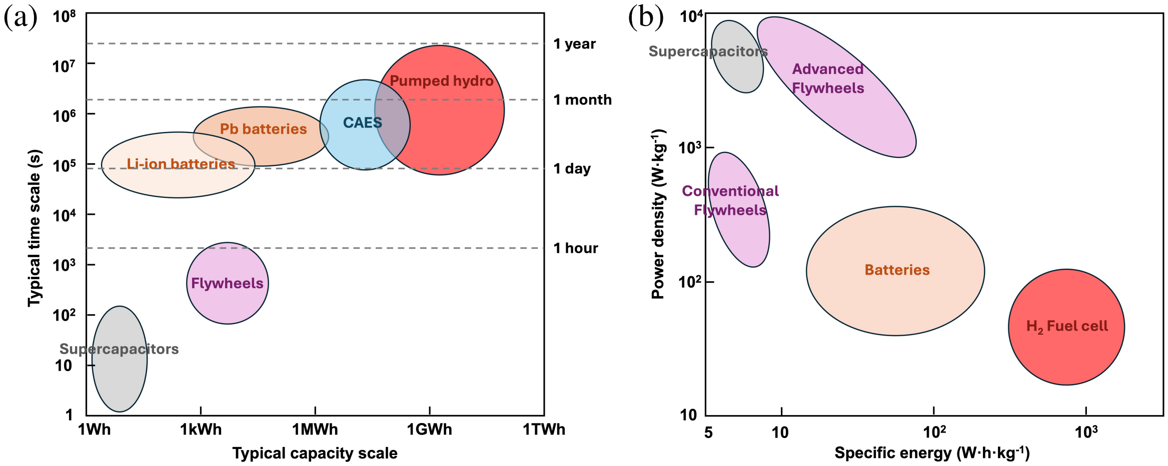

Figure 1.1 (a) Time scales, and (b) power density vs energy density for various energy storage systems with different storage capacities. (a) adapted from Ref. [3] and (b) adapted from Ref. [4].

performance of electrodes.

From here on, in this chapter, we outline some key foundations necessary for understanding the rest of the thesis. Firstly, the workings of a typical Li-ion battery are detailed. Then, an introduction to modeling and simulation for batteries is presented. Finally, the chapter concludes with an outline of the rest of the dissertation.

1.2 Background

1.2.1 Working of a Lithium-ion batteries

A standard lithium-ion battery is composed of a cathode, an anode, and an electrolyte. Both electrodes have current collectors at one end. Fig. 1.2 shows a general schematic of a typical lithium-ion battery. These electrodes primarily consist of lithium-storage particles capable of accommodating the insertion or extraction of lithium ions [11, 17]. Consequently, the porosity and particle sizes influence the capacity and rate performance of an electrode. Additionally, electrodes also comprise of a small fraction of electrochemically inactive additives and binder particles, which enhance electronic conduction and structural integrity, respectively. A separator layer, typically a porous insulating polymer membrane, is interposed between the two electrodes. This layer prevents any physical short between the two electrodes and facilitates ion transport in the cell. The liquid electrolyte resides in the electrodes' interparticle space and the separator's pores facilitating the migration of lithium salt ions between the electrodes.

During a standard charge cycle of a Li-ion battery, once a load is applied, lithium ions diffuse from the cathode to the anode through the electrolyte. Correspondingly, electrons move in the opposite direction through the current collectors and outer circuit. This results in the electrochemical storage of external energy in the battery, converting it into chemical energy in the anode and cathode materials which have different chemical potentials. The movements of the lithium ions and the electrons are reversed during a prototypical discharge cycle as illustrated in Fig. 1.2. The chemical energy is released through Faradaic reactions on the two electrode surfaces, where the choice of the two electrodes determines the total energy change [17]. Thus, morphological factors, such as porosity, tortuosity, particle sizes, and reactive area significantly impact the cell's performance, particularly under high charge/discharge rates [18, 19]. In addition to the microstructures, the choice of electrode and electrolyte materials also determines the cell's performance.

Wittingham [20] pioneered the use of a layered TiS_2 cathode in the first rechargeable lithium battery. Subsequently, several other cathodes including, but not restricted to, layered $LiCoO_2$ and manganese spinel were explored. Contemporary cathode materials predominantly consist of lithium metal oxides due to their higher cell voltage and equivalent energy density. Examples of such metal oxides include $LiCoO_2$ (LCO), $LiNi_{1-y-z}Mn_yCo_zO_2$ (NMC), $LiMn_2O_4$ (LMO), and $LiFePO_4$ (LFP) [20]. These materials undergo intercalation reactions when lithium is inserted or extracted without changing the host crystal lattice. Similarly, intercalation-type materials like graphite, hard or soft carbon, and $Li_4Ti_5O_{12}$ (LTO) currently dominate the anode market in lithium-ion batteries. There is a growing interest in conversion-type materials for both cathodes (such as LiFeOF and $LiFeO_2$) and anodes (including silicon-based and lithium metal). Despite their high energy densities and material abundance , these conversion-type materials remain largely confined to laboratory investigations due to the changes induced in their crystal structure upon lithiation/delithiation [21]. Significant volume changes can be observed during the conversion reactions. Current conversion-type electrodes also suffer from poor cycle life due to the breakdown of electrode structures. [21] The study and enhancement of the microstructures and materials of each component are imperative in striving towards the aforementioned key objectives in advancing Li-ion battery technology.

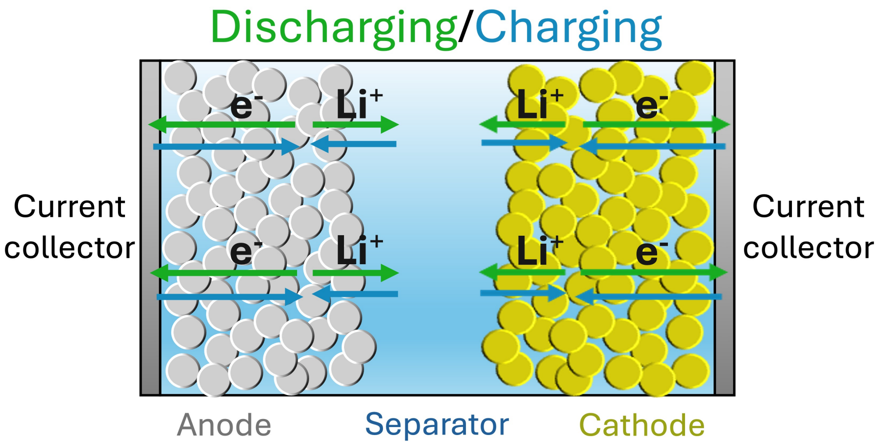

Figure 1.2 Schematic of a cell during discharge/charge processes.

Modeling and computer simulations can offer a promising avenue for delving into the intricate electrochemical dynamic within Li-ion batteries [22, 23]. Understanding these dynamics can help improve Li-ion battery technology. The next section discusses electrochemical modeling and illuminates its advantages in improving battery technology.

1.3 Modeling and Simulations

Modeling and computer simulations offer a promising avenue for delving into the intricate electrochemical dynamic within Li-ion batteries [22, 23]. Broadly speaking, there are three basic approaches to modeling dynamic electrochemical simulations [23, 24]. One such approach involves Equivalent Circuit and Impedance models [25–27], which employ simple electrical elements like resistors, capacitors, and constant phase elements to replicate battery behavior driven by complex underlying electrochemical processes within the cell. These methods facilitate fast and straightforward modeling of batteries and are typically used for battery control or load management. However, the accuracy of their predictions relies on the precision of representative input model parameters. Moreover, these models lack the ability to offer physical insights into electrochemical processes within electrode microstructures.

A second approach is data-driven models. These models leverage historical or real-time data [28–31] to predict battery behavior in new setups and new operating conditions. While these techniques bypass the need for understanding and modeling underlying physics, they suffer from a similar drawback of disconnect between simulation results and the physical mechanism within the battery cells. Additionally, empirical models require reconstruction or retraining once the battery configurations are altered.

The third approach for electrochemical modeling involves mechanistic models, which utilize physical principles and mathematical equations to describe the system [32–35]. These models offer the most insights into battery performance, capturing the underlying physics. However, their applicability is limited to the systems being simulated, requiring new simulations if any changes are made to the system. Currently, the most commonly used technique to simulate electrochemical processes at a macroscopic level is Porous Electrode Theory (PET) [32], developed by Newman et. al. PET treats a porous electrode as a homogeneous medium, utilizing average physical properties (averaged over volume) to solve governing equations and study the dynamics within the 'homogeneous' electrode. This approach simplifies diffusion in a three-dimensional (3D) interparticle space to a one-dimensional (1D) diffusion problem using an effective diffusivity. Consequently, these models alleviate computational burdens associated with explicitly defining complex electrode microstructures. However, since PET models treat electrodes as homogeneous media and focus primarily on macroscopic behavior, they do not capture or reveal electrochemical dynamics at the microstructure level. In reality, electrodes significantly deviate from perfect homogeneity and periodic structures. The non-uniformity in the microstructures leads to variation in porosity and tortuosity resulting in varying degrees of (de)lithiation in the electrode. Thus, necessitating explicit consideration of their complex microstructures and morphology to accurately capture the dynamics within an electrode.

The finite element method (FEM) stands as a widely adopted technique for microscopic electrochemical simulations which can account for any complexities in the microstructures [36, 37]. FEM solves the governing equations (typically partial differential equations, PDEs) on meshes conformal to the geometries of the electrode microstructure. In FEM, the governing equations are generally developed based on a sharp-interface description. In our work, we define sharp interfaces as sharp boundaries with no thickness between different components in a system. Numerically solving these equations necessitates generating body-conformal meshes. Generating such meshes, especially for complex 3D electrode microstructures and tortuous interparticle spaces is an arduous and time-consuming task. In many cases, broken meshes need to be manually fixed [38] before running any simulations. Finite volume methods (FVM) face similar challenges, requiring body-conforming meshes when solving sharp-interface described governing equations, thus demanding comparable pre-simulation efforts. Some researchers have utilized voxels in 3D reconstructed electrode microstructures directly as elements in simulations [39–41]. While this approach overcomes the challenge of generating complex meshes, the highly non-smooth particle-electrolyte interfaces may introduce numerical errors and instability. Additionally, the computational costs can escalate significantly with a large number of voxels in a system. A few voxel-based simulations [42, 43] divide cubic voxels by their diagonal planes to improve the smoothness of interfaces. Nevertheless, computational demands will remain high for a large number of voxels.

1.4 Dissertation outline

This thesis is divided into eight chapters including this introduction. An electrochemical simulation framework is developed and utilized for 3D microscopic simulations on electrodes. We validate and test our framework on several electrodes (both cathodes and anodes) and employ it to study mechanisms for improving electrodes' performance. We briefly outline the rest of the chapters here. Chapter 1 introduces the motivation and highlights some relevant background information.

Chapter 2 presents the developed modeling framework. First, we detail the electrochemical governing equations solved in our framework in a half-cell. Then we describe the methods, Smoothed Boundary Method (SBM), Adaptive Mesh Refinement (AMR), and Finite Difference Methods (FDM) employed in the framework. SBM is used to reformulate the governing equations such that to allow them to be solved on uniform, non-conformal meshes. AMR complements SBM by enabling us to generate finer meshes near interfaces and coarser meshes in the bulk. FDM is the choice of numerical technique in our work to solve differential governing equations.

Chapter 3 validates and uses the developed framework for the NMC-333 electrode using 1D and 3D simulations. Two synthetic 3D microstructures are created using the Discrete Element Method (DEM) for these simulations. Material properties obtained from existing literature are incorporated into the model for more accurate results. Additional simplistic mechanical and thermal simulations are also performed and presented. Chapter 3 demonstrates the applicability and versatility of our developed framework. Chapter 4 modifies the presented framework with the Cahn-Hilliard equation for phase separation and presents several studies on reconstructed 3D graphite microstructures. Through these studies, we can examine the physical fields in several graphite anodes, and using these fields we explore ways of improving graphite anode performance, particularly delaying the onset of plating.

The next two Chapters 5 and 6 explore two different approaches to alleviate lithium plating in graphite. Chapter 5 uses a thermodynamic approach of introducing a buffer of hard-carbon particles with graphite particles to alleviate plating on the graphite anode. With the introduction of the hard-carbon particles, we observe a three-stage lithiation process in the hybrid electrode. We explore several configurations and parameters of the hybrid electrode that can affect the performance of the electrode. On the other hand, Chapter 6 looks at a kinetic approach by creating new pathways through graphite anodes allowing better utilization and higher capacity of the anode before reaching the plating condition. We examine the impact of such tunnels on electrode performance in this chapter. Furthermore, we investigate the effect of tunnel arrangement, size, and tunnel-to-tunnel distance on the improvement offered by the tunnels. The hexagonal arrangement of tunnels is identified to be more efficient than the square arrangement. Optimal tunnel radii are determined for various electrode thicknesses and tunnel arrangements (including their pattern and separation).

Chapter 7 culminates the development of this framework by presenting full-cell simulations with both cathode and anode. The microstructures presented in Chapters 3, 4, 5, and 6 are utilized along with a new separator microstructure to perform these full-cell simulations. This chapter acts as a demonstration of the full-cell framework which opens new avenues for electrode design by studying their behavior in a full-cell.

Lastly, Chapter 8 summarizes and concludes the dissertation. It also briefly discusses applications of the developed framework for Electrochemical Impedance Spectroscopy (EIS) simulations by Danqi et al. Additionally, we suggest several avenues for extending our research in the future.

CHAPTER 2

MODELING FRAMEWORK AND NUMERICAL METHODS

This chapter outlines a framework developed to solve electrochemical equations in 3D electrodes with complex microstructures. This framework is utilized through Chapters 3-7. Any variations in the modeling for a chapter are specified at the beginning of that chapter. In this chapter, for simplicity of understanding, only the governing equations of a half-cell are presented. Chapter 7 details extending these equations to a full cell. During the charge/discharge cycle of a Li-ion battery, several mechanisms operate simultaneously, including (1) Li-ion transport within the electrode particles, (2) current continuity in the electronically conductive solid phases, (3) ionic transport within the electrolyte, (4) current continuity in the ionically conductive electrolyte, and (5) electrochemical reactions at the particle-electrolyte interfaces. All these mechanisms are mathematically described by classical differential equations, which are coupled to each other. Refer to Fig. 2.1 (a) for an illustration.

For solving differential equations in a complex system, conventional sharp-interface methods like Finite Element Method (FEM) or Finite Volume Method (FVM) necessitate meshes conforming to the geometries. Thus, presenting a significant challenge for simulating phenomena in complex 3D electrode microstructures which are highly tortuous and porous. In the developed framework, we employ the Smoothed Boundary Method (SBM) [44–48] to overcome the need for body-conforming meshes in solving the governing equations. For some simulations in this work, SBM is used in conjunction with Adaptive Mesh Refinement (AMR) [49], a technique that can generate fine meshes near interfaces while keeping a course mesh everywhere else. Combining SBM with AMR allows for enhanced simulation accuracy of SBM by allowing the use of thin interfaces. The refined meshes utilized in the simulations also do not conform to the complex, irregular particle-electrolyte interfaces, thus simplifying mesh generation. The conventional equations that describe the physical phenomena within the three regions— electrode particles, electrolyte, and interface— are outlined first. Then, we describe the SBM reformulation of those equations and the AMR mesh generation used in the framework. In our simulations, we integrate the SBM+AMR framework with Finite

Difference Method (FDM) stencils due to their straightforward implementation. The numerical method is also presented in this chapter. The complete framework was first presented in Malik et al, Journal of The Electrochemical Society, 169(7):070527, Jul 2022 [24] and subsequently extended with a phase-field in Malik et al, 77:109937, January 2024 [50]. This chapter is substantially drawn from these publications.

2.1 Conventional governing Equations

In this section, we detail and describe the governing equations, which serve as the foundation of our framework. These equations pertain to a half-cell with the assumption of a lithium metal counter electrode on the other side of the cell.

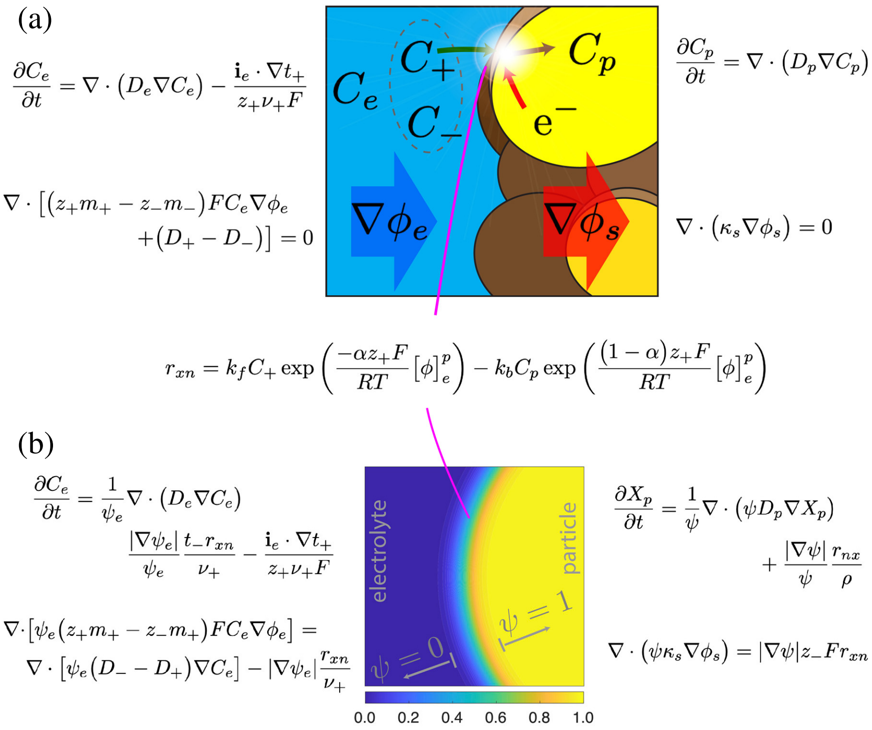

Figure 2.1 (a) Schematic illustration of electrolyte and particle regions with the associated electrochemical governing equations. The yellow color indicates the inside of particles, the brown color indicates particle surfaces, and the light blue color indicates the electrolyte. (b) Illustration of diffuse interface and domain parameter with the SBM-reformulated governing equations. Domain parameter ψ continuously transitions across the electrolyte-particle interface.

2.1.1 Electrode particles

Intercalation materials represent the predominant choice for electrode materials in lithium-ion batteries. An intercalation reaction inserts a lithium ion into the host crystal without altering its structure. The chemical formula can be typically described by

$$x\mathrm{Li}^{+} + x\mathrm{e}^{-} + \mathrm{G} \rightleftharpoons \mathrm{Li}_{x}\mathrm{G} \tag{2.1}$$

where G denotes an intercalation electrode material. In the context of this work, G can signify one of the three materials: NMC, graphite, or hard carbon. Once intercalated into electrode particles, lithium ions diffuse/migrate through the host crystal's interstices (or vacant sites), as indicated by the brown arrow in Fig. 2.1(a). The Li transport can be described generally by

$$\frac{\partial X_p}{\partial t} = -\nabla \cdot \vec{j}_p = \nabla \cdot \left(M_p \nabla \mu_p \right) \in \Omega_p, \tag{2.2}$$

where X_p, M_p, and μ_p are the site occupancy fraction, transport mobility, and chemical potential, respectively, of Li in the host crystal, $\vec{j}_p = -M_p \nabla \mu_p$ is the Li flux, t denotes time, and Ω_p denotes the domain of the particle. The subscript p denotes the particle for Li storage. The lithium concentration in the particle is $C_p = \rho X_p$, where ρ is the site density. On the particle surface, the insertion/extraction rate is described by $r_{xn}/\rho = \vec{n} \cdot \vec{j} \in \partial\Omega_a$, where $\vec{n}$ is the inward unit vector of the particle surface, $\vec{j} = -M_p \nabla \mu_p$ is the (de)intercalation flux vector, and $\partial\Omega_a$ is the active surface where the reaction occurs. Please note that $\partial\Omega_a$ represents the active surface, which may not encompass all particle surfaces. Regions covered by inactive materials, such as binders, are considered inactive. However since binder phases are not included in our model, all particle-electrolyte interfaces count as active. Consequently, in this work, $\partial\Omega_a$ is equivalent to $\partial\Omega_p$. Eq. (2.2) can be simplified to Fick's diffusion equation [51] if a solid-solution mechanism is assumed for lithation/delithiation in the electrode. The simplified equation defines lithium fraction evolution as

$$\frac{\partial X_p}{\partial t} = \nabla \cdot \left(D_p \nabla X_p \right) \in \Omega_p, \tag{2.3}$$

where D_p is the Li diffusivity in the particles. The boundary condition stays the same even after this simplification. For phase-separating electrode materials, μ_p will be formulated in a more complicated form (e.g., as in the phase-field models [52–54]). This behavior is detailed further in Chapter 4 as it pertains more to graphite anodes.

The electric current density in the conductive solid regions is given by $\mathbf{i}_s = -\kappa_s \nabla \phi_s$ and describes electron transport. The current continuity condition, therefore, is described by

$$\nabla \cdot \mathbf{i}_s = 0 \in \Omega_s \implies \nabla \cdot \left(\kappa_s \nabla \phi_s\right) = 0 \in \Omega_s, \tag{2.4}$$

where κ_s and ϕ_s are the electrical conductivity and electrostatic potential, respectively. This equation is subject to the boundary condition, $\mathbf{i}_s = -\kappa_s \nabla \phi_s = F r_{xn} \in \partial\Omega_a$, where F is the Faraday constant. As mentioned earlier, Ω_s specifies all conductive solid regions, which may include additives in addition to electrode particles as well. The additive phases can be incorporated into the electrochemical simulations by including an additional domain parameter function [44]. However, we do not consider additives in the work presented here.

2.1.2 Electrolyte

Within an electrolyte, both cations and anions undergo electro-diffusion, which combines the diffusion driven by gradients of ion concentration and the migration driven by electrostatic potential gradients. For a binary electrolyte, that contains only one species of cations and anions each, the diffusion and migration terms can be consolidated [55], resulting in the equation:

$$\frac{\partial C_e}{\partial t} = \nabla \cdot D_e \nabla C_e - \frac{\mathbf{i_e} \cdot \nabla t_+}{z_+ \nu_+ F} \in \Omega_e, \tag{2.5}$$

where C_e, D_e, and $\mathbf{i}_e$ are the salt concentration, the ambipolar diffusivity of the salt, and the ionic current in the electrolyte, respectively. z_i, ν_i, and t_i are the charge number, dissolution number, and transference number, respectively, where the subscript '+' denotes cation. Here, we assume that the electrolyte is binary, comprising solely one species of monovalent cation and one species of anion. The salt concentration is related to the ionic concentration by $C_e = \nu_+ C_+ = \nu_- C_-$. The ambipolar diffusivity is expressed as $D_e = (z_+ m_+ D_- - z_- m_- D_+)/(z_+ m_+ - z_- m_-)$, where m_i is the transport mobility and D_i is the diffusivity of the ions with the subscripts indicating cations and anions. The derivation of Eq. (2.5) can be found in Ref. [55]. Ω_e specifies the domain of electrolyte. The salt concentration is subject to the boundary condition: $r_{xn} = \nu_+ \vec{n} \cdot \vec{j}_e \in \partial\Omega_e$, where $\vec{j}_e = -D_e \nabla C_e + t_+ \mathbf{i}_e / (z_+ \nu_+ F)$ is an effective salt flux vector and $t_+ = 1 - t_- = z_+ m_+ / (z_+ m_+ - z_- m_-)$.

Assuming current continuity in the electrolyte (i.e., charge separation in diffuse double layer regions is ignored), $\nabla \cdot \mathbf{i}_e = 0$, where $\mathbf{i}_e = -F z_+ \nu_+ [(z_+ m_+ - z_- m_-) F C_e \nabla \phi_e + (D_+ - D_-) \nabla C_e]$ and ϕ_e is the electrostatic potential in the electrolyte. Thus, we obtain the equation governing the electrostatic potential field in the electrolyte regions as

$$\nabla \cdot [(z_+ m_+ - z_- m_-) F C_e \nabla \phi_e + (D_+ - D_-) \nabla C_e] = 0 \in \Omega_e, \tag{2.6}$$

with the boundary condition $z_+ F r_{xn} = \vec{n} \cdot \mathbf{i}_e \in \partial\Omega_e$.

2.1.3 Interface reaction and Butler-Volmer equation

At the particle-electrolyte interfaces, lithium ions in the electrolyte react with electrons in the electrode particle and are then intercalated into the particle, see Fig. 2.1(a) for an illustration. Lithium concentrations, as well as the electrostatic potentials, on both sides of the interface, are involved in determining the surface reaction rate, which is typically expressed by the Butler-Volmer equation [24, 55]:

$$r_{xn} = \frac{i_0}{z_+ F} \left[\exp\left(\frac{-\alpha z_+ F}{RT} \eta \right) - \exp\left(\frac{(1-\alpha) z_+ F}{RT} \eta \right) \right], \tag{2.7}$$

where α is the symmetry factor, R is the ideal gas constant, T is the absolute temperature, $\eta = [\phi]_e^p - \phi_{eq}$ is the overpotential on the particle surfaces. $[\phi]_e^p = \phi_p - \phi_e \in \partial\Omega_a$ is the electrostatic potential drop across the electrolyte-particle interface. ϕ_{eq} is the equilibrium voltage, which is also the open circuit voltage for a reversible electrode system. In this work, the dissolution number is assumed to be one. Also, the symmetry factor is assumed to be 0.5 for simplicity, which is generally valid for non-insulator electrode materials [56].

The reaction rate obtained in Eq. (2.7) serves as the common boundary condition that couples Eqs. (2.2) – (2.6) and the values of r_{xn} are also determined by the results of those equations. Solving these equations in the conventional FEM or FVM requires discretizing the complex particle (Ω_p) and electrolyte ((Ω_e) domains with conformal meshes, which forms the largest challenge of complex microstructure simulations.

2.2 Smoothed Boundary Method

We solve these equations on complex electrode microstructures by modifying them using the smoothed boundary method [24, 50, 57, 58, 58, 59]. Following ideas from Refs. [44–47, 47, 48], we introduce a continuous domain parameter (ψ) to define the regions occupied by electrode particles. The value of ψ is uniformly one inside the particles and uniformly zero outside. Since no additive phases are considered in this work, $\psi_e = 1 - \psi$ serves as the domain parameter for the electrolyte region. The particle-electrolyte interface is implicitly defined by the region of $0 < \psi < 1$. The narrow regions where ψ transitions from one to zero define the locations of particle-electrolyte interfaces implicitly. See Fig. 2.1(b) for an illustration. Please note that the finite-thickness diffuse interface in the SBM is a numerical smeared interface, not a physical interface. The domain parameters have a similar form to the order parameters in the phase-field methods. The original electrochemical governing equations can be reformulated with ψ such that body-conforming mesh is no longer required in solving the reformulated equations. The equations are reformulated as follows.

2.2.1 Electrode/Particles

As mentioned earlier, a domain parameter ψ is used to define the space occupied by the electrode particles. The value of ψ is one inside the particles and zero outside as mentioned earlier. Multiplying ψ on both sides of Eq. (2.3), we obtain

$$\psi \frac{\partial X_p}{\partial t} = \psi \nabla \cdot (D_p \nabla X_p), \tag{2.8}$$

Using the product rule of differentiation on the right-hand side of Eq. (2.8), we further write

$$\psi \nabla \cdot (D_p \nabla X_p) = \nabla \cdot (\psi D_p \nabla X_p) - \nabla \psi \cdot (D_p \nabla X_p), \tag{2.9}$$

Combining these two equations results in

$$\psi \frac{\partial X_p}{\partial t} = \nabla \cdot (\psi D_p \nabla X_p) - \nabla \psi \cdot (D_p \nabla X_p), \tag{2.10}$$

The second term on the right-hand side serves as an ‘internal’ boundary condition within the computational domain. The Neumann boundary condition on the particle surface ($r_{xn}/\rho = \vec{n} \cdot \vec{j} \in$

$\partial\Omega_a$) can be expressed in the diffuse interface description as

$$\frac{r_{xn}}{\rho} = \vec{n} \cdot \vec{j} = \frac{\nabla\psi}{|\nabla\psi|} \cdot (-D_p \nabla X_p), \tag{2.11}$$

where $\vec{n} = \nabla\psi/|\nabla\psi|$ is the unit inward normal vector of the diffuse interface. Substituting Eq. (2.11) to Eq. (2.10), we obtain the SBM version of the Li transport equation:

$$\frac{\partial X_p}{\partial t} = \frac{1}{\psi}\nabla \cdot \left(\psi D_p \nabla X_p\right) + \frac{|\nabla\psi|}{\psi}\frac{r_{xn}}{\rho}, \tag{2.12}$$

Following a similar procedure, we can derive the SBM version of the current continuity equation for the electrode particles by starting with multiplying Eq. (2.4) with ψ and implementing the product rule to obtain

$$\psi\nabla \cdot (\kappa_s \nabla\phi_s) = \nabla \cdot (\psi\kappa_s \nabla\phi_s) - \nabla\psi \cdot (\kappa_s \nabla\phi_s) = 0, \tag{2.13}$$

Again, substituting the boundary condition $\vec{n} \cdot \mathbf{i}_s = \nabla\psi/|\nabla\psi| \cdot (-\kappa_s \nabla\phi_s) = -z_- F r_{xn}$ into Eq. (2.13) gives the SBM version of the current continuity equation in the electrode particles:

$$\nabla \cdot (\psi\kappa_s \nabla\phi_s) - |\nabla\psi| z_- F r_{xn} = 0, \tag{2.14}$$

2.2.2 Electrolyte

Similar to the SBM formulation of the electrode, we multiply Eq. (2.5) with ψ_e and use the product rule to obtain

$$\frac{\partial C_e}{\partial t} = \frac{1}{\psi_e}\nabla \cdot (\psi_e D_e \nabla C_e) - \frac{1}{\psi_e}\nabla\psi_e \cdot (D_e \nabla C_e) - \frac{\mathbf{i_e} \cdot \nabla t_+}{z_+ \nu_+ F}, \tag{2.15}$$

where $\psi_e = 1 - \psi$. Recall that $D_e \nabla C_e = -\vec{j_e} + t_+ \mathbf{i}_e/(z_+ \nu_+ F)$. Thus, we have

$$-\nabla\psi_e \cdot (D_e \nabla C_e) = \nabla\psi_e \cdot \vec{j_e} - \frac{t_+}{z_+ \nu_+ F}\nabla\psi_e \cdot \mathbf{i}_e, \tag{2.16}$$

Recalling the boundary conditions that $r_{xn}/\nu_+ = \vec{n} \cdot \vec{j_e} = (\nabla\psi_e/|\nabla\psi_e|) \cdot \vec{j_e}$ and $z_+ F r_{xn} = \vec{n} \cdot \mathbf{i}_e = (\nabla\psi_e/|\nabla\psi_e|) \cdot \mathbf{i}_e$ in Section 2.1.2, Eq. (2.15) can be rewritten as

$$\frac{\partial C_e}{\partial t} = \frac{1}{\psi_e}\nabla \cdot (\psi_e D_e \nabla C_e) + \frac{1}{\psi_e}\left(|\nabla\psi_e|\frac{r_{xn}}{\nu_+} - |\nabla\psi_e|\frac{t_+ r_{xn}}{\nu_+}\right) - \frac{\mathbf{i_e} \cdot \nabla t_+}{z_+ \nu_+ F}, \tag{2.17}$$

which is further organized to

$$\frac{\partial C_e}{\partial t} = \frac{1}{\psi_e}\nabla \cdot (\psi_e D_e \nabla C_e) + \frac{|\nabla \psi_e|}{\psi_e}\frac{r_{xn} t_-}{\nu_+} - \frac{\mathbf{i_e} \cdot \nabla t_+}{z_+ \nu_+ F}, \tag{2.18}$$

where $t_- = 1 - t_+$. If the transference number is constant, the last term vanishes.

For the current continuity in electrolyte (Eq. (2.6)), we follow a similar procedure to obtain

$$\begin{aligned} &\nabla \cdot \left[\psi_e (z_+ m_+ - z_- m_-) F C_e \nabla \phi_e\right] - \\ &\quad \nabla \psi_e \cdot \left[(z_+ m_+ - z_- m_-) F C_e \nabla \phi_e + (D_+ - D_-) \nabla C_e\right] \\ &\qquad\qquad = \nabla \cdot \left[\psi_e (D_- - D_+) \nabla C_e\right], \end{aligned} \tag{2.19}$$

Recall that $z_+ F r_{xn} = \vec{n} \cdot \mathbf{i}_e = (\nabla \psi_e / |\nabla \psi_e|) \cdot \left\{-z_+ \nu_+ F \left[(z_+ m_+ - z_- m_-) F C_e \nabla \Phi_e + (D_+ - D_-) \nabla C_e\right]\right\}$, which leads to

$$\nabla \cdot \left[\psi_e \left(z_+ m_+ - z_- m_-\right) F C_e \nabla \phi_e\right] + |\nabla \psi_e| \frac{r_{xn}}{\nu_+} = \nabla \cdot \left[\psi_e \left(D_- - D_+\right) \nabla C_e\right], \tag{2.20}$$

In summary, Eqs. (2.12), (2.14), (2.18), and (2.20) are the SBM governing equations reformulated from the classical Eqs. (2.3), (2.4), (2.5), and (2.6), respectively.

$$\frac{\partial X_p}{\partial t} = \frac{1}{\psi}\nabla \cdot \left(\psi D_p \nabla X_p\right) + \frac{|\nabla \psi|}{\psi}\frac{r_{xn}}{\rho}, \tag{2.12}$$

$$\nabla \cdot (\psi \kappa_s \nabla \phi_s) - |\nabla \psi| z_- F r_{xn} = 0, \tag{2.14}$$

$$\frac{\partial C_e}{\partial t} = \frac{1}{\psi_e}\nabla \cdot (\psi_e D_e \nabla C_e) + \frac{|\nabla \psi_e|}{\psi_e}\frac{r_{xn} t_-}{\nu_+} - \frac{\mathbf{i_e} \cdot \nabla t_+}{z_+ \nu_+ F}, \tag{2.18}$$

$$\nabla \cdot \left[\psi_e \left(z_+ m_+ - z_- m_-\right) F C_e \nabla \phi_e\right] + |\nabla \psi_e| \frac{r_{xn}}{\nu_+} = \nabla \cdot \left[\psi_e \left(D_- - D_+\right) \nabla C_e\right], \tag{2.20}$$

The reaction rate obtained from the Butler-Volmer equation also serves as the internal boundary condition that couples the kinetic and static equations above.

$$r_{xn} = \frac{i_0}{z_+ F}\left[\exp\left(\frac{-\alpha z_+ F}{RT}\eta\right) - \exp\left(\frac{(1-\alpha) z_+ F}{RT}\eta\right)\right], \tag{2.7}$$

These equations can be solved on grid systems (mesh) non-conformal to the complex electrode microstructures while imposing the reaction flux at the diffuse interfaces that are located by nonzero values of $|\nabla\psi|$. A quick view of those classical and SBM-reformulated equations and their associated domains is presented in Fig. 2.1(b).

2.3 Adaptive Mesh Refinement

The Smoothed Boundary Method (SBM) enables the utilization of a grid system that is not conformal to the internal boundaries when solving governing equations, thus facilitating numerical simulations on a uniform Cartesian grid system [44]. Typically, four grid points across the diffuse interface are required to maintain numerical stability. However, employing a uniform, fine grid system throughout the entire computational domain to resolve a thin diffuse interface would impose a significant computational burden. In practice, fine grids are primarily necessary near the diffuse interface. Adaptive Mesh Refinement (AMR) [49,60,61] is a technique that allows for the generation of a fine mesh only near interface regions while keeping a coarse grid away from the interface. In our approach, we employ the Finite Difference Method (FDM) to solve the SBM equations on AMR grid systems for ease of implementation. It's important to note that the SBM equations are not restricted to the solvers presented here and can also be implemented with FEM or FVM instead.

In our work, octree and quadtree adaptive mesh refinement (AMR) techniques [49,59–61] were employed to generate grid systems in 3D and 2D, respectively. The quadtree refinement process is similar to octree refinement but simpler, given that it is a two-dimensional simplification of the former. Thus we only describe the octree AMR here. First, the computational domain is discretized into uniform equal-sized cubes, which are referred to as root-level cells. Each such cell comprises eight vertices, also known as nodes or grid points. A cell list is then created to store the cell labels along with the labels of vertices for each cell. Additionally, a node list is generated to store the node labels and their corresponding positions. To determine the shortest distance of each node to the internal boundary (i.e., the particle-electrolyte interface), the level-set distancing method was utilized [44,62]. Subsequently, the center position of each cell is calculated by averaging the positions of its eight vertices. If the distance from a cell center to the internal boundary is shorter than a specified threshold value, the cell is split into eight equal-sized cubes, with each having an edge length half that of the parent cell. The original cell is then eliminated, and the newly created cells are referred to as the first-level cells. Additionally, new nodes are inserted into the node list (as vertices of the new cells) if the position of a new node is not already occupied by an existing node.

During the refinement processes, neighbor nodes are systematically identified and recorded. For each node, direct neighbors are determined along each axial direction as the nearest nodes to that particular node. An illustration can be seen in Fig. 2.2(a), where the black node represents the center node, and the magenta dots denote the six direct neighbors. At the boundary between two levels of cells, if no direct neighbor exists in a given direction, the second nearest neighbors are selected as the indirect neighbors in that direction. Fig. 2.2(b) demonstrates this scenario, where the cyan dots represent the two indirect neighbors in the west direction. These procedures of cell splitting, node insertion, and neighbor searching can be executed successively to achieve higher levels of refinement. By refining the mesh in the interfacial regions, a domain parameter with a very thin diffuse interface can be utilized while maintaining a resolution of four to six nodes across the interface. It's noteworthy that the threshold value for each level of refinement is meticulously chosen to ensure that there is only one level of difference in adjacent cells. Neighboring cells differing by more than one level of refinement can cause instability in the numerical solver.

2.4 Numerical methods

We use the Finite Difference Methods (FDM) to solve the governing equations, with the stencil of a variable-coefficient second-order derivative operator in 3D as [59, 63]

$$\begin{aligned}\nabla \cdot \left(\psi \nabla u_C\right) =& \frac{2}{s_W + s_E}\left(\xi_E \cdot \frac{u_E - u_C}{s_E} - \xi_W \cdot \frac{u_C - u_W}{s_W}\right) \cdot \left(1 - \beta_{21} - \beta_{31}\right) + \\ & \frac{2}{s_N + s_S}\left(\xi_N \cdot \frac{u_N - u_C}{s_N} - \xi_S \cdot \frac{u_C - u_S}{s_S}\right) \cdot \left(1 - \beta_{12} - \beta_{32}\right) + \\ & \frac{2}{s_T + s_B}\left(\xi_T \cdot \frac{u_T - u_C}{s_T} - \xi_B \cdot \frac{u_C - u_B}{s_B}\right) \cdot \left(1 - \beta_{13} - \beta_{23}\right)\end{aligned} \tag{2.21}$$

where the subscripts W, E, S, N, B, and T indicate the west, east, south, north, bottom, and top directions, respectively, the subscript C indicates the center node, u_i are the values at different nodes, and s_i are the distances from the center node to its (direct or virtual) neighbors in the i direction. $\xi_i = (\psi_i + \psi_C)/2$ is the average value of ψ between the center node and its (direct or virtual) neighbor. β_{ij} are the correction factors for nodes with any indirect neighbors.

Different types of nodes can arise based on a given configuration. If a node has six direct neighbors, each along one of the axial directions (as illustrated in Fig. 2.2(a)), it is termed a regular node. For such nodes, all β_{ij} coefficients are zero. Equation (2.21) simplifies to a standard seven-point FDM stencil. On the other hand, if a node has two indirect neighbors along a specific direction, it is labeled as a T-junction. Fig. 2.2(b) provides an example of a west-facing T-junction on the x-y plane. In this scenario, $\beta_{12} = s_S s_N / \big(s_W(s_W + s_E)\big)$, while all other β coefficients are zero. The value of ψ_W on the virtual west neighbor (marked by the green circle) is determined by

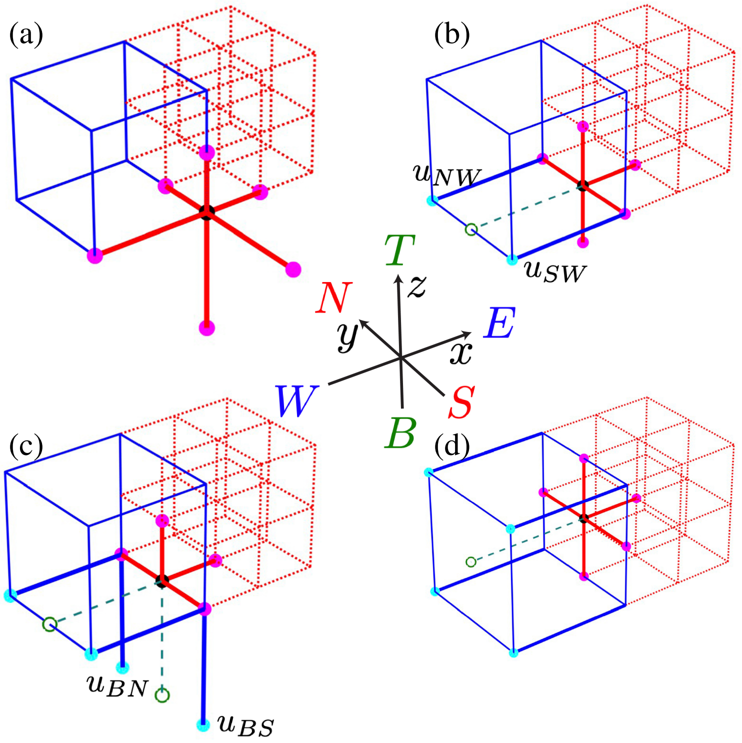

Figure 2.2 Schematic illustration of (a) a regular node (black dot) with six direct neighbor nodes (magenta dots). (b) A west-facing T-junction node (black dot) that has five direct neighbor nodes (magenta dots) and two indirect neighbors (cyan dots) in the west ($-x$) direction. (c) A node that is simultaneously a west-facing and bottom-facing T-junction node. (d) A west-facing face-centered node that has four indirect neighbors in the west direction. The green circles in (b), (c), and (d) indicate virtual neighbor nodes.

averaging ψ at the two indirect neighbors (marked by the cyan dots). Similarly, the value of u_W on the virtual west neighbor is calculated by a weighted average of those at the two indirect neighbors.

$$u_W = \frac{(\psi_{SW} + \psi_C)u_{SW} + (\psi_{NW} + \psi_C)u_{NW}}{(\psi_{SW} + \psi_C) + (\psi_{NW} + \psi_C)}. \tag{2.22}$$

The β values for T-junctions along different directions and on different planes are listed in Table 2.1. It is important to note that a node can simultaneously be classified as a T-junction in two axial directions. For instance, Fig. 2.2(c) shows a node that serves as a west-facing T on the x-y plane and a bottom-facing T on the y-z plane. The west and bottom virtual neighbors are indicated as green circles. The values at those virtual neighbor nodes can be determined using similar methods as described above.

Another type of node is a face-centered junction, see Fig. 2.2(d) for an example of a west-facing face-centered junction. In this scenario, both β_{12} and β_{13} are nonzero and the values can be computed using the formulas in Table 2.1. The ψ value on the virtual neighbor node (marked by the green circle) is determined by averaging the values at the four indirect neighbors (marked by the cyan dots). The value of u_W is calculated as the weighted average, given by $u_W = \sum (\psi_i + \psi_C)u_i / \sum (\psi_i + \psi_C)$, where i denotes the subscripts of the indirect neighbors. In some cases, a node can function as T-junctions on two orthogonal planes facing the same axial direction. Such nodes will have four indirect neighbors along that direction. The formulas for calculating β values, ψ, and u at the virtual neighbor node remain the same as in the face-centered case. When calculating gradients, the FDM stencils are

$$\frac{\partial u}{\partial x} = \frac{s_E}{s_W + s_E} \cdot \frac{u_C - u_W}{s_W} + \frac{s_W}{s_W + s_E} \cdot \frac{u_E - u_C}{s_E} + \alpha_{12} u_{yy} + \alpha_{13} u_{zz} \tag{2.23a}$$

$$\frac{\partial u}{\partial y} = \frac{s_N}{s_S + s_N} \cdot \frac{u_C - u_S}{s_S} + \frac{s_S}{s_S + s_N} \cdot \frac{u_N - u_C}{s_N} + \alpha_{21} u_{xx} + \alpha_{23} u_{zz} \tag{2.23b}$$

$$\frac{\partial u}{\partial z} = \frac{s_T}{s_B + s_T} \cdot \frac{u_C - u_B}{s_B} + \frac{s_B}{s_B + s_T} \cdot \frac{u_T - u_C}{s_T} + \alpha_{31} u_{xx} + \alpha_{32} u_{yy} \tag{2.23c}$$

where the correction factors α_{ij} are provided in Table 2.1. Example derivations of the FDM stencils, α, and β coefficients from Taylor series are given in Appendix A. For regular nodes, α

Table 2.1 Correction factors for the finite difference stencils used in this work. Adapted from Ref. [63].

Note that $\alpha_{ij}(T_*)$ and $\beta_{ij}(T_*)$ refer to the $\alpha_{ij}(T_*)$ and $\beta_{ij}(T_*)$ value from T-junction type of T_*.				
node type	α_{12}	α_{13}	β_{12}	β_{13}
T_{w-xy}	$\frac{s_s s_n s_e}{2s_w(s_w+s_e)}$	0	$\frac{s_s s_n}{s_w(s_w+s_e)}$	0
T_{w-xz}	0	$\frac{s_b s_t s_e}{2s_w(s_w+s_e)}$	0	$\frac{s_b s_t}{s_w(s_w+s_e)}$
$T_{w-xy-xz}$	$0.5\alpha_{12}(T_{w-xy})$	$0.5\alpha_{13}(T_{w-xz})$	$0.5\beta_{12}(T_{w-xy})$	$0.5\beta_{13}(T_{w-xz})$
T_{w-4i}	$\alpha_{12}(T_{w-xy})$	$\alpha_{13}(T_{w-xz})$	$\beta_{12}(T_{w-xy})$	$\beta_{13}(T_{w-xz})$
T_{e-xy}	$-\frac{s_s s_n s_w}{2s_e(s_w+s_e)}$	0	$\frac{s_s s_n}{s_e(s_w+s_e)}$	0
T_{e-xz}	0	$-\frac{s_b s_t s_w}{2s_e(s_w+s_e)}$	0	$\frac{s_b s_t}{s_e(s_w+s_e)}$
$T_{e-xy-xz}$	$0.5\alpha_{12}(T_{e-xy})$	$0.5\alpha_{13}(T_{e-xz})$	$0.5\beta_{12}(T_{e-xy})$	$0.5\beta_{13}(T_{e-xz})$
T_{e-4i}	$\alpha_{12}(T_{e-xy})$	$\alpha_{13}(T_{e-xz})$	$\beta_{12}(T_{e-xy})$	$\beta_{13}(T_{e-xz})$
node type	α_{21}	α_{23}	β_{21}	β_{23}
T_{s-xy}	$\frac{s_w s_e s_n}{2s_s(s_s+s_n)}$	0	$\frac{s_w s_e}{s_s(s_s+s_n)}$	0
T_{s-yz}	0	$\frac{s_b s_t s_n}{2s_s(s_s+s_n)}$	0	$\frac{s_b s_t}{s_s(s_s+s_n)}$
$T_{s-xy-yz}$	$0.5\alpha_{21}(T_{s-xy})$	$0.5\alpha_{23}(T_{s-yz})$	$0.5\beta_{21}(T_{s-xy})$	$0.5\beta_{23}(T_{s-yz})$
T_{s-4i}	$\alpha_{21}(T_{s-xy})$	$\alpha_{23}(T_{s-yz})$	$\beta_{21}(T_{s-xy})$	$\beta_{23}(T_{s-yz})$
T_{n-xy}	$-\frac{s_w s_e s_s}{2s_n(s_s+s_n)}$	0	$\frac{s_w s_e}{s_n(s_s+s_n)}$	0
T_{n-yz}	0	$-\frac{s_b s_t s_s}{2s_n(s_s+s_n)}$	0	$\frac{s_b s_t}{s_n(s_s+s_n)}$
$T_{n-xy-yz}$	$0.5\alpha_{21}(T_{n-xy})$	$0.5\alpha_{23}(T_{n-yz})$	$0.5\beta_{21}(T_{n-xy})$	$0.5\beta_{23}(T_{n-yz})$
T_{n-4i}	$\alpha_{21}(T_{n-xy})$	$\alpha_{23}(T_{n-yz})$	$\beta_{21}(T_{n-xy})$	$\beta_{23}(T_{n-yz})$
node type	α_{31}	α_{32}	β_{31}	β_{32}
T_{b-yz}	0	$\frac{s_s s_n s_t}{2s_b(s_b+s_t)}$	0	$\frac{s_s s_n}{s_b(s_b+s_t)}$
T_{b-xz}	$\frac{s_w s_e s_t}{2s_b(s_b+s_t)}$	0	$\frac{s_w s_e}{s_b(s_b+s_t)}$	0
$T_{b-yz-xz}$	$0.5\alpha_{31}(T_{b-xz})$	$0.5\alpha_{32}(T_{b-yz})$	$0.5\beta_{31}(T_{b-xz})$	$0.5\beta_{32}(T_{b-yz})$
T_{b-4i}	$\alpha_{31}(T_{b-xz})$	$\alpha_{32}(T_{b-yz})$	$\beta_{31}(T_{b-xz})$	$\beta_{32}(T_{b-yz})$
T_{t-yz}	0	$-\frac{s_s s_n s_b}{2s_t(s_b+s_t)}$	0	$\frac{s_s s_n}{s_t(s_b+s_t)}$
T_{t-xz}	$-\frac{s_w s_e s_b}{2s_t(s_b+s_t)}$	0	$\frac{s_w s_e}{s_t(s_b+s_t)}$	0
$T_{t-yz-xz}$	$0.5\alpha_{31}(T_{t-xz})$	$0.5\alpha_{32}(T_{t-yz})$	$0.5\beta_{31}(T_{t-xz})$	$0.5\beta_{32}(T_{t-yz})$
T_{t-4i}	$\alpha_{31}(T_{t-xz})$	$\alpha_{32}(T_{t-yz})$	$\beta_{31}(T_{t-xz})$	$\beta_{32}(T_{t-yz})$

coefficients are zero, and Eqs. (2.23) reduces to the standard central difference stencils. The values of s_i, α_{ij}, and β_{ij} are determined based on the node positions and the neighboring relationship recorded in the neighbor list generated during the refinement processes. Therefore, when solving the SBM-formulated equations with pre-calculated α and β coefficients, the implementation of FDM with AMR is essentially similar to the standard finite difference method.

Instead of storing data in 3D arrays as in typical FDM simulations on uniform Cartesian grid systems, the values of u (which can represent C_p, C_e, ϕ_p, or ϕ_e) are stored in 1D vectors in our work, with the indices to corresponding to the node labels. The labels of neighbor nodes in the FDM stencil, Eq. (2.21), are referenced from the neighbor list created during AMR mentioned earlier.

The flowchart illustrating the simulation procedures is depicted in Fig. 2.3. For a NMC cathode, the lithium fraction is updated using Eq. (2.12) with the Euler explicit time scheme. No-flux boundary conditions are applied to the six faces of the computational domain, including the particle-current collector interface.

Given that the salt diffusivity in the electrolyte is approximately five orders of magnitude larger than the Li diffusivity in the particles, the stable time step for Eq. (2.12) is too large for the Eq. (2.18). Therefore, a fully implicit time scheme with a simple Jacobi relaxation method is utilized for Eq. (2.18) to update the salt concentration in the electrolyte. At the electrolyte-anode interface, a uniform influx (or outgoing flux) of lithium ions, calculated based on the total reaction rate, r_{xn}, is enforced to ensure the conservation of lithium ions. Here, it is the counter domain box boundary to the cathode-current collector box boundary. No-flux boundary conditions are imposed on the remaining five faces of the computational domain.

Within each time step, an internal iteration to solve ϕ_p, ϕ_e, and r_{xn} is implemented as follows. First, Eq. (2.14) is solved for ϕ_p subject to the Dirichlet boundary condition ($\phi_p|_c$) on the electrode current collector. Additionally, the flux boundary condition (r_{xn}) is calculated using Eq. (2.7) on the particle-electrolyte interface. Similarly, ϕ_e is obtained by solving Eq. (2.20) with the Dirichlet boundary condition ($\phi_e|_a$) on the other electrode surface (assumed to be lithium metal for half-cells) and the r_{xn} on the particle-electrolyte interface. No-flux boundary conditions are imposed on the computational domain boundaries, except for those with Dirichlet conditions. Equations (2.14) and (2.20) are solved using a simple Jacobi relaxation method. The obtained values of ϕ_p and ϕ_e are substituted to Eq. (2.7) to calculate r_{xn}. Note that the values of r_{xn} on all the grid points within the diffuse interface are calculated. By multiplying with $|\nabla\psi|$ in Eqs. (2.14) and (2.20), the reaction rates are distributed over the diffuse interface region. The iterative process is repeated until all three fields reach numerical equilibrium. Although more aggressive solvers can potentially accelerate the calculations, we currently do not implement other solvers.

For a constant current simulation, the boundary values ($\phi_p|_c$ or $\phi_e|_a$) are adjusted to match

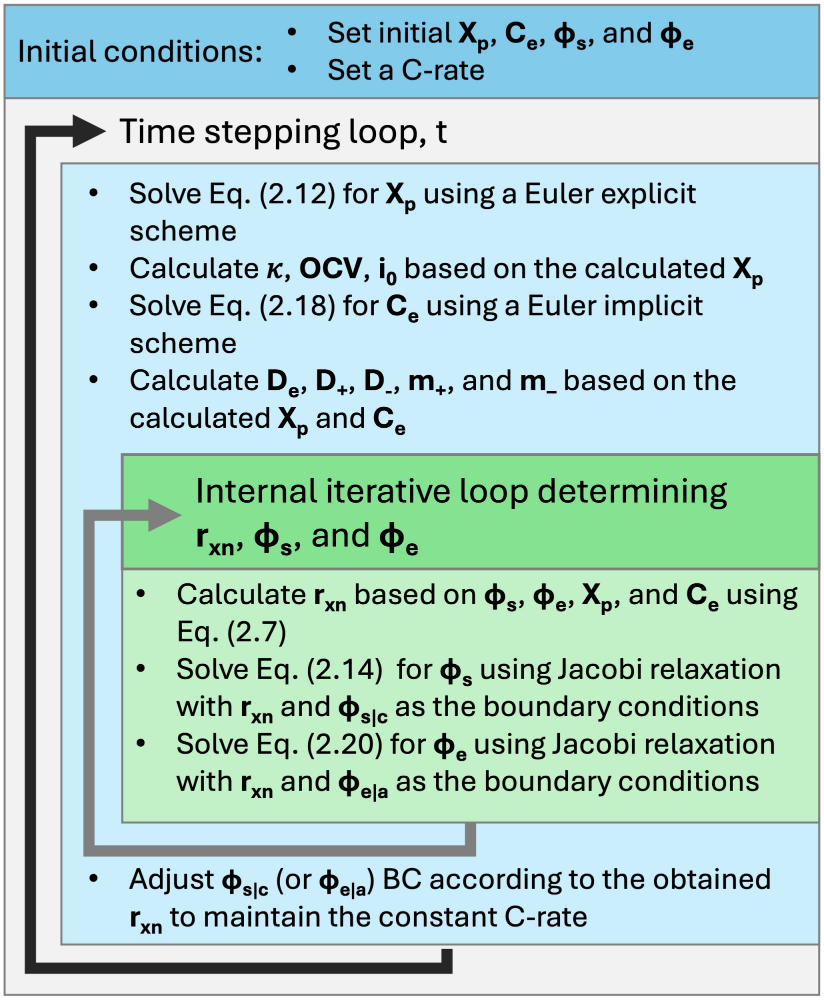

Initial conditions:

- Set initial $\mathbf{X_p}$, $\mathbf{C_e}$, $\boldsymbol{\phi_s}$, and $\boldsymbol{\phi_e}$
- Set a C-rate

Time stepping loop, t

- Solve Eq. (2.12) for $\mathbf{X_p}$ using a Euler explicit scheme
- Calculate κ, **OCV**, $\mathbf{i_0}$ based on the calculated $\mathbf{X_p}$
- Solve Eq. (2.18) for $\mathbf{C_e}$ using a Euler implicit scheme
- Calculate $\mathbf{D_e}$, $\mathbf{D_+}$, $\mathbf{D_-}$, $\mathbf{m_+}$, and $\mathbf{m_-}$ based on the calculated $\mathbf{X_p}$ and $\mathbf{C_e}$

Internal iterative loop determining $\mathbf{r_{xn}}$, $\boldsymbol{\phi_s}$, and $\boldsymbol{\phi_e}$

- Calculate $\mathbf{r_{xn}}$ based on $\boldsymbol{\phi_s}$, $\boldsymbol{\phi_e}$, $\mathbf{X_p}$, and $\mathbf{C_e}$ using Eq. (2.7)
- Solve Eq. (2.14) for $\boldsymbol{\phi_s}$ using Jacobi relaxation with $\mathbf{r_{xn}}$ and $\boldsymbol{\phi_{s|c}}$ as the boundary conditions
- Solve Eq. (2.20) for $\boldsymbol{\phi_e}$ using Jacobi relaxation with $\mathbf{r_{xn}}$ and $\boldsymbol{\phi_{e|a}}$ as the boundary conditions

- Adjust $\boldsymbol{\phi_{s|c}}$ (or $\boldsymbol{\phi_{e|a}}$) BC according to the obtained $\mathbf{r_{xn}}$ to maintain the constant C-rate

Figure 2.3 Flowchart of simulation scheme for solving the coupled governing equations in a half-cell.

the value of $\int |\nabla\psi| r_{xn} d\Omega$ with the desired C rate at each time step. Then, the time-stepping is continued, and the entire procedure is repeated until termination criteria are satisfied (either cutoff voltage or lithium fraction). Based on our tests, the adjustment of $\phi_p|_c$ (or $\phi_e|_a$) boundary value to control the C rate can also be conducted within the internal iteration loop (described above) without significantly impacting the results.

CHAPTER 3

MICROSTRUCTURE-LEVEL SIMULATIONS OF NMC-333 ELECTRODE

3.1 Introduction

This chapter introduces and demonstrates the framework we developed for 3D microstructure electrochemical simulations of electrodes. The framework employs the Smoothed Boundary Method (SBM) [44] introduced in the previous chapter to circumvent the challenge of generating body-conformal meshes on complex electrode microstructures. The SBM-reformulated equations presented in Chapter 2 are solved on 3D microstructures. To mitigate errors incurred from the thickness of the interface in SBM, Adaptive Mesh Refinement (AMR) is also incorporated in the framework to reduce the thickness of the interface. AMR can generate mesh systems such that fine mesh is located near the interface regions and coarse mesh is in the bulk regions as detailed in the previous chapter [49]. Using AMR meshes can decrease the computational burden by reducing the number of grid points in the bulk region while keeping the same interface thickness without sufficiently deteriorating the accuracy. The SBM+AMR method described here was implemented utilizing Finite Difference Method (FDM) stencils akin to those employed in a uniform grid system. FDM was selected due to its simplicity and ease of implementation. Nevertheless, the equations formulated within the SBM framework can also be solved on Adaptive Mesh Refinement (AMR) grid systems employing Finite Element Method (FEM) or Finite Volume Method (FVM).

In this chapter, we showcase the capabilities of our framework through 3D simulations of a $Li_xNi_{1/3}Mn_{1/3}Co_{1/3}O_2$ (NMC-333) cathode. NMC was selected due to its widespread use in contemporary battery applications. We present simulation results for the NMC half cell during discharge and charge cycles at various C rates. First, we validate the accuracy of our simulation framework and investigate its error behavior on a 1D geometry. Subsequently, we extend our analysis to two 3D complex microstructures: one characterized by a non-uniform particle size distribution and the other featuring uniform particle size. Using these simulations we demonstrate the efficacy of the SBM with AMR approach in 3D simulations. Our simulations explicitly calculate the physical fields within the system, including concentrations and electrostatic potentials, while explicitly considering electrode microstructures. While the SBM accurately captures the distribution of these fields as expected, inaccuracies in predicted cell voltages may arise due to the exponential terms in the Butler-Volmer equation when using a diffuse-interface approach, which is studied in this work. Cyclic voltammograms extracted from the simulations for the 3D complex microstructures exhibit behavior consistent with literature data. Additionally, we present thermal and mechanical simulations to highlight the versatility of the SBM+AMR framework in studying discharge/charge-induced multiphysics phenomena. Given the pivotal role of intrinsic material properties in determining electrode performance, we include parameterization of measured data as input simulation parameters. Although our simulations were conducted on computationally generated synthetic electrode microstructures in this study, the proposed method readily extends to simulations on experimentally reconstructed electrode microstructures. By circumventing the need for tedious body-conforming mesh generation processes, this approach enables rapid simulations of complex electrode microstructures. This work was published in Malik et al, Journal of The Electrochemical Society, 169(7):070527, Jul 2022 [24] and significantly influences this chapter.

3.2 Modeling and equations

3.2.1 Governing equations

For NMC, the electrochemical intercalation reaction in (2.1) can be expressed as

$$x\mathrm{Li}^+ + x\mathrm{e}^- + \mathrm{Ni}_{1/3}\mathrm{Mn}_{1/3}\mathrm{Co}_{1/3}\mathrm{O}_2 \rightleftharpoons \mathrm{Li}_x\mathrm{Ni}_{1/3}\mathrm{Mn}_{1/3}\mathrm{Co}_{1/3}\mathrm{O}_2. \tag{3.1}$$

We use the SBM reformulations of the governing equations with AMR and the associated FDM stencils described in Chapter 2 for all the 3D simulations and the diffuse interface 1D simulations. The relevant equations are listed here again for reference. Fick's diffusion equation:

$$\frac{\partial X_p}{\partial t} = \frac{1}{\psi}\nabla \cdot \left(\psi D_p \nabla X_p\right) + \frac{|\nabla \psi|}{\psi}\frac{r_{xn}}{\rho}, \tag{2.12}$$

Current continuity on NMC electrode:

$$\nabla \cdot (\psi \kappa_s \nabla \phi_s) - |\nabla \psi| z_- F r_{xn} = 0, \tag{2.14}$$

Ion diffusion in electrolyte:

$$\frac{\partial C_e}{\partial t} = \frac{1}{\psi_e}\nabla \cdot (\psi_e D_e \nabla C_e) + \frac{|\nabla \psi_e|}{\psi_e}\frac{r_{xn} t_-}{\nu_+} - \frac{\mathbf{i_e} \cdot \nabla t_+}{z_+ \nu_+ F}, \tag{2.18}$$

Current continuity in electrolyte:

$$\nabla \cdot \left[\psi_e \left(z_+ m_+ - z_- m_-\right) F C_e \nabla \phi_e\right] + |\nabla \psi_e| \frac{r_{xn}}{\nu_+} = \nabla \cdot \left[\psi_e \left(D_- - D_+\right) \nabla C_e\right], \tag{2.20}$$

We also use the classical electrochemical governing equations without SBM or AMR for the sharp-interface description for comparison in a 1D simulation shown here —

$$\frac{\partial X_p}{\partial t} = \nabla \cdot \left(D_p \nabla X_p\right), \tag{2.3}$$

$$\nabla \cdot \left(\kappa_s \nabla \phi_s\right) = 0, \tag{2.4}$$

$$\frac{\partial C_e}{\partial t} = \nabla \cdot D_e \nabla C_e - \frac{\mathbf{i_e} \cdot \nabla t_+}{z_+ \nu_+ F} \in \Omega_e, \tag{2.5}$$

$$\nabla \cdot \left[\left(z_+ m_+ - z_- m_-\right) F C_e \nabla \phi_e + \left(D_+ - D_-\right) \nabla C_e\right] = 0, \tag{2.6}$$

These sets of equations are solved in conjunction with the Butler-Volmer equation, Eq. (3.2) in their respective setups. Butler-Volmer equation:

$$r_{xn} = k_f C_+ \exp\left[\frac{-\alpha z_+ F}{RT}\,[\phi]_e^p\right] - k_b C_p \exp\left[\frac{(1-\alpha)\, z_+ F}{RT}\,[\phi]_e^p\right], \tag{3.2}$$

This version of the Butler-Volmer equation differs slightly from the formulation presented in Chapter 2, as it utilizes reaction constants instead of exchange current density. Functionally, both formulations are equivalent because the reaction constants depend on the exchange current density, as detailed further in Section 3.2.2.2. This version of the Butler-Volmer equation is used only in this chapter and was part of our initial framework development. It was later replaced with the formulation presented in Chapter 2 in Eq. (2.7) to eliminate the need for unnecessary additional parameters (reaction constants).

3.2.2 Simulation setup – material parameters

The coupled electrochemical mechanisms and resulting electrode performance are strongly linked to the intrinsic materials properties, which often depend on lithium concentration in both the particles and electrolyte. In this section, we present the procedures for parameterizing measured literature data to establish concentration-dependent material property functions as input simulation parameters.

3.2.2.1 Li diffusivity and electric conductivity

The green circles in Fig. 3.1(a) represent a set of measured Li diffusivity in NMC disk pellets at different average lithium fractions (X) taken from Ref. [64], where the measurements were conducted using electrochemical impedance spectroscopy techniques. The red curve overlaid on the same plot depicts a fitted function derived from those data points and is provided in Appendix B. It is worth noting that although the diffusivity in the region $X < 0.2$ is extrapolated, this approach is acceptable here as the operation range in our simulations is confined to $0.2 < X < 0.95$.

In Fig. 3.1(b), the markers represent the measured electric conductivity of solid NMC disk pellets at various average Li fractions, sourced from [64], where only five data points are available. It is observed that the electric conductivity decreases significantly as X increases. This decline corresponds to a decrease in the valence number of the transition metal elements and an increase in the formation of ionic bonds in the host crystal. A function describing the electric conductivity was fitted from these data points, as indicated by the red curve in Fig. 3.1(b). Any missing values in the low X region were extrapolated. The obtained function is provided in Appendix B. Again, since the operational range in our simulations is above $X = 0.2$, this extrapolation is not expected to result in significant issues.

We assumed a binary electrolyte, with $LiPF_6$ dissolved in an arbitrary organic solvent. The ionic diffusivties for Li^+ and PF_6^- at 1 M of $LiPF_6$ salt in the electrolyte were selected to be 1.25×10^{-7} cm^2/s and 4.0×10^{-6} cm^2/s, respectively as reported in Ref. [45]. Experimental measurements indicate that electrolyte diffusivity varies with salt concentration with high concentration leading to lower diffusivity [65]. Therefore, concentration-dependent ionic diffusivities are considered in our model, while maintaining constant transference numbers as experimentally observed in Ref. [65]. The red curve in Fig. 3.1(c) shows the salt-concentration-dependent ambipolar diffusivity based on the function reported in Ref. [65]. This red curve was normalized to satisfy the D_+ and D_- values at 1 M mentioned above, resulting in a constant transference number $t_- = 0.76 = 1 - t_+$. Any terms associated with ∇t_+ in Eqs. (2.5) and (2.18) vanish in this work. The blue and green curves in the same figure represent the D_+ and D_- functions, respectively. In this work, we assumed the Einstein relation, $m_i = D_i/(RT)$, such that ϕ_e in Eq. (2.20) is solved with salt-concentration-dependent mobilities. Detailed diffusivity functions are provided in Appendix B.

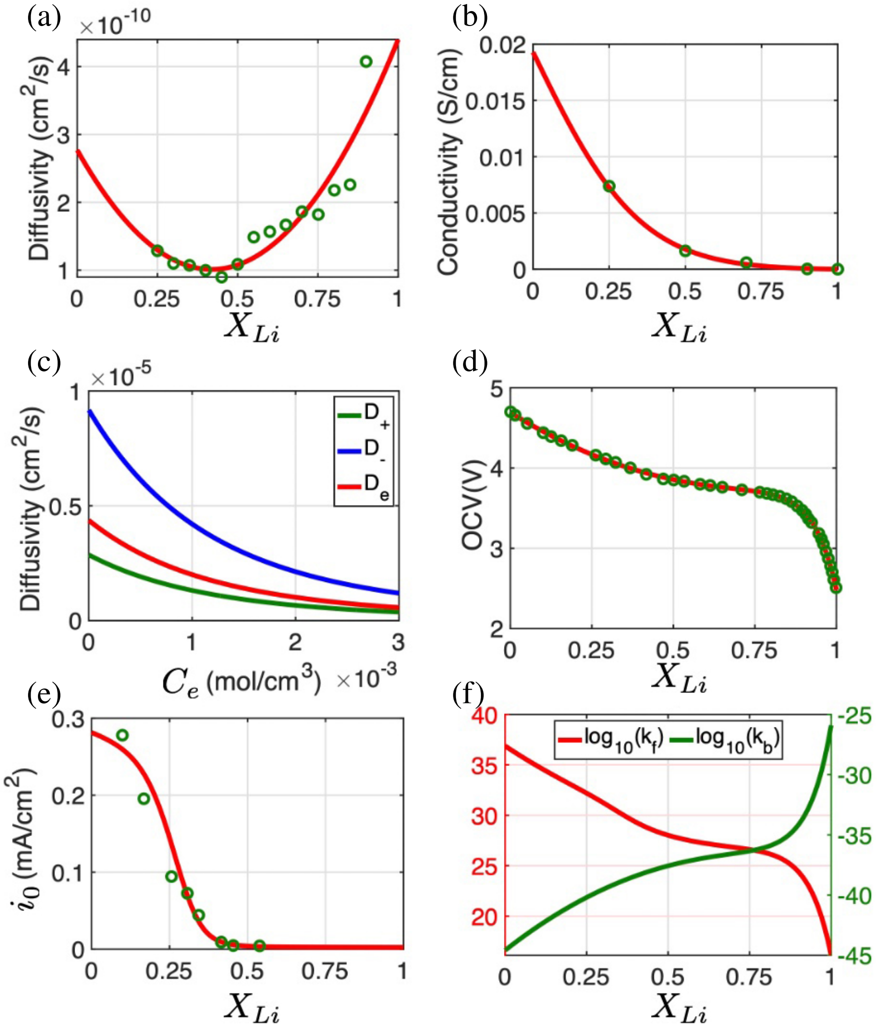

Figure 3.1 (a) Li diffusivity in NMC, (b) electric conductivity in NMC, (c) diffusivity in the electrolyte, (d) OCV as a function of X_{Li}, (e) exchange current density as a function of X_{Li} at $C_e = 1$ M, and (f) calculated forward and backward reaction constants from the exchange current density and OCV. The unit of k_f and k_b is s^{-1}.

3.2.2.2 Open circuit voltage (OCV), exchange current density, and rate constants in the Butler-Volmer equation

The open circuit voltage (OCV) refers to the electrostatic potential difference between the cathode and anode at a zero net current, i.e., the equilibrium cell voltage that counterbalances the lithium chemical potential difference between the cathode and anode. Mathematically, the cell voltage (ϕ) is related to the chemical potential of charge-carriers by $\phi = -\left(\mu_{\mathrm{Li}}^{\mathrm{cathode}} - \mu_{\mathrm{Li}}^{\mathrm{anode}}\right)/\mathrm{e}$, where e is the elementary charge and μ_{Li}^{i} is the chemical potential of lithium in corresponding electrodes.

In quasi-equilibrium OCV measurements, the Li concentration is nearly uniform throughout all cathode particles for Li solid-solution materials. Lithium salt concentration is also almost uniform in the electrolyte, with a typical value of 1 M. Metallic Li foils are generally used as the reference anode in such OCV measurements, making $\mu_{\mathrm{Li}}^{\mathrm{anode}}$ a constant value. The data points (green markers) in Fig. 3.1(d) represent ϕ_{OCV} for an NMC cathode [66], with a fitted function (the red curve). Since OCV is measured at near-equilibrium conditions, $\phi_{\mathrm{OCV}} = \phi_{eq}$, which is used to calculate the reaction constants from the Butler-Volmer equation as shown later. On a particle surface $[\phi]_e^p - \phi_{eq}$ is typically referred to as the surface overpotential. The fitted OCV function is provided in Appendix B.

Exchange current density (i_0) is the current density on the electrolyte-particle interfaces where the net anodic and cathodic reactions are at equilibrium. Therefore, it can be used along with measured equilibrium potential (ϕ_{eq}) to calculate the reaction constants for the Butler-Volmer equation. The exchange current density values (i_0) can be measured experimentally using techniques such as Tafel plotting or impedance techniques. The green markers in Fig. 3.1(e) represent reported values of i_0 at different Li fractions, measured using impedance techniques of single NMC particles [67]. However, the data points are scarce and unavailable beyond $X > 0.54$. A fitted function (the red curve), including extrapolations, is provided in Appendix B.

The intercalation reaction at electrode-electrolyte interfaces is described by Eq. (3.1), where the forward and backward reactions occur simultaneously. The first and second terms in Eq. (3.2) correspond to the rates of the forward and backward reactions, respectively. At equilibrium, the net reaction is zero, and $[\phi]_e^p$ is the equilibrium potential, which is also the OCV ($[\phi]_e^p = \phi_{eq} = \phi_{\mathrm{OCV}}$). Thus, solving

$$k_f C_+ \exp\left[\frac{-\alpha z_+ F}{RT}\phi_{eq}\right] = k_b C_p \exp\left[\frac{(1-\alpha) z_+ F}{RT}\phi_{eq}\right], \tag{3.3}$$

leads to the reaction rate constants as

$$k_f = \frac{i_0}{z_+ F C_+}\exp\left(\frac{\alpha z_+ F}{RT}\phi_{eq}\right), \text{ and } k_b = \frac{i_0}{z_+ F C_p}\exp\left(\frac{(\alpha-1) z_+ F}{RT}\phi_{eq}\right), \tag{3.4}$$

where $C_+ = C_e$ [mol/cm^3] and $C_p = \rho X_p$. For NMC, $\rho = 0.0501$ mol/cm^3. The calculated k_f and k_b are given in Fig. 3.1(f) as the red and green curves, respectively, based on the OCV in Fig. 3.1(d) and i_0 in Fig. 3.1(e). The i_0 here for calculating rate constants have a unit of mA/cm^2.

3.3 Simulation results and discussion

3.3.1 Pseudo 1-D results

A 1D virtual half-cell was created by setting the left region ($x < 12.1$ μm) to be the electrolyte and the right region ($x > 12.1$ μm) to be a 1D particle. The total length of the domain is 18 μm, and the size of the 1D particle is 6 μm. The grid system in Fig. 3.2(a) shows the setup for the 1D sharp-interface simulation, in which the light blue grid points and the light gray grid points indicate the regions for the electrolyte and particle, respectively. The particle-electrolyte interface is located between light blue and light gray grid points. The grid spacing is uniformly $\Delta x = 0.2$ μm. In the sharp-interface simulation, 1D versions of Eqs. (2.3) and (2.4) were solved in the right domain, and 1D versions of Eqs. (2.5) and (2.6) were solved in the left domain. The r_{xn} was calculated between the two grid points on the two different sides of the interface. The simulation was performed following the procedure described in the previous section.

In the SBM, the domain parameter is defined by a hyperbolic tangent function $\psi = 0.5 \times \big(1 + \tanh(d/\zeta)\big)$, where ζ is a parameter controlling the thickness of the diffuse interface and d is the signed distance function to the interface. Here, $d = x - 12.1$ μm. Figure 3.2(b) shows the ψ profiles for the zero-level (Lv0, blue dots) and two-level (Lv2, red circles) refinements. The grid spacing at the root level is the same as in the sharp-interface case. Here, $\zeta = 1.5\Delta x/(2^0)$, $1.5\Delta x/(2^1)$, and $1.5\Delta x/(2^2)$ in the Lv0, Lv1, and Lv2 cases, respectively, such that the diffuse interfaces span approximately six smallest grid spacings in all three cases but the interfacial thickness in Lv2 case is 1/4 of that in Lv0. Note that the interfacial thickness in SBM serves as a numerical parameter to control the modeling error between the diffuse-interface and sharp-interface approaches. It is not the thickness of the physical particle-electrolyte interface. We used quadtree refinement to generate the grid systems for the simulations. The domain parameter has no gradient in the lateral direction such that the 2D simulation is equivalently 1D (i.e., pseudo-1D simulations). Figure 3.2(c) shows the pseudo-1D domain parameters used in the Lv0 and Lv2 simulations. The gradient of ψ near the particle-electrolyte interface in the Lv2 case is much sharper than that in the Lv0 case. The Lv2 quadtree refined grid system is shown in Fig. 3.2(d), in which the root-level, first-level, and second-level cells can be clearly distinguished. Equations (2.12), (2.14), (2.18), and (2.20) were

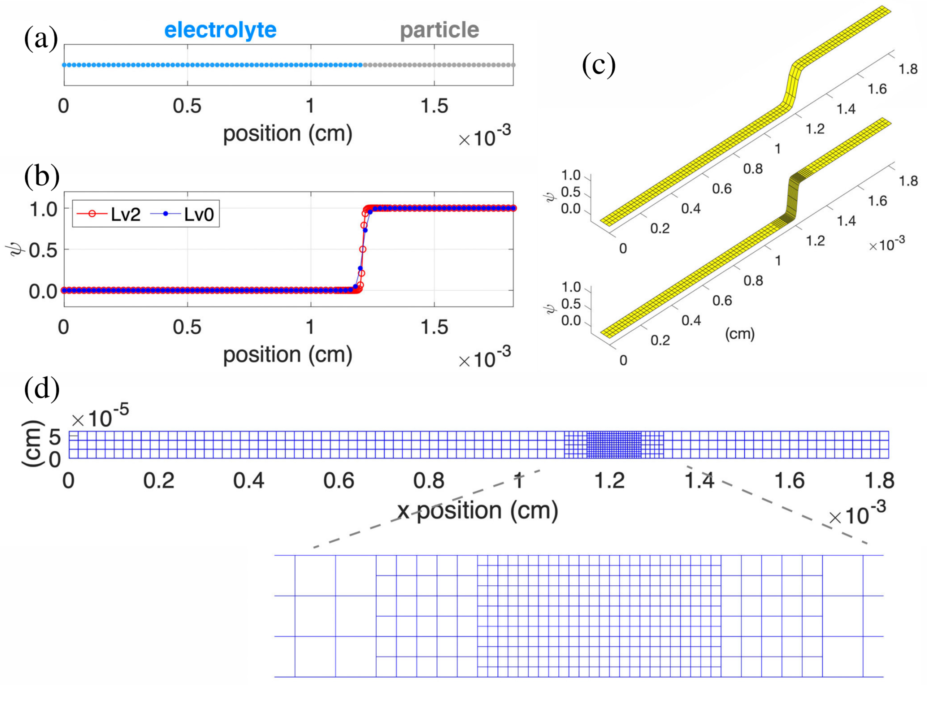

Figure 3.2 (a) Computational domain of 1D electrochemical simulations in the sharp-interface model. The light blue and gray dots are the grid points for the electrolyte and particle domains, respectively. (b) The ψ_p profiles along the primary direction in the Level-0 and Level-2 AMR cases. (c) The domain parameter ψ_p in the pseudo-1D SBM simulations. The interfacial thickness is controlled to be approximately 4–6 grid spacings. (d) The Level-2 quadtree refined grid system in the pseudo-1D SBM simulations.

solved on the grid system following the procedure mentioned in the previous section. Note that since Eq. (2.12) was solved using the Euler explicit scheme, the smallest stable time step in the Lv2 case is 1/16 of that in Lv0. However, we used $\Delta t = 1.25 \times 10^{-4}$ s, which is stable for all the pseudo-1D simulations, to mitigate the numerical errors associated with different Δt sizes. X_p was initially uniform 0.2 throughout the NMC particle, and C_e was uniform 1 M (0.001 mol/cm^3) throughout the electrolyte. The electrostatic potential ($\phi_e|_a$) on the anode was fixed, and the current collector's potential ($\phi_p|_c$) was continuously adjusted during the simulations to maintain constant C-rates for the discharge (lithiation). In this work, the cell capacity was defined according to the lithiation range from $X = 0.2$ to 0.95, a typical utilization range of layered transition metal oxides. This range is selected because exfoliation between layers occurs when $X < 0.2$ and the material transforms into an electrical insulator when $X > 0.95$. A cutoff cell voltage of 2.5 V was set to terminate the discharge simulations.

Figures 3.3(a) through (d) show the simulated C_e, X_p, ϕ_e, and ϕ_p profiles, respectively, taken at $t = 346.73$ s ($X = 0.48$) during a 3C lithiation (discharge) process. The gray, blue, and red curves are obtained from the sharp-interface, Lv0, and Lv2 cases, respectively. The purple dashed vertical lines indicate the position of the particle-electrolyte interface ($\psi = 0.5$ at $x = 12.1$ μm), on the left/right of which is the electrolyte/particle domain (shaded in blue/gray color). In the SBM simulations, the obtained values of C_e and ϕ_e in the particle region (gray-shade areas in Figs. 3.3(a) and (c)) have no physical meaning [44, 68, 69]. Similarly, the values of X_p and the ϕ_p in the electrolyte (blue-shade regions in Figs. 3.3(b) and (d)) have no physical meaning. Note that while Lv1 simulation was also performed, its results are not presented to keep the clarity of the plot. As shown by the gray, blue, and red curves in Fig. 3.3(a), C_e in the electrolyte decreases as the position moves toward the particle-electrolyte interface, indicating that Li ions flow to the particle-electrolyte interface. The obtained C_e profiles in the three results almost overlap within the electrolyte region. Across the interface, Li is intercalated into the particle, raising X_p at the particle surface. X_p gradually decreases towards the current collector (the right domain boundary). The X_p profiles have flat tails at the current collector ($x = 18$ μm) due to the no-flux boundary condition imposed there. The X_p profiles from the three simulations almost overlap within the particle, except for the values in the regions within the diffuse interface on the left of the purple dashed line. In Figs. 3.3(a) and (b), the red curves overlap the gray ones more closely than the blue ones do, reflecting the fact that the SBM results approach the sharp-interface one as the interfacial thickness decreases, which is achieved by using a higher level of refinement.

The ϕ_e profiles in Fig. 3.3(c) have a shape similar to that of C_e profiles in Fig. 3.3(a). The negative gradient of ϕ_e indicates Li-ion flux pointing toward the particle. Due to the high ionic mobility (equivalently the electric conductivity) in the electrolyte, the variations of ϕ_e throughout the electrolyte region are small. Figure 3.3(d) shows the simulated ϕ_p profiles. Since the electric conductivity of NMC at $X \sim 0.48$ is high, the gradients of ϕ_p throughout the particle in the three presented results are very small, see Fig. 3.3(e) for a magnified view of (d). Uniform shifts between the ϕ_p from SBM and sharp-interface results are observed: the difference between Lv0 and sharp-interface results is approximately 56 mV, while the difference between Lv2 and sharp-interface results is approximately only 3 mV. When those shifts are subtracted from the SBM results, the ϕ_p profiles in the Lv0 and Lv2 simulations overlap well with the sharp-interface one, except for values in the diffuse interfaces. Throughout the simulations, high ϕ_p gradients only appear when NMC is close to being fully lithiated, which is consistent with the fact that the electric conductivity is low when $X > 0.95$. The C_e, X_p, ϕ_e, and ϕ_p profiles from Lv1 simulation are similar to the Lv2 ones. The uniform shift between ϕ_p from Lv1 and sharp-interface results is approximately 8 mV. The agreements between the obtained SBM profiles and sharp-interface ones manifest that the SBM-formulated equations can properly produce results close to the sharp-interface ones with the same boundary conditions. The accuracy increases with a thinner interfacial thickness [44]. In this pseudo-1D test, Lv0 SBM and sharp-interface simulations are still in good agreement even though the interface is thick (spanning over six root-level grid points).

The cell voltage is the electrostatic potential difference between the current collector and anode plate as $V_C = \phi_p|_c - \phi_e|_a$. Figure 3.4(a) shows the V_C curves recorded during 3C discharge from the 1D sharp-interface, Lv0, Lv1, and Lv2 SBM simulations, with the OCV on the same plot for comparison. In the sharp-interface case, V_C monotonically decreases from 4.2 to 2.5 V as X increases from 0.2 to 0.65 until the simulation reaches the cutoff voltage; see the solid green curve in Fig. 3.4(a). The shape of the V_C curve exhibits some similarity to the OCV curve but with an overpotential 0.5–1 V below the OCV curve. ($V_C - \phi_{OCV}$ is the cell overpotential.) The V_C from the

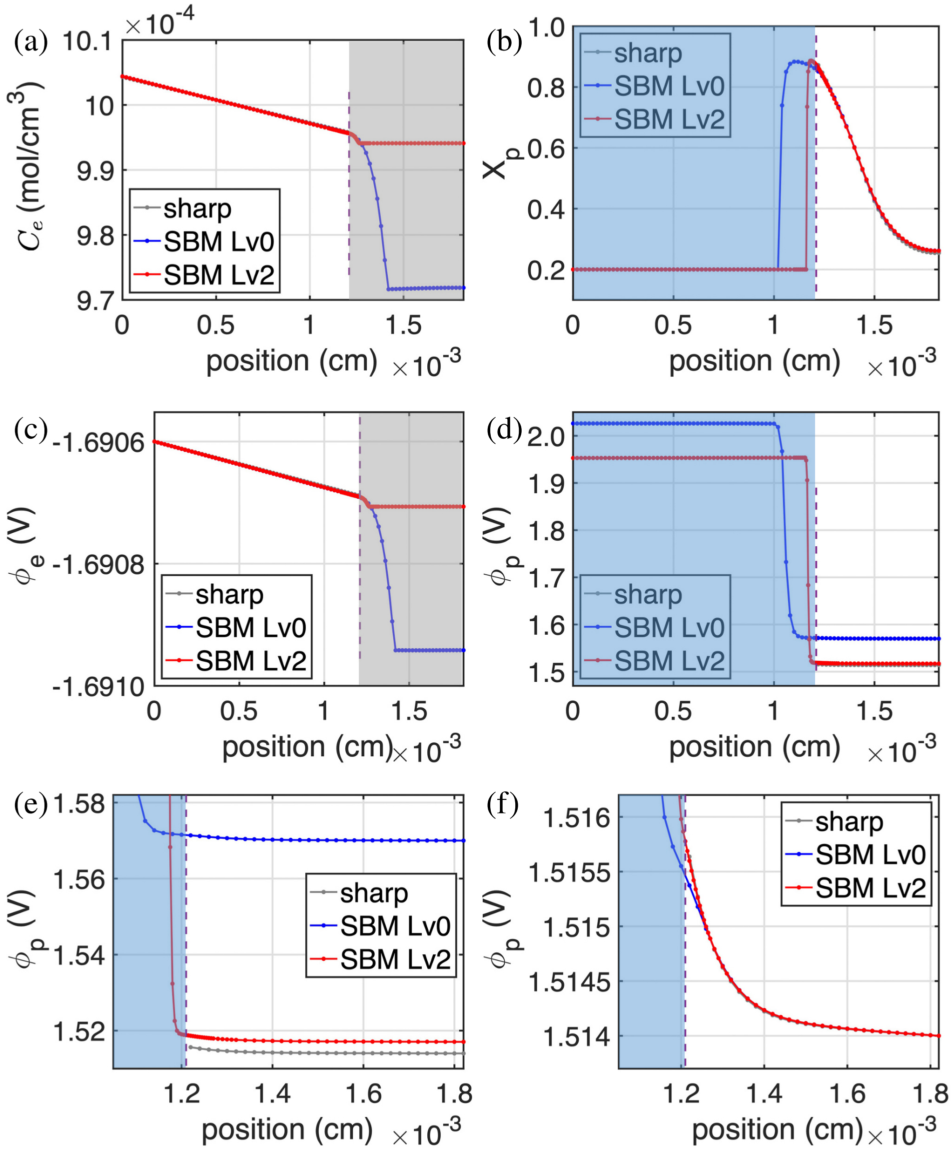

Figure 3.3 Simulated (a) C_e, (b) X_p, (c) ϕ_e, and (d) ϕ_p profiles along the primary direction in the sharp, SBM Lv0, and SBM Lv2 cases. The profiles are taken under 3C lithiation at $\bar{X} = 0.48$ and $t = 346.73$ s. (e) Magnified view of ϕ_p in the particle region. (f) ϕ_p profiles after subtracting the differences in the boundary values of ϕ_p. Note that the gray curves in (a), (b), (c), (d), and (f) closely overlap with the respective red curves because of the high accuracy of Lv2 simulations. The gray and blue shaded regions denote the domain of particle and electrolyte regions.

Lv2 simulation mostly overlaps with the sharp-interface one, except for a slight deviation near the end of the simulation; see the dashed green curve in Fig. 3.4(a). The V_C curve (the cyan curve) from the Lv1 simulation overlaps well with the sharp-interface one in the range $0.2 < X < 0.55$; however, its deviation from the green curve increases as $X > 0.55$. The V_C curve from the Lv0 simulation significantly deviates from the sharp-interface result, especially when $X > 0.5$. As mentioned earlier, the C_e, X_p, and ϕ_e profiles from SBM simulations well overlap the sharp-interface ones, but the ϕ_p profiles exhibit uniform shifts from the sharp-interface result. The deviation between Lv0 and sharp-interface V_C curves is due to that uniform shift in the ϕ_p profiles. This shift decreases as the interfacial thickness is thinner with a higher level of refinement.

All the concentration and potential profiles have almost identical shapes, indicating that the SBM can properly solve the governing equations with the flux boundary conditions imposed at the particle-electrolyte interface. However, as the interfacial thickness increases, the variations of ϕ_e and ϕ_p over the diffuse interface increase, which further leads to the variation of $[\phi]_e^p$. Due to the presence of the exponential terms in the Butler-Volmer equation (Eq. (2.7)), with a thicker interface, a slight decrease of $\phi_p|_c$ is enough to maintain the magnitude of r_{xn} during the simulation. Therefore, the cell voltage in the Lv0 simulation is significantly overestimated. This effect is more pronounced when the magnitude of r_{xn} is larger. Namely, at a higher C rate, the overestimation

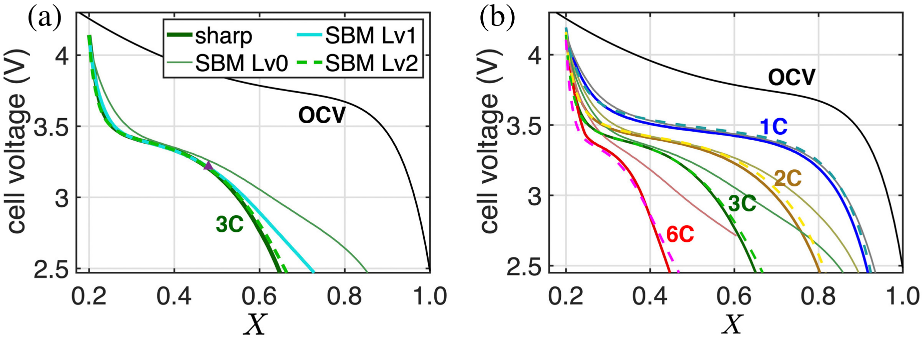

Figure 3.4 (a) Simulated cell voltage at 3C lithiation of the 1D cases. The solid dark green curve is from the sharp-interface simulation. The thin gray-green curve, cyan curve, and dashed green curve are from the SBM pseudo-1D with 0, 1, and 2 levels of quadtree refinement. (b) Simulated cell voltages at different C rates of the 1D cases. Note that the solid curves, thin curves, and dashed curves are from the sharp-interface, Lv0, and Lv2 SBM-AMR simulations, respectively. For the clarity of view, figure legends are not included.

will be more prominent. Figure 3.4(b) shows simulated V_C curves at 1, 2, 3, and 6C discharge. For clarity of view, legends are removed from the figure. At 1C discharge, which requires a relatively lower cell overpotential, the V_C curves from Lv0, Lv2, and sharp interface simulations overlap well. As the C rate increases, a larger cell overpotential is needed, and the Lv0 results deviate more away from the sharp-interface ones, see the corresponding V_C curves in Fig. 3.4(b). However, since the interfacial thickness in the Lv2 case is very thin, the Lv2 results are still close to the sharp-interface ones. Compared to the Lv0 curves, the Lv1 ones have less deviation from the sharp-interface results, but they are not presented in the figure for clarity of view. In these pseudo-1D simulations, two levels of refinement are sufficient to match the sharp-interface result. The 1D studies also indicate that thick interfaces can be adequate in low C-rate simulations, but thin interfaces will be necessary to maintain the accuracy of V_C in high C-rate simulations.

3.3.2 3-D simulations of synthetic NMC-333 microstructure

The capabilities of simulating coupled electrochemical processes in complex electrode microstructures were demonstrated via simulating discharge-charge cycles of 3D microstructures containing multiple NMC particles, in which the presented SBM equations were solved using FDM on AMR grids.

3.3.2.1 Log-normal particle size distribution

The 3D complex geometry simulations used synthetic cathode microstructures computationally generated via discrete element method (DEM) [70], in which the particle radii follow a truncated log-normal distribution with a lower bound at 6 μm and an upper bound at 12.5 μm. There were 119 spheres initially randomly placed in a rectangular domain. Those particles were relaxed, under an arbitrary body force in the $+x$ direction, and eventually ‘descended’ to the current collector. This agglomerate was truncated on the east, south, north, bottom, and top sides to fit the rectangular computational domain, as the virtual cell is shown in Fig. 3.5(a).

The root-level computational domain was $200 \times 190 \times 150$ grid points in the x, y, and z directions and with a grid spacing of $\Delta x = 0.5$ μm. A signed distance function (positive values inside particles) from each grid point to the particle-electrolyte interface was calculated using the level-set distancing method [62]. The ψ function was obtained by substituting the distance function into the hyperbolic tangent function as in the previous sections. The total reactive surface area was approximately 7.92×10^4 μm^2 obtained by summing all triangular isosurface patches generated by MATLAB for the particle-electrolyte interfaces. The total volume of NMC agglomerate in the virtual cell was around 3.04×10^5 μm^3 and the solid volume fraction was around 0.656 calculated for the region $40 < x < 100$ μm. In this work, we do not include porous microstructures of separator membranes due to the lack of such information. Instead, the empty space ($0 < x < 32$ μm) between the virtual anode and cathode serves as the separator. Hereafter, this set of simulations is referred to as the LN case. Simulations on Lv0, Lv1, and Lv2 were performed, for which the total numbers of grid points are 5,700,000, 17,232,520, and 63,758,793. The refinement thresholds were 2.20 and 1.05 root-level Δx for Lv1 and Lv2, respectively. In the SBM, generally, at least four to six grid spacings across the interface should be used to ensure numerical stability. In the 3D

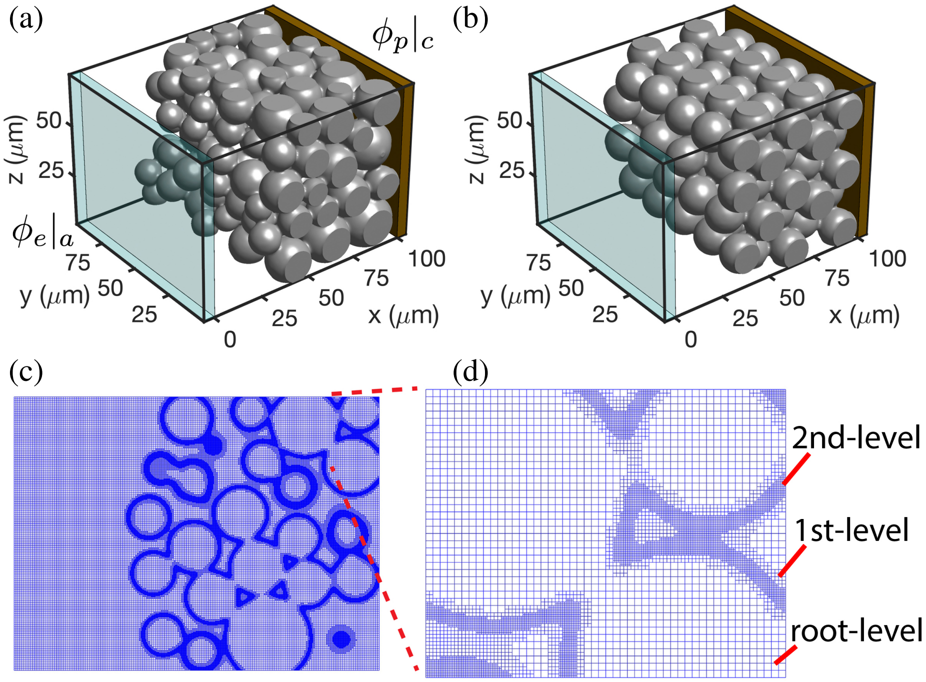

Figure 3.5 (a) The virtual cell generated using the DEM result of 119-particle agglomerate and (b) the virtual cell generated using the DEM result of 119 equal-sized particle agglomerate. (c) Lv2 AMR grid on the plane of $y = 47.5$ μm of the NMC cathode microstructure in (a). (d) Magnified view of a portion of (c), in which root-level, 1st-level, and 2nd-level cells can be clearly seen.

cases, we chose four grid spacings, compared to six grid spacings in the pseudo-1D cases earlier, across the interfacial region to decrease the total number of grid points after AMR. Again, as in the pseudo-1D cases, we used the same time step ($\Delta t = 4 \times 10^{-3}$ s) for all three levels of simulations. Figures 3.5(c)-(d) show the Lv2 grid on the plane at $y = 47.5$ μm, in which the refinement in particle surface regions can be clearly seen. Since the AMR grid is non-conformal to the irregular particle-electrolyte interfaces, the refinement is fast. The Lv2 grid system (~64 million grid points) was generated within 1.5 minutes using 32 CPUs with Message Passing Interface (MPI) on the High-Performance Computing Center(HPCC) nodes at Michigan State University.

Figure 3.6(a) shows the simulated cell voltage curves of 6C and 1C discharge-charge cycles for this synthetic microstructure with Lv0, Lv1, and Lv2 AMR. The cutoff voltages are set at 2.5, and 4.2 V. Similar to the 1D case, the V_C curves of 6C discharge deviate more from the OCV curve than

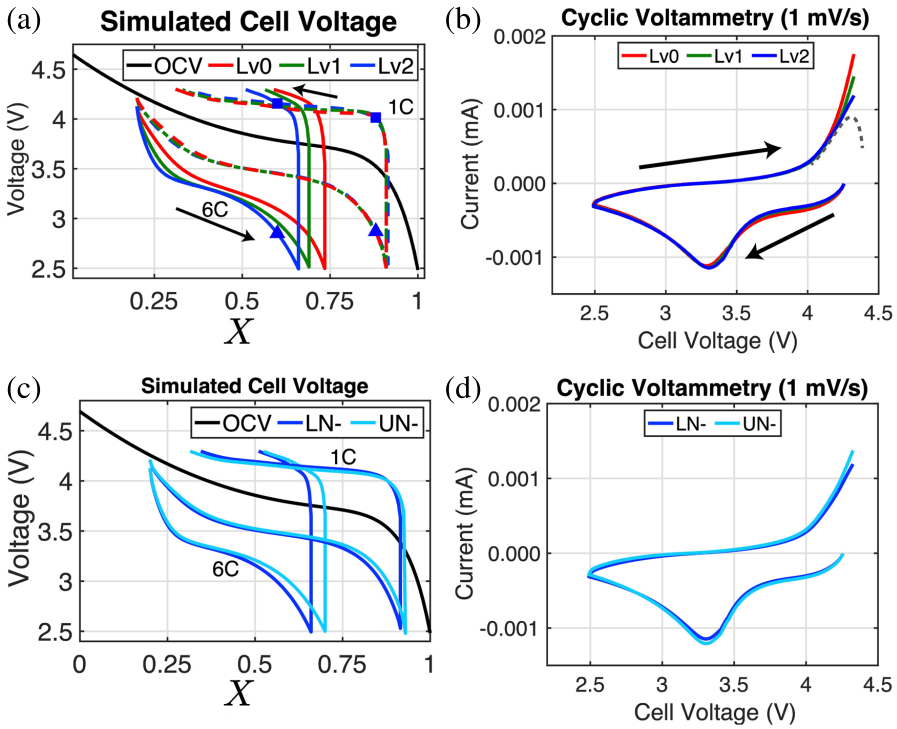

Figure 3.6 (a) Simulated cell voltage for 1C and 6C lithiation in the LN synthetic microstructure. (b) Simulated cyclic voltammograms at 1 mV/s for the LN microstructure. SBM Lv0, Lv1, and Lv2 results are marked in red, green, and blue colors, respectively. and (c) Simulated cell voltage curves for 6C and 1C lithiation in the LN, and UN microstructures. (d) Simulated cyclic voltammograms at 1 mV/s in the LN, and UN microstructures. The results are from SBM Lv2 simulations.

the 1C discharge curves do. Hysteresis can be observed in the V_C curve loops. A ~1.1 V voltage gap presents between the discharge and charge curves of the 6C cycle, and a ~0.7 V voltage gap exists in the V_C loop of the 1C cycle. The V_C curves of the three different levels of AMR in the 1C case are almost overlapping. In the 6C case, significant deviations between the V_C curves of the Lv0, Lv1, and Lv2 simulations are observed. The variation between the Lv1 and Lv2 curves is much smaller than that between the Lv0 and Lv1 curves. As demonstrated in the 1D case, a thinner diffuse interface, which is achieved by using a higher-level AMR grid, will increase the accuracy of SBM simulations. High levels of refinement are more effective in enhancing modeling accuracy in high C-rate cases, where large overpotentials are expected.

The C_e, X_p, ϕ_e, and ϕ_p at $t = 320$ s ($X = 0.6$, corresponding to the blue triangle on the 6C curve in Fig. 3.6(a)) during 6C discharge in Lv2 simulation are shown in Figs. 3.7(a) through (d), respectively. The general observations are similar to those in the 1D simulations. Negative C_e and ϕ_e gradients along the $+x$ direction are seen in Fig. 3.7(a) and (c), indicating Li-ion flow toward the NMC cathode during discharge. Significant depletion of Li salt concentration ($C_e \sim 2 \times 10^{-4}$ mol/cm^{-3}) occurs near the cathode current collector region, leading to less intercalation in that area. Core-shell concentration distribution of X_p is clearly observed in all the NMC particles (see Fig. 3.7(b)). However, the ϕ_p does not show similar core-shell patterns in NMC particles. Instead, a negative ϕ_p gradient along $+x$ direction over the entire NMC cathode is observed in Fig. 3.7(d). This difference originates from the fact that ϕ_p can reach equilibrium distribution immediately while X_p requires time for diffusion (i.e., Eq. (2.14) is static but Eq. (2.12) is time-dependent), in addition to the effect of different boundary conditions imposed on the east computational domain boundary.

Figures 3.7(e) and (f) show C_e and X_p during the charge process at $X = 0.6$ (corresponding to the blue square on the 6C curve in Fig. 3.6(a)). As expected, C_e exhibits a positive gradient $+x$ direction as Li-ions are moving away from the NMC cathode. Because diffusion through the tortuous interparticle space limits the transport of Li-ions toward the anode, high C_e is observed near the current collector ($x \sim 100$ μm). During charge, deintercalation starts from the particle

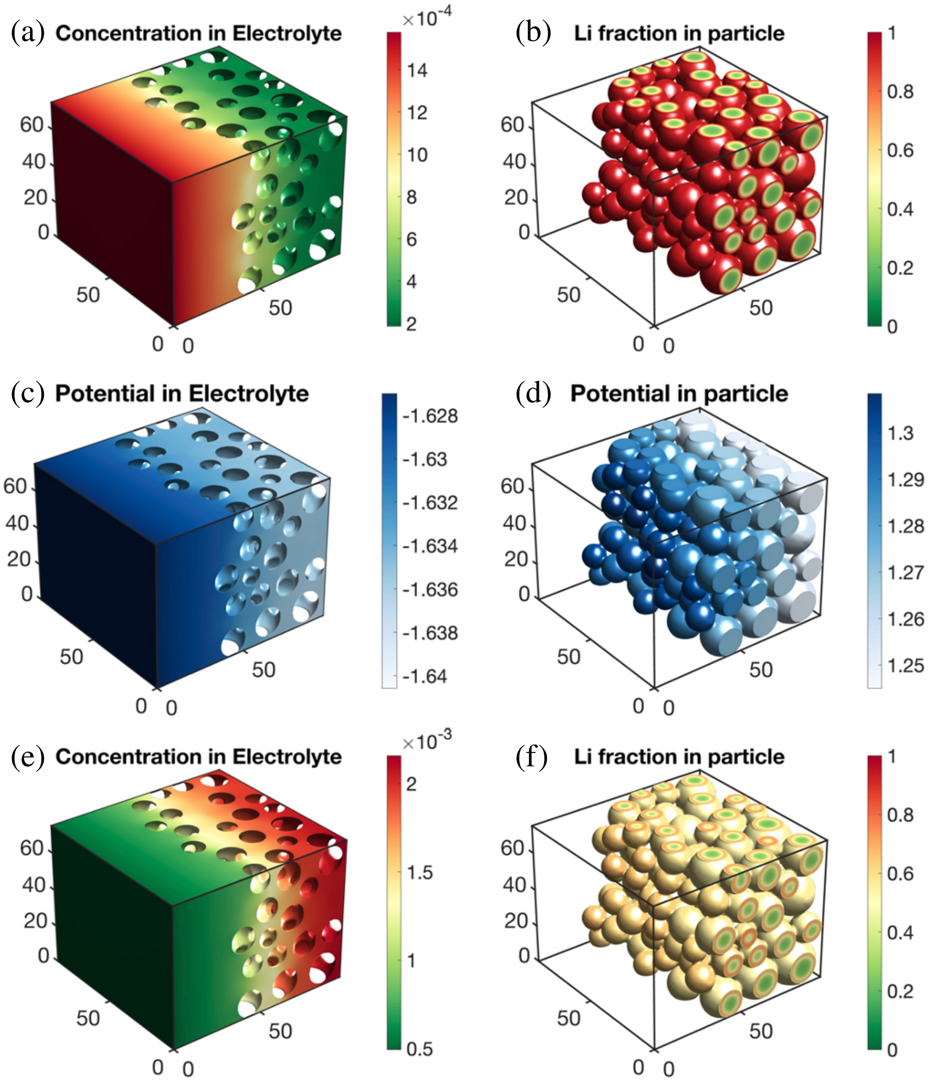

Figure 3.7 Simulated (a) C_e, (b) X_p, (c) ϕ_e, and (d) ϕ_p distributions under 6C lithiation at $t = 319.37$ s and $X = 0.595$. (e) C_e and (f) X_p profiles under 6C delithiation at $t = 429.07$ s and $X = 0.595$. The distributions are for LN synthetic microstructure in the SBM Lv2 case.

surfaces. In this set of simulations, the charge process followed the discharge immediately once the cell voltage reached the cutoff value (2.5 V). Thus, an interesting core-shell X_p distribution is exhibited in the particles as shown in Fig. 3.7(f): low-high-low X_p profile along the radial direction inward. If stress is considered, such an onion-layer concentration distribution would be detrimental, leading to cracks in the particles.

C_e and X_p during 1C discharge at $t = 3290$ s ($X = 0.88$, corresponding to the blue triangle on the 1C Lv2 curve in Fig. 3.6(a)) are provided in Figs. 3.8(a) and (b), respectively. This point is selected to be at the same cell voltage as in Figs. 3.7(a)–(b). Compared to the 6C case, the C_e gradient along the primary direction and X_p gradient along the radial direction in the 1C case is small.

When the system was switched to the charge mode, Li ions were released to the electrolyte. The process starts in the regions near the separator, as indicated by the increased C_e shown in Fig. 3.8(c), taken at $X = 0.88$ corresponding to the blue square on the 1C charge curve in Fig. 3.6(a).

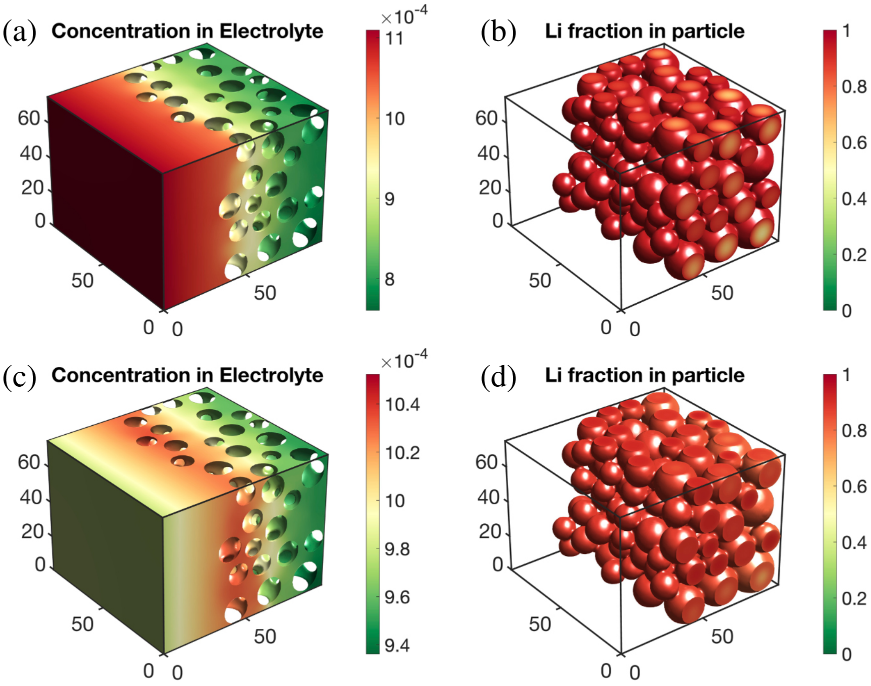

Figure 3.8 Simulated (a) C_e, (b) X_p distributions under 1C lithiation $t = 3290.00$ s and $X = 0.880$. (c) C_e and (d) X_p distributions under 1C delithiation at $t = 3659.61$ s and $X = 0.880$. The distributions are for LN synthetic microstructure in the SBM Lv2 case.

The reaction region will eventually expand over the entire NMC cathode. Since the C rate was low, the X_p distribution was fairly uniform in the particles as can be seen in Fig. 3.8(d), taken at the same X corresponding to when Fig. 3.8(c) was taken. In this 1C simulation, deintercalation began roughly uniformly over the cathode because the NMC particles were moderately conductive at the beginning of the charge. Our other test simulations exhibited different behavior: deintercalation was more concentrated near the current collector at the start (where electrons left the systems) because the entire NMC electrode was insulating if the charge began at a very high Li fraction (e.g., $X > 0.95$).

Cyclic voltammetry is a widely used technique to study Faradaic reactions versus redox potentials. The measurements are conducted by varying the loading voltage to a cutoff value and sweeping back at a constant scan rate (units of mV/s). The reaction current is recorded during the sweeping and plotted against the cell voltage. Figure 3.6(b) shows cyclic voltammograms obtained at a scan rate of 1 mV/s from our simulations for the three levels of refinement. The cell voltage was set to sweep over 4.2 → 2.5 → 4.2 V. The entire sweeping took approximately 3400 s. The overall discharge-charge rate might be around a 2–3 C rate. Since the C rate was not large, the simulated cyclic voltammograms from the three AMR levels almost overlap. In the discharge sweep, as the cell voltage decreased, the magnitude of reaction current increased up to where the cell voltage was ~3.3 V, after which the magnitude of current decreased. In the charge sweep, the magnitude of the current monotonically increased until reaching the cutoff voltage. Interestingly, the voltammograms did not drop toward the end of the charge sweeps as in many experimental observations [71, 72] in which a typical voltammogram near the end of the sweep should behave like the gray dashed curve in Fig. 3.6(b): reaction current fades as the particles are close to fully delithiated. Here, we attribute the rise at the end of simulated voltammograms mainly to the fact that the i_0 used in the simulations monotonically increases as X_{Li} decreases (see Fig. 3.1(e)), which is different from general expectations for transition metal oxide cathode materials: low exchange current density when particles are close to fully delithiated or fully lithiated [45, 56, 73–75]. Also, the cutoff was set to be significantly away from the fully delithiated state ($X \sim 0$).

An Lv3 simulation of a 6C discharge was performed to verify whether the Lv2 simulations were sufficiently accurate. The Lv3 mesh system contains 244,033,870 grid points (approximately four times that in the Lv2 case), which was generated in 17 minutes. The V_C curve from the Lv3 simulation is shown in Fig. 3.9. The obtained curve (gray) is close to that from Lv2 (blue), although a small difference can still be discerned in the early and later stages of the simulations. The 6C Lv2 discharge simulation took ~8 hours with MPI parallel computing on 160 CPUs. The code scaling was fairly linear: the Lv3 simulations required approximately four times the computational hours. Since the difference between Lv3 and Lv2 results is small, we did not further pursue simulations with higher levels of refinement. Furthermore, as concluded in the 1D case, the 3D simulations also suggested that AMR is needed for high C-rate simulations. For low C rate simulations, using root-level grids can be adequate. As mentioned earlier, AMR can significantly reduce the total number of grid points. We conducted a performance test of the code on a uniform grid with a grid spacing equal to the refined Lv1 Δx. The system contains a total of 45,215,079 grid points, which is 2.62 times the AMR one. The computation time for the uniform grid case was 10.3 hours (to $X = 0.58$ at a 6C lithiation on 80 CPUs), which is approximately 2.23 times the AMR one (4.67

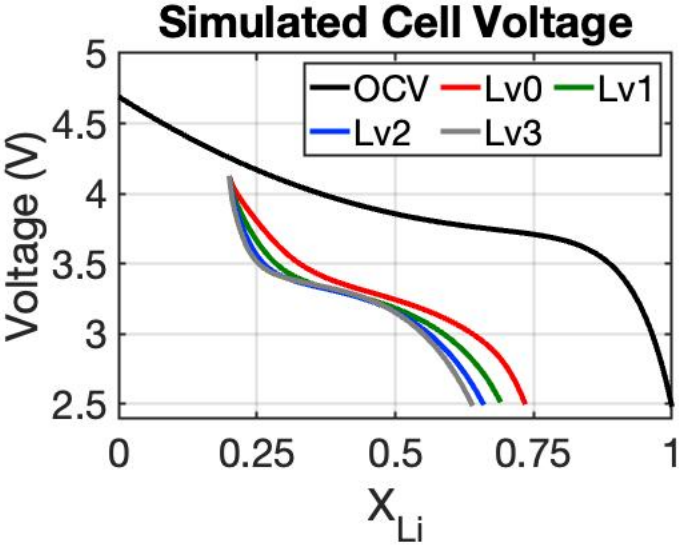

Figure 3.9 Simulated cell voltage for 6C lithiation in LN synthetic microstructure for SBM Lv0, Lv1, Lv2, and Lv3 cases. The Open Circuit Voltage (OCV) curve is shown in black. The Lv0, Lv1, Lv2, and Lv3 curves are marked in red, green, blue, and gray colors, respectively.

hours). A slight super-linear speed-up is observed, which we attribute to the possible reasons: (1) a decrease in the operations of multiplying the correction factors, and (2) the convergence rate in Jacobi relaxation is faster in the uniform-grid case. This comparison clearly demonstrates the efficiency of AMR in reducing the computation burden.

Moreover, we used an Allen-Cahn type phase-field approach to remove the cusps in the initial geometries generated from the DEM particle arrangements, as in Ref. [44]. We set 40 Allen-Cahn steps in this work. The smoothing slightly increased the particle contact areas. The particle contacts can affect the overall electric conduction in the electrode. Since NMC is reasonably conductive, we do not expect a significant change in the results. Nevertheless, investigating how the contact areas affect the electrochemical performance of an electrode can be a future topic.

3.3.2.2 Uniform particle size distribution

Another synthetic microstructure was created by DEM with equal-sized 119 spheres (radius of 8.6 μm) to demonstrate the microstructure's effects on electrode performance. This radius was chosen such that the total volume of the 119 particles was approximately the same as that in the previous case. Hereafter, this set of simulations is referred to as the uniform (UN) case. The resulting virtual cell is shown in Fig. 3.5(b). The total reactive surface area, NMC solid volume, and solid volume fraction are 8.39×10^4 μm^2, 3.05×10^5 μm^3, and 0.643, respectively. While the total solid volume is similar to the LN case, the reactive surface is approximately 6% more than in the previous case. The volume fraction in the UN case is slightly lower than that in the LN case because the smaller particles can fit into the space between large particles in the LN case. Only Lv2 simulations were performed in this set of simulations. There were 67,337,857 grid points in the mesh system with 2.20 and 1.05 for the Lv1 and Lv2 refinement criteria, respectively. All initial and boundary conditions were the same as in the LN case.

The cyan curves in Fig. 3.6(c) are the 6C and 1C V_C curves obtained from the UN simulations. The trends are generally similar to those in Fig. 3.6(a), but the 6C curve during discharge in the UN case is slightly above that in the LN case. The 6C charge curve is on the right to that in the LN case. This is expected because the UN case has a larger reactive surface area and slightly higher porosity than the LN case, which leads to better electrochemical performance and smaller overpotential. It is noticed that the discrepancy between the 6C discharge curves is more pronounced at the late stage, which is due to the increase in electric resistance of NMC particles at a high Li fraction. The NMC particles have high Li concentration near the surfaces, thus forming high-resistance shells. As a result, the effect of increasing active surface area to reduce overpotential is more significant. The 1C curves of the UN case similarly show a slightly smaller overpotential compared to the LN case, also because the UN case has a slightly larger active surface area. Cyclic voltammetry was also simulated in the UN case with the identical setup as in Section 3.3.2.1. The voltammogram shown in Fig. 3.6(d) is slightly below that of the LN case during the discharge sweep and slightly above the LN curve during the charge sweep; i.e., the reaction current magnitude of the UN case is slightly larger. This is also expected as the reactive surface area in the UN case is larger than that in the LN case.

The behavior of C_e, X_p, ϕ_e, and ϕ_p distributions are similar to those in Section 3.3.2.1. Therefore, we do not show those 3D results here. Figure 3.10 shows the C_e, X_p, ϕ_e, and ϕ_p averaged within the corresponding phases on each y-z plane, taken at $V_C = 2.875$ V ($X = 0.6$ and 0.63 for the LN and UN cases, respectively). The C_e and ϕ_e curves have similar shapes: linear in the separator region ($0 < x < 32$ μm), and the values decay asymptotically as the position approaches the cathode current collector, reflecting that the intercalation reactions occur in the cathode region. The profiles from the LN and UN cases almost overlap. However, the X_p profile (yellow curve in Fig. 3.10(b)) in the UN case exhibits pronounced undulation, which is very different from that in the LN case (red curve). The undulation reflects the periodicity of particle arrangement when the particles have similar sizes. The valleys in the X_p profile (yellow curve) indicate the locations of particle centers in different layers, while the peaks correspond to the regions of particle-particle contacts. This fact can be discerned in the ϕ_p profile as well, where the layers of particle centers have a larger cross-section area, resulting in a smaller electric resistance. The particle-particle contact regions have smaller contact areas, leading to a larger electric resistance. As a result, the ϕ_p in the UN case exhibits a step-like curve, in which the high-slope regions have high resistance.

Because the LN case has a disordered particle arrangement, its X_p and ϕ_p profiles are smoother. Interestingly, the nature of DEM tends to descend larger (heavier) particles to the bottom (the cathode current collector in this case). The valley in the red curve in Fig. 3.10(b) and the step in the blue curves in Fig. 3.10(d) both reflect that there is a layer of large particles with center positions near $x \sim 90$ μm. While profiles similar to those in the LN case can be obtained from conventional PET simulations, the undulation and steps in X_p and ϕ_p profiles in the UN case are difficult to detect. This is because the length scale of ordered particle arrangement is significantly larger than the scale of Δx in PET simulations. These subtle features resulting from particle arrangements can only be observed when microstructures are explicitly considered. The presented 3D simulation method can be utilized to calculate the effective homogeneous electrode properties. Those input parameters will improve the macroscopic approximations in PET simulations.

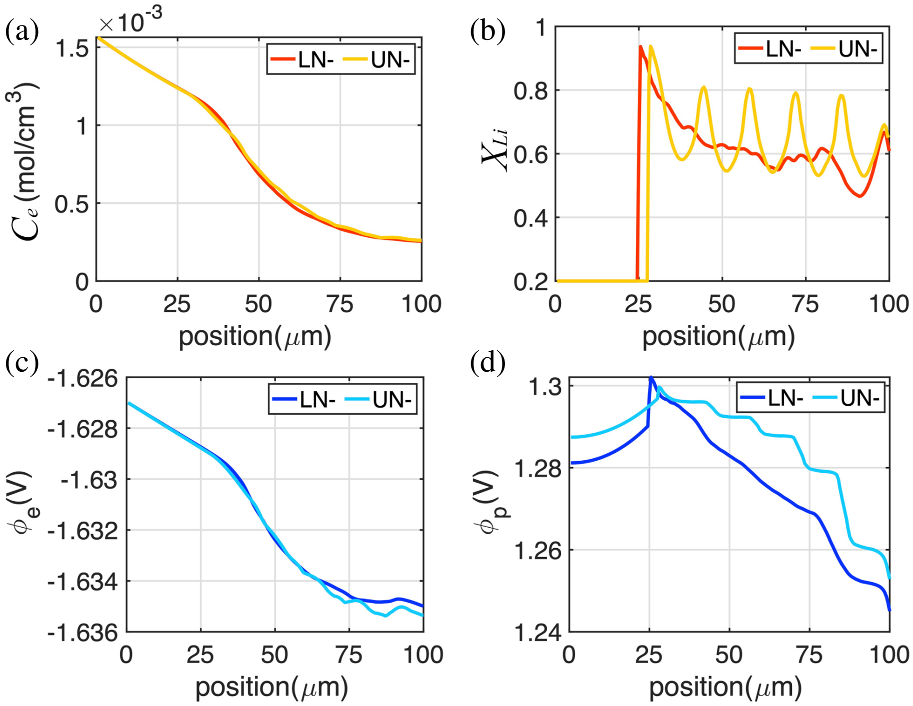

Figure 3.10 (a) C_e, (b) X_p, (c) ϕ_e, and (d) ϕ_p profiles along the primary direction (x-axis), obtained by averaging the values in the corresponding phases on the y-z planes, in the LN and UN Lv2 cases. The profiles are taken under 6C lithiation at V_C = 2.875 V.

3.4 Extension to Multiphysics phenomena

The differential equation solvers and AMR grids can be employed to study other phenomena accompanying electrochemical processes. Heat transport and linear elastic mechanics associated with charge/discharge cycles are chosen to demonstrate the adaptability of the SBM+AMR framework. Since we intend to promote the diffuse-interface method for simulating complex electrode phenomena, the investigation of those additional physics is left for future extensions.

3.4.1 Thermal simulations

Joule heating occurs during electrochemical processes. Heat is generated in the particles, electrolyte, and particle-electrolyte interfaces associated with the electrical currents. The temperature evolution equation can be derived based on energy balance with a diffuse-interface description as shown in the next section. Here, we ignore any other thermal and thermoelectric effects, such as enthalpy, the Seeback effect, the Peltier effect, and others. The only source of heat is Joule heating.

3.4.1.1 Equations and Parameters

The heat equation governs temperature evolution in the particles based on the conservation of energy:

$$\rho_p s_p \frac{\partial T}{\partial t} = \nabla \cdot \lambda_p \nabla T + \frac{i_p^2}{\kappa_p} \in \Omega_p, \tag{3.5}$$

with the boundary condition of heat flux: $\mathbf{n}_p \cdot \lambda_p \nabla T = -\dot{q}_p \in \partial\Omega_p$, where T is the temperature, ρ_p is the density, s_p is the specific heat, λ_p is the thermal conductivity, and κ_p is the electrical conductivity of the particles. i_p is the magnitude of electrical current density in the particle as defined in Section 2.1.1 and the term i_p^2/κ_p accounts for the Joule heating in the particles. $\dot{q}_p$ is the magnitude of inward heat flux density normal to the particle surface and related to the temperature gradient according to the Fourier 1st law. Similarly in the electrolyte, we can write

$$\rho_e s_e \frac{\partial T_e}{\partial t} = \nabla \cdot \lambda_e \nabla T_e + \frac{i_e^2}{\kappa_e} \in \Omega_e, \tag{3.6}$$

with the boundary condition: $\mathbf{n}_e \cdot \lambda_e \nabla T_e = -\dot{q}_e \in \partial\Omega_e$, where the subscript e indicates electrolyte. Note that $\dot{q}_e = \mathbf{n}_p \cdot \lambda_e \nabla T_e$ since $\mathbf{n}_e = -\mathbf{n}_p$. The electrical conductivity of the electrolyte is related to the ionic diffusivities and salt concentration by

$$\kappa_e = F\left(\frac{D_+}{RT} + \frac{D_-}{RT}\right)FC_e, \tag{3.7}$$

which has the same physical unit as κ_p. The two heat equations can be formulated to the SBM version as:

$$\rho_p s_p \psi_p \frac{\partial T_p}{\partial t} = \nabla \cdot \psi_p \lambda_p \nabla T_p + \psi_p \frac{i_p^2}{\kappa_p} + |\nabla \psi_p| \dot{q}_p, \tag{3.8}$$

$$\rho_e s_e \psi_e \frac{\partial T_e}{\partial t} = \nabla \cdot \psi_e \lambda_e \nabla T_e + \psi_e \frac{i_e^2}{\kappa_e} - |\nabla \psi_p| \dot{q}_e, \tag{3.9}$$

where $\psi_e = 1 - \psi_p$. Summing Eqs. (3.8) and (3.9) leads to

$$\begin{aligned}\left[\psi_p \rho_p s_p + (1-\psi_p)\rho_e s_e\right]\frac{\partial T}{\partial t} = \nabla \cdot \left[\psi_p \lambda_p + (1-\psi_p)\lambda_e\right]\nabla T + \\ \left[\psi_p \frac{i_p^2}{\kappa_p} + (1-\psi_p)\frac{i_e^2}{\kappa_e}\right] + |\nabla \psi_p| \cdot Fr_{xn} \cdot \left([\phi]_e^p - \phi_{eq}\right),\end{aligned} \tag{3.10}$$

Note that the energy balance at the particle surface is described by

$$\dot{q}_e - \dot{q}_p + i \cdot \left([\phi]_e^p - \phi_{eq}\right) = 0 \Longrightarrow \dot{q}_p - \dot{q}_e = Fr_{xn} \cdot \left([\phi]_e^p - \phi_{eq}\right), \tag{3.11}$$

where $i \cdot \left([\phi]_e^p - \phi_{eq}\right)$ accounts for the Joule heating across the particle-electrolyte interface. The material properties used in the thermal simulation are $\rho_p = 4.476$ g/cm^3, $s_p = 0.8036$ J /(g·K), $\lambda_p = 0.0175$ W/(cm·K), $\rho_e = 1.249$ g/cm^3, $s_e = 1.6478$ J /(g·K), $\lambda_e = 0.0017$ W/(cm·K) [76, 77]. The unit of T is K.

3.4.1.2 Simulation results

Equation (3.10) was solved using the Crank-Nicolson time scheme on the Laplace term because the Δt for Eq. (2.12) is too large for a stable time integration here. The thermal conductivity (λ_p) is approximately nine orders of magnitude larger than the particles' Li diffusivity (D_p). Note that the material properties (such as diffusivities, exchange current density, electrical conductivity, and thermal conductivity) were still set to be the values at 300 K in the electrochemical simulations. At the same time, the accompanying temperature evolution was simulated. The temperature-dependent effects of those material properties were ignored because the required data were not widely accessible.

Figure 3.11(a) shows the simulated evolution of average cell temperature during a 6C discharge cycle in Section 3.3.2.1. An adiabatic boundary condition was imposed on this simulation. The temperature consistently rose as thermal energy was continuously generated. Our analysis shows that the surface reaction (the last term in Eq. (3.10)) dominated the total heat generation as the voltage drop across the particle-electrolyte interface was much greater than the electropotential variations in the particles or electrolyte. It is acknowledged that the total temperature increase may be overestimated, which is attributed to the fact that the exchange current used here is very small when $X > 0.35$ on particle surfaces. If a larger i_0 in that region is used, the particle-electrolyte interface voltage drop would be much smaller such that significantly less heat would be generated during the charge transfer reaction.

The temperature distribution in the cell is fairly uniform, as shown in Fig. 3.11(b): the overall temperature variation is less than 0.01 K. This result is expected because the thermal conductivities

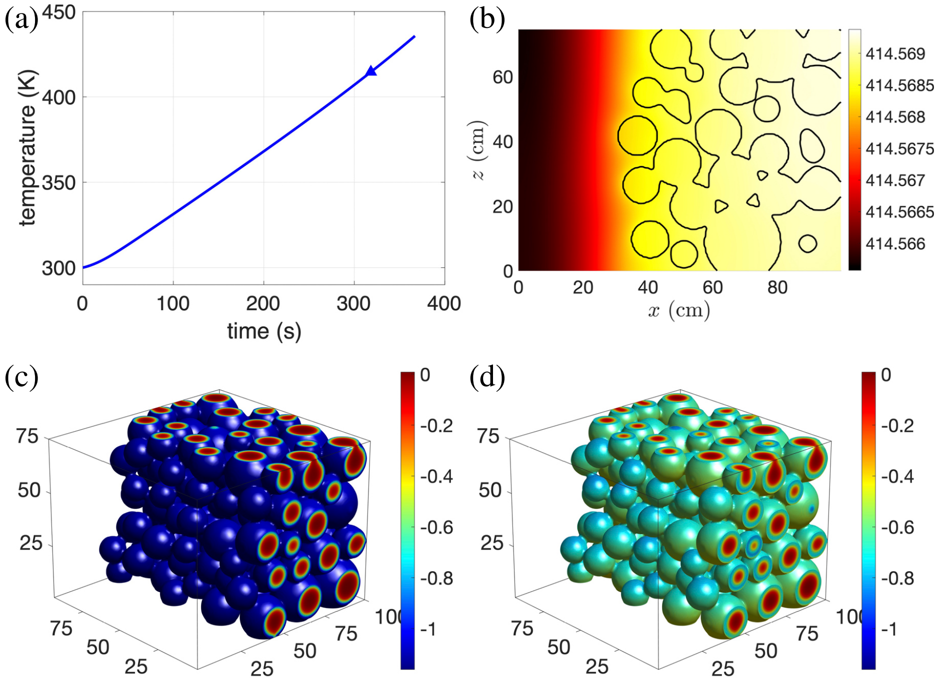

Figure 3.11 (a) Simulated cell temperature versus time during 6C discharge. (b) Temperature on the x-z plane at $y = 47.5$ μm. The black contour lines indicate the particle surface. Calculated dilation stresses at $X = 0.595$ at 6C (c) discharge and (d) charge, corresponding to the Li fraction in Figs. 3.7(b) and (f), respectively. The unit on the color bar is GPa.

in the particles and electrolyte are much larger than the respective diffusivities. Thus, the temperature field can reach its near-equilibrium distribution very quickly. This set of thermal simulations exhibits the transferability of the SBM+AMR method in solving other relevant governing equations and highlights the impact of input material parameters on the prediction.

3.4.2 Mechanical Simulations

Lithiation/delithiation leads to the expansion/contraction of electrode particles. In the linear elastic regime, the SBM-formulated mechanical equilibrium equation is given as [44, 78]

$$\frac{\partial}{\partial x_j}\left[\psi_p L_{ijkl}\frac{1}{2}\left(\frac{\partial u_k}{\partial x_l}+\frac{\partial u_l}{\partial x_k}\right)\right]+|\nabla\psi_p|N_i=\frac{\partial}{\partial x_j}\left(\psi_p L_{ijkl}\varepsilon^0_{kl}\right), \tag{3.12}$$

where L_{ijkl} is the elastic constant tensor, u_i is the displacement, ε^0_{kl} is the eigenstrain due to lattice expansion/contraction upon lithiation/delithiation, and the repeated indices indicate Einstein notation of summation. N_i is the surface traction along the i-th axial direction. For a free surface, the second term on the left-hand side vanishes.

3.4.2.1 Equations and parameters

The Young's modulus of NMC is $E_L = 142.5$ and $E_D = 117.0$ GPa at $X = 1$ and 0 [79], where the subscripts L and D denote fully lithiated and delithiated states, respectively. A simple Vegard's law gives $E = E_D+(E_L-E_D)X = E_D\cdot p(X)$ GPa, where $p(X) = 1+(E_L/E_D-1)X$. For an isotopic case, the Voigt notation can be used to define $C_{11} = L_{1111}$, $C_{12} = L_{1122}$, and $C_{44} = L_{1212}$. Those quantities are related to Young's modulus and Poisson's ratio as $C_{11} = E(1+2\nu)/(1+\nu)/(1-2\nu) = C^D_{11}p(X)$, $C_{12} = E\nu/(1+\nu)/(1-2\nu) = C^D_{12}p(X)$, and $C_{44} = E/2/(1+\nu) = C^D_{44}p(X)$, where the superscript D denotes the quantities at the delithiated state. We assume the value of Poisson's ratio is a constant $\nu = 0.25$ [80]. The relative volume expansion of a unit NMC lattice cell is +1.7% [67] from $X = 0$ to 1. Assuming a linear interpolation, the eigenstrain is $\varepsilon^0_{11} = \varepsilon^0_{22} = \varepsilon^0_{33} = (0.017/3)(X - X^0) = 0.0057(X - X^0) = \varepsilon^0(X - X^0)$, where X^0 is the reference stress-free composition. Equation (3.12) is expanded along the three coordinate directions as

$$\begin{gathered}
C_{11}^D\frac{\partial}{\partial x}\left(\psi p(X)\frac{\partial u}{\partial x}\right)+C_{44}^D\frac{\partial}{\partial y}\left(\psi p(X)\frac{\partial u}{\partial y}\right)+C_{44}^D\frac{\partial}{\partial z}\left(\psi p(X)\frac{\partial u}{\partial z}\right)= \\
(C_{11}^D+2C_{12}^D)\varepsilon^0\frac{\partial}{\partial x}\left(\psi p(X)(X-X^0)\right)- \\
\left[C_{12}^D\frac{\partial}{\partial x}\left(\psi p(X)\frac{\partial v}{\partial y}\right)+C_{44}^D\frac{\partial}{\partial y}\left(\psi p(X)\frac{\partial v}{\partial x}\right)+C_{12}^D\frac{\partial}{\partial x}\left(\psi p(X)\frac{\partial w}{\partial z}\right)+C_{44}^D\frac{\partial}{\partial z}\left(\psi p(X)\frac{\partial w}{\partial x}\right)\right],
\end{gathered} \tag{3.13a}$$

$$\begin{gathered}
C_{44}^D\frac{\partial}{\partial x}\left(\psi p(X)\frac{\partial v}{\partial x}\right)+C_{11}^D\frac{\partial}{\partial y}\left(\psi p(X)\frac{\partial v}{\partial y}\right)+C_{44}^D\frac{\partial}{\partial z}\left(p(X)\frac{\partial v}{\partial z}\right)= \\
(C_{11}^D+2C_{12}^D)\varepsilon^0\frac{\partial}{\partial y}\left(\psi p(X)(X-X^0)\right)- \\
\left[C_{12}^D\frac{\partial}{\partial y}\left(\psi p(X)\frac{\partial u}{\partial x}\right)+C_{44}^D\frac{\partial}{\partial x}\left(\psi p(X)\frac{\partial u}{\partial y}\right)+C_{12}^D\frac{\partial}{\partial y}\left(\psi p(X)\frac{\partial w}{\partial z}\right)+C_{44}^D\frac{\partial}{\partial z}\left(\psi p(X)\frac{\partial w}{\partial y}\right)\right],
\end{gathered} \tag{3.13b}$$

$$\begin{gathered}
C_{44}^D\frac{\partial}{\partial x}\left(\psi p(X)\frac{\partial w}{\partial x}\right)+C_{44}^D\frac{\partial}{\partial y}\left(\psi p(X)\frac{\partial w}{\partial y}\right)+C_{11}^D\frac{\partial}{\partial z}\left(\psi p(X)\frac{\partial w}{\partial z}\right)= \\
(C_{11}^D+2C_{12}^D)\varepsilon^0\frac{\partial}{\partial z}\left(\psi p(X)(X-X^0)\right)- \\
\left[C_{12}^D\frac{\partial}{\partial z}\left(\psi p(X)\frac{\partial u}{\partial x}\right)+C_{44}^D\frac{\partial}{\partial x}\left(\psi p(X)\frac{\partial u}{\partial z}\right)+C_{12}^D\frac{\partial}{\partial z}\left(\psi p(X)\frac{\partial v}{\partial y}\right)+C_{44}^D\frac{\partial}{\partial y}\left(\psi p(X)\frac{\partial v}{\partial z}\right)\right].
\end{gathered} \tag{3.13c}$$

Here, we have used x, y, and z to replace x_1, x_2, and x_3 in the coordinates, and u, v, and w to replace u_1, u_2, and u_3, respectively, in the displacements. These equations are solved using the Jacobi relaxation similar to the electro-potential solvers. For each of the equations, the displacement on the left-hand side was relaxed according to the value on the right-hand side, and the obtained value was updated to the right-hand side of the next equation. This process was repeated until all displacements reached numerical equilibrium.

3.4.2.2 Simulation results

Equation (3.12) can be solved with fully anisotropic mechanical properties if those data are available. However, only isotropic calculations were performed, as a demonstration of solving Eq. (3.12) on an AMR grid, due to the lack of available data. Here, the stress-free state was assumed to be the initial state of the electrochemical cycling, i.e., $X_p = 0.2$. Figures 3.11(c) and (d) show the calculated dilatational stress $\sigma_{dil} = \left(\sigma_{11} + \sigma_{22} + \sigma_{33}\right)/3$ stemming from cycling, corresponding to the X_p distribution in Figs. 3.7(b) and (f), respectively. As Li was inserted into the particles, the host lattice near the particle surface expanded. However, the expansion was constrained by the lattice coherency imposed in the model, thus exhibiting compressive stress as shown in the deep blue color in Fig. 3.11(c). As Li was extracted upon charging, the compressive state was relaxed as indicated by the light blue to green colors shown in Fig. 3.11(d). As a numerical demonstration, we did not include strain energy as an additional driving force for Li transport, which can be easily incorporated into the electrochemical simulation if needed. The presented calculation shows the ease of performing cycling stress simulations using SBM on AMR grids, although the mechanical equilibrium equation is a more complicated tensor equation. The investigation of mechanical physics is beyond the current scope.

3.5 Comparison with FEM COMSOL solver

The accuracy of the SBM-AMR solver was verified with a commercial FEM software, COMSOL. In both pseudo-1D and single sphere 3D cases, the SBM-AMR produces nearly identical results to the COMSOL ones. Since we do not have access to the coupled electrochemistry module in COMSOL, the comparison was made only for X_{Li} with a constant insertion flux. Figure 3.12(a) shows the pseudo-1D simulation results using COMSOL and SBM-AMR with Lv2 grid at $t = 350$ s. The element size in COMSOL was set to be similar to the root-level grid spacing. A flux of 3C insertion was imposed at $x = 0$ μm and a constant diffusivity $D = 1 \times 10^{-10}$ cm^2/s was set in both simulations. The black dashed line in Fig. 3.12(a) indicates the position of the left boundary, at which the flux boundary condition was imposed.

Note that some additional domain was included in the SBM case since the diffuse interface is an internal boundary in the computational domain. The profiles of X_{Li} along the x direction are provided in Fig. 3.12(b), which shows the two results closely match each other. Figures 3.12(c) and (d) show the simulated concentrations in a spherical particle of a 6 μm radius obtained from COMSOL and the SBM-AMR solver, respectively. The images correspond to the time at 350s under a constant insertion flux of 3C rate. The same constant diffusivity as in the pseudo-1D case above was used in the 3D test. Again, the two results are almost identical, as can be verified by the X_{Li} profiles along the radial positions in Fig. 3.12(e).

3.6 Conclusions

We demonstrate the novel framework utilizing the Smoothed Boundary Method (SBM) with Adaptive Mesh Refinement (AMR) to simulate electrochemical processes within electrode microstructures, facilitating the prediction of electrode performance. This approach eliminates the need for laborious body-conforming mesh generation tasks typically associated with conventional sharp-interface methods, thereby significantly accelerating the pre-processing time for complex microstructure simulations. First, we conduct 1D simulations to investigate error behaviors. Comparative analysis between 1D SBM simulations and sharp-interface simulations reveals the SBM's

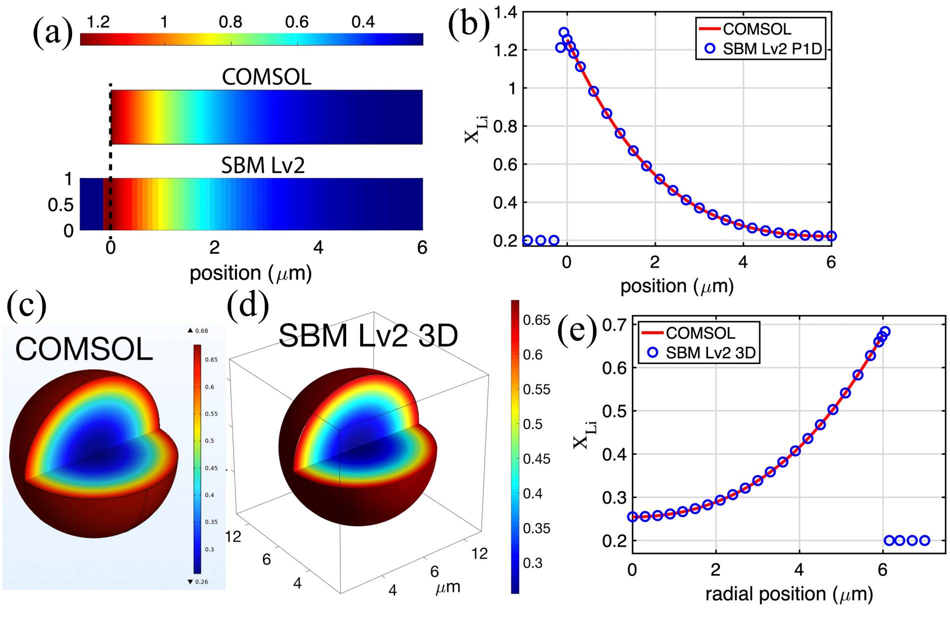

Figure 3.12 Verification of SBM-AMR solver against COMSOL package. All results shown correspond to t = 350 s. (a) A color plot of concentration distribution in a pseudo-1D case. (b) Concentration profiles along the x axis. Simulated concentration in a sphere using (c) COMSOL and (d) SBM-AMR solver. The color ranges in the color bars of both (c) and (d) are the same. A quarter of the sphere is made transparent to show the concentration inside the particle. (e) Concentration profiles from the 3D simulations were plotted along the radial position. The results from COMSOL and the SBM-AMR solver are nearly identical. The COMSOL images were exported from COMSOL directly, while the SBM-AMR images were generated using Matlab.

adequacy in accurately capturing thin interface phenomena. Subsequently, we extend the framework to a 3D model to simulate the distribution and evolution of Li concentration, salt concentration, and electrostatic potentials within complex microstructures. We emphasize the influence of microstructures on electrode performance through simulated cell voltage curves and cyclic voltammograms of synthetic NMC electrodes. Moreover, the simulation outcomes emphasize the significance of input material parameters. Furthermore, we demonstrate the versatility of our method by extending it to thermal and mechanical calculations. Finally, we again validate the accuracy of our framework by comparing it with COMSOL Finite Element Method (FEM) simulations, both in 1D and 3D settings. While this work primarily employs Finite Difference Method (FDM), it's important to note that the presented SBM with AMR framework is adaptable to other numerical methods such as Finite Element Method (FEM), Finite Volume Method (FVM), or spectral methods. This versatility allows for the simulation of microstructure-level phenomena in various battery electrodes and electrochemical systems, including fuel cells and photovoltaic cells.

In summary, the pseudo-1D and 3D simulations suggest that SBM with a thick interface is suitable for simulating low-rate cases, while a thin interface is necessary for high C-rate cases. The UN and LN 3D simulations showcase the adaptability of the framework for microstructure simulations. Mesh refinement can be executed in a fast manner, facilitating the exploration of a broad range of electrode microstructures. Furthermore, this approach can accommodate the incorporation of additional physical effects such as temperature or stress calculations. Although our study focused on constant current and cyclic voltammetry loadings, oscillating loadings can also be imposed to investigate electrochemical impedance spectroscopic behavior at the microstructure level. [58] We anticipate that the SBM+AMR method will find widespread use in studying microstructure phenomena and estimating macroscopic performance across various electrochemical systems and materials.

CHAPTER 4

PHASE TRANSFORMATIONS AND UNDERSTANDING LITHIUM PLATING IN GRAPHITE ELECTRODES

4.1 Introduction

In this chapter, we focus on simulating electrochemical processes in complex graphite electrode microstructures due to graphite's widespread use and importance in lithium-ion batteries. Graphite electrodes consist of stacks of graphene sheets. Lithium migrates between these graphene sheets during lithiation. This migration of lithium ions within graphite is highly anisotropic, occurring rapidly within the interlayer space but slowly across graphene layers. As lithium fraction in the graphite increases, they undergo ordering across the graphene layers, leading to phase transformations in graphite [81, 82]. Graphite can exhibit four different phases based on the lithium fraction in it. A simplistic illustration of these phases is presented in Fig. 4.1. First, at a low Li fraction, Li randomly distributes in the whole graphite particle (Stage 1'). Next, Li fills one per three inter-graphene layers (Stage 3). Then, Li fills one of two layers (Stage 2), and finally, every layer is filled (Stage 1). These phase transitions are second-order phase transformations, i.e., no changes are observed in the crystal structure. Within each single phase regime, the open circuit voltage (OCV) of graphite exhibits a solid-solution type form, monotonically decreasing as the Li fraction increases. Notably, the OCV curve shows a flat plateau when two phases coexist in graphite. Fig. 4.1 illustrates the interlayer ordering of the phases and graphite OCV upon lithiation. The delithiation follows an opposite sequence of phase transformations. These phase transformations are crucial for simulating the electrochemical behavior of graphite electrodes.

Despite graphite's popularity in current Li-ion batteries, graphite anodes still suffer from Li plating at fast charging [81,82]. The precipitated Li metal results in internal shorting in the batteries, causing catastrophic issues like fires. This is one of the biggest bottlenecks that prevent a complete charging of an electric vehicle within 10–15 minutes (6–4 C). A 1C rate (1 C-rate) is defined as a charge/discharge rate that completes a full charge in 1 hour. Without a comprehensive understanding of the multiphysics electrochemical processes occurring within the graphite electrodes during fast charging operations, advancing microstructure designs to effectively delay or mitigate lithium plating on graphite anodes remains challenging. Three-dimensional electrochemical simulations can serve as a viable tool to tackle such complex challenges and can elucidate the detailed dynamics to complement experimental studies [22, 23, 83, 84].

We employ the Cahn-Hilliard phase-field equation [54, 85–87] to model the phase transformations in graphite replacing the Fick's diffusion equation in the framework. The Cahn-Hilliard equation is detailed in the next section and requires a parameterized lithium chemical potential. This treatment differs from using the regular solution model to construct a thermodynamic free energy function [88, 89] as typical in phase-field modeling. This equation is coupled with other electrochemical governing equations in the framework similar to Fick's diffusion equation. It is worth noting that the Cahn-Hilliard equation has previously been employed to simulate the phase transition in the inter-graphene layers [88–90]. Distinctively, in our work, the Cahn-Hilliard equation models the phase transformation at the graphite particle scale. We introduced the Cahn-Hilliard equation in our SBM framework [50]. While previous research has conducted Cahn-Hilliard simulations of phase separations in various electrode materials, including LFP [54, 91], Si [92, 93], and FeF_2 [94], these efforts were primarily limited to a single-particle scale. Our work extends such simulations to the scale of electrode microstructures through the utilization of SBM. A significant part of this work focuses on thick electrodes, an area of considerable interest in recent studies [95, 96]. Our framework offers a computational guide for the design of such thick electrodes, which can be valuable for advancing research in this direction.

In this chapter, we demonstrate the effectiveness of our simulation framework on a single graphite disk. We find that the Cahn-Hilliard equation accurately captures the multi-phase transition process observed in the experimental setup of the disk [81]. Despite the highly anisotropic nature of lithium transport in graphite, we show that using an isotropic model yields comparable results for spherical or sphere-like particles, where isotropic mobility is calculated as the volumetric average of anisotropic mobility. Consequently, we employ isotropic mobility in subsequent three-dimensional microstructure simulations. For 3D simulations, we utilize three different graphite microstructures reconstructed from X-ray computed tomography data [98, 99]. We compare the results obtained using the Cahn-Hilliard model and the Fickian diffusion model on one of these microstructures, highlighting the differences in performance estimation, particularly at low C-rate operations where Fick's diffusion can lead to overestimation of cell voltage. Our simulations can identify when and where of the theoretical onset of lithium plating on graphite anodes under various charging conditions, allowing for the optimization of electrode thickness and pore channel tortuosity to improve high-rate performance. By using this onset as the termination condition for lithiation, we investigate how electrode thickness and pore channel tortuosity impact high-rate performance across the three electrodes. Finally, we explore lithiation protocols aimed at improving the achievable capacities of the electrodes. Since our interest lies in the fast charging of batteries (corresponding to the lithiation of graphite), delithiation simulations are not presented in this chapter.

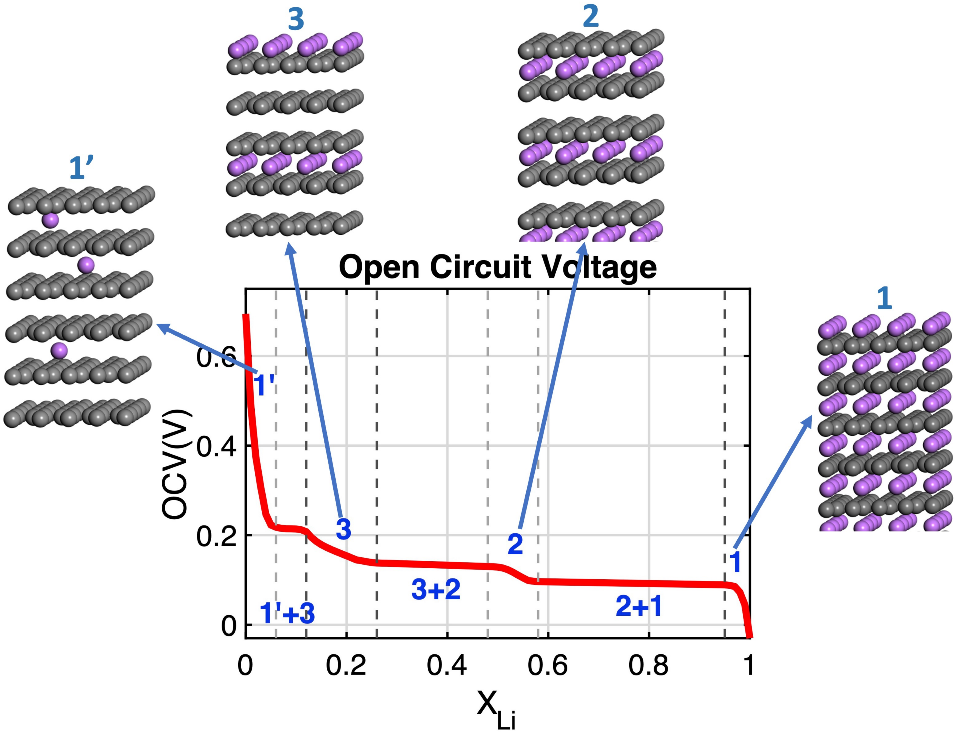

Figure 4.1 OCV obtained from Ref. [97]. 1',3, 2, and 1 label the four different graphite phases upon lithiation simplistically represented by the ball figures. Purple and gray colors represent Li and C atoms respectively. Phase 1' is observed for $X_{Li} < 0.06$. Phase 3 exists between $0.12 < X_{Li} < 0.26$. Phase 2 exists between $0.48 < X_{Li} < 0.58$. For $0.95 < X_{Li}$, phase 1 is observed. Flat plateaus are observed when two phases coexist.

With our solver, we can study several operations of a graphite anode versus lithium metal, providing valuable insights for optimizing and enhancing anode performance. Overall, our simulation framework serves as a versatile tool for designing better electrodes and optimizing their operating conditions, particularly in the context of fast charging of lithium-ion batteries. This chapter is derived from the published work of the author in Malik et al, 77:109937, January 2024 [50].

4.2 Model and Equations

In this chapter, we modify the framework utilized in Chapters 2 and 3 for graphite simulations. Unlike the previous chapters, the framework employed here uses solely the smoothed boundary method (SBM) [44, 50, 57]. For the three-dimensional simulations in this chapter, we use real microstructures reconstructed from voxel data sourced from literature [98, 99]. The voxel centers extracted from the 3D voxels serve as the grid points for meshing. It's worth noting that utilizing voxel data results in a fine root-level refinement, minimizing the need for further refinement. Consequently, adaptive mesh refinement (AMR) is not utilized in these simulations to avoid any additional computational burden. Nonetheless, a depiction of an AMR grid on reconstructed graphite microstructure is detailed in Appendix C for interested readers. A continuous domain parameter ψ is utilized to define the region occupied by the graphite particles ($\psi = 1$) versus the electrolyte regions ($\psi = 0$). The particle-electrolyte interface is implicitly defined by the region of $0 < \psi < 1$. With a properly selected small thickness, the SBM results can be very close to those obtained in the conventional sharp-interface simulations [24, 50].

Another significant change introduced in this chapter compared to the framework in Chapters 2 and 3 is the replacement of Fick's diffusion equation with the Cahn-Hilliard equation to model diffusion in the electrode particles. We start with Eq. (2.2) to detail the Cahn-Hilliard equation —

$$\frac{\partial X_p}{\partial t} = -\nabla \cdot \vec{j}_p = \nabla \cdot \left(M_p \nabla \mu_p\right) \in \Omega_p. \tag{2.2}$$

The chemical potential comprises contributions from bulk and interface: $\mu_p = \mu_b - \nabla \cdot \varepsilon \nabla X_p$, where the chemical potential in the bulk region is defined by the derivative of Gibbs free energy with respect to the composition as $\mu_b = \partial G(X_p)/\partial X_p$, where G function has multiple wells. Each well valley (local minimum) corresponds to the respective composition of a stable phase. ε is the gradient energy coefficient penalizing the sharp composition variation across the phase boundaries. Thus, Eq. (2.2) is rewritten as

$$\frac{\partial X_p}{\partial t} = \nabla \cdot \left(M_p \nabla \mu_p\right) = \nabla \cdot M_p \nabla \left(\frac{\partial G}{\partial X_p} - \nabla \cdot \varepsilon \nabla X_p\right), \tag{4.1}$$

As demonstrated later, the four-well Gibbs free energy function leads to four uniform X_p values, each of which corresponds to its respective stable phase, with narrow transition regions across different phases within the graphite particles. As before, Eq. (4.1) is reformulated for SBM with the domain parameter ψ. Multiplying ψ on both sides of Eq. (4.1) gives

$$\psi \frac{\partial X_p}{\partial t} = \psi \nabla \cdot \left(M_p \nabla \mu_p\right), \tag{4.2}$$

Using the product rule of differentiation on the right-hand side of Eq. (4.2), we further write

$$\psi \nabla \cdot (M_p \nabla \mu_p) = \nabla \cdot (\psi M_p \nabla \mu_p) - \nabla \psi \cdot (M_p \nabla \mu_p), \tag{4.3}$$

Combining these two equations results in

$$\psi \frac{\partial \mu_p}{\partial t} = \nabla \cdot (\psi M_p \nabla \mu_p) - \nabla \psi \cdot (M_p \nabla \mu_p), \tag{4.4}$$

The second term on the right-hand side serves as an ‘internal’ boundary condition within the computational domain. The Neumann boundary condition on the particle surface ($r_{xn}/\rho = \vec{n} \cdot \vec{j} \in \partial\Omega_a$) can be expressed in the diffuse interface description as

$$\frac{r_{xn}}{\rho} = \vec{n} \cdot \vec{j} = \frac{\nabla \psi}{|\nabla \psi|} \cdot (-M_p \nabla \mu_p), \tag{4.5}$$

where $\vec{n} = \nabla\psi/|\nabla\psi|$ is the unit inward normal vector of the diffuse interface. Substituting Eq. (4.5) and $\mu_p = \mu_b - \nabla \cdot \varepsilon \nabla X_p$ into Eq. (4.4) and dividing both sides by ψ, we obtain the SBM version of the Li transport equation — Cahn-Hilliard equation:

$$\frac{\partial X_p}{\partial t} = \frac{1}{\psi} \nabla \cdot \left[\psi M_p \nabla \left(\mu_b - \nabla \cdot \varepsilon \nabla X_p\right)\right] + \frac{|\nabla \psi|}{\psi} \frac{r_{xn}}{\rho}, \tag{4.6}$$

where $\mu_b = \partial G(X_p)/\partial X_p$. Similar to Chapter 3 Eq. (4.6) is solved in conjunction with the other SBM reformulated electrochemical governing equations listed here— Current continuity on graphite particle surface:

$$\nabla \cdot (\psi \kappa_s \nabla \phi_s) - |\nabla \psi| z_- F r_{xn} = 0, \tag{2.14}$$

Ion diffusion in electrolyte:

$$\frac{\partial C_e}{\partial t} = \frac{1}{\psi_e}\nabla \cdot (\psi_e D_e \nabla C_e) + \frac{|\nabla \psi_e|}{\psi_e}\frac{r_{xn} t_-}{\nu_+} - \frac{\mathbf{i_e} \cdot \nabla t_+}{z_+ \nu_+ F}, \tag{2.18}$$

Current continuity in the electrolyte:

$$\nabla \cdot [\psi_e (z_+ m_+ - z_- m_-) F C_e \nabla \phi_e] + |\nabla \psi_e| \frac{r_{xn}}{\nu_+} = \nabla \cdot [\psi_e (D_- - D_+) \nabla C_e], \tag{2.20}$$

Butler-Volmer equation:

$$r_{xn} = \frac{i_0}{z_+ F}\left[\exp\left(\frac{-\alpha z_+ F}{RT}\eta\right) - \exp\left(\frac{(1-\alpha) z_+ F}{RT}\eta\right)\right], \tag{2.7}$$

Since no additive phases are considered in this work, $\psi_e = 1 - \psi$. The details of these formulations and the procedure for solving these coupled equations can be found in Ref. [24, 50]. Because the complex electrode microstructures are defined by the continuous domain parameter, these equations can be solved on grid systems that are not conformal to the particle geometries. Thus, by circumventing the efforts for generating body-conforming meshes required in conventional sharp-interface modeling, the presented complex microstructure simulations can be implemented much faster.

4.3 Simulation setup - microstructure and parameters

4.3.1 Material Properties

The values of material properties, which appear in the governing equations, strongly affect the electrochemical processes. In this work, we parameterized those coefficients (material properties) from available literature data. They are mostly concentration-dependent quantities such that the evolution of Li composition influences the electrochemical dynamics. For the Cahn-Hilliard equation, Eq. (4.6), there are three material parameters: chemical potential, gradient coefficient, and transport mobility. A cell OCV is the electrical potential difference in a cell at a disconnected state. Essentially, the Li ions in the cathode and in the anode are in equilibrium at this voltage, thus no net Li migration between the two electrodes. The Li chemical potentials are related to the OCV by

$$\mu_{cathode} - \mu_{anode} = -e \cdot \phi_{OCV} \text{ (eV)}, \tag{4.7}$$

where $\mu_{cathode} = \mu_p$ and e is the unit charge. If Li metal is used as the anode, we can set $\mu_{anode} = 0$ as a reference value. The red curve in Fig. 4.1(a) shows a measured graphite OCV curve [97] against Li metal. There are three voltage plateaus, each of which indicates a two-phase coexisting region (i.e., miscibility gaps). Shown in Fig. 4.2(b) is the constructed μ_b curve. The segments colored in green are $-e \cdot \phi_{OCV}$ in the single-phase regions. Since no phase boundaries will be present in single-phase regions, $\mu_b(X_p) = \mu_{cathode}$.

To allow phase separation, we extrapolated the μ_b from the single-phase regions to the two-phase regions, as shown by the red segments in Fig. 4.2(b). These red segments are non-monotonic such that if X_p is within the miscibility gap, spinodal decomposition will occur to move the value of X_p to those corresponding to the lower or upper single phases. Note that phase separation will not occur if flat plateau values are used for the miscibility regions. The value of the chemical potential gap (the difference between the maximum and minimum in the non-monotonic function)

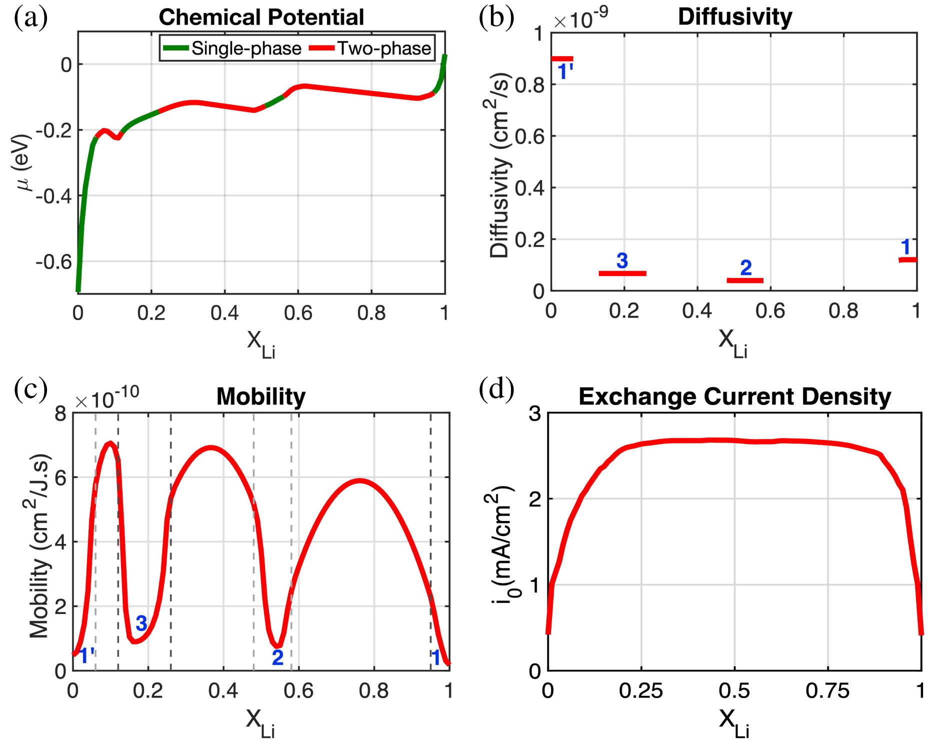

Figure 4.2 Material properties obtained from literature data. (a) Chemical Potential (eV) constructed from the OCV curve [97]. (b) Diffusivity (cm^2/s) in the four single-phase regions [100]. (c) Mobility (cm^2/J.s) constructed from the diffusivity curve, and (d) Exchange current density (mA/cm^2) [75].

can be parameterized from intrinsic voltage hysteresis exhibited on the OCV measurements. The constructed μ_b function led to an approximately 25 mV voltage hysteresis (see Fig. 4.3 (a)), which was close to experimentally observed values (20–25 mV) [101]. The Gibbs free energy of Li in graphite corresponding to the μ_b function is shown in Fig. 4.3 (b) and (c). It has four local energy minima corresponding to the four single-phase regions. This free energy function is completely parameterized from measured data, demonstrating a different methodology from conventional regular-solution models.

The gradient energy coefficient ε is related to the interfacial energy and width of the phase boundaries. Typically, its value can be estimated by integrating the Gibbs free energy along the thickness direction over the phase boundary. Unfortunately, due to the lack of experimental data on the interfacial energy between the different phases in graphite, we selected a value of $(0.8l)^2$, where l is a characteristic length ($l = 0.1625$ μm, which is half of the voxel edge length of the reconstructed microstructures in this work). This value was selected to ensure a stable phase field simulation, such that the phase boundary width remained to be approximately $4l$. We acknowledge that more accurate parameterization can be achieved if more material data are available.

Mobility determines how fast mass transport occurs under a driving force: $\vec{j}_p = -M_p \nabla \mu_p$. (The driving force is typically the gradient of chemical potential.) If the flux is described by Fick's

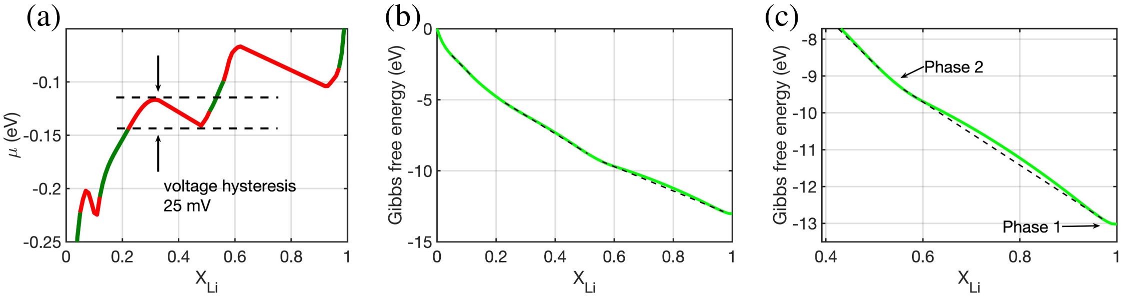

Figure 4.3 (a) Parameterized Li chemical potential with voltage hysteresis. The green color represents the single-phase regions while the red color represents the two-phase regions. (b) Parameterized Gibbs free energy of Li in graphite. The black dashed lines are the common tangent lines between two adjacent single phases. There are four single well regions corresponding to the four stable phases. (c) A magnified view of (b).

law, it is $\vec{j}_p = -D_p \nabla X_p$. Thus, the mobility is related to the diffusivity according to

$$M_p = \frac{D_p}{\partial \mu_p / \partial X_p}. \tag{4.8}$$

In this work, we used a set of report D_p data [100], which have four distinct values in the four single phases. The D_p value is close to a constant value in each respective phase. However, we multiplied the values by a factor of $100 \times 2/3$, in which the factor of 100 is to increase the value of D_p to be closer to the more commonly observed values [102, 103]. The factor of 2/3 stems from a volumetric average of the diffusivities parallel and perpendicular to the graphene layers in graphite particles. The diffusivity perpendicular to the graphene sheets is assumed to be negligible here. As demonstrated later in Section 4.4.1.2, using the average diffusivity can produce equivalent results to those obtained from a fully anisotropic model. Since the graphite orientations in the reconstructed microstructures are unavailable in this work, we treated the graphite particles as an isotropic material for Li transport and used the 'average' diffusivity for parameterizing the mobility, unless otherwise stated. The D_p values for the four single phases are shown as the solid line segments in Fig 4.2(b).

Figure 4.2(c) shows the M_p function used in the simulations. The M_p in each of the stable single-phase regions are obtained using Eq. (4.8). Because phase separation occurs in the miscibility gaps, diffusivity data are not available for the composition within the miscibility gaps. Thus, M_p within the miscibility gaps was extrapolated from the data in the stable single-phase regions. The M_p curve in the miscibility gaps has high values shown as the humps on the red curve in Fig 4.2(c).

Exchange current density, i_0 in Eq. (2.7), is the current density on an electrode surface established at the equilibrium between the salt concentration in the electrolyte, Li fraction in the particle, and the electric potential drop across the electrolyte-particle interface. The i_0 value can be measured using Tafel plotting or impedance techniques. However, the measurement processes are sometimes highly tedious. Thus, a Li composition-dependent i_0 function for graphite-electrolyte interfaces is not widely available in the literature. Most of the available experimental data are just one single value at a specific Li fraction. Here, we used an i_0 function obtained using kinetic Monte Carlo simulations [75], as shown in Fig 4.2(d). This data set spans the entire Li composition range.

The i_0 value is small in the near fully delithiated and fully lithiated regions and has a plateau in the intermediate composition region. We acknowledge that more quantitative predictions can be achieved with more accurate data if they are available for material parameterization. The presented μ_b, M_p, and i_0 functions are difficult to be fitted with closed-form functions. Therefore, we tabulated them into tables and interpolated their values based on X_p in the simulations. Furthermore, graphite is a highly conductive material. We set a uniform $\kappa_s = 3.3$ S/cm for Eq. (2.14). We assume the same binary electrolyte from Chapter 3, with $LiPF_6$ dissolved in an arbitrary organic solvent. We use the same ambipolar diffusivity in Eq. (2.18) and ionic diffusivities in Eq. (2.20) as in Chapter 3 and Refs. [24, 50, 57, 58].

4.3.2 Electrode Microstructures and Simulation Setups

Electrochemical processes were simulated using the presented approach on three different openly available reconstructed graphite electrode microstructures [98, 99]. The downloaded TIFF-stack image files were converted to 3D voxel arrays, where the voxel edge size is 325 nm. A region of $180 \times 170 \times 160$ voxels was cropped from each of the datasets, corresponding to the dimensions of $58.5 \times 55.2 \times 52\ \mu\text{m}^3$. They are shown in Fig. 4.4(a) through (c) and referred to as E_II, E_III, and E_IV, respectively. As can be observed, E_II consists of relatively large sphere-like particles and serves as the standard case in this work. E_III has a smaller particle size, which leads to higher porosity and a higher surface-to-volume ratio compared to the other two electrodes.

E_IV has plate-like/flake-like particles. It can be clearly seen that the primary direction

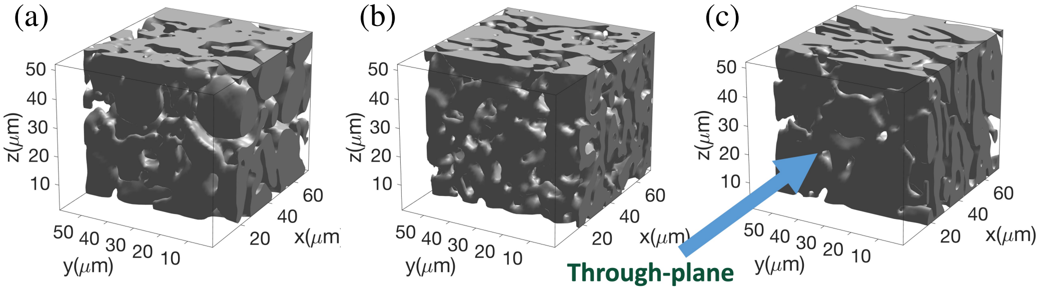

Figure 4.4 (a) Electrode II (E_II), (b) Electrode III (E_III), and (c) Electrode IV (E_IV). Morphological properties of the shown electrodes are provided in Table 4.1.

(electrode thickness direction or the x-direction in Fig. 4.4) is perpendicular to the graphite plates in E_IV. This leads to a high through-plane tortuosity compared to the other electrodes. These three microstructures were chosen in this study because of their different characteristics. Table 4.1 summarizes the key microstructure properties. Note that morphological properties were calculated for both the through-plane (TP) and in-plane (IP) configurations. The TP configurations are those in Fig. 4.4. The IP configurations were obtained by rotating the electrodes by 90 degrees around the y-axis. In this case, for the E_IV IP case, the primary direction (Li metal anode to the graphite electrode current collector) is parallel to the graphite plates. In the simulations presented later, the default setups were in the TP configurations unless otherwise mentioned.

In this work, we doubled the grid resolution using the MATLAB function 'imresize3'. Similar to Ref. [24], an empty space was included to serve as the separator region (100 grid spacings). Thus, the grid system in our simulation contained $360 \times 440 \times 320$ uniform grid points, for which the grid spacing was $\Delta x = 162.5$ nm (half of the voxel size). Using the voxel centers directly as the grid points, we employed the level-set distancing method as in Ref. [44] to calculate the distance to the nearest particle surface of each grid point. The domain parameter for the graphite particle regions was defined using $\psi = \left[1 + \tanh\left(d/\zeta\right)\right]/2$, where d was the shortest distance to particle surfaces and ζ was a numerical parameter to control the thickness of the diffuse interface. Here, we set $\zeta = \Delta x$, such that the diffuse interface of ψ spanned approximately $4\Delta x$. The time step size

Table 4.1 Morphological properties for the three reconstructed graphite electrodes in the simulations. The quantities outside and inside the parentheses are for the cropped regions and the entire microstructure data, respectively.

Microstructure / Parameter	Electrode II	Electrode III	Electrode IV
Feature	Large spherical particles	Small particles	Plate-like/flake-like particles
Porosity*	33.70 (32.52)	35.96 (36.65)	32.71 (33.04)
Through-plane pore tortuosity*	1.50 (1.59)	1.52 (1.67)	2.86 (2.64)
In-plane pore tortuosity*	1.29 (1.39)	1.23 (1.47)	1.24 (1.46)
Simulation cell size (μm^3)	$58.5 \times 71.5 \times 52$	$58.5 \times 71.5 \times 52$	$58.5 \times 71.5 \times 52$
solid volume (μm^3)	108,130	104,437	112,039
particle surface area in TP (μm^2)	30,892	33,464	32,380
particle surface area in IP (μm^2)	29,679	33,514	29,476

was $\Delta t = 2.6 \times 10^{-3}$ s in the following 3D simulations. The boundary conditions were imposed similarly to those in Section 4.4.1.2. A cut-off voltage of 0.00 V was used in all the following simulations to avoid the overcharging condition explained in Section 4.4.1.1.

All the physical fields involved in the electrochemical processes in the graphite electrode microstructures, i.e., X_p, ϕ_s, C_e, and ϕ_e, were solved simultaneously in our simulations according to the equations presented in Section 4.2. The SBM microstructure simulations here did not require body-conformal mesh. Instead, the uniform Cartesian grid system for the calculations was built directly using the cuboidal voxels. Thus, we skipped the processing time for generating mesh conforming to the complex electrode microstructures. As a demonstration, Fig. 4.5(a) through (d) show the four fields for E_II at the cut-off point under a 6C constant current lithiation.

The primary direction (electrode thickness direction) is along the x-axis. As can be seen in Fig. 4.5(a), X_p exhibits a radial variation in each particle. In the electrode scale, the particle surface X_p exhibits a variation along the primary direction. There are gradients present in the other three

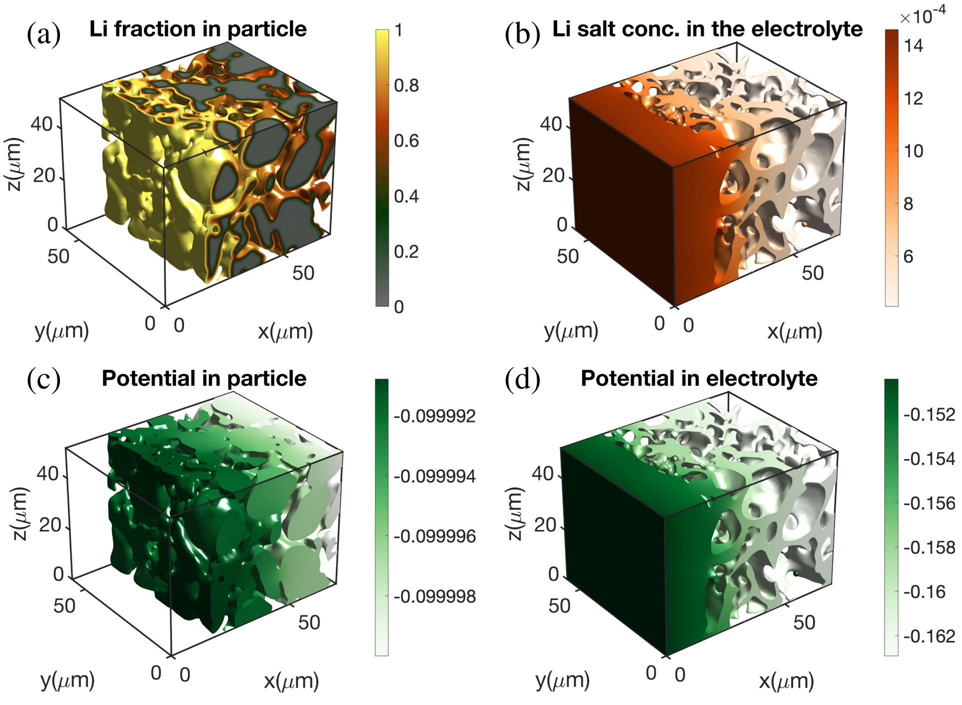

Figure 4.5 (a) Lithium fraction in particle, (b) lithium salt concentration, (c) electropotential in particle, and (d) electropotential in the electrolyte for 6C lithiation in the TP E_II configuration at the cut-off point $X = 0.53$.

fields. All these gradients agree with the flow directions of the ions in the electrolyte and electrons in the particle network. A more extensive description of these fields can be found in Ref. [24]. As this behavior is generally similar to that in Ref. [24], we do not emphasize these three fields further in this work.

4.4 Results and Discussion

4.4.1 Model examination

4.4.1.1 Single disk simulation

Firstly, we validate if the presented Cahn-Hilliard phase-field equation coupled with other electrochemical equations can properly emulate the phase transformation processes in a graphite particle. A virtual battery cell containing a single circular graphite disk was used in this simulation as shown in Fig. 4.6(a). The disk radius was 2.5 μm. It was placed at the west end of the computational domain, contacting the current collector on the west domain boundary. This acted as the boundary condition of the electropotential in the graphite disk.

To simplify and accelerate the simulation, the east, south, and north boundaries were assumed

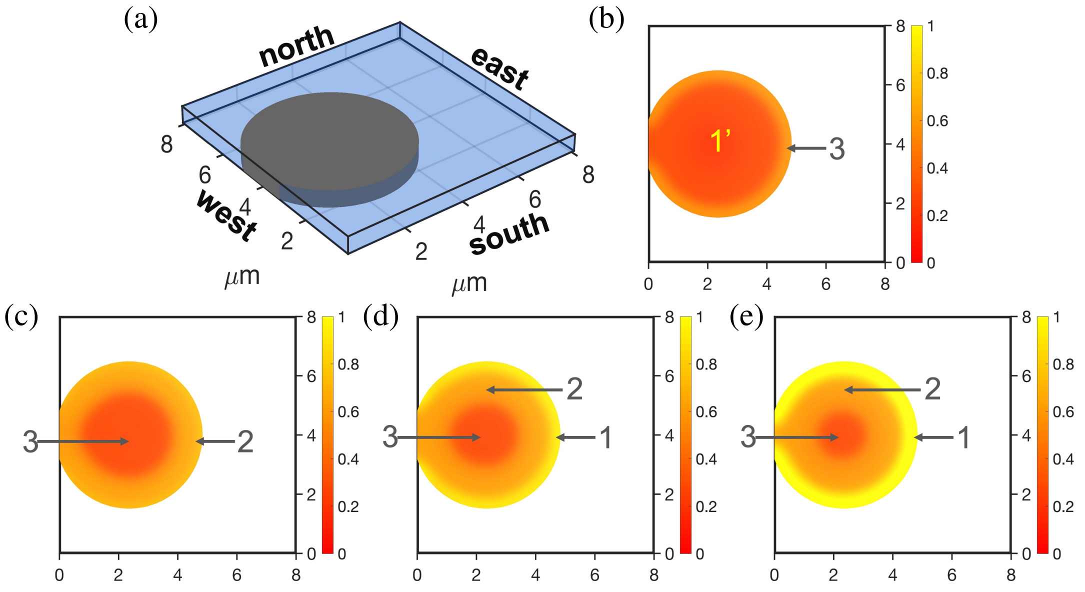

Figure 4.6 (a) Virtual battery cell containing a single circular graphite disk. The disk was lithiated at a 0.5C rate. X_p distributions in the disk from the simulation at (b) ~ 2240s; Phases 1' and 3 can be observed. (c) ~ 3380s; Phase 1' has disappeared and Phase 2 is visible now. (d) ~ 4140s; Phases 3, 2, and 1 can be observed here, and (e) ~ 4900s; all Phases 3, 2, and 1 can be seen.

to be Li metal, which provided the electropotential boundary condition for the electrolyte and the ion sources for the electrolyte. This can be viewed as a scenario that a graphite disk is surrounded by infinite Li sources. The computational domain was of dimensions of $8.1 \times 8.1 \times 0.6$ μm^3, which was discretized with a uniform grid (with a grid spacing of $\Delta x = 0.1$ μm). The time step size was $\Delta t = 1.056 \times 10^{-2}$ s. The SBM interfacial thickness was approximately $4\Delta x$. As a structure indicator, the SBM diffuse interface stays stationary since we assume particle deformation (morphology change) is negligible. The space not occupied by the graphite disk was assumed to be filled with electrolytes. No-flux boundary conditions were imposed on the top and bottom boundaries, thus, acting as a quasi-2D simulation. The cell voltage (CV) is the difference between the electropotential on the current collector and the Li metal. In the simulation, the electropotential on the Li metal was set to 0.00 V and the lithiation current was controlled by adjusting the electropotential on the current collector. The box boundary conditions are set for solving ϕ_s and ϕ_e, i.e., Eqs. (2.14) and (2.20) respectively, such that the Butler-Volmer reaction, Eq. (2.7), at the particle-electrolyte interface, provides the insertion/extraction flux to move the phase boundary within the disk.

A constant 0.5C loading was set for the lithiation process with a cut-off voltage of 0.00 V. Note that a 1C rate (1 C-rate) is defined as a charge/discharge rate that completes a full charge in 1 hour, so 0.5C corresponds to a full charge in 2 hours. The cut-off threshold was set to avoid overcharging. Reaching this overcharging condition could result in a negative electropotential drop across the graphite-electrolyte interface, which thermodynamically favors lithium plating on the graphite surface over insertion into the graphite particle [104].

Figures 4.6(b) through (e) show the snapshots of Li fraction (X_p) evolution in the disk. Note that while other physical fields, such as electropotentials and salt concentration, were simultaneously simulated, they are not presented here as our focus is the phase transformation dynamics in the graphite particle. The initial Li fraction was set to be uniformly 0.02 throughout the disk. Li site density in graphite was set to be $\rho = 0.0312$ mol/cm^3. As Li was inserted into the disk, X_p near the surface region increased, exhibiting a gradient along the radial direction. A clear coexistence of

Phase 1' and 3 can be observed in Fig. 4.6(b). Further lithiation led to continuous increases of X_p in the outer region of the disk and formed a new phase near the surface. Phase 1' quickly disappeared because of two factors: 1) its miscibility gap ($0.06 < X_{Li} < 0.12$) to Phase 3 is very small and 2) Phase 1' chemical potential is much higher than Phase 3. Thus, Phase 1' rapidly transitioned to Phase 3. Phase 2 can be observed in Fig. 4.6(c). The region of the new phase expanded inward at the expense of the old phase. This type of phase transformation continued as lithiation proceeded. Figure 4.6(e) shows the morphology of the coexistence of Phase 3, 2, and 1 in the disk at the late stage of lithiation. The single disk simulation exhibits a phase distribution that closely resembles the phase morphology experimentally observed by Guo et al [81], demonstrating the proper emulation of phase transitions in graphite using the presented model. The minor difference arises from the difference in setups, wherein the experiment [81] had lithium metal placed only on the northeast corner. However, due to the lack of exact material parameters in the experiments, quantitative comparison cannot be offered in this work.

4.4.1.2 Anisotropic Li transport

Graphite due to its layered structure is highly anisotropic in the intra-particle Li transport behavior. The presented SBM model allows fully anisotropic simulations, where the mobility in Eq. (4.6) will be a tensor:

$$\mathbf{M}_p = \begin{bmatrix} M_{x'} & 0 & 0 \\ 0 & M_{y'} & 0 \\ 0 & 0 & M_{z'} \end{bmatrix}. \tag{4.9}$$

Here, the subscripts z' and y' indicate the in-plane directions of the graphene sheets within a graphite particle, and x' indicates the through-plane (TP) direction. In this test, we assume the in-plane (IP) mobility is four orders of magnitude greater than the TP mobility; i.e., $M_{z'} = M_{y'} = 10000 M_{x'}$. We set $M_{z'} = 1.5 \times M_p$ for the anisotropic simulation. (The factor of 1.5 will be explained later.) Because the crystal orientations of the graphite particles in the reconstructed microstructures are not available, we employed the discrete element method (as in Ref. [24]) to generate a synthetic microstructure, in which the crystal orientation of each spherical particle was randomly assigned.

The particle size follows a truncated log-normal distribution as in Ref. [105]. The colors in Fig. 4.7(a) indicate the crystal orientation of each particle using a color scheme of the inverse-pole figure.

The computational domain contains approximately 1300 particles and has 360 × 220 × 320 grid points with $\Delta x = 0.5$ μm. A Li metal serving as the Li source is placed on the west domain boundary ($x = 0$), thus the primary Li transport direction is along the west-east direction (the x-axis direction in Fig. 4.7(b), which is also the electrode thickness direction).

Figure 4.7(b) shows the simulated Li fraction at $X = 0.29$ under a 6C lithiation. (X is the average Li fraction throughout the entire electrode, which is equivalently the degree of discharge, DoD.) Interestingly, although the Li transport is highly anisotropic within each spherical graphite particle, the X_p only varies along the sphere radial direction as in a typical isotropic case. This is attributed to the fact that X_p has distributed axisymmetrically in each circular inter-graphene layer. (Here, the graphene layers are parallel to the latitude planes of the sphere). The size of each circular layer decreases as the distance from the center plane increases. The smaller layers (near the pole regions) fill fast and the larger layers (near the equator plane) fill slowly. As a result, the overall X_p varies only radially. Figure 4.8 offers a scheme illustration for this phenomenon.

For comparison, a fully isotropic simulation was performed on the same microstructure, but

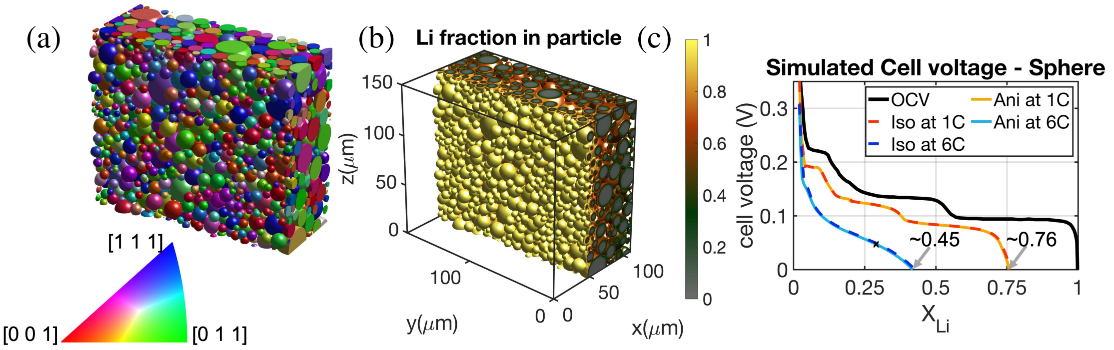

Figure 4.7 (a) Pole figure for the synthetic spherical microstructure with the colors indicating the fast diffusion direction of each particle. (b) Lithium fraction in the particle at $X = 0.29$, and (c) CV curve comparison for the anisotropic and isotropic cases at 1C and 6C rates. The lithium fraction at the cut-off voltage is highlighted by the grey arrows.

with a scalar mobility value given as

$$M_p = \frac{1}{3}\left(M_{x'} + M_{y'} + M_{z'}\right) \approx \frac{2}{3} M_{z'}. \tag{4.10}$$

The X_p distribution from the isotropic simulation taken at the same X is very similar to the anisotropic case. The cell voltage curves of 1C and 6C lithiation from the anisotropic and isotropic simulations are plotted in Fig. 4.7(c). In both 1C and 6C cases, the anisotropic (solid) and isotropic (dashed) curves almost overlap. As demonstrated by this test, a fully isotropic transport model produces electrochemical simulation results very similar to those obtained from fully anisotropic simulations if the electrode is comprised of randomly oriented spherical particles. Therefore, a fully isotropic model was employed to simulate the electrochemical processes in reconstructed graphite electrodes because the crystal orientations are unavailable in those data.

4.4.2 Cahn-Hilliard(CH) vs Fick's Diffusion(FD): Electrode II

In section 4.4.1.1, we substantiate the Cahn-Hilliard (CH) equation's effectiveness in simulating phase transition in a single graphite disk. However, graphite particles were sometimes inaccurately modeled as Li solid-solution using Fick's law for Li transport within [106–108], without considering the phase transformation process during (de)lithiation. In this section, we further investigate the difference in modeling graphite particles as a phase-separating or solid-solution material by comparing Cahn-Hilliard (CH) and Fick's diffusion (FD) simulation results. As FD does not include

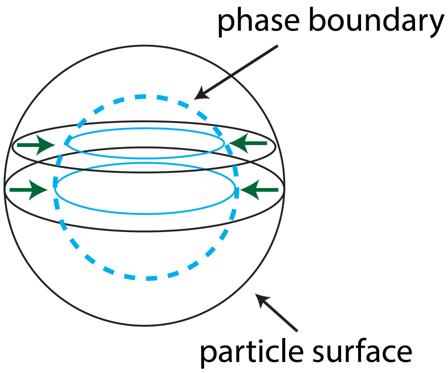

Figure 4.8 The solid black lines indicate the sphere surface and the cyan dashed circle indicates the internal phase boundary. The green arrows indicate Li insertion flux. As the inter-graphene layer is away from the center plane, the circular plane becomes smaller and will be filled faster. As a result, the internal phase boundary remains a spherical shape concentric to the sphere surface.

phase transition behavior, the energy that would be otherwise consumed in these transformations goes into electrochemical reactions. Therefore, theoretically, FD is expected to overestimate the electrode's performance.

We performed two additional sets of constant-current simulations for 1C and 6C lithiation using Fick's diffusion equation, Eq. (2.12), for Li transport in graphite particles in E_II. The values of Li diffusivity in the four stable phases are shown as the red segments in Fig. 4.2(b), and the values in the two-phase regions are linearly interpolated from the single-phase regions. All other material properties and simulation conditions were the same as in the previous E_II simulations.

Fick's diffusion equation:

$$\frac{\partial X_p}{\partial t} = \frac{1}{\psi}\nabla \cdot \left(\psi D_p \nabla X_p\right) + \frac{|\nabla\psi|}{\psi}\frac{r_{xn}}{\rho}. \tag{2.12}$$

Figure 4.9(a) shows simulated CV curves for 1C and 6C cases. The 1C results of the FD and CH simulations are plotted as the yellow dashed and red solid curves, respectively. While the FD model treats graphite particles as a Li solid solution, the FD curve still shows step-like profiles upon lithiation as in the CH case, reflecting the plateaus on the OCV. However, the FD curve extended to a higher achievable DoD (0.87) than the CH curve (0.78).

Despite the step-like CV curve, the X_p in the FD model, shown in Fig. 4.9(b) and (d), exhibits a continuous inward gradient in the particles, which significantly differs from the multiphasic coexistence morphology in the CH results, see in Fig. 4.9(c) and (e). Without accounting for the phase transitions, the Fickian diffusion model results in only a continuous gradient of Li concentration within each particle, as well as across the electrode. Experimentally observed sharp color changes across different phases either within a graphite disk [81] or across a graphite anode [82] are only replicated in the CH results. Since the system at a 1C lithiation is thermodynamically closer to the equilibrium, without the hindrance of phase boundary motion during phase transitions, the FD model clearly overestimated the achievable DoD.

In contrast, in the 6C simulations, the total achievable DoDs in the CH and FD results are very similar. This is because the particle surfaces in the two models all reached Li saturation in a short time due to the kinetic limitations of inward transport. However, the intrinsic difference in the thermodynamics of the two models is still reflected in the shapes of the CV curves. Specifically, the FD curve (cyan dashed curve) exhibits a much less step-like profile in the 3-2 phase region ($0.12 < X < 0.22$), where the curve monotonically decreases as opposed to the plateau in the same region on the blue solid curve (CH model). In the 6C lithiation, both CH and FD have high inward gradients in the X_p distributions. Although the morphologies are different (FD has continuous inward gradients, but CH has multiphasic coexistence layers), the overall distributions are similar. Thus, their overall achievable DoDs are similar.

As pointed out by Bazant's work [109], it is important to model graphite correctly as a phase-separating material, rather than a Li solid-solution. Our results demonstrate that the CH model more accurately depicts Li transport and phase transition behavior in graphite particles. The FD model can significantly overestimate graphite electrodes' performance at low C rates. At high C rates, even though the predicted achievable DoDs are similar, the two models can lead to CV curves with different shapes. In the rest of this work, we will perform only CH simulations for the graphite

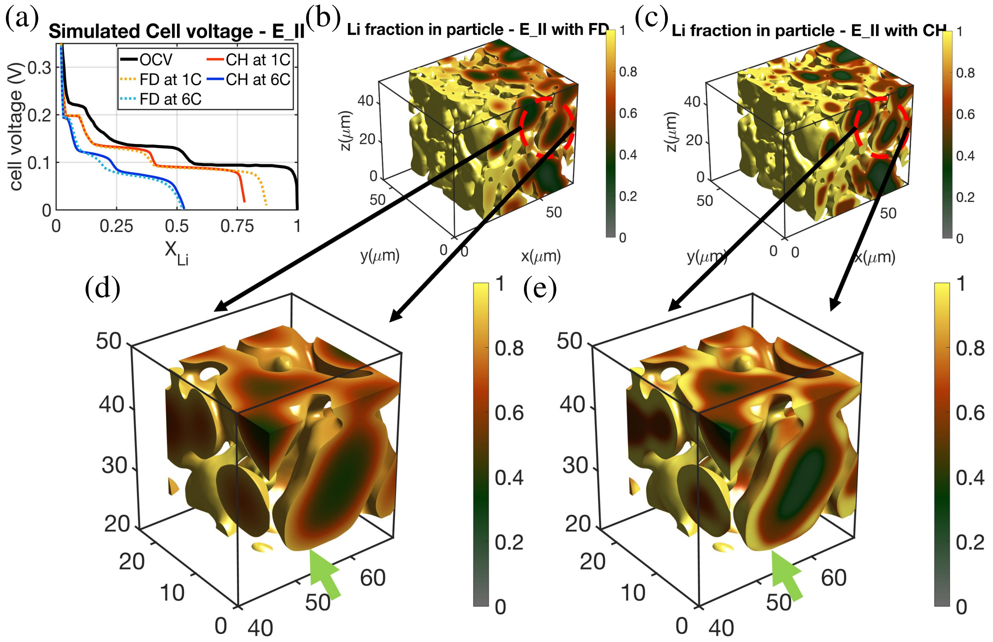

Figure 4.9 (a) CV curves for Cahn-Hilliard and Fick's diffusion at 1C and 6C rates. Lithium fraction distributions in particles at 1C, taken at $X = 0.73$, for (b) FD case and (c) CH case, with zoomed-in views in (d) and (e), respectively. The green arrow in (d) points to a particle showing a continuous inward gradient. The arrow in (e) indicates a particle exhibiting Phases 1, 2, and 3 with yellow, red, and dark green colors, respectively.

electrodes.

4.4.3 Electrode behaviour comparison

E_II, E_III, and E_IV have significant differences in their morphological properties. See Table 4.1. While thermodynamics determines the material's intrinsic properties, microstructures will dictate the kinetic behavior. Therefore, although the electrodes were all made of the same graphitic carbon, they are expected to have different electrochemical performances. Among the three electrodes, E_III has a significantly higher surface-to-volume ratio (approximately 11%) than those of the other two electrodes. E_III also has a higher porosity (approximately 10%) than the other two.

Microstructure electrochemical simulations were performed for these three electrodes. Here, the setups are the TP configurations. Figure 4.10(a) shows the cell voltage curves extracted from the simulations at 1C lithiation. E_III (the green curve) showed the largest achievable DoD (0.87) before reaching the cut-off voltage, which is much greater than those of the other two electrodes (0.785 and 0.775 for E_II and E_IV, respectively). Evidently, the high surface-to-volume ratio (equivalently, a small average particle size) of E_III has the most influential role on the electrochemical performance in this case. Even though E_II and E_IV have obvious differences in particle morphologies, their performances are nearly identical at this low C rate.

Figure 4.10(b) shows the CV curves for these three electrodes at 6C lithiation. The high rate

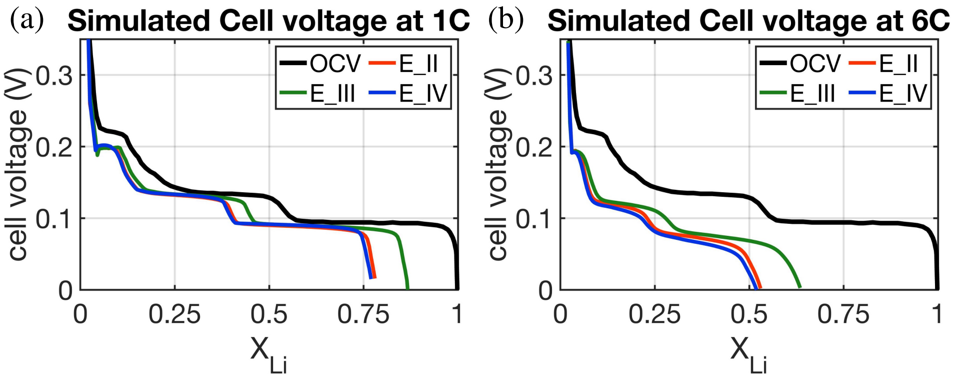

Figure 4.10 Simulated CV curves for the through-plane (TP) configurations of the three electrode microstructures (a) at 1C rate and (b) at 6C rate.

performances of E_II and E_IV are expected to be notably distinct because they have a substantial difference in the pore tortuosities. Interestingly, E_II and E_IV did not perform very differently and they had similar achievable DoD (0.52 for E_II and 0.53 for E_IV). Similar to the 1C case, E_III had a much larger achievable DoD (0.64) at 6C lithiation. These results indicate that, for electrodes of this thickness (55.2 μm), pore tortuosity does not strongly impact the performance even though at high rates. Rather, it is still the surface-to-volume ratio dominating the performance. To examine the thickness effect, we extended the thicknesses of E_II and E_IV microstructures to 110.4 μm (i.e., double thickness) and performed another set of simulations. Hereafter, we refer these microstructures to as E_II-2X and E_IV-2X. Shown in Fig. 4.11 are the CV curves of E_II-2X and E_IV-2X at a 6C rate. The two dotted lines are the CV curves from the original thickness cases provided for comparison. The achievable DoD for E_II-2X is 0.505, significantly larger than 0.415 for E_IV-2X.

Evidently, the high pore tortuosity of E_IV substantially hindered the cell performance (from DoD = 0.52 to 0.41) by doubling its thickness. For E_II, on the other hand, the achievable DoD only marginally decreased from 0.53 to 0.505. In this case, the capacity of intercalated Li in the double-thickness E_II-2X is roughly twice that of the original-thickness case. Figure 4.11(b) shows the CV curves plotted versus moles of intercalated Li for E_II and E_IV of original and double thicknesses. Although the double-thickness electrodes have poorer performances, they still achieve larger capacities because of the increase in volume.

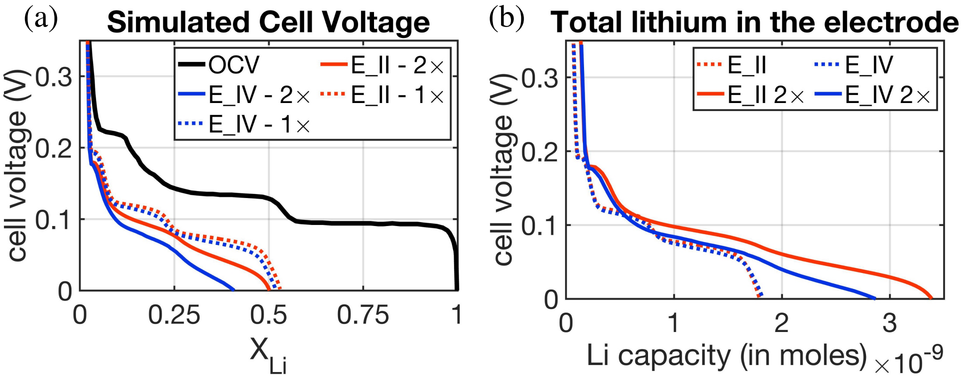

Figure 4.11 (a) Simulated CV curve comparison, and (b) total inserted lithium in E_II and E_IV for single thickness (1×) and double thickness (2×) cases.

Furthermore, even though the original and double-thickness E_II have achieved similar DoD, their energy efficiencies are different. Energy efficiency can be defined as the ratio of released energy during a lithiation process to the theoretical energy that can be obtained from an equilibrium process. The area below a CV curve is the released energy and the area below the OCV curve is the theoretical energy. The difference between these two quantities is the waste heat generated in the process. Figure 4.12 offers an illustration. Here the theoretical energy is calculated up to the cut-off DoD.

For E_II, increasing from the original to double thickness changes the efficiency from 58.5% to 47.4%. Note that while the achievable DoD for E_II did not change much by increasing its thickness, the energy efficiency varied significantly. For E_IV, the efficiency changed from 55.3% to 40.2% as the thickness was doubled. The variation is larger than the E_II case. Since the Li capacity in the double-thickness configuration was twice the original one, the total waste heat generated was also much larger.

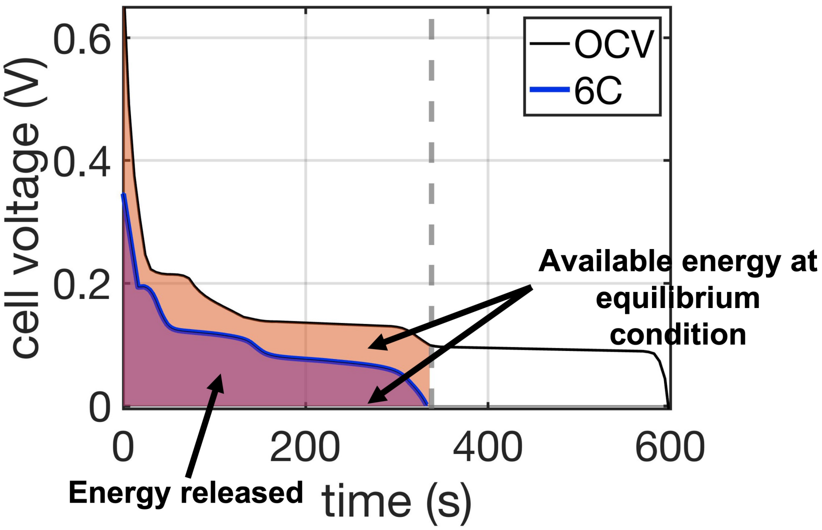

Figure 4.12 Cell voltage vs time for E_II at 6C lithiation. As this is a constant current lithiation, the purple area under the 6C curve gives an estimate for the energy released in 6C lithiation, which can be calculated using $E_r = \int I \cdot V_c dt$ where I is the cell current and V_c is the cell voltage. The orange + purple area estimates the available energy at the equilibrium condition until the cut-off point. The ratio between the released energy and the theoretical energy is the energy efficiency for this lithiation process.

High contrast between the TP tortuosity (2.86) and the IP tortuosity (1.24) of E_IV can be noted in Table 4.1. The apparent difference in these two tortuosities can be inferred from the plate-like particles in the E_IV microstructure. Additional simulations were conducted to examine the performance of E_IV in the IP configuration. Figure 4.13(a) displays the cell voltage curves for E_IV at 6C and 1C lithiation in the TP and IP configurations. In either 6C or 1C cases, the CV curves for the two configurations almost overlap, indicating that the electrode thickness (55.2 μm) is too small to reflect the impact of pore tortuosity.

Thus, we extended the electrode microstructure to double and triple the original thickness and performed simulations at 6C lithiation on those electrodes. Despite the inherent challenges in poor kinetics, mechanical strengths, etc., appropriate designs of thick electrodes can lead to a higher loading and overall energy density by reducing the volume occupied by inactive components (such as separators and current collectors) [95]. While several recent studies [95,96] have experimentally explored the strategies for designing better thick electrodes, the following results can provide insights into such developments using simulations.

The CV curves are plotted in Fig. 4.13(b). For the TP case, increasing the thickness from the original (55.2 μm) to double (110.4 μm) and then to triple (165.6 μm) thicknesses decreased the achievable DoD from 0.52 to 0.41 and further to 0.175, respectively. See the three solid curves in Fig. 4.13(b). Even though the achievable DoD decreased, because of the increase in volume,

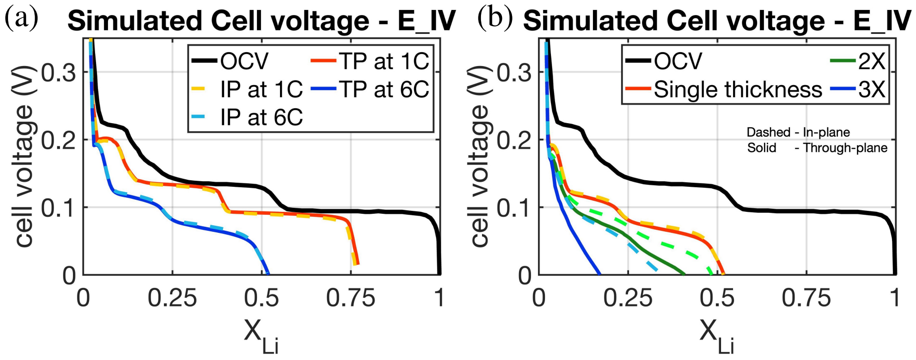

Figure 4.13 (a) Simulated CV curves for E_IV in the TP and IP directions at 1C and 6C rates. (b) Simulated CV curves for E_IV in the TP (solid lines) and IP (dashed lines) directions at 6C for single, double, and triple thicknesses.

the double-thickness TP E_IV-2X still has a nearly 57% more achievable Li capacity than the original-thickness one. However, the triple-thickness TP E_IV-3X only reached nearly the same Li capacity as the original case. The achievable Li capacities are 1.83×10^{-9}, 2.88×10^{-9}, and 1.84×10^{-9} moles of TP E_IV, TP E_IV-2X, and TP E_IV-3X, respectively. Clearly, increasing the thickness has a diminishing effect on the total achievable Li capacity at this rate, indicating an optimal thickness for the highest Li capacity for a specific microstructure. The energy efficiency changed from 55.3% to 40.2% and to 34.9%. The shapes of the CV curves also varied as the thickness increased. The original-thickness curve (solid red) shows slight multiple steps, indicating phase transitions during lithiation. In contrast, the curve (solid blue) of the triple-thickness case appears smooth with a negative slope. We interpret the linear curve for the thick electrode to be due to the strong non-uniformity of lithiation across the length of the electrode.

Figures 4.14(a) and (b) exhibit the simulated X_p for the TP E_IV and TP E_IV-3X cases, respectively, at a point close to the cut-off. Almost all particle surfaces in the original-thickness case reached a fully lithiated state throughout the entire electrode (as indicated by the bright yellow color). In contrast, in the triple-thickness case, only the particle surfaces in the front region ($16 < x < 40$ μm) reached a fully lithiated state. The particle surfaces in the remainder of the electrode were still at the Stage-3 phase ($X_p = 0.25$, indicated by the dark green color). Although only a portion of the particle surfaces was saturated with Li, those regions dominated the cell voltage to the cut-off value. Correspondingly the blue curve in Fig. 4.13(b) dropped rapidly and exhibited a monotonic negative slope.

The simulated CV curves for the IP configurations are plotted as the dashed curves in Fig. 4.13(b). Extending the electrode from the original to double and further to triple thicknesses decreased the achievable DoD from 0.52 to 0.489, and to 0.355, respectively. The corresponding energy efficiency are 57.5%, 46.3%, and 41.0%, respectively. Clearly, the low tortuosity in the IP configurations leads to smaller decreases in both achievable DoD and energy efficiency, compared to the TP cases. The triple-thickness IP configuration retained nearly twice that of the TP configuration in the achievable DoD. The slope of the CV curve (dashed blue) in the IP E_IV-3X here is smaller than that in the TP E_IV-3X (solid blue), suggesting that the X_p on the particle surfaces in the IP case will be more homogeneous throughout the electrode compared to the TP case. Experimental work has shown that aligning plate-like graphite particles along the primary diffusion direction significantly enhances the cell performance in comparison to unaligned particle configurations [95, 110, 111]. Our simulations fulfill the need for a quantitative evaluation of such effects.

Figure 4.14(c) displays the simulated X_p, in which the particle surfaces with saturated X_p were in the region approximately $16 < x < 70$ μm, and the particle surfaces in the remainder of the electrode were in Stage 2 ($X_p = 0.54$). These TP versus IP simulations support the experimental observations of enhancing cell performance by aligning the plate-like graphite particles along the primary direction [110].

Respective simulations were also performed on the original-thickness E_II and E_III in their IP

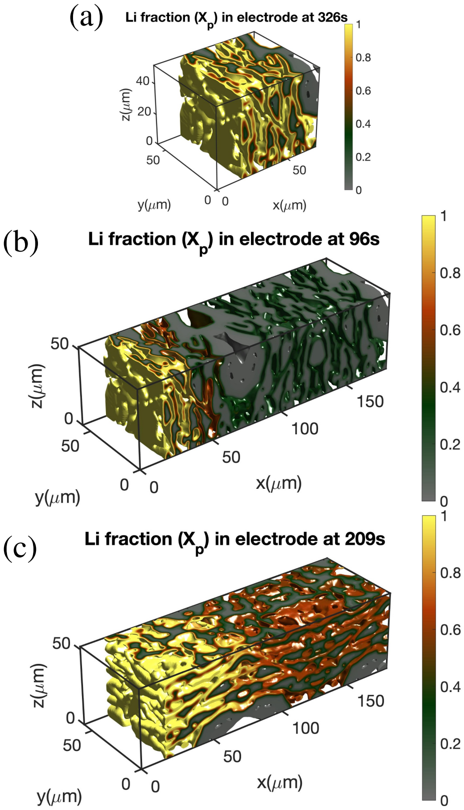

Figure 4.14 Lithium fraction in particle at 6C lithiation at the cut-off point for (a) TP single thickness at $X = 0.52$, (b) TP triple thickness at $X = 0.175$, and (c) IP triple thickness at $X = 0.35$.

configurations to compare them. The CV curves are provided in Fig. 4.15.

The TP and IP configurations performed very similarly. This is not surprising because tortuosity only has a minimal effect on the performance of electrodes of the original thickness examined here. Additionally, the TP and IP tortuosities of E_II or E_III have similar values.

In summary, these simulations demonstrate that, for electrodes of the original thickness (55.2 μm), the performance is affected only by particle sizes. The impact of pore tortuosity becomes prevalent once the thickness increases to double or more of the original case. In thick electrodes, a higher tortuosity will decrease the achievable DoD and energy efficiency more rapidly. As thick electrodes garner increasing attention for high-capacity applications and have been actively explored [95,112,113], the presented methodology offers the necessary quantitative tool to estimate their electrochemical performances without explicitly using their microstructures.

4.4.4 Lithiation protocols

Fast charging capability is crucial for the market penetration of electric vehicles. A full charge in ten minutes corresponds to a 6C rate. When graphite particle surfaces are saturated with intercalated Li, the electropotential across the particle-electrolyte interfaces becomes negative [104]. In this case, Li metal formation on particle surfaces is thermodynamically favored over insertion, resulting in Li plating. Thus, a negative electropotential drop across graphite surfaces

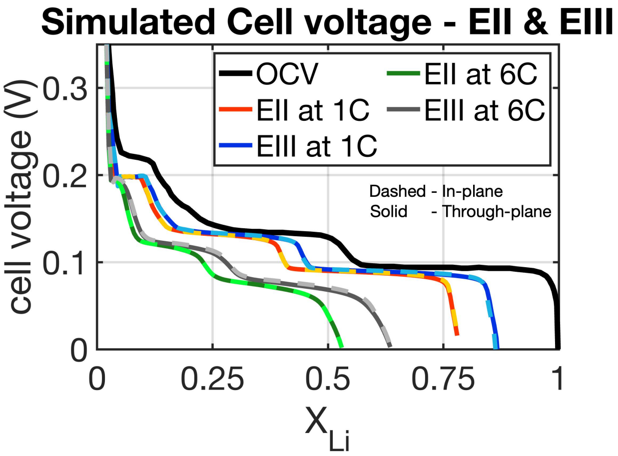

Figure 4.15 Simulated cell voltage curves at 6C and 1C rates for E_II and E_III in TP (solid lines) and IP (dashed lines) configurations. The TP and IP results are very similar.

indicates an overcharging condition, which is used as the cut-off criterion in the simulations. In this section, we use microstructure simulations to explore an approach to increasing electrodes' high C-rate capacity.

Figure 4.16(a) shows CV versus time for 6C lithiation of E_II for both TP and IP configurations. The CV curve reached the cut-off point at approximately 333 s, roughly half of the expected 6C duration (600 s).

In this section, we perform additional electrochemical simulations to explore how much further electrode utilization can be achieved at full 600 s without reaching the cut-off plating voltage (~ 0 V). The simulations were performed on E_II in the TP configuration and were terminated when either the lithiation process reached 10 minutes or the cell voltage reached the cut-off voltage. Several lithiation protocols, started with 6C, were examined and the details are in Table 4.2.

Table 4.2 Lithiation protocols, started with a 6C rate, examined in simulations.

	protocols	achievable DoD	duration
Case 1	6C → plating point	0.53	333 s
Case 2	6C → constant voltage	0.68	600 s
Case 3	6C → 4C → plating point	0.58	381 s
Case 4	6C → 4C → 1C	0.61	600 s
Case 5	6C → 1C	0.59	600 s
Case 6	6C → 2C	0.66	600 s

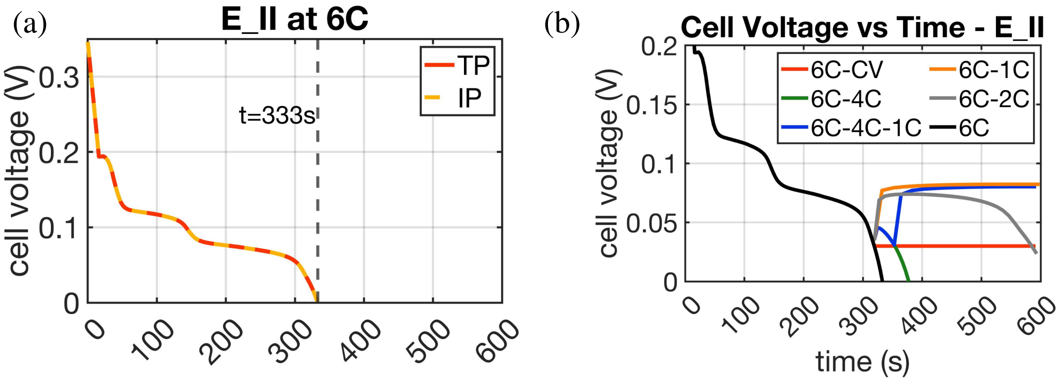

Figure 4.16 (a) Cell voltage vs time at 6C for TP and IP configuration. (b) Cell voltage vs time curves for lithiation protocols shown in the table 4.2. The green curve is beneath the blue curve when $316 < t < 355$ s. All the curves before 316 s are beneath the black curve.

In these simulations, once the CV reached 0.03 V, we reduced the insertion fluxes, which moved the electrode away from the plating point and allowed it to slowly accept Li until it reached the 10-minute duration (or the plating point again). The value of the switch point (0.03 V) was conservatively chosen to be close to but still above the Li-plating condition of the electrode at a 6C rate.

The simulated CV curves under these protocols are plotted in Fig. 4.16(b), in which only Case 1 (full-6C) and Case 3 (6C-followed-by-4C) were terminated before 600 s. Case 2 followed the typical constant-current-constant-voltage (CC-CV) protocol. It reached an achievable DoD of 0.68 at 600 s, showing a significant increase (∼ 0.15) relative to Case 1 during the additional 267 s. In Case 3, the initial 6C rate was reduced to a 4C rate after the CV reached the switch point. Clearly, there was a short relaxation period (316–325 s), during which the cell voltage increased. See the green curve in Fig. 4.16(b). During this relaxation period, the inward flux dictated by the X_p gradient (established by the 6C insertion) was larger than the 4C surface insertion flux. Thus, the particle surface X_p decreased and the CV increased. In the relaxation period, the Biot number is greater than one. Once the inward X_p gradient matched that for the 4C surface flux, surface X_p accumulated again and CV dropped. This 6C→4C case reached plating condition at 381 s with an achievable DoD of 0.58, only a 0.05 increase compared to a full-6C case. See the values reported in Table 4.2. Case 4 included an additional constant 1C insertion after Case 3 reached the switch point. The 1C period proceeded for about 220 s (37% of the total time). However, it

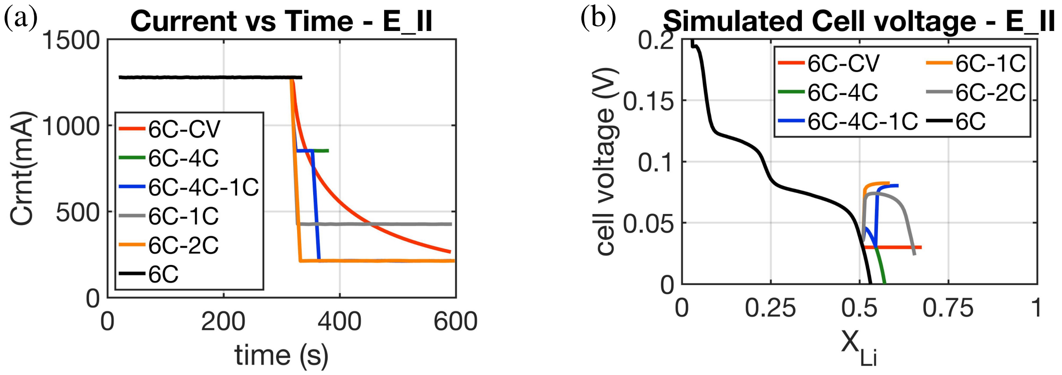

Figure 4.17 (a) Current vs time, and (b) CV curves for lithiation protocols shown in Table 4.2

only marginally increased the DoD by 0.03. Case 5 switched the current to 1C after 6C lithiation reached the switch point. Compared to Case 1, the additional 284 s of 1C lithiation increased the DoD from 0.53 to 0.59. Comparing Case 5 with Case 4, the short 4C period (316–353 s) increased DoD by 0.02. The plots of cell current versus time and CV curves versus DoD corresponding to those in Fig. 4.16(b) are provided in Fig. 4.17. The achievable DoDs for the cases examined above can be read from those figures.

Table 4.3 lists the results of several additional lithiation protocols, which did not start with a 6C rate. Cases 7 through 10 were all CC-CV lithiation protocols with increasing currents.

Compared with Case 2 (6C-CV), a higher initial C rate increased the achievable DoD. For instance, Case 10 (8C-CV) achieved a DoD of 0.694 at 600 s. However, the increase is marginal and seems to approach a limiting value. With initial lower C rates (Cases 7 and 8), the achievable DoDs are lower than the 6C-CV case. Overall, the results show that a high constant current in the CC-CV protocols can slightly increase the achievable DoD within the total 600 s duration. The curves of DoD versus time for these CC-CV simulations are shown in Fig. 4.18.

However, the high currents also lead to heat waste. The electrochemical energy released in the lithiation processes is also provided in Table 4.3, which shows a gradual decrease in energy release as a higher current is used in the CC-CV protocols. Thus the balance of achievable DoD and energy efficiency should be considered in terms of optimization. Based on the data presented in Table 4.3, it is likely that 5C-CV would be a sensible choice for a 600 s charging over 6C-CV, as the increase in DoD from 5C-CV to 6C-CV is marginal (~ 0.016). Still, a 5C start can reduce the stress on the particles which may help prolong the cycle life of the particles.

Table 4.3 CC-CV lithiation protocols examined in simulations

	protocols	achievable DoD	energy release
Case 7	4C → constant voltage	0.627	2.03×10^{-5} J
Case 8	5C → constant voltage	0.664	1.93×10^{-5} J
Case 2	6C → constant voltage	0.680	1.82×10^{-5} J
Case 9	7C → constant voltage	0.689	1.71×10^{-5} J
Case 10	8C → constant voltage	0.694	1.60×10^{-5} J

These simulations confirmed that the CC-CV lithiation, originally set up as a protective measure to avoid plating, can also deliver a significant increase in electrode DoD. The constant-voltage treatment leads the system to a relaxation by itself, which better performs than imposing another high rate insertion. While some of these facts may already be qualitatively known by battery researchers, this work provides a facile tool to assess such effects quantitatively. Note that the lithiation protocol study presented here is specific to E_II. If the system was changed to another electrode (e.g., E_III or E_IV), the exact quantitative results might be different, and the optimal protocols might differ as well. Nevertheless, our tool and framework are capable of identifying the optimum protocol for any electrode microstructure with any material properties.

4.4.5 Anisotropic effect in E_IV

In Section 4.4.1.2, we demonstrated that anisotropy in Li transport has only a negligible impact on the performance of electrodes consisting of randomly oriented spherical graphite particles. In Sections 4.4.3 through 4.4.4, we restrained the simulations to isotropic models for investigating the microstructure effects on graphite electrodes. However, E_IV has plate-like particles, which leads the through-plane direction to be easily identified as the slow transport direction. Here, we include the anisotropic Li transport in a new 6C simulation, in which the through-plane Li mobility is four orders of magnitude smaller than the in-plane mobility. The X_p distribution at the cut-off point

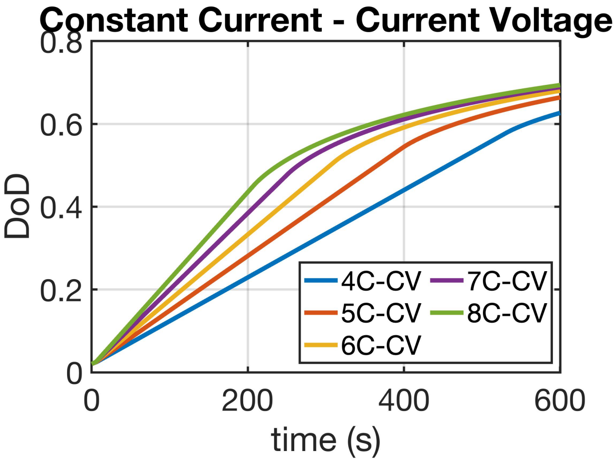

Figure 4.18 Simulated DoD versus time for different CC-CV lithiation protocols. The DoDs at 600 s are provided in Table 4.3)

(DoD =0.41) is shown in Fig. 4.19(a).

Figure 4.19(b) shows the simulated CV curve, plotted with a cyan dashed line. The isotropic result (presented earlier) is also provided (the blue curve) here for comparison. A significant decrease in cell performance is observed as the cell voltage is considerably lower in the anisotropic result. The achievable DoD at 6C is much lower at 0.41. Figures 4.19(c) and (d) compare the same zoomed-in section for an anisotropic and an isotropic simulation at the same DoD (0.41). The anisotropic result shows sharper gradients of X_p in the through-plane direction (x-direction) while relatively more uniform lithium distribution can be observed in the isotropic case. Furthermore, the isotropic particles have a higher X_p in their core centers. Evidently, the anisotropy in Li transport should be included for accurate simulations for graphite particles with a large aspect ratio. Thus, for all E_IV simulations presented earlier, the CV curves are expected to move toward the left if including transport anisotropy. Conversely, the isotropic results should be still valid for the simulations of sphere-like particles (E_II and E_III). Nevertheless, while our model is capable of

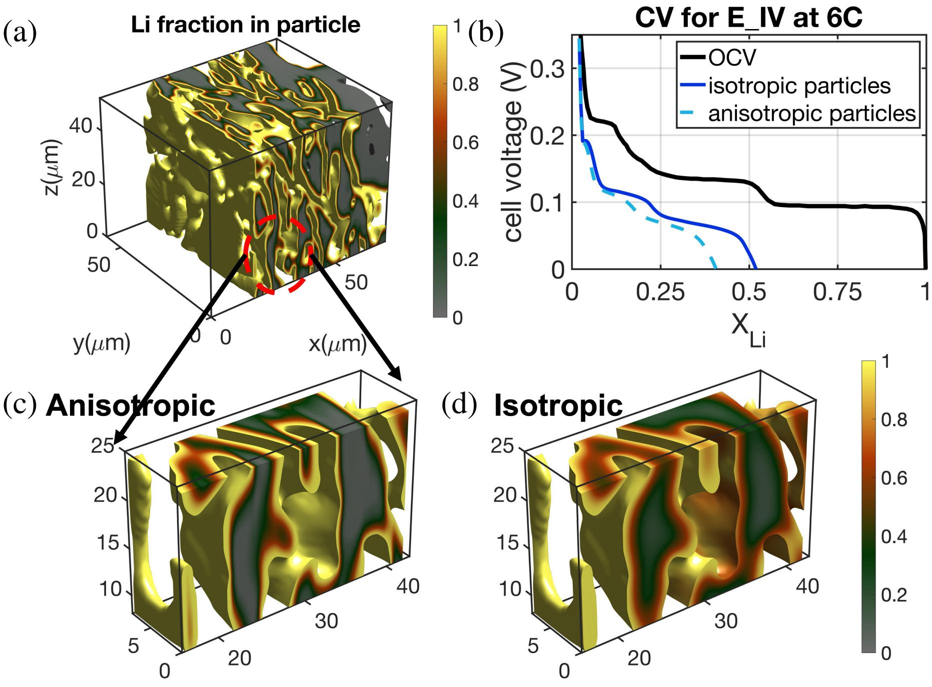

Figure 4.19 (a) Lithium fraction in particle for E_IV with anisotropy at 6C lithiation at the cut-off point $X = 0.41$, (b) CV curves for anisotropic and isotropic models for E_IV; (c) and (d) zoomed-in comparison for anisotropic and isotropic lithium concentration distribution.

including crystal orientations explicitly, it is difficult to detect graphite particles' crystal orientations in X-ray CT scans. Thus, using isotropic models is a forced choice due to the lack of orientation information. For spherical particles, the isotropic assumption is valid regardless.

4.5 Conclusion

We utilize the Cahn-Hilliard phase-field equation with the smoothed boundary method to simulate lithium transport and phase transitions in graphite particles within electrode microstructures, using input material properties parameterized from existing literature. Our simulations leverage direct voxel data specifically for graphite anodes but can be applied to analyze a wide range of other microstructures and materials. By establishing this framework, we demonstrate its efficacy in conducting in-silico(virtual) experiments to explore intricate details within electrode microstructures.

Our findings highlight the importance of considering phase transitions in electrode simulations. Neglecting these transitions by employing Fick's diffusion law to model Li transport in graphite particles leads to overestimating the electrode's performance. We investigate the influence of morphological properties such as porosity and tortuosity at the microstructural level by comparing three different reconstructed graphite electrodes. While pore tortuosity appears to have only a minor impact on electrode performance for thicknesses less than approximately $<\sim 100\ \mu$m, it becomes significant for thicker electrodes. These findings are consistent with experimental observations, further validating our simulation approach. Additionally, our simulations explore the effect of different lithiation protocols on extending electrodes' achievable Depth of Discharge (DoD). Within a target 6C duration, we quantitatively demonstrate that a constant-current constant-voltage protocol marginally outperforms other constant-current protocols. While these insights align with physical intuitions, our simulations provide valuable quantitative predictions based on explicit considerations of microstructures.

This work establishes a versatile framework transferable to the study of various electrodes. It has been successfully applied to investigate hybrid anodes [57], optimize tunnels in electrodes, and explore full-cell dynamics. Moreover, our work demonstrates the feasibility of simulating multiphysics phenomena in highly complex microstructures using modest computational resources.

While accurate material property parameters are essential for quantitative performance predictions, acquiring high-quality material properties experimentally can be challenging. Therefore, besides serving as a digital design tool for electrodes, we propose that our SBM framework could be employed to calibrate intrinsic material parameters in electrochemical measurements accurately.

CHAPTER 5

UNRAVELING HYBRID ANODE DYNAMICS AND ALLEVIATING PLATING

In this chapter, we investigate hybrid graphite-hard carbon anodes using the framework demonstrated in the previous chapters. As highlighted in Chapter 4, while graphite remains widely utilized in lithium-ion batteries, it exhibits limitations under fast charging conditions. Fast charging in graphite can result in poor electrode utilization due to spatially inhomogeneous current [114]. Additionally, Li plating becomes significantly favorable during fast charging on graphite anodes [115–117]. This chapter focuses on addressing these challenges via a thermodynamic approach, exploring hybrid anodes. Mixing various carbon-based materials [118, 119], and incorporating hard carbon to graphite anode [120–122] have been subjects of study in the literature, aiming to harness the benefits of both materials while minimizing their drawbacks. Recently, a graphite/hard carbon hybrid anode has shown potential in delaying and mitigating Li plating [123]. Chen et al. recently demonstrated that a graphite-hard carbon hybrid electrode offers significant advantages over a pure graphite or a pure hard-carbon electrode [123]. Hard carbon, composed of graphene fragments in an amorphous arrangement, exhibits a lower Li site density than graphite. Although hard carbon displays lower energy density, it demonstrates a more homogeneous current [124–126], which can be advantageous in delaying plating. Hereafter, we refer to hard carbon simply as “carbon.”

We adapt the framework presented in Chapter 4 for hybrid anodes. The smoothed boundary method (SBM) is employed to circumvent the need for conformal meshes at the microstructure level. While we continue using the Cahn-Hilliard equation to describe Li diffusion in graphite particles, Fick’s diffusion equation is adequate to model Li diffusion in carbon particles as carbon anode does not undergo any phase transformations during lithiation. As in Sections 3.3.2 and 4.4.1.2, a discrete element method is utilized to create synthetic electrode microstructures, allowing individual electrode particles to be distinguished and easily assigned to different active materials. Concentration-dependent material properties, parameterized from reported experimental data, are incorporated in the simulations.

In this chapter, the SBM simulations revealed an interaction between graphite and carbon particles at the microstructure level, which agrees with the Porous Electrode Theory (PET) modeling in Ref. [123]. During lithiation of the hybrid electrode, Li insertion is initially concentrated on carbon particles as it is thermodynamically favored in the first stage. Then, as the Li fraction in carbon increases, leading to a higher Li chemical potential in carbon particles compared to graphite particles, lithiation switches to graphite particles in the second stage. A third stage is revealed upon saturation of graphite particle surfaces where lithiation to carbon is favored again. This third stage of lithiation is especially beneficial at high C rates in delaying the onset of plating conditions. At these high C rates, graphite particle surfaces saturate much faster and the carbon particles act as a buffer to accommodate the additional lithium intake. This phenomenon represents another coupling behavior in addition to the physical mechanisms mentioned earlier, introducing a new aspect of electrode design. Thus, Li migration across graphite-hard carbon interfaces is examined as well. Microstructure arrangements, such as particle sizes and positions, can be manipulated to kinetically enhance or hinder the thermodynamics-driven interaction, as demonstrated in the simulations. Moreover, the simulations indicate that a hybrid graphite-carbon (HGC) electrode has a lower chance of Li plating than a pure graphite electrode, supporting reported experimental observations [123]. The impact of intrinsic material properties, such as Li diffusivity and exchange current density on carbon particles is also examined in the simulations. The SBM offers a significant advantage of fast implementation of electrode microstructure simulations, enabling easy rearrangement of particle configurations and reassignment of material properties to different particles. As a result, we expect this method to be widely employed to computationally study the effects of microstructure and intrinsic material properties on battery performance.

The content presented in this chapter is adapted from the author's publication in Affan Mailk et al., Electrochemical dynamics in hybrid graphite–carbon electrodes, MRS Communications (2022) [57].

5.1 Modeling and equations

As described previously, SBM employs a continuous domain parameter (ψ) to differentiate between regions occupied by electrode particles and the electrolyte. In Chapters 3 and 4, we explored half-cells with electrodes containing a single active material, while the hybrid anode in this chapter is composed of two active materials: graphite and hard carbon. SBM allows us to easily incorporate multiple domain parameters to define different materials within a system. In this work, we utilize two solid domain parameters: ψ_g and ψ_c representing graphite and hard carbon particles, respectively. The third domain parameter representing the electrolyte is defined as $\psi_e = 1-\psi_g-\psi_c$. The Li transport process in graphite is described by the Cahn-Hilliard equation, as in Chapter 4. The Cahn-Hilliard equation for graphite in hybrid anode:

$$\frac{\partial X_g}{\partial t} = \frac{1}{\psi_g}\nabla \cdot \left[\psi_g M_g \nabla \left(\mu_g^b - \nabla \cdot \varepsilon \nabla X_g\right)\right] + \frac{|\nabla\psi|_{ge}}{\psi_g}\frac{r_{xn,ge}}{\rho_g}. \tag{5.1}$$

where the subscript ‘g’ corresponds to graphite and $\mu_g^b = \partial f_g/\partial X_g$. X_i, ψ_i, M_i, μ_i, f_i, and ρ_i are Li fraction, domain parameter, mobility, chemical potential, free energy function, and Li site density, respectively. t is time, ε is the gradient energy coefficient, and $r_{xn,i}$ is the surface reaction rate.

The three domain parameters in the hybrid half-cell lead to three different interfaces. We differentiate different interfaces by using

$$|\nabla\psi|_{ij} = \sqrt{|\nabla\psi_i||\nabla\psi_j|}. \tag{5.2}$$

Thus, $|\nabla\psi|_{ge}$ denotes the interface between graphite and electrolyte, $|\nabla\psi|_{ce}$ denotes the interface between carbon and electrolyte, and $|\nabla\psi|_{gc}$ denotes the interface between graphite and carbon.

The kinetic equation for Li fraction evolution in hard carbon is similar to Eq. (5.1), except that the gradient coefficient vanishes because Li stays as a solid solution in amorphous carbon. The equation is shown here—

$$\begin{aligned}\frac{\partial X_c}{\partial t} &= \frac{1}{\psi_c}\nabla \cdot \psi_c M_c \nabla \mu_c + \frac{|\nabla\psi|_{ce}}{\psi_c}\frac{r_{xn,ce}}{\rho_c} \\ &= \frac{1}{\psi_c}\nabla \cdot \psi_c M_c \nabla\left(\frac{\partial f_c}{\partial X_c}\right) + \frac{|\nabla\psi|_{ce}}{\psi_c}\frac{r_{xn,ce}}{\rho_c},\end{aligned} \tag{5.3}$$

where the subscript ‘c’ indicates carbon and ‘ce’ indicates hard carbon-electrolyte interface. The subscripts ‘ge’ and ‘ce’ indicate graphite-electrolyte and carbon-electrolyte interfaces, respectively.

The magnitude of $|\nabla\psi|$ is nonzero only at particle-electrolyte interfaces, thus effectively delineating these interfaces. The current continuity equation, Eq. (2.14), requires modification to accommodate both graphite and hard carbon particles. We have two distinct particle surfaces within the hybrid anode, each with its own reaction flux and electrical conductivity. To address this, we introduce equivalent reaction fluxes and equivalent conductivities derived using the two domain parameters. These are then substituted into Eq. (2.14) to account for the new particle surfaces introduced in the hybrid anode. The modified equation is shown here. Current continuity in the hybrid anode:

$$\nabla \cdot \left[\left(\psi_g \kappa_g + \psi_c \kappa_c\right)\nabla\phi_s\right] - \left(|\nabla\psi|_{ge} r_{xn,ge} + |\nabla\psi|_{ce} r_{xn,ce}\right)\left(z_- F\right) = 0, \tag{5.4}$$

where κ_i and ϕ_s are the electrical conductivities and the electropotential, respectively. The subscript 's' indicates the entire solid i.e., the electropotential spreads over the entire solid, including both graphite and hard carbon. The domain of solid can be expressed by $\psi_s = \psi_g + \psi_c$, but $|\nabla\psi|_{ge}$ and $|\nabla\psi|_{ce}$ are two different types of reactive surfaces. F is the Faraday constant, and z_- is the charge number. The subscript '$-$' indicates anion.

Similar adjustments are made to ion diffusion and current continuity in the electrolyte expressed in Eqs. (5.5) and (5.6), respectively. Ion diffusion in electrolyte:

$$\frac{\partial C_e}{\partial t} = \frac{1}{\psi_e}\nabla \cdot \left(\psi_e D_e \nabla C_e\right) + \frac{\left(|\nabla\psi|_{ge} r_{xn,ge} + |\nabla\psi|_{ce} r_{xn,ce}\right)}{\psi_e}\frac{t_-}{\nu_+} - \frac{\mathbf{i_e} \cdot \nabla t_+}{z_+ \nu_+ F}, \tag{5.5}$$

Current continuity in the electrolyte:

$$\begin{aligned} \nabla \cdot \left[\psi_e \left(z_+ m_+ - z_- m_-\right) F C_e \nabla\phi_e\right] + \left(|\nabla\psi|_{ge} r_{xn,ge} + |\nabla\psi|_{ce} r_{xn,ce}\right)\frac{1}{\nu_+} &= \\ \nabla \cdot \left[\psi_e \left(D_- - D_+\right) \nabla C_e\right], \end{aligned} \tag{5.6}$$

The surface reaction is calculated using the Butler-Volmer equation on the graphite-electrolyte interfaces, Eq. (5.7) —

$$r_{xn,ge} = k_f^g C_+ \exp\left[\frac{-\alpha z_+ F}{RT}\left[\phi\right]_e^g\right] - k_b^g C_g \exp\left[\frac{(1-\alpha)\, z_+ F}{RT}\left[\phi\right]_e^g\right] \tag{5.7}$$

and on the carbon-electrolyte interfaces, Eq. (5.8) —

$$r_{xn,ce} = k_f^c C_+ \exp\left[\frac{-\alpha z_+ F}{RT}\left[\phi\right]_e^c\right] - k_b^c C_c \exp\left[\frac{(1-\alpha)\, z_+ F}{RT}\left[\phi\right]_e^c\right] \tag{5.8}$$

individually, where k_f^i and k_b^i are the forward and backward reaction rate constants, respectively, given by

$$k_f^g = \frac{i_{0,g}}{z_+ F C_+} \exp\left(\frac{\alpha z_+ F}{RT} \phi_{eq}^g\right) \;\; and \;\; k_b^g = \frac{i_{0,g}}{z_+ F C_g} \exp\left(\frac{(\alpha - 1) z_+ F}{RT} \phi_{eq}^g\right). \tag{5.9}$$

Similarly, for carbon, we have

$$k_f^c = \frac{i_{0,c}}{z_+ F C_+} \exp\left(\frac{\alpha z_+ F}{RT} \phi_{eq}^c\right) \;\; and \;\; k_b^c = \frac{i_{0,c}}{z_+ F C_c} \exp\left(\frac{(\alpha - 1) z_+ F}{RT} \phi_{eq}^c\right). \tag{5.10}$$

The SBM equations are then solved on a regular grid system, with a standard finite difference method [45–48] similar to Chapter 4.

The gradients of chemical potential drive Li transport in electrode particles. The chemical potential is related to the open-circuit voltage (OCV) by $\Phi_{\mathrm{OCV}} = \left(\mu - \mu_{\mathrm{Li}^0}\right)/\mathrm{e}$, where μ_{Li}^0 is the chemical potential of metallic Li (a constant value), and e is the elemental electron charge. Note that here we have assumed that metallic Li is the counter-electrode. Figure 5.1(a) shows experimentally measured OCVs of graphite-Li [97] and carbon-Li [123] cells versus the degree of discharge (DoD), from which μ_g and μ_c were extracted for the simulations. (Here, we used a graphite OCV curve slightly different from Ref. [123] to maintain consistency with our other work [50].) The four single-phase regions of $\mathrm{Li}_x\mathrm{C}_6$ are indicated by the numbers 1' through 1 on the gray curve, and the plateaus are the two-phase regions. The green curve monotonically decreases, indicating that Li stays a solid solution in carbon. The red curve is an expected OCV of a 50-50 hybrid electrode, obtained by linear interpolation from graphite and carbon OCVs. For the 50-50 hybrid electrode, the distribution is based on cell volume for ease of implementation. However, this approach can be easily adjusted to a weight-based ratio in any future studies. The curve is reasonably similar to the measured one in Ref. [123].

The Li mobility in graphite was parameterized from reported diffusivity data [100] according to $D_g = M_g(\partial \mu_g / \partial X_g)$, where D_g has four respective values of the four phases. Exchange current density (i_0), crucial in determining the rate constants of (de)intercalation reaction, is scarce in the literature. Thus, a Kinetic Monte Carlo simulated X_g-dependant i_0 [75] was used in this work. Due to the lack of experimental data for carbon, we assumed that Li diffusivity in carbon is a constant with a similar magnitude to that in graphite, and i_0 on the carbon-electrolyte surface is the same as that of graphite. Furthermore, since there is no available data, Li migration across particle contacts was considered in two extreme cases. The permeability was chosen to be zero for most of the simulations to eliminate interparticle transport. However, in two of the presented simulations, the other extreme of infinitely large permeability was examined by setting a substantially high value of permeability (relative to the mobility). The material parameters are detailed in the next section.

While SBM is uniquely powerful for directly using reconstructed microstructures in the sim-

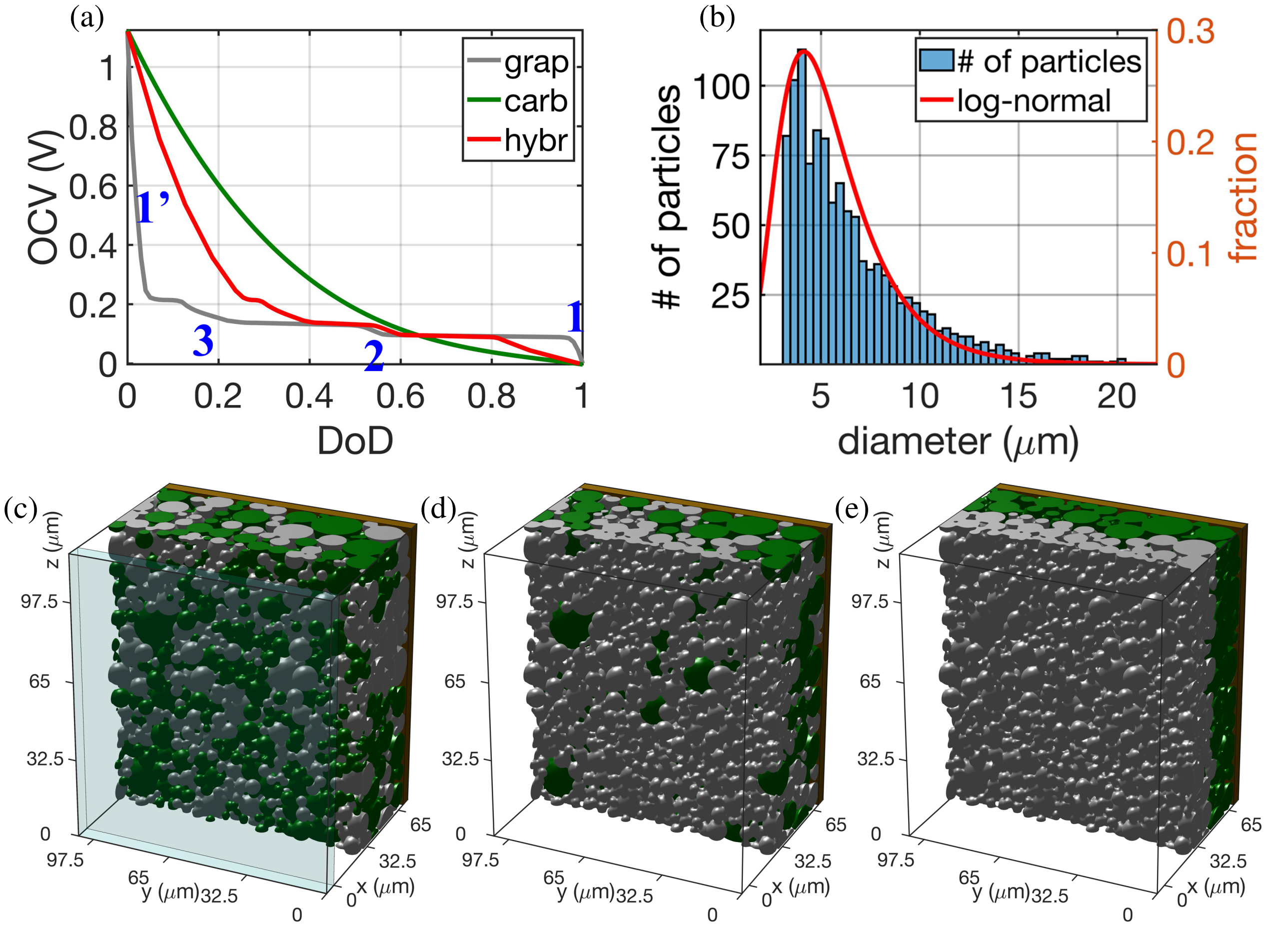

Figure 5.1 (a) OCV curves of graphite, carbon, and 50-50 hybrid electrodes. (b) Particle size distribution of the synthetic electrode microstructure in the simulations. (c) The virtual battery cell in the simulations, in which the gray and green colors indicate graphite and carbon particles, respectively, the semi-transparent cyan plate indicates the Li metal anode, the brown plate in the back indicates the current collector and the empty space between Li foil and hybrid electrode serves as the separator. Synthetic 50-50 hybrid electrodes in which graphite and carbon are assigned to (d) the small and large particles, respectively, and (e) front and back, respectively.

ulations [44, 127], we do not have access to X-ray computed-tomography reconstructed hybrid graphite-carbon (HGC) electrode microstructures that can clearly distinguish graphite and carbon. Thus, synthetic HGC microstructures made of spheres were computationally generated using the discrete element method for the simulations. The electrode contains 1159 spherical particles with a size distribution shown in Fig 5.1(b), approximately following a log-normal function. The gray and green colors in Fig 5.1(c) indicate graphite and carbon particles, respectively, in which the particles were randomly assigned to the two active materials, but the volume fractions were kept approximately equal. A virtual battery cell, comprised of Li foil (cyan slab), separator (empty space between cyan slab and electrode), HGC electrode, and current collector (brown slab), was used in the electrochemical simulations; see Fig 5.1(c).

5.1.1 Material parameters

Graphite and carbon OCV (ϕ_{OCV}) curves are shown in Fig 5.2(a). The chemical potentials of Li in graphite and carbon are

$$\mu_g = -\phi_{OCV,g} \ \text{(eV)} \tag{5.11}$$

$$\mu_c = -\phi_{OCV,c} \ \text{(eV)}, \tag{5.12}$$

respectively, versus metallic Li. The curves are shown in Fig 5.2(b). Note that $\phi_{OCV,g}$ has plateaus in two-phase regions. To impose chemical potential for phase separation, we extrapolate the curve from single-phase to two-phase regions. Thus, there are non-monotonic (laid-down S-shaped) regions on the gray curve in Fig 5.2(b). Li diffusivities in graphite are assumed to be 8.99×10^{-10}, 6.67×10^{-11}, 3.93×10^{-11}, and 1.20×10^{-10} cm^2/s for Phase-1' ($X < 0.06$), Phase-3 ($0.12 < X < 0.26$), Phase-2 ($0.48 < X < 0.58$), and Phase-1 ($X > 0.95$), respectively. The four segments of Li diffusivity are shown as the four gray horizontal lines in Fig 5.2(c). Here, we have multiplied the values in the data [100] by $100 \times 2/3$ for the simulations, such that the input parameters are close to many other measurements [103]. The Li diffusivity in hard carbon is assumed to be 1.0×10^{-11} cm^2/s, shown as the green horizontal line in Fig 5.2(c). Li mobilities are calculated from diffusivities and chemical potentials using Einstein's relationship. Li mobilities in graphite and carbon are shown as the gray and green curves, respectively, in Fig 5.2(d). The hump

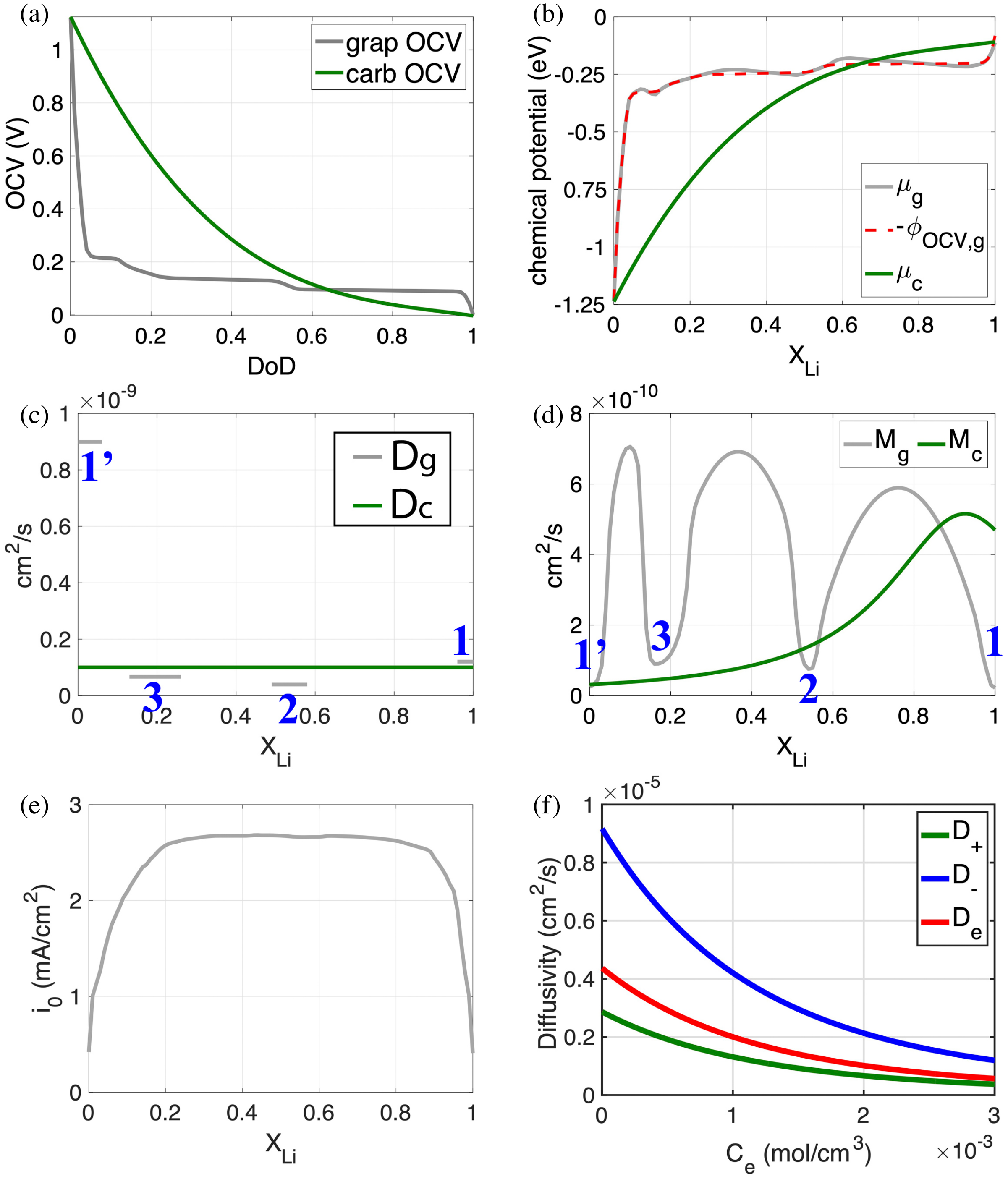

Figure 5.2 Material parameters used in the simulations. (a) OCV curves of graphite and carbon electrodes. (b) The chemical potential of Li in graphite and carbon. (c) Li diffusivities in graphite and carbon. (d) Li mobilities in graphite and carbon. (e) Exchange current density. (e) Ambipolar diffusivity and ionic diffusivities.

regions in M_g (gray curve) are extrapolated from the valley regions. Exchange current density is parameterized from reported KMC simulation results [75] and is shown as the gray curve in Fig 5.2(e). Ambipolar salt diffusivity, cation diffusivity, and anion diffusivity are shown as the red, green, and blue curves in Fig 5.2(f). The function of D_e is

$$D_e = 0.00489 \times \exp(-7.02 - 830C_e + 50000C_e^2) \quad \mathrm{cm}^2/\mathrm{s}. \tag{5.13}$$

We scaled the concentration-dependent Li salt diffusivity in Ref. [65] such that the values of D_+ and D_- at 1 M are 1.25×10^{-6} cm^2/s and 4.0×10^{-6} cm^2/s, respectively, as in Ref. [45]. The electrical conductivities of graphite and carbon used in the simulations are 3.3 and 1.0 S/cm, respectively. Li site densities used in the simulations for graphite and carbon are 0.0312 and 0.0227 mol/cm^3, respectively. In this work, we tabulated μ_g, μ_c, M_g, M_c, and reaction constants into tables, instead of fitting them to functions. Those quantities were interpolated from the tables in the simulations. The simulation domain has a dimension of $320 \times 215 \times 360$ Cartesian grid with $\Delta x = 0.325$ μm. We again adopt the binary electrolyte, LiPF$_6$ dissolved in an arbitrary organic solvent, as detailed in Chapter 3. The ambipolar diffusivity in Eq. (2.18) and ionic diffusivities in Eq. (2.20) are also identical to the ones used before. More details can be found in Chapter 3 and Refs. [24,50,57,58].

5.2 Results and Discussion

5.2.1 Simulations on 50% hybrid anode

Figures 5.3(a) through (c) display snapshots of simulated Li fraction in the hybrid electrode at three different times during a constant 6C-rate lithiation. Here, C rates represent the rates of charge or discharge in terms of capacity. Specifically, 6C means a full charge or discharge in 1/6 hours (10 minutes). The total capacity of this hybrid electrode is 1.041×10^{-8} mol of Li (or 1.004 mAh), for which a 6C rate corresponds to 2.790×10^{-4} mA. Detailed calculation is provided in the Appendix D.1. At the initial state, the Li fraction in graphite is $X_g \sim 0.02$, and that in carbon is $X_c \sim 0.23$. See the gray and green arrows in Fig 5.3(a) for the initial Li fractions in the graphite and carbon particles, respectively. These lead to an average Li faction ($\bar{X}$, equivalent to DoD) of the electrode to be $\bar{X} \sim 0.125$.

Here, we set the initial X_g to be 0.02 instead of 0 to ease numerical implementation. A small time step size will need to be used for a stable simulation if $X_g = 0$ because the magnitude of μ_g at $X_g = 0$ is large. We do not expect additional insights to be gained in much longer simulations in which the initial X_g is 0. The initial values of X_g and X_c are equilibrated at an initial cell voltage of 0.5265 V. Since Li fractions determine chemical potential and Butler-Volmer reaction rate, the cell voltage, and OCV curves are plotted versus Li fraction, i.e., DoD. Note that DoD in this chapter is normalized with each electrode's total capacity. The simulation reveals a three-stage lithiation process. Initially, Li is predominantly inserted into carbon particles, after which intercalation shifts considerably towards graphite particles. Subsequently, Li insertion in carbon particles becomes favored again. These three stages correspond to the three segments with different slopes on the blue curve, simulated cell voltage (CV), in Fig 5.4(a). In the first stage, graphite particles are in Phase-1' ($X_g < 0.06$, indicated as 1' in Fig 5.1(a)). Increasing X_g requires a substantial increase in chemical potential (μ_g), as inferred from the steep slope of the gray curve in Phase-1' in Fig 5.2

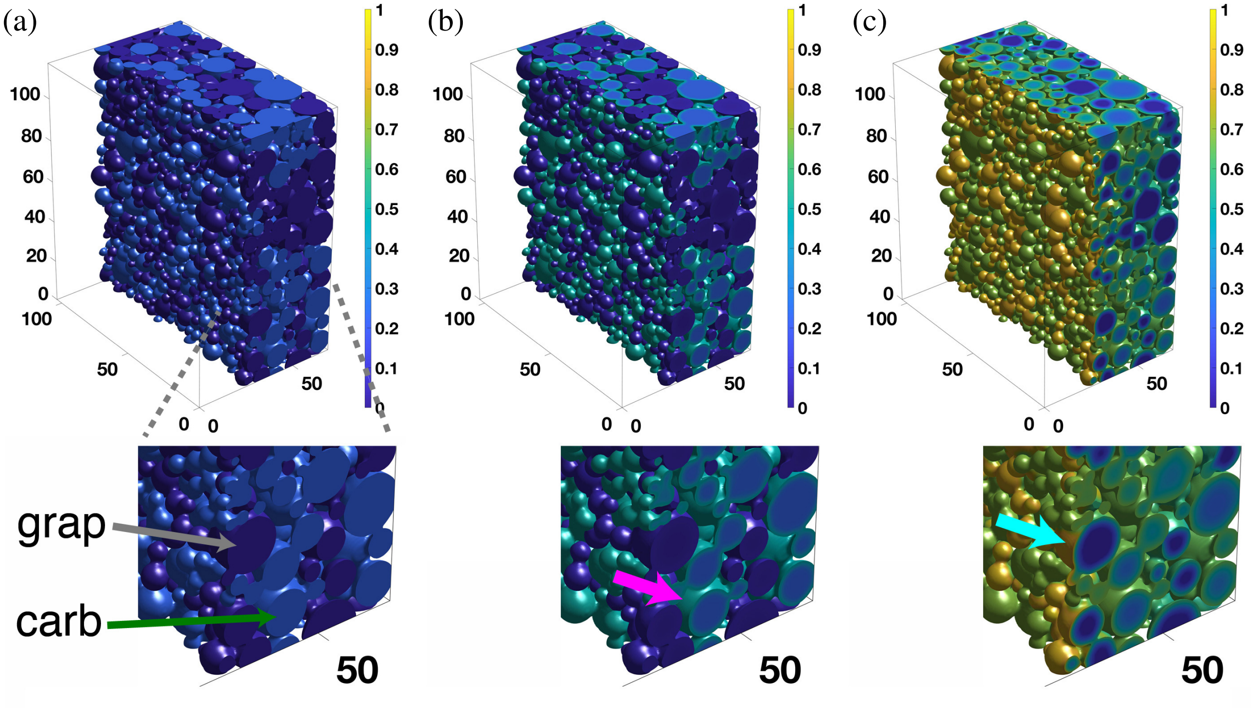

Figure 5.3 Simulated Li fraction in the hybrid electrode for a 6C lithiation at depth of discharge (DoD) equal to (a) 0.125 (t = 0 s), (b) 0.185 (t = 35 s), and (c) 0.41 (t = 183 s). The row below shows the magnified views.

(which corresponds to the gray curve in Phase-1’ in Fig 5.1(a)); i.e., the resistance of Li insertion to graphite is large. As a result, Li insertion mainly occurs in the carbon particles, leading to high

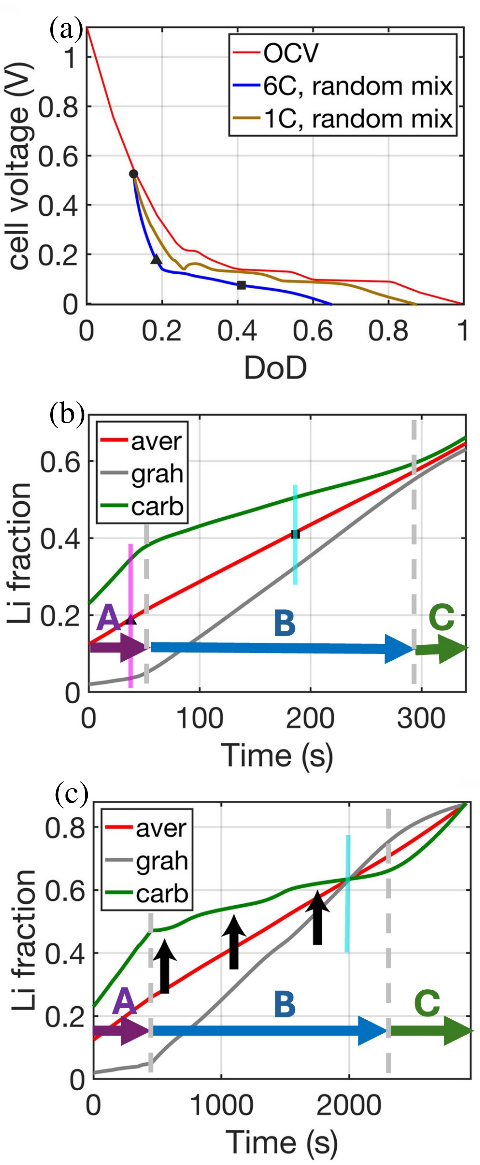

Figure 5.4 (a) Simulated cell voltage: blue and brown curves are for the 6C and 1C lithiation, respectively. Li fraction over time for (b) 6C and (c) 1C lithiation. The three markers on the blue curve in (a) indicate the corresponding DoDs to Fig 5.3(a) through (c). The red, gray, and green curves in (b) and (c) are the fractions of the whole electrode, graphite particles, and carbon particles, respectively. The magenta line and triangle in (b) indicate the time corresponding to Fig 5.3(b). The cyan line and square in (b) indicate the time corresponding to Fig 5.3(c). The cyan line in (c) indicates the time when graphite and carbon curves intersect. The three black arrows in (c) point to the three plateaus on the carbon curve. The three arrows labeled A (magenta), B (blue), and C (green) highlight the three stages of lithiation, respectively.

X_c on carbon particle surfaces; see the magenta arrow in Fig 5.3(b) for an example.

Note that the governing equations of Li salt concentration evolution and electrostatic potential in the electrolyte, electrostatic potential in the particles, and reaction rate on the particle surfaces are also simultaneously solved in the SBM at the microstructure level. However, since the X evolution most intuitively represents the cell voltage behavior, we focus our discussions only on X distribution in the particles in this chapter. Examples of other fields are provided in Figs. 5.5 and 5.6. Given their similarity with the fields presented in previous chapters, in-depth discussions of those fields are not presented here. Readers are referred to Ref. [24,50,123] to study the relevant impacts from those fields. Although both X_c and X_g increase during this stage, X_c increases much faster. Figure 5.4(b) shows the evolution of average Li fractions of the entire electrode (red), carbon particles (green), and graphite particles (gray). The curves are plotted versus time to highlight the time scale. Since a constant 6C rate was used, time is linearly scaled with DoD: $t = 600$ s corresponds to DoD = 1. At the point that Fig 5.3(b) was taken (corresponding to the black triangle markers in Fig 5.4(a) and (b)), X_c has increased from 0.23 to 0.34 while X_g only increased from 0.02 to 0.03.

As X_g in graphite particles exceeds the solubility limit of Phase 1', intercalation into graphite becomes much easier because a large X_g variation requires only a small change in μ_g. Within the multiple-plateau regime ($0.06 < X_g < 0.83$), the total decrease of OCV over the entire multiple-plateau regime is small, as shown on the gray curve in Fig 5.1(a). Thus, Li intercalation to graphite occurs increasingly, as indicated by the steep slope of the gray curve in Fig 5.4(b), passing the vertical magenta line. This stage corresponds to the second part of the blue CV curve ($0.2 <$ DoD < 0.56) in the 6C simulation in Fig 5.4(a). Figure 5.3(c) shows the Li fraction at $t = 183$ s and DoD = 0.41 corresponding to the black square markers in Fig 5.4(a) and (b), at which average $X_g = 0.32$ and $X_c = 0.5$, but surface X_g has reached > 0.8 on some graphite particle surfaces; see the cyan arrow in Fig 5.3(c). However, large graphite particles still have their cores at Phase 1' ($X_g < 0.05$) due to the inherent phase separation in graphite. The coexistence of the four different phases in a concentric core-shell structure can be observed for those particles. An illustrative image is shown in 5.7 to show the distribution of four phases in the graphite particles.

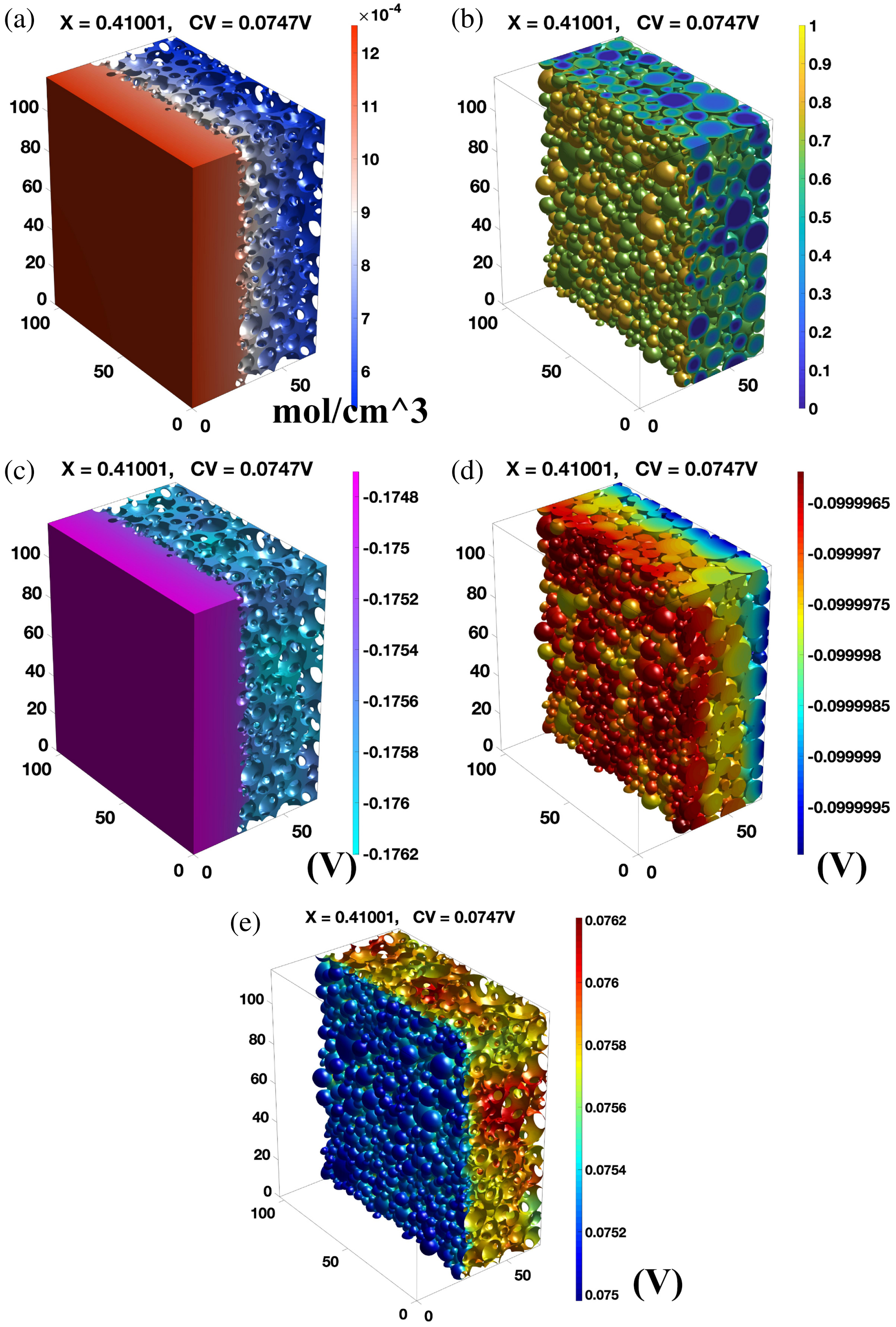

Figure 5.5 Simulated (a) Li salt concentration in the electrolyte, (b) Li fraction in electrode particles, electrostatic potentials in the (c) electrolyte and (d) particles, and (e) SEPD on particle surfaces at $X = 0.41$ at $t = 183$ s at 6C lithiation.

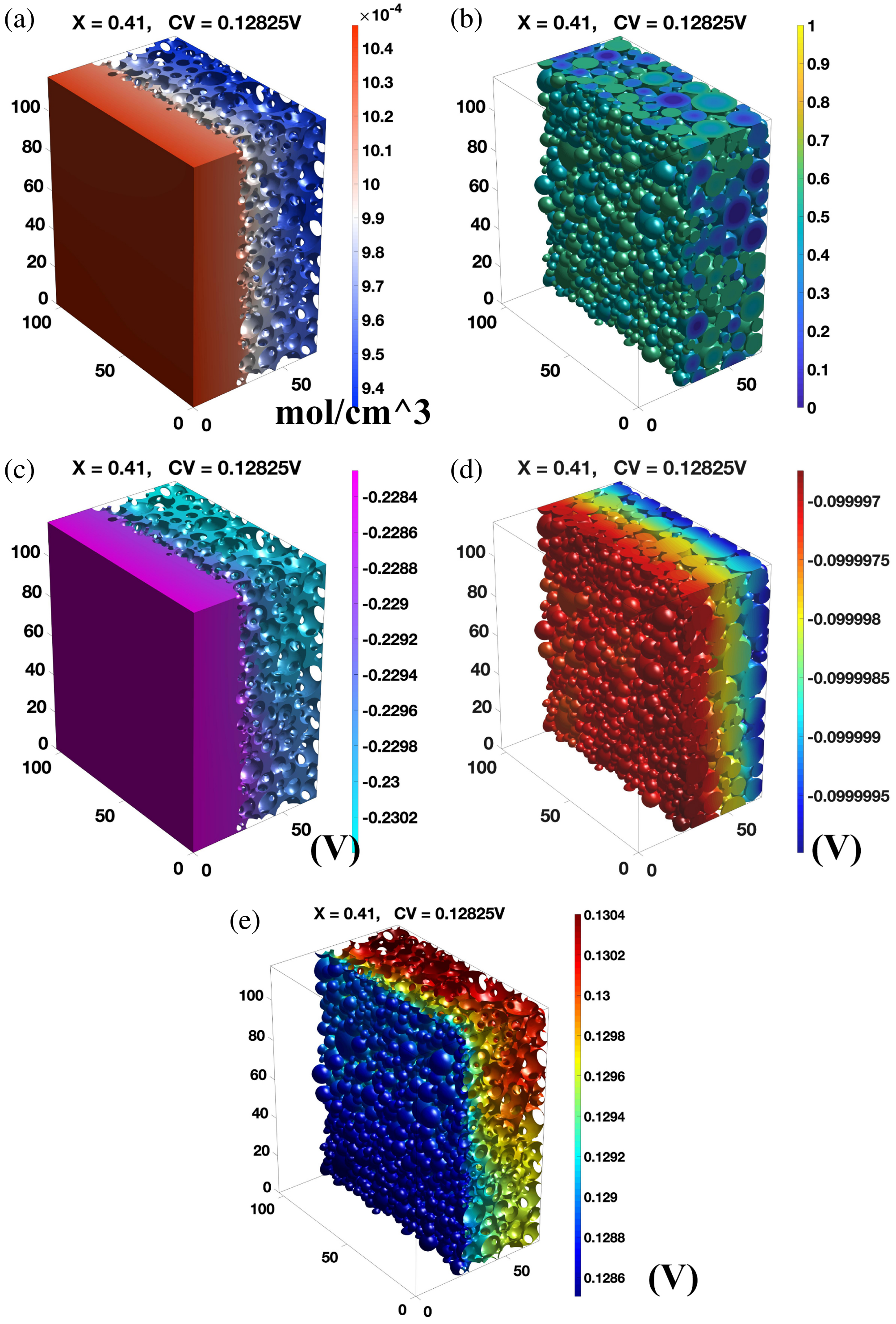

Figure 5.6 Simulated (a) Li salt concentration in the electrolyte, (b) Li fraction in electrode particles, electrostatic potentials in the (c) electrolyte and (d) particles, and (e) SEPD on particle surfaces at $X = 0.41$ at $t = 1068$ s at 1C lithiation.

A third stage is also observed, albeit briefly before meeting the termination criteria, where lithiation to carbon once again becomes favored over graphite. This shift occurs because graphite particle surfaces become saturated with lithium, significant resisting further Li insertion. In contrast, carbon surfaces maintain a lower lithium concentration due to lithium forming a solid solution within the carbon, unlike the phase separation observed in graphite. This allows the carbon particles to act as a buffer for lithiation, which is not present in a pure graphite anode, thus alleviating plating. We further discuss this phenomenon in Sections 5.2.2 and 5.2.3. This third stage corresponds to the third segment of the blue CV curve (0.56 < DoD < 0.63) in the 6C simulation in Fig. 5.4(a). During this stage, X_g on graphite surfaces is significantly higher than X_c on carbon surfaces, although the average Li fraction in graphite is still marginally lower than that in carbon, as observed in Fig. 5.4(b). The three stages of lithiation are highlighted as A, B, and C in Figs. 5.4 (b) and (c), respectively. Henceforth, this 6C lithiation simulation serves as the baseline

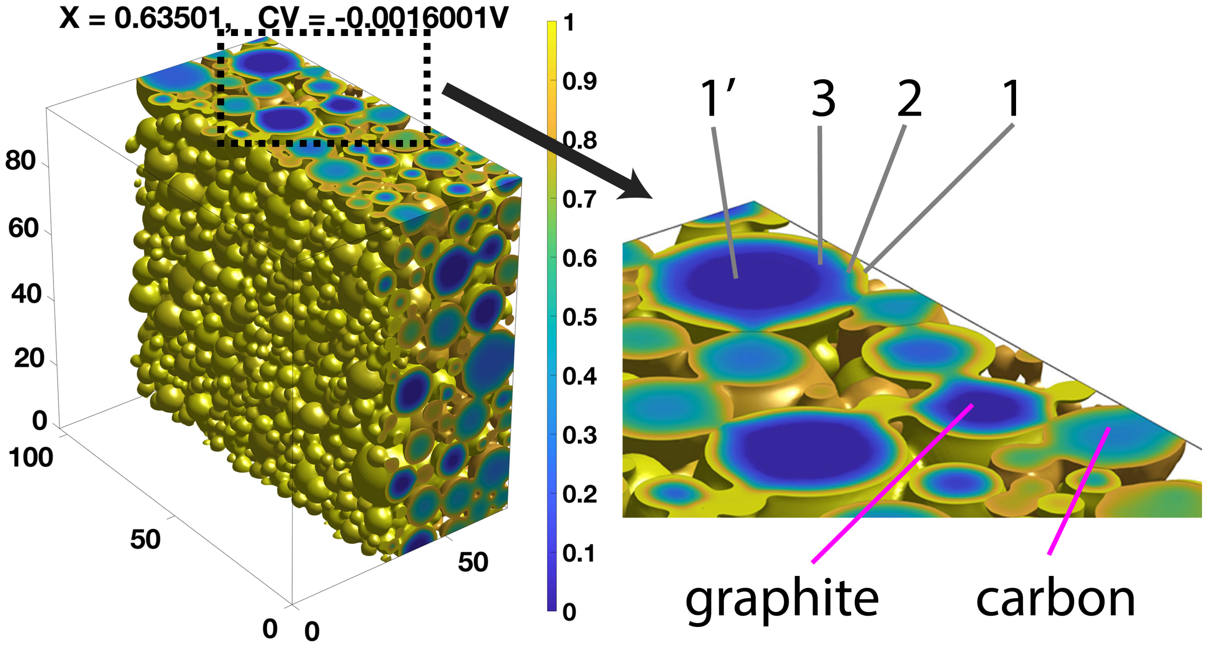

Figure 5.7 Li fraction in graphite and carbon particles for 6C lithiation at $X = 0.635$. The magnified view shows that there are four phases in graphite particles: from the core to the surface are Phase 1' (dark blue), 3 (light blue), 2 (green), and 1 (bright yellow). The average X_g and X_c are similar, but X_c is more uniform in carbon particles. The carbon particle surfaces are less saturated than the graphite surfaces.

result and is referred to as the standard case for future comparisons.

In addition to the high C rate case, simulation was performed on the same synthetic electrode for a 1C lithiation, and the obtained CV is plotted as the brown curve in Fig 5.4(a). As expected, the CV is closer to the OCV at a low rate, and the CV curve exhibits a more pronounced multiple-plateau region (with three plateaus). A small dip is observed near DoD = 0.26, which indicates a sudden decrease in Gibbs free energy of graphite when Phase 3 nucleates from a Li-saturated, metastable Phase 1'. Similar small CV drops are commonly seen in simulations of phase-separating materials yet not reported in experimental measurements. Phase separation (nucleation of a new phase) from a metastable (supersaturated) state will suddenly reduce the system's free energy according to classical thermodynamics, leading to a sudden change in cell voltage. This phenomenon is widely observed in phase-field simulations of electrochemical materials involving phase transformations, for example, in the simulations of intercalation of Li_xFePO_4 [34, 45, 56, 128–130]. The simulated cell voltage curves will exhibit a dip or peak when a new phase nucleates in the particles. While a

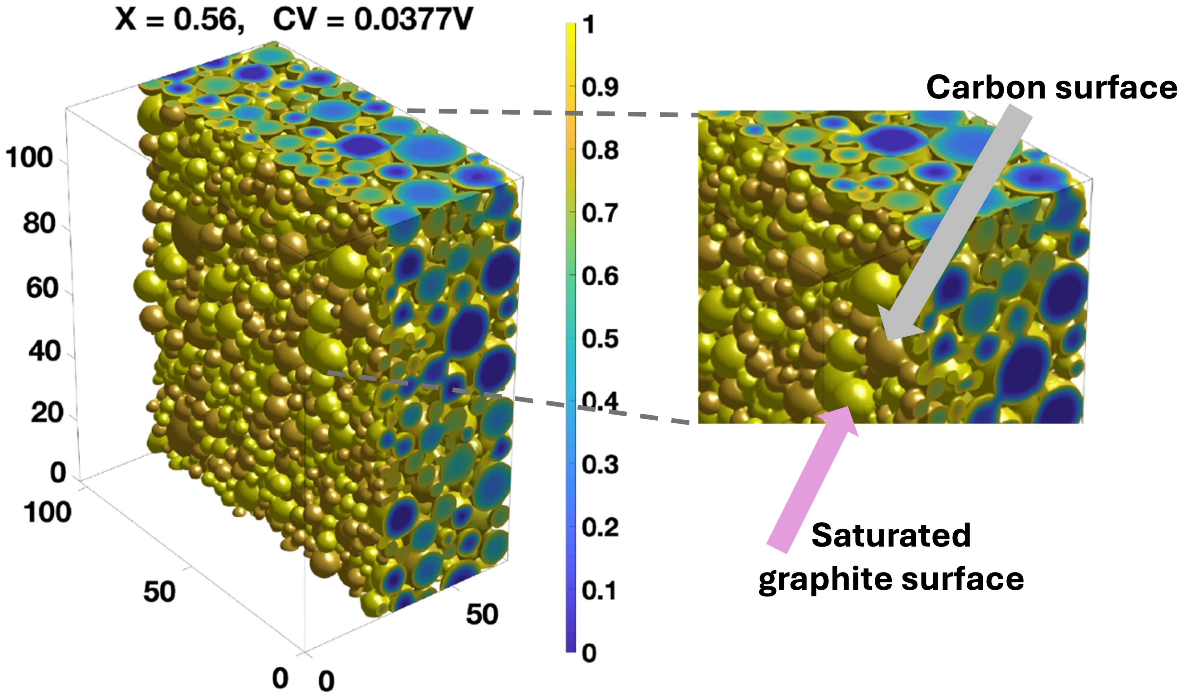

Figure 5.8 Li fraction in graphite and carbon particles for 6C lithiation at $X = 0.56$. The magnified view highlights the difference in surface Li concentration between graphite and carbon particles.

20–30 mV nucleation barrier for Li_xFePO_4 has been measured from the intrinsic hysteresis [131] of cell voltage on cycling, such a dip/peak on cell voltage curves, corresponding to the nucleation barrier, has not been reported in experiment observations. It is generally believed that the dip/peak associated with the nucleation event in each individual particle is averaged out in the aggregate of a real electrode [131], which usually contains a large number of particles. Therefore, dips/peaks cannot be resolved on an electrode's measured cell voltage curve.

The three-stage dynamics is more clearly observed in the 1C case as it is closer to an equilibrium process. Initially, intercalation occurs mainly into carbon, then switches to graphite, as indicated by the steep slope of the green curve in Fig 5.4(c) before $t = 452$ s, and finally switches back to graphite ($t >\sim 2400$ s). In contrast to the 6C case, the intrinsic thermodynamic behavior of phase separation in graphite is more pronounced in the second-stage dynamics at 1C. For instance, three plateaus can be observed on the green X_c curve; see the black arrows in Fig 5.4(c). it is important to note that Li remains a solid solution in amorphous carbon throughout the whole process. Each plateau corresponds to one of the two-phase regions of graphite. These slow carbon lithiation speeds can be understood as follows. At low rates, graphite lithiation during a two-phase process requires only a small μ_g variation (μ_g variation would be zero in an equilibrium phase transformation). Thus, when graphite is in a two-phase transformation, most Li is inserted into the graphite, leading to reduced carbon lithiation rates.

This thermodynamic behavior is even more prominent at the final stage ($t > 2000$ s or DoD $>$ 0.635), during which the average X_g is higher than the average X_c, see the curves passing the cyan vertical line in Fig 5.4(c). The cross-over point is where the graphite and carbon OCV curves in Fig 5.1(a) intersect, after which the thermodynamics favor a higher X_g than X_c. The video files of 6C and 1C simulations are available on Ref. [57] SI web page and are detailed in Appendix D.2 (phase transformation wave sweeping through the electrode can be observed in some of the videos, which is equivalent to the 'heterogeneous reaction rate' discussed in Ref. [123].).

The moles of Li intercalated to graphite and carbon are shown in Fig. 5.9(a) and (b) for 6C lithiation and 1C lithiation, respectively. The red, gray, and green curves are for the hybrid

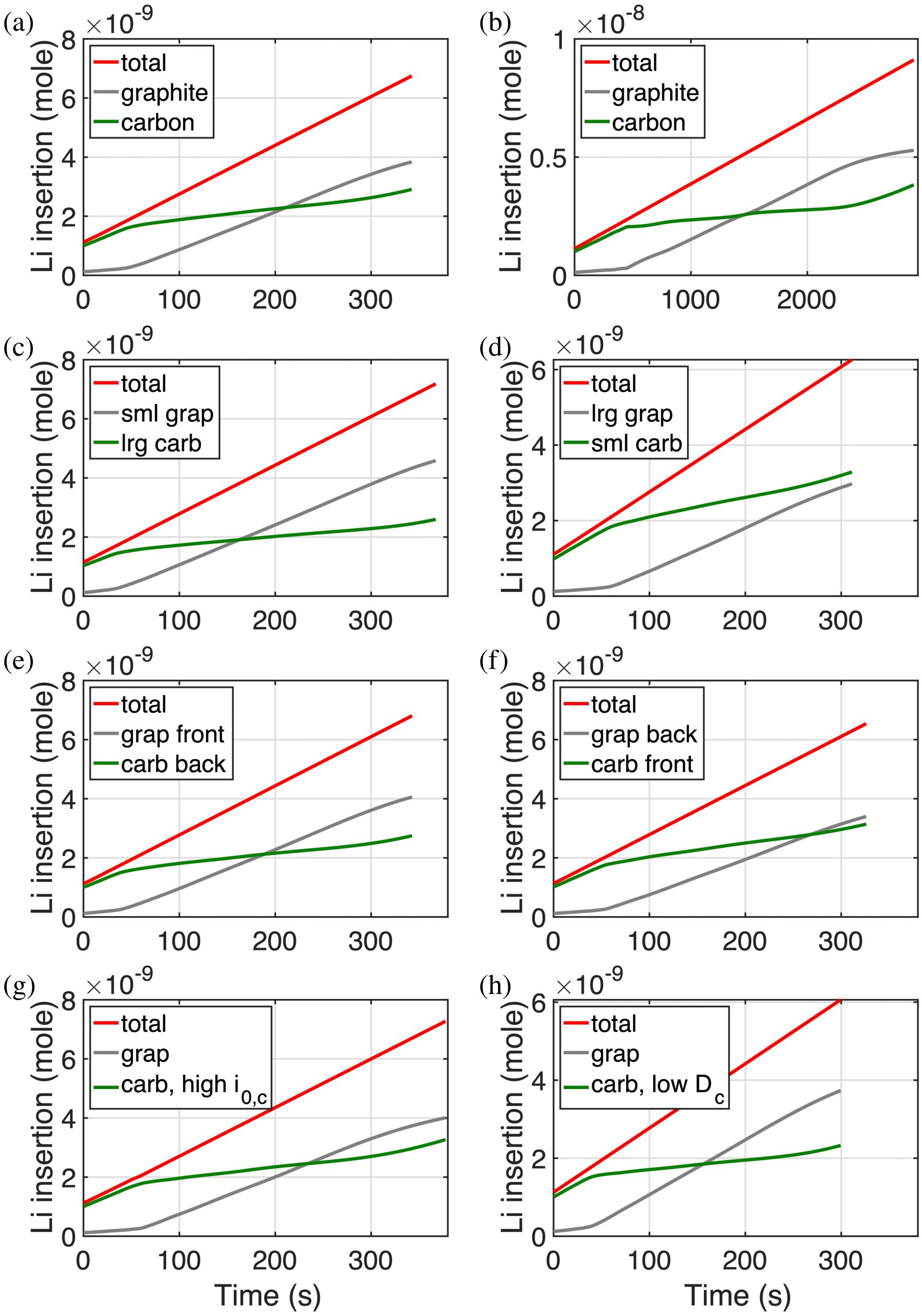

Figure 5.9 Simulated Li intakes over time. The standard case: (a) 6C lithiation and (b) 1C lithiation. Cases of 6C lithiation in (c) small graphite and (d) small carbon particles. Cases of 6C lithiation in (e) graphite and (f) carbon in the front region. Cases of 6C lithiation in (g) high carbon i_0 and (h) low carbon diffusivity.

electrode, graphite particles, and carbon particles, respectively. It should also be noted that although X_c increases in a similar range to that of X_g in Fig 5.4(b) and (c), the total amount of Li intercalated to graphite is much larger than that to carbon because Li site density in graphite is approximately 1.5 times that of carbon.

5.2.2 Surface electropotential drops (SEPDs)

5.2.2.1 Pure carbon vs pure graphite vs 50% hybrid

Surface electropotential drops (SEPDs, electrostatic potential across the particle-electrolyte interface) were examined in simulations of a pure carbon electrode, a pure graphite electrode, and a 50-50 hybrid electrode at 6C lithiation. Since Li fractions determine particle overpotential, we examine the electrochemical performance with the same initial DoD for all three electrodes. Again, the initial DoD was set to be 0.04 for the ease of numerical implementation. Note that because the capacity of each electrode is different, a 6C rate corresponds to different current densities. The quantities are provided in Appendix D.1. The cutoff point was set at the state that intercalation was no longer thermodynamically favored on active surfaces throughout the entire electrodes; i.e., SEPDs were all below zero. (Negative SEPD indicates that the chemical potential for forming Li metal is lower than that for intercalation, and thus Li-plating is thermodynamically favored [104].) Figure 5.10(a) shows the simulated cell voltages of those three electrodes. The cutoff occurred at similar times in the three simulations. The respective cell voltage curves versus capacity are provided in Fig. 5.11. The SEPD distributions at cutoff are shown in Fig 5.10(b) through (d). In the pure carbon and pure graphite electrodes, SEPDs monotonically descend toward the separator regions, but SEPDs in the hybrid electrode strongly correlate to the type of particles. The SEPD is more negative on graphite particle surfaces than on carbon particle surfaces. See the magenta and cyan ovals in Fig 5.10(d).

The simulations showed that X_g on graphite surfaces is much higher than that in the bulk because of the inherent phase separation. On the other hand, X_c is more uniform in the particles. Even when the average X_c is higher than X_g, the carbon surface is still unsaturated with Li. Carbon particles can further accommodate Li that would be plated on graphite surfaces; i.e., carbon serves

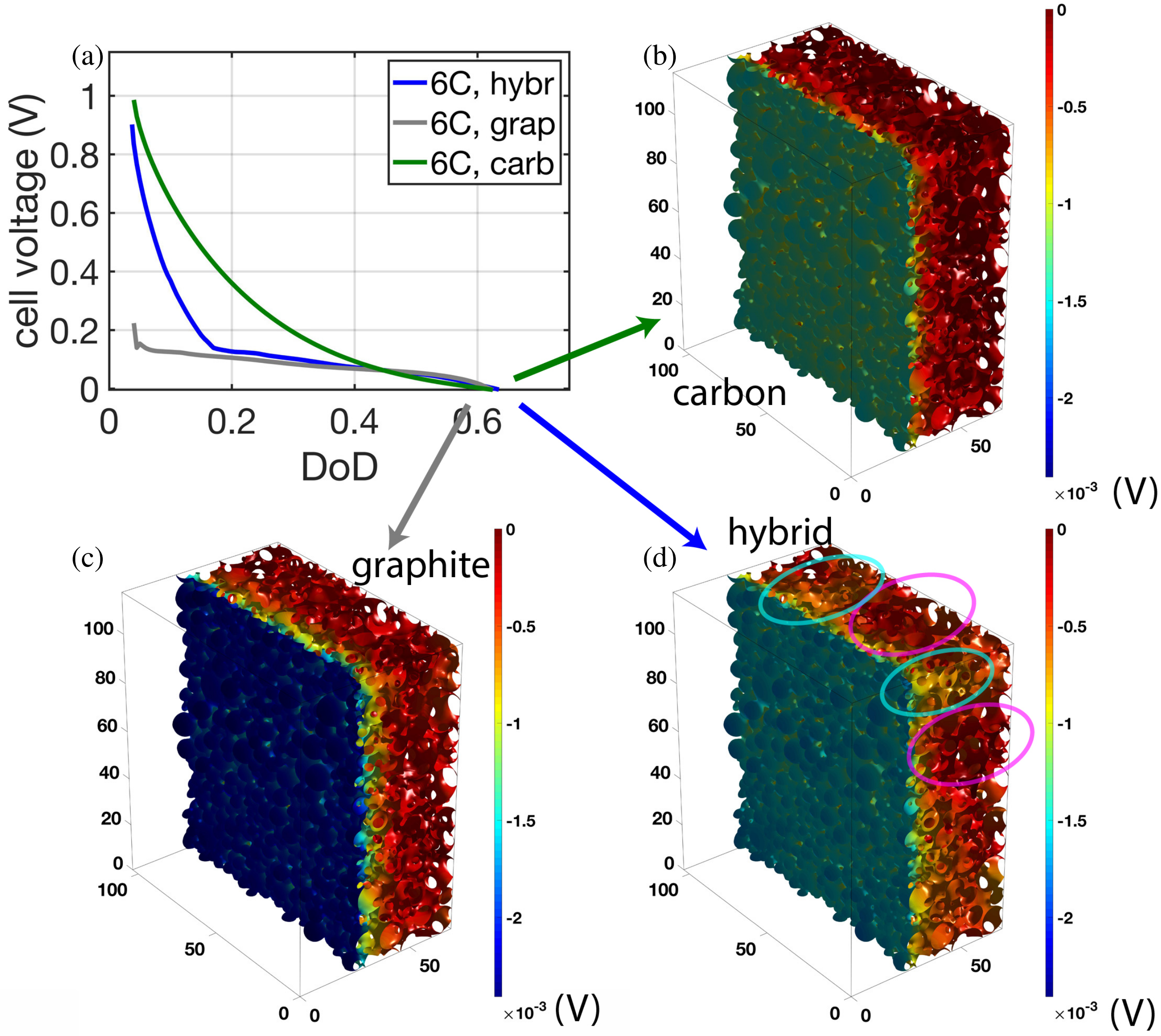

Figure 5.10 (a) Simulated cell voltage at 6C lithiation of carbon (green curve), graphite (gray curve), and hybrid (blue curve) electrodes. Simulated particle surface electropotential drop (Volt) at the cutoff point for (b) carbon, (c) graphite, and (d) hybrid electrodes. The particle surface electropotential drops at the regions near the separator are approximately -1, -2.45, and -1.6 mV in carbon, graphite, and hybrid electrodes, respectively. The magenta and cyan ovals indicate regions with more graphite and carbon particles, respectively.

as a buffer for excessive Li in the hybrid electrode. Thus, less Li plating would occur on the saturated graphite surface. The SEPDs near the separator are approximately −2.45, −1.6, and −1 mV in the graphite, hybrid, and carbon electrodes, respectively, indicating that Li plating is more favored on the graphite electrode than on the other two. This result directly supports the experimental observations [123] that Li plating is less observed on hybrid electrodes than on a pure graphite electrode. While the role of phase separation in graphite on Li plating has been previously discussed by Chen et al [123] and Gao et al [109], the SBM simulations illustrate this mechanism at the particle-microstructure level.

5.2.3 Exploration of hybrid anode arrangements

5.2.3.1 Effect of permeability

The fact that a hybrid electrode exhibits a three-stage lithiation process indicates a difference in the driving force of Li intercalation between carbon and graphite particles. Such a deviation may lead to Li migration across graphite-carbon contact interfaces. Thus, two additional simulations were performed to study such an effect from a modeling perspective, in which permeability of 1×10^{-5} cm/(s·eV) per Li was assigned to graphite-carbon interfaces (similar to the treatment in

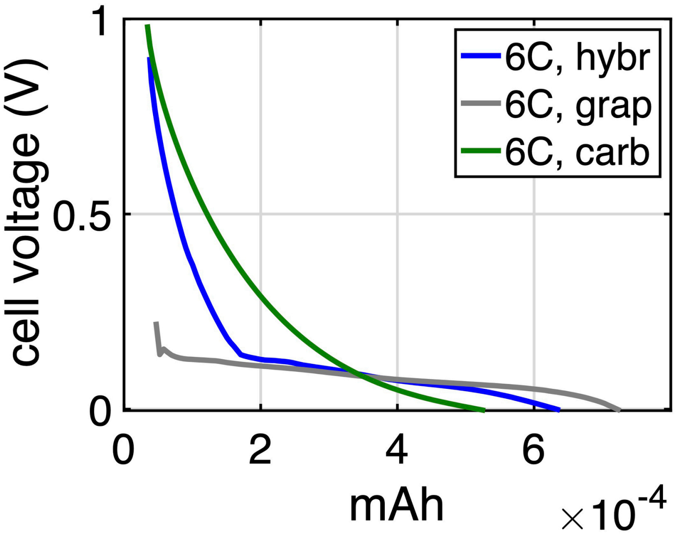

Figure 5.11 Simulated cell voltage curves of hybrid, pure graphite, and pure carbon electrodes at 6C lithiation. The curves are plotted versus Li capacity. As can be seen, the capacity of a pure graphite electrode is larger than that of hybrid and pure carbon electrodes.

Ref. [46]). This value, several orders of magnitude greater than Li mobility, was chosen such that the permeability will not limit Li migration. The blue curves in Fig 5.12(a) and (b) show the Li migration rates from graphite to carbon particles (across the interfaces) at 6C and 1C lithiation, respectively.

In the first stage ($t < 52$ s) of 6C lithiation, Li migrates from graphite to carbon as intercalation into carbon is thermodynamically favored. During this stage, Li insertion into carbon via

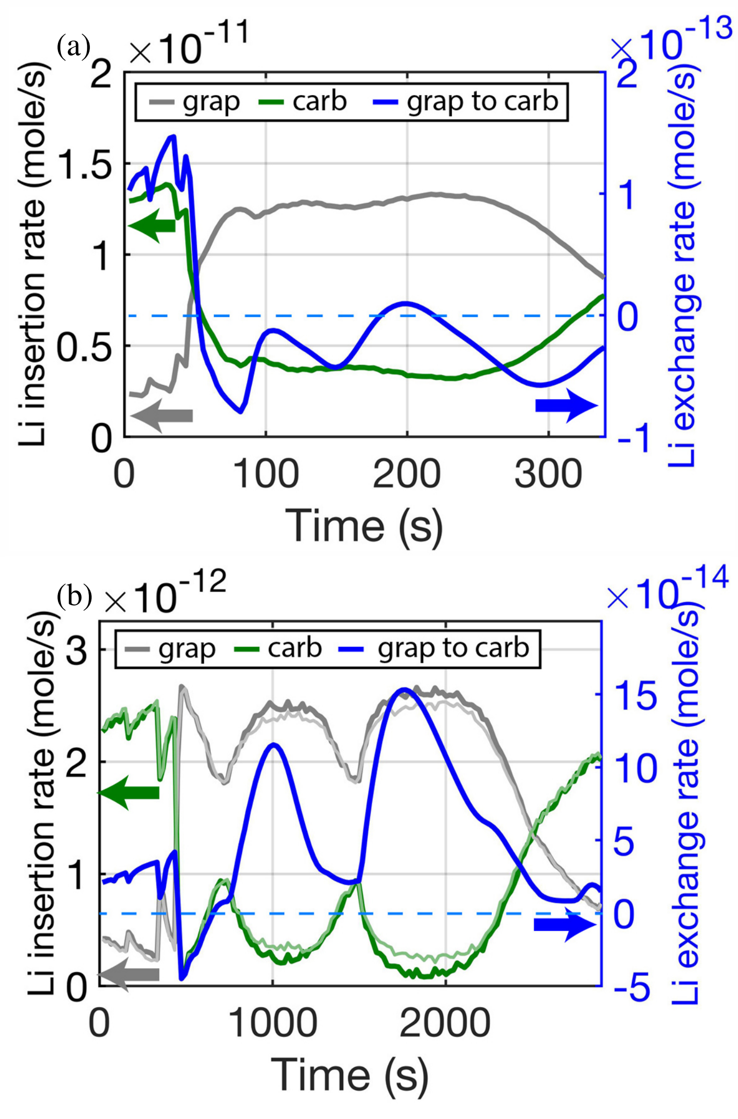

Figure 5.12 Li exchange rate (blue curve) between graphite and carbon particles at (a) 6C and (b) 1C lithiation. A positive value indicates migration from graphite to carbon. The blue curves reference the y-axis on the right. The gray and green curves are the electrochemical insertion rates of graphite and carbon, respectively. They refer to the y-axis on the left.

electrochemical reaction through the carbon-electrolyte interface is approximately five times the insertion to graphite via electrochemical reaction (see the green and gray curves before t = 52 s in Fig 5.12(a)). The fluctuations on the gray, green, and blue curves indicate phase separation events in graphite (surface regions). Upon entering the second stage, graphite particles started to absorb Li from carbon particles, as indicated by the negative exchange rate on the blue curve. During this stage, the electrochemical insertion into carbon is reduced to roughly a quarter of that into graphite. In the third stage ($t > 280$ s), the electrochemical insertion to carbon increases while the insertion to graphite decreases as illustrated by the green and gray curves in Fig 5.12. Although, the Li exchange between graphite and carbon remains graphite-favored, indicated by the negative exchange rate (the blue curve), the trend appears to shift towards a carbon-favored exchange. Throughout the 6C lithiation, Li across the interfaces of the two particles is less than 1% of the electrochemical insertion flux to either graphite or carbon.

As shown in Fig 5.12(b), Li migration from graphite to carbon occurred during most of the entire 1C lithiation, except for a short period during the transition between the first and second stages ($450 < t < 780$ s, where the blue curve is below zero). In this 1C case, the magnitude of the electrochemical insertion rate to the thermodynamically favored particles is roughly eight to ten times that to the non-favored particles (see the overall magnitudes of the gray and green curves in Fig 5.12(b)) because the lithiation process reflects more intrinsic thermodynamic behavior at a low rate. Compared to the 6C case, surges of electrochemical insertion to graphite are more pronounced in the second stage, as indicated by the clear humps on the gray curve, corresponding to the recessions on the green curve. Those surges of Li electrochemical insertion to graphite were accompanied by ‘leakage to carbon particles,’ indicated by the humps on the blue curve in 5.12(b). In this 1C simulation, Li migration to carbon through particle contacts could sometimes be greater than Li insertion via surface electrochemical insertion. Nevertheless, Li migration across particle contacts was fairly low: the overall lithiation rates of graphite and carbon were very similar to those from the standard case (zero permeability case, the insertion rates are plotted as the thin, light-colored curves in Fig 5.12(b) for comparison). In principle, we found that the permeability of particle contact interfaces has no significant influence on the lithiation behavior.

5.2.3.2 Effects of particle size

It is interesting to examine the effects of particle size on the performance of the hybrid electrode. Figure 5.1(d) shows a synthetic electrode microstructure with the same particle configuration, but in which particles with a diameter smaller than 11.34 μm are assigned with graphite properties (marked in gray), and the rest are carbon (marked in green), resulting in a 49 : 51 graphite-carbon volume ratio. (Here, 49 : 51 is the ratio closest to 50 : 50 by dividing particle population with diameters.) We first discuss the results of 6C simulations here. Simulations of 1C lithiation are presented later. The gray curve in Fig 5.13(a)-i is the simulated CV. As in Fig 5.4(a), CV curves are plotted versus DoD. The total capacity of this electrode is close to that in the standard case because graphite and carbon each occupy ~50% of the total volume.

In the first stage, the CV curve falls below the standard case (the thin blue curve), indicating a larger cell overpotential (or less efficient electrochemical performance) compared to the standard case (randomly assigning particles). Cell overpotential is the deviation between cell voltage and cell OCV. A smaller cell overpotential is equivalent to a higher electrochemical efficiency. The decrease in performance is because insertion to carbon is hindered by the low surface-to-volume ratio of large carbon particles, even though insertion to carbon is thermodynamically favored during this stage. In contrast, in the second stage (during which intercalation to graphite is favored), the high surface-to-volume ratio of small graphite particles facilitates the lithiation. Thus, the CV curve is lifted above that in the standard case. The evolutions of average Li fraction in graphite and carbon particles are plotted in the dark gray and dark green curves in Fig 5.13(a)-(ii), respectively. As in Fig 5.4(b), Li fraction evolution curves are plotted versus time. Compared to the standard case (the thin dotted curves), intercalation to graphite is much enhanced by using small graphite particles. X_g even exceeds X_c after $t = 225$ s. (The X_g and X_c curves of the standard case in Fig 5.4(b) are presented as the thin dotted curves in Fig 5.13(a)-(ii) for comparison). The third stage is barely reached before meeting the termination criteria in these simulations, as observed from Fig. 5.13(a)-ii. At the simulation cutoff, the average X_g has increased from 0.02 to 0.78, but the average

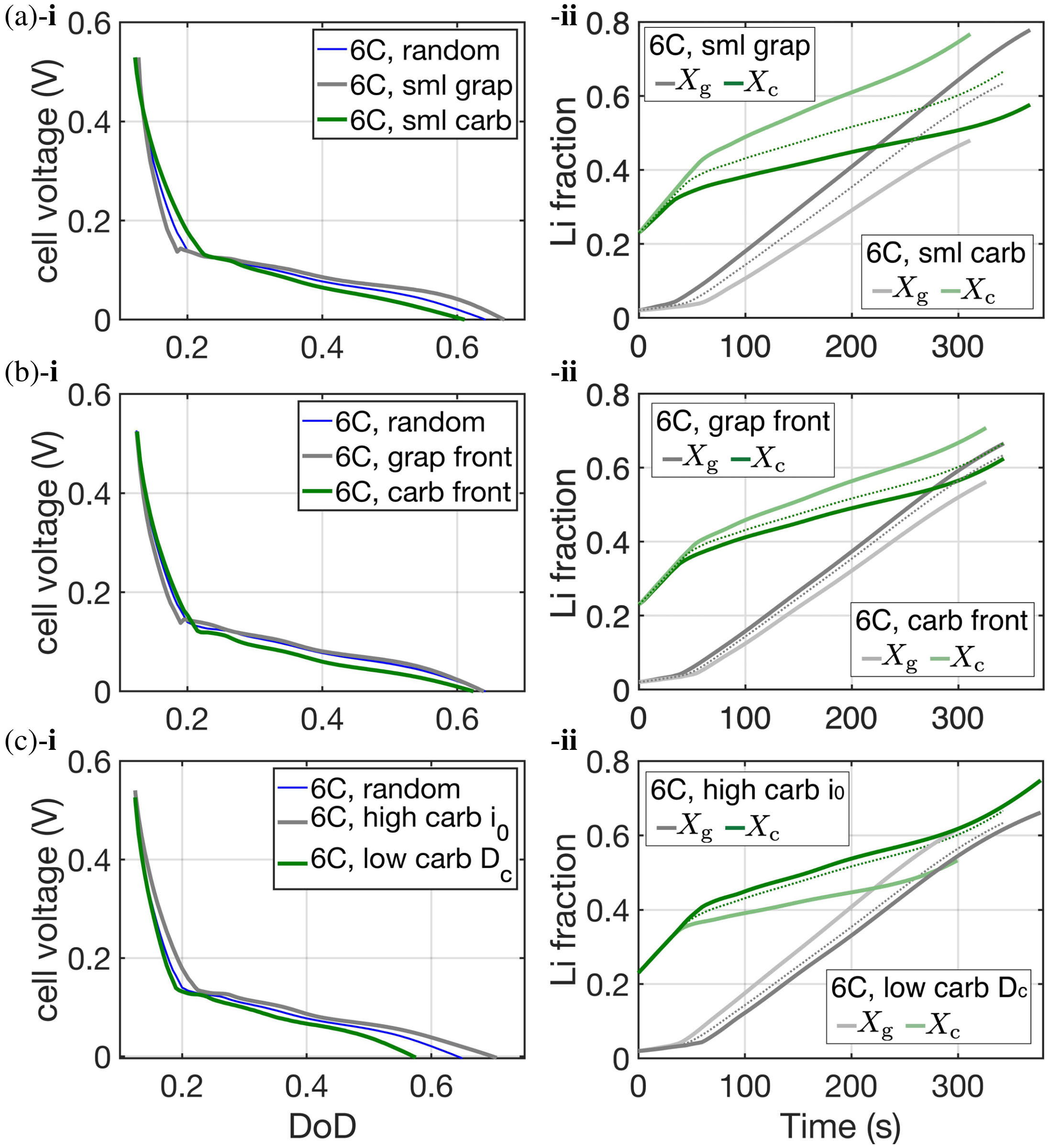

Figure 5.13 Simulated cell voltages and Li fraction evolution at 6C lithiation for (a)-(i) and (ii) of large-versus-small graphite particles, (b)-(i) and (ii) of front-versus-back graphite particle locations, and (c)-(i) and (ii) of high carbon i_0 and low D_c cases, respectively. The dotted lines represent the standard case, a 6C lithiation in 50% hybrid anode with random distribution shown in Fig. 5.1(c)

X_c only increased from 0.23 to 0.58.

The green curve in Fig 5.13(a)-i is the simulated CV of the flipped case, in which particles with diameters larger than 11.34 μm are assigned with graphite properties. Due to the enhanced insertion into carbon particles (with smaller sizes), the CV curve in the first stage of lithiation falls on the right to that of the standard case, indicating an enhanced electrochemical performance. However, in the second stage, intercalation to graphite particles is hindered by graphite particles' large sizes. Thus, the CV curve falls below the thin blue curve. The effect of enhanced Li insertion to carbon, stemming from smaller particle sizes, can also be observed from the higher slope of the light green curve compared to the dark green one in Fig 5.13(a)-ii. Furthermore, the operation time of this small carbon particle case (up to 311 s) is significantly reduced compared to that in the small graphite particle case (up to 367 s).

Fig. 5.14(a) displays the simulated cell voltage curve for 1C lithiation for both small graphite and small carbon cases. The thermodynamic effect in 1C cases is similar to that in 6C cases. Small graphite particles facilitate the second stage of lithiation. Small carbon particles facilitate the first stage of lithiation. Li fraction evolution and accumulated Li intake to graphite and carbon in the 1C lithiation is also presented in Fig. D.3(a)-(i) and (ii) in the Appendix D.3.

5.2.3.3 Effects of particle locations

Next, we examined the effect of particle locations. Figure 5.1(e) shows the microstructure configuration (the same particle configuration), in which particle centers located in $x < 44.5$ μm were assigned with graphite properties in the first case and otherwise assigned with carbon properties in the second case; i.e., graphite and carbon particles were located in the 'front' and 'back' regions of the electrode. The volume fraction ratio is 50 : 50 between graphite and carbon. The simulated CV for 6C lithiation is plotted as the gray curve in Fig 5.13(b)-i. The fact that carbon particles were away from the counter electrode hindered the insertion into the carbon particles in the first stage of lithiation. Thus, the CV (gray) curve is shifted to the left of the standard case (thin blue curve). In the second stage (insertion to graphite is favored), the shorter distance between graphite and the counter electrode improved the electrochemical performance slightly: the gray curve is slightly above the thin blue one. While in the third stage, the two effects roughly balance each other placing the gray curve almost on top of the standard blue curve. Overall, the position of graphite particles slightly enhanced the Li intact, as can be seen in the dark gray curve in Fig

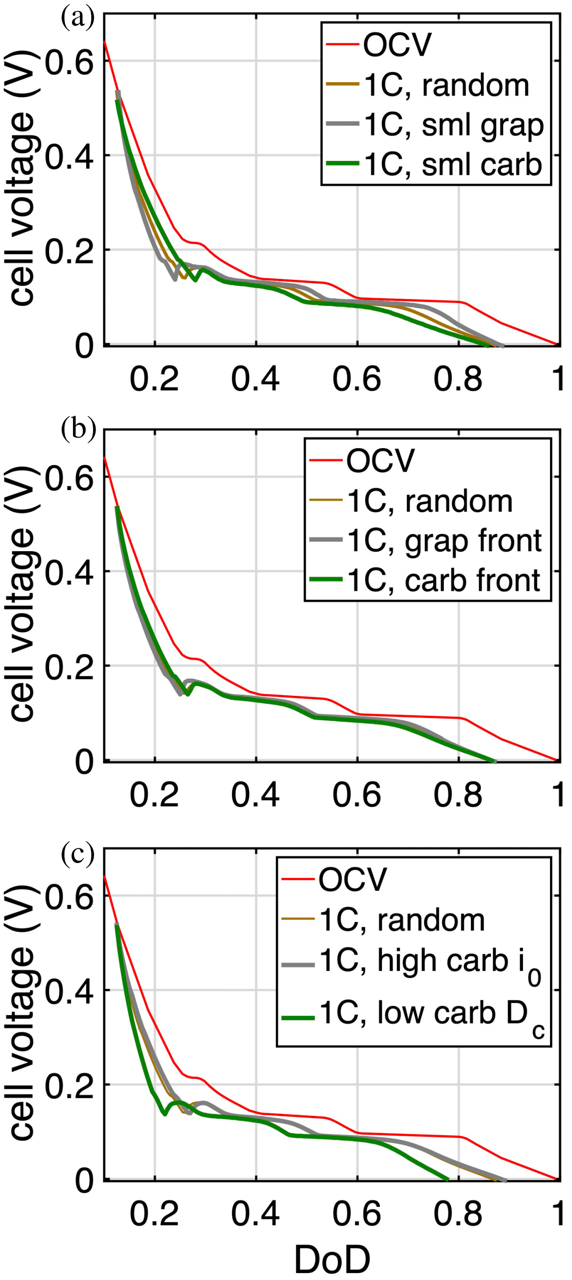

Figure 5.14 Simulated cell voltage versus DoD at 1C lithiation. (a) Case for comparison between small graphite and small carbon particles. (b) Case for comparison between graphite or carbon particles in the front region. (c) The cases of high carbon i_0 and low carbon D_c.

5.13(b)-ii compared to the standard case (the thin dotted gray curve). The green curve in Fig 5.13(b)-i is the simulated CV of the 'flipped' case, in which carbon particles were located in the front region. The fact that carbon particles were located closer to the counter electrode led to a slightly improved electrochemical performance in the first stage, as indicated by the green curve falling slightly on the right to the standard case. In the second and third stages, the effect of the graphite particles being located in the back region decreased the electrochemical performance, as indicated by the green curve being below the thin blue curve.

In terms of increase in Li fraction over time, placing carbon particles in the front region facilitated the Li intake to carbon, as indicated by the slope of the light green curve in 5.13(b)-ii. However, such an arrangement also decreases Li intake to graphite. Because graphite possesses a much larger Li capacity than carbon, there is no improvement in the total Li intake in this case compared to the standard case as shown in Figs. 5.9(e) and (f). A similar observation can be inferred from 1C lithiation curves displayed in Figs. D.3 in Appendix D.3. The effect of placing graphite or carbon particles in the front region is minimal in the 1C case as seen in Fig. 5.14(b) where the curves are very similar to the standard case.

5.2.3.4 Effects of exchange current density and mobility

The exchange current density on the carbon surface is an uncertain material parameter in the presented simulations because we do not have access to measured data for hybrid anodes. An additional simulation with carbon $i_{0,c}$ ten times that of graphite $i_{0,g}$ was performed on the electrode microstructure of the standard case to examine the impact of carbon $i_{0,c}$ on the simulation results. The simulated CV for 6C lithiation is plotted as the gray curve in Fig 5.13(c)-(i), and the Li fraction evolutions are plotted in the dark-colored curves in Fig 5.13(c)-(ii). In the first stage (DoD < 0.225 or $t < 60$ s), the high $i_{0,c}$ enhanced Li insertion to carbon, and thus the CV curve falls on the right to the thin blue curve (the standard case where $i_{0,c} = i_{0,g}$). This effect extended to the second and third stages, during which the enhanced insertion to carbon slightly decreased the amount of Li insertion to graphite, thus reducing the overpotential on graphite surfaces and leading the CV (gray) curve to be slightly above the thin blue curve. The overall Li fraction evolutions (the dark-colored curves in Fig 5.13(c)-(ii)) in this simulation are very similar to those in the standard case (the thin dotted curves) but with an extension in the operation time (378 s compared to 342 s in the standard case). Interestingly, even though $i_{0,g}$ was kept the same as in the standard case, the SEPD (−0.15 mV, shown in Fig. 5.15) at the cutoff of this simulation is only approximately 10% of that in the standard case, implying that much less Li-plating will be observed with a high $i_{0,c}$. This may be the case observed in experiments. Unfortunately, no exact value of carbon i_0 is available to examine this hypothesis.

Li mobility in carbon (M_c) is another uncertain material parameter in this work. The green curve in Fig 5.13(c)-(i) is the simulated CV for 6C lithiation, in which M_c is set to be one order of magnitude smaller than that in graphite (M_g). As expected, Li insertion to carbon was hindered, leading the CV (green) curve to fall to the left of the standard case (the thin blue curve) in the first stage. This effect extended to the second and third stages, during which insertion flux to graphite

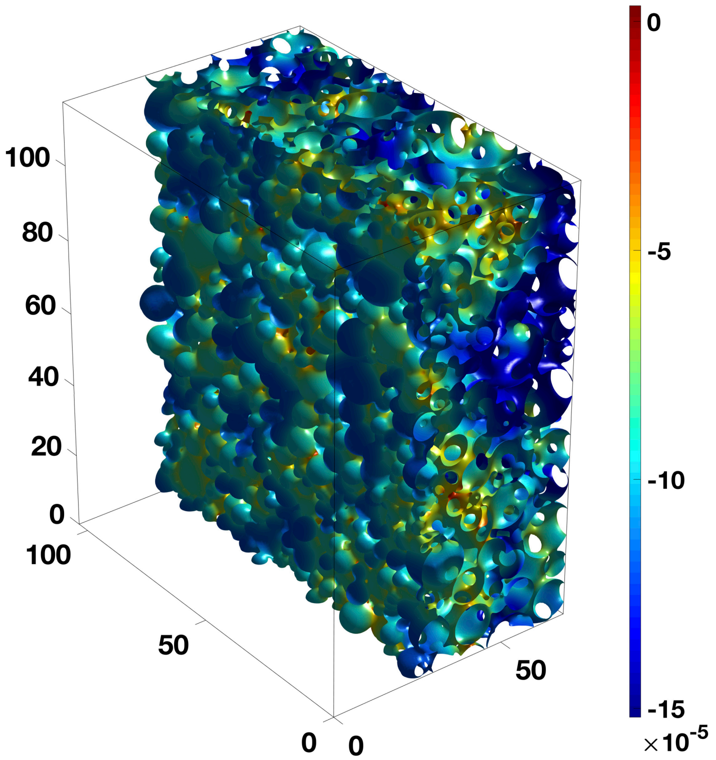

Figure 5.15 Simulated SEPD on HGC surfaces at 6C lithiation for the case of high carbon $i_{0,c}$. The unit of the color bar is V. The dark blue regions are graphite particles.

was larger than that in the standard case to maintain the same C rate. The net effect led to a large overpotential on graphite particle surfaces. Consequently, the green CV curve fell below the thin blue curve. The reduced insertion rate to carbon and increased insertion rate to graphite during the second stage can be inferred by the low and high slopes of the light green and light gray curves, respectively, in Fig 5.13(c)-ii. The light gray curve even intersects the light green one near $t \sim 223$s. This set of simulations implies that the impact of M_c is not as pronounced as $i_{0,c}$ in the first stage of lithiation, although the majority of Li insertion occurs on the carbon particles. Furthermore, the lithiation dynamics in a hybrid electrode are affected in a complex way by the status of the two active materials. For instance, as illustrated in the previous simulation, increasing carbon $i_{0,c}$, which enhances lithiation to carbon, will also increase Li insertion to graphite. A decrease in insertion to carbon (e.g., due to low diffusivity in this simulation) will force the insertion toward graphite. The lithiation behavior cannot intuitively reflect only one of the intrinsic material properties. This complexity makes predicting and analyzing cell performance difficult without detailed simulations, such as those presented in this text.

5.3 Conclusion

In this chapter, we demonstrate the efficacy of our framework utilizing the smoothed boundary method to simulate electrochemical processes within computationally generated, synthetic graphite-carbon hybrid electrode microstructures. In this approach, a phase-field method is utilized to model the complex multi-phase lithiation processes of graphite. Despite carbon being a lithium solid solution, the multi-phase behavior of graphite induces a multi-stage lithiation process in the hybrid electrode. Initially, the lithiation of carbon is thermodynamically favored, followed by a shift towards favored lithiation of graphite in the second stage. In this stage, the surface concentration of graphite increases rapidly. In the third stage, the carbon particles start getting lithiated again where the surface concentration of graphite is extremely high while carbon surface concentration is relatively low. The simulation outcomes align with observations indicating significantly reduced Li plating on hybrid graphite-hard carbon anodes compared to pure graphite counterparts. Additionally, we find that electrode performance can be influenced by manipulating particle sizes and positions within the microstructure. Among the various arrangements explored, employing smaller graphite particles appears to be the most efficient approach.

CHAPTER 6

HIGH-THROUGHPUT INVESTIGATION OF FREE PATHWAYS/ TUNNELS IN GRAPHITE ANODES FOR IMPROVED LITHIUM-ION BATTERY PERFORMANCE

6.1 Introduction

As briefly mentioned in Chapter 4, thick electrodes have gained renewed interest in designing lithium-ion batteries for high-capacity applications. [95, 112, 113] For the same thickness of a stack of battery cells, the one with thick electrodes will have fewer inactive components, such as separators and current collectors. Therefore, careful and pedantic design of such electrodes can lead to a higher loading and overall energy density. However, thick electrodes inherently have poor kinetics and lack mechanical strength. Several researchers have explored the design of better thick electrodes using experiments. [95, 96] In our work, we use simulations to gain insight into the design of better thick electrodes. Introducing free pathways/tunnels in the electrodes can enhance the salt ion migration through the electrodes, thus, combating the challenges of poor kinetics faced by thick electrodes mentioned in Refs. [95, 132]. These types of electrodes are also called perfoliated electrodes. Recently, a few experimental studies have shown tunnels to delay reaching the overcharging condition (cut-off condition) [107, 133, 134]. Porous Electrode Theory (PET) modeling has also been employed to simulate the performance of graphite electrodes with laser-ablated tunnels [107, 135]. However, the microstructural-level details were not resolved in the PET simulations. Additionally, resolving tunnels with PET involves simulating PET spheres in 3D, effectively creating pseudo-4D simulations, which substantially increase computational time and memory requirements.

In this chapter, we examine the effects of introducing straight cylindrical tunnels in the electrode microstructures. More specifically, we study graphite microstructures as we demonstrated in Chapter 4 the need for improved salt diffusion toward the back of the electrode, especially for thick electrodes and high C-rates. We use an automated high throughput strategy to compare and contrast various factors that affect the impact of tunnels in an electrode as well as compare several thicknesses of the electrodes. The idea of high-throughput computations has been common in

Density Functional Theory (DFT) and Molecular Dynamics (MD) calculations [136–139] serving the dual purpose of screening existing and novel materials and generating new data for machine learning applications. Following similar principles, high-throughput electrochemical simulations with tunnels can allow us to identify and study patterns and empirical relations between tunnels and their electrochemical performance. Furthermore, the generated data can be used in data-driven approaches to predict tunnel behavior. Since the simulations in this work require only the voxel microstructural data, it is extremely easy to introduce tunnels by removing some voxels. The simulations were performed only for 6C lithiation because the effect of tortuosity is not significant at a low C rate as discussed in Chapter 4.

6.2 Model

6.2.1 Governing equations

We used the same modeling framework as discussed in Chapters 2, 4, and 5. We briefly summarize the framework here. The SBM reformulated equations solved for the engineered graphite electrodes are listed here —

Cahn-Hilliard equation:

$$\frac{\partial X_p}{\partial t} = \frac{1}{\psi}\nabla \cdot \left[\psi M_p \nabla \left(\mu_b - \nabla \cdot \varepsilon \nabla X_p\right)\right] + \frac{|\nabla \psi|}{\psi}\frac{r_{xn}}{\rho}. \tag{4.6}$$

Current continuity on graphite particle surface:

$$\nabla \cdot (\psi \kappa_s \nabla \phi_s) - |\nabla \psi| z_- F r_{xn} = 0. \tag{2.14}$$

Ion diffusion in electrolyte:

$$\frac{\partial C_e}{\partial t} = \frac{1}{\psi_e}\nabla \cdot (\psi_e D_e \nabla C_e) + \frac{|\nabla \psi_e|}{\psi_e}\frac{r_{xn} t_-}{\nu_+} - \frac{\mathbf{i_e} \cdot \nabla t_+}{z_+ \nu_+ F}, \tag{2.18}$$

Current continuity the in electrolyte:

$$\nabla \cdot \left[\psi_e \left(z_+ m_+ - z_- m_-\right) F C_e \nabla \phi_e\right] + |\nabla \psi_e| \frac{r_{xn}}{\nu_+} = \nabla \cdot \left[\psi_e \left(D_- - D_+\right) \nabla C_e\right], \tag{2.20}$$

Butler-Volmer equation:

$$r_{xn} = \frac{i_0}{z_+ F}\left[\exp\left(\frac{-\alpha z_+ F}{RT}\eta\right) - \exp\left(\frac{(1-\alpha) z_+ F}{RT}\eta\right)\right] \tag{2.7}$$

These equations are detailed in previous Chapters 2, 4, and 5.

6.2.2 Tunneled microstructures

As in Chapter 4, the 3D simulations on graphite in this chapter use real microstructures reconstructed from experimental data. Data for graphite is publicly available at [99]. The graphite reconstructed microstructures E_II and E_IV are detailed in Chapter 4 and displayed in Fig. 4.4. The first demonstration of a tunnel uses E_IV-3X used in Chapter 4 with dimensions of $58.5 \times 55.2 \times 52$ μm^3 where 165.6 μm is the triple thickness. A tunnel was introduced at the center of this electrode with a radius of 12 μm. This tunnel removed approximately 15% of the active material.

For our high throughput studies, we use different variations of E_II, some demonstrated in Fig. 6.1. Due to the enormity of the data required to analyze the impact of tunnels on several thicknesses of the electrodes, we designed an automated process to create cylindrical tunnels in the electrode. A trick to save computational effort is using unit cells like those shown in Fig. 6.1. These microstructures can be assumed as a unit cell of the entire bigger electrode and can be duplicated to extrapolate results for multiple tunnels as demonstrated in Figs. 6.3 and 6.1. Namely, symmetric boundaries are used to represent self-repeating unit cells. Thick electrodes were obtained by repeating a single unit of the electrode and connecting them back to back as

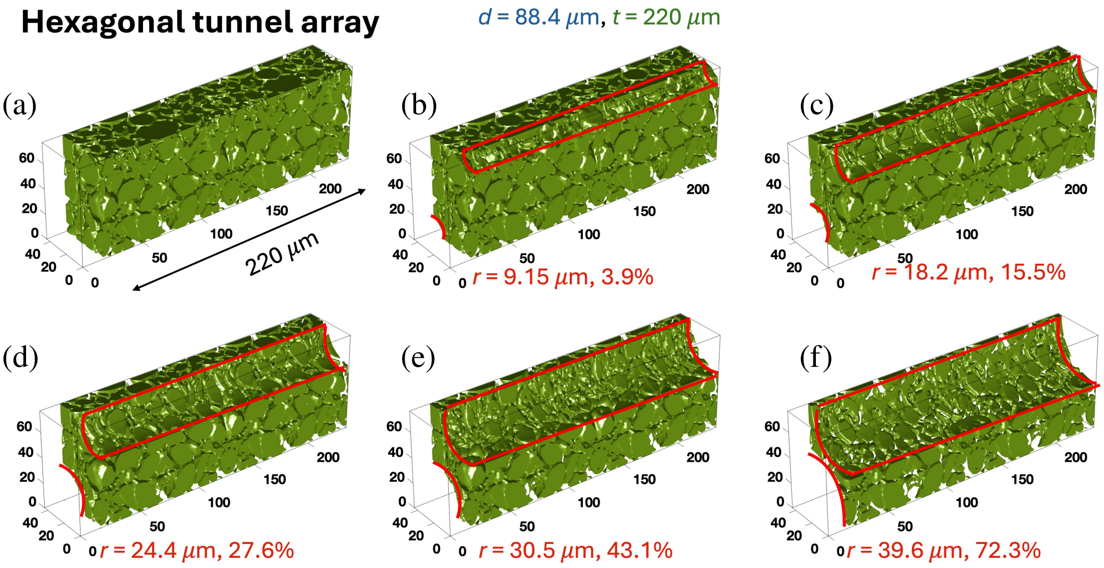

Figure 6.1 Illustration of a hexagonal tunnel array in E_II microstructures with thickness, t=220μm, and different tunnel volume/radius: (a) no tunnel, (b) 3.9% tunnel volume, (c) 15.5% tunnel volume, (d) 27.6% tunnel volume, (e) 43.1% tunnel volume, and (f) 72.3% tunnel volume,

illustrated in Fig. 4.14(b). Four different electrode thicknesses were created and studied ~ 55μm, ~ 110μm, ~ 165μm and ~ 220μm further referred to as 1X, 2X, 3X, and 4X in this chapter.

6.2.2.1 Factors affecting tunnel performance

For the rest of the chapter, we shorthand improvements shown by introducing tunnels to tunnel performance for the sake of brevity. To quantitatively analyze a tunnel performance, we look at several simulation results from a cell cycle including total achievable capacity, Before we present any simulation results in the upcoming sections, let us define three parameters — achievable SoC (state of charge), tunnel volume fraction, and achievable Li capacity. We define achievable SoC as the maximum lithium fraction attained before reaching the overcharging condition, tunnel volume fraction as the fraction of the volume of the electrode covered by the tunnel, and achievable Li capacity as the maximum capacity attained before reaching the overcharging condition. Additionally, we use normalized Li capacity to highlight comparisons between different electrodes which is calculated by normalizing the capacity of any electrode with respect to the capacity of the electrode with no tunnels. These three parameters will be essential in analyzing the impact of tunnels on electrode behavior. Furthermore, we hypothesize that the parameters listed below are the primary influential factors of a tunnel in an electrode.

- **Radius of the tunnel (r):** As tunnels aim to provide easy diffusive transport channels for the electrolyte, the radius of the tunnels is an apparent determining factor for improving the electrode's achievable capacity. Through our studies discussed later in this chapter, we found that an optimal radius can be identified for a given thickness of the electrode. A small tunnel doesn't provide enough of a channel for ion migration, while a thick wide tunnel leads to too much capacity loss due to the removed electrode volume.

- **Inter-tunnel Distance/Tunnel separation (d):** Additionally, the placement of the tunnels also affects their performance. We hypothesize that each tunnel has an "affected region" around it. This "affected region" is a volume surrounding the tunnel illustrated in Fig. 6.6, where a noticeable improvement in Li diffusion can be observed due to the introduction of that tunnel. This "affected region" renders placements of the tunnels with respect to each other crucial to the overall enhancement of performance. Inter-tunnel distance or tunnel separation is defined as the center-to-center distance between tunnels.

- **Thickness of the electrode (t):** While the thickness of the electrode doesn't directly determine improvements made by the introduction of a tunnel, it changes the optimal radius and arrangement for the tunnels.

6.3 Results and Discussions

6.3.1 Impact of a tunnel in thick electrodes

Figure 4.14(b) indicates that the back of TP E_IV-3X is barely utilized during a 6C lithiation. This directly results from the highly tortuous path for salt ion migration. We create a straight cylindrical tunnel in the E_IV-3X. To highlight the enhancement of tunnels in ion migration, we select TP E_IV-3X in the simulations because it has a larger pore tortuosity than those of E_II and E_III. Since the simulations in this work require only the voxel microstructural data, it is extremely easy to introduce tunnels by removing some voxels (i.e., setting voxel values to zero). The simulations were performed only for 6C lithiation because the effect of tortuosity is not significant at a low C rate.

Figure 6.2(a) shows the simulated CV curves for TP E_IV-3X at a 6C rate with and without a tunnel. As shown in the previous section, TP E_IV-3X without a tunnel can reach only 0.175 DoD (corresponding to $t = 105$ s) at the cut-off condition. On the other hand, with the tunnel, the electrode's achievable DoD was increased by nearly threefold: 0.505 (corresponding to $t = 307$ s). Even after accounting for the loss of active materials, the tunneled electrode still had a total achievable Li capacity of 2.45 ($= 0.505 \times 0.85/0.175$) times the one without the tunnel.

Figure 6.2(b) displays the X_p in the tunneled electrode at the cut-off point. A uniform lithiation throughout the electrode is observed. This is noticeably different from the no-tunnel case in Fig. 4.14(b), in which the back of the electrode is barely lithiated. Even though tunnels can enhance the spread of salt ions, some large graphite particles still have cores devoid of lithium, highlighting that particle size is a limiting factor at high-rate (de)lithiation. Figures 6.2(c) and (d) contrast the salt ion concentration in the electrolyte in the no-tunnel and tunneled cases. Both images were taken at the cut-off points (reaching the Li-plating point). Clearly, the tunnel alleviated the depletion of salt ions in the electrode. See the light-blue colors in Fig. 6.2(d), as opposed to the dark-blue colors in Fig. 6.2(c). Additionally, as indicated by the red color in Fig. 6.2(c), salt ions are highly concentrated in the separator region because they cannot be distributed deeply into the electrode. As a result, lithiation was highly concentrated on the front side (near the separator) of the electrode

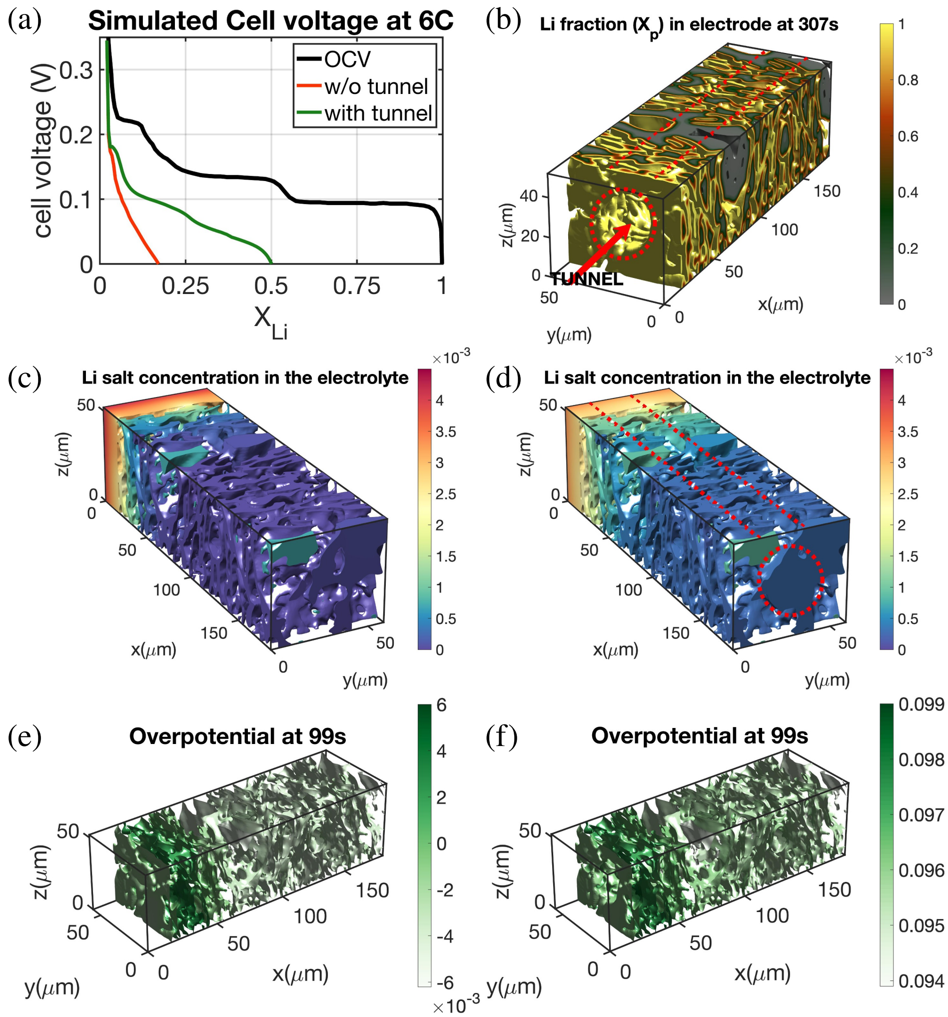

Figure 6.2 (a) CV curves for TP E_IV-3X at 6C with and without a tunnel. (b) X_p in particles in TP E_IV-3X with a tunnel. C_e in TP E_IV-3X (c) without a tunnel and (d) with a tunnel. Note that (c) and (d) have been rotated along the z-axis to show the back side of the electrodes. Electropotential drop across the particle surfaces (e) without a tunnel and (f) with a tunnel. Subfigures (b) through (e) are plotted at the cut-off point.

and the electrode reached the cut-off point much earlier than the tunneled electrode.

Figures 6.2 (e) and (f) show the electropotential drop across the electrode particle surfaces for the no-tunnel and tunneled cases, respectively, at the time when the no-tunnel case reaches the cut-off condition. While some regions in the no-tunnel case reached the plating condition (negative electropotential drop), all surfaces in the tunneled case still had a positive electropotential drop, indicating that insertion was still thermodynamically favored. This result supports the experimental observations in Ref. [107, 133, 134].

In summary, we found that while tunnels allow the spread of the reactions more uniformly throughout an electrode, the enhancements are prominent only in thick (> 150 μm) graphite electrodes. We also demonstrate the ease of using direct voxel simulations to examine the microstructure effects. A further comprehensive study of the engineering design of electrode microstructures can be a future extension.

6.3.2 Systematic study of tunnels

6.3.2.1 Arrangements: Square vs Hexagonal and effects of tunnels with different electrode thicknesses.

A key factor in studying the behavior of tunnels is their arrangement with respect to each other. We examine two such arrangements, square and hexagonal, as illustrated in Fig. 6.3.

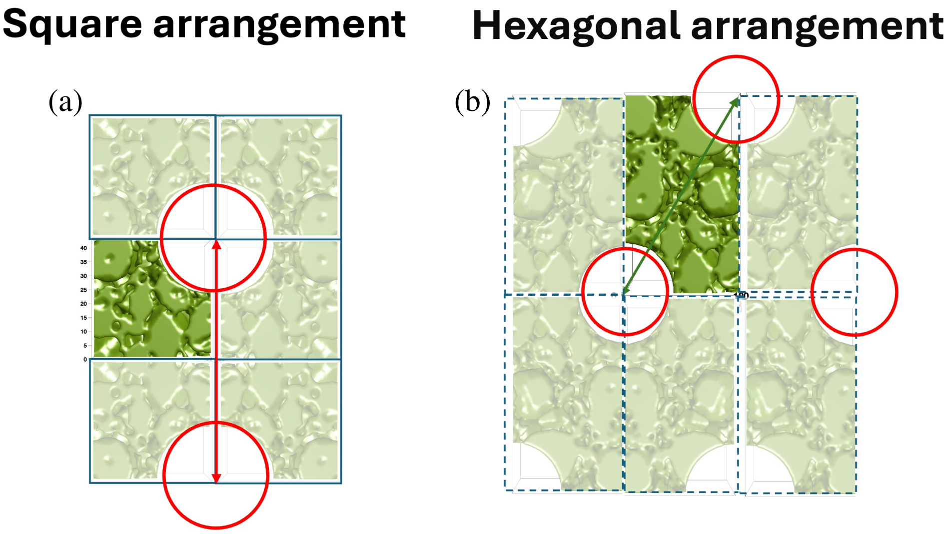

Figure 6.3 Singular units of tunnels of a (a) Square arrangement, and (b) Hexagonal arrangement.

The key differences in the two arrangements as highlighted in Fig. 6.3 is the relative position of any two tunnels. In the square arrangement, any two tunnels are at a 90° angle while in the hexagonal arrangement, tunnels are at a 60° angle. Note that for the two arrangements, the thickness and the width of the unit cell are kept the same with different heights to accommodate for the two different angles between any two tunnels as illustrated in Fig. 6.3.

We run automated simulations with increasing tunnel radius for the four different thicknesses for both arrangements. The tunnel separation, d, is kept at ∼ 88μm for all these simulations. The width of a unit cell is chosen to be 44.2μm for both arrangements. Accordingly, the depth of the unit cell is set to 44.2μm for the square arrangement and 76.7μm for the hexagonal arrangement. As in Chapters 4 and 5, cell voltage = ∼ 0V is set as the cut-off condition for these simulations. Fig. 6.4 (a) shows the achievable SoC for all four electrode thicknesses with the two arrangements at a 6C lithiation rate. The solid lines represent the hexagonal arrangement while the dashed lines represent the square arrangement. Fig. 6.4 (a) clearly indicates that the hexagonal arrangement performs better than the square arrangement, displaying higher achieved SoC over increasing tunnel volume fractions in electrodes. Fig. 6.4 (b) distinctly highlights the contrast in achievable SoC

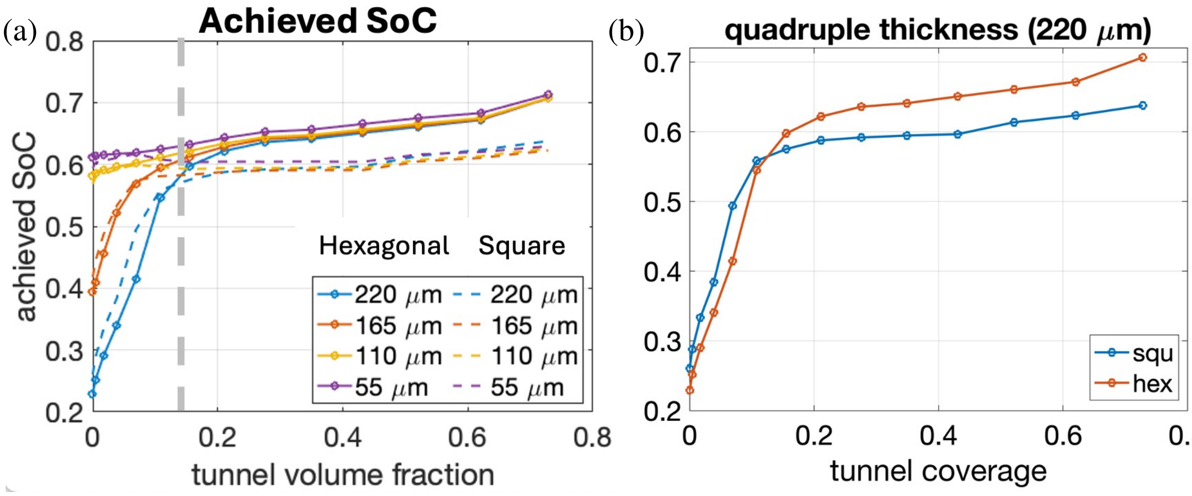

Figure 6.4 Achieved State of Charge (SoC) vs tunnel volume fraction/coverage for both hexagonal and square arrangements (a) for four different thicknesses of the electrode: 55μm, 110μm, 165μm and 220μm, and (b) for quadruple thickness (220μm) at 6C lithiation and tunnel separation, d = ∼ 88μm. The gray line delineates the two behaviors of achievable SoC observed over increasing tunnel volume fractions.

for the quadruple thickness (220μm) between the two arrangements. In the plateau region of the curves, the hexagonal arrangement cases achieved approximately 5% higher SoC. Fig. 6.5 displays

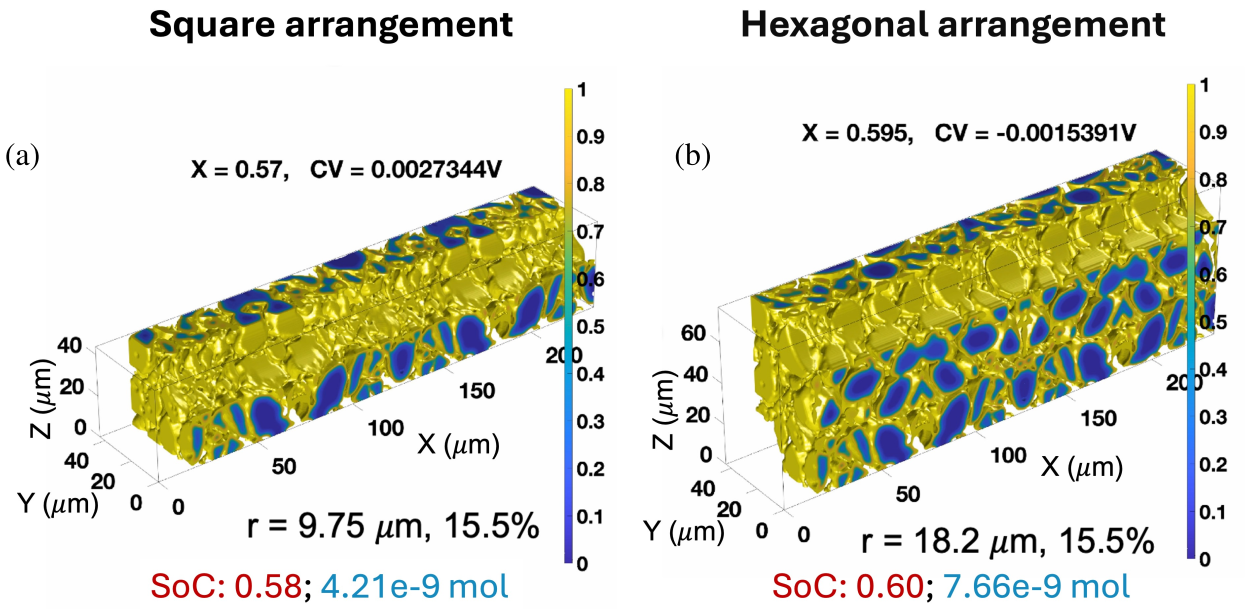

Figure 6.5 Li concentration for a quadruple thickness electrode (220μm) at a 6C lithiation rate in a (a) square arrangement, and (b) hexagonal arrangement. Both arrangements are compared with the same tunnel volume fraction, 15.5%. The hexagonal arrangement displays a higher achievable SoC.

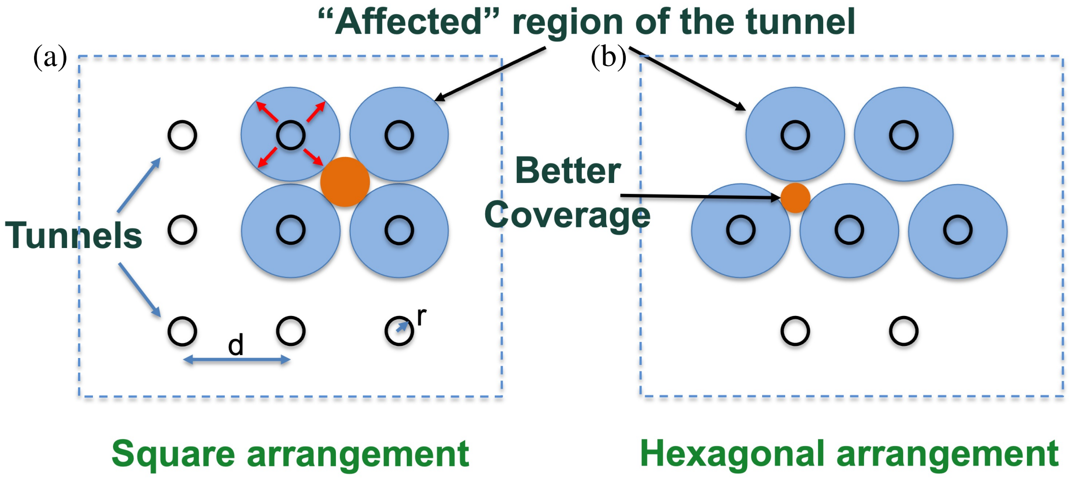

Figure 6.6 (a) Square arrangement, and (b) Hexagonal arrangement. The blue area signifies the "affected" region of a tunnel. The orange area indicates the area "unaffected" by tunnels. We can clearly see that the "unaffected" area is larger for the square arrangement.

the lithium concentration profile at the cut-off voltage in both arrangements. A higher SoC is observed for the hexagonal arrangement (0.60 vs 0.58) at this cut-off for the same tunnel volume fraction of 15.5%. These observations indicate that the hexagonal arrangement of tunnels induces a higher performance increase than the square arrangement. To explain this behavior, we hypothesize an "affected" region of the tunnel is defined as a region surrounding a tunnel where the introduction of that particular tunnel enhances the diffusion in the electrode. This is simply due to the ease of diffusion of Li through the new pathways and the surrounding region having more access to Li ions. An illustration of the "affected" regions for the two arrangements is shown in Fig. 6.6. A higher coverage of the electrode by this "affected" region (shown in blue color) is observed in the hexagonal arrangement. Consequently, for any further simulations and studies, we primarily focus on the hexagonal arrangement of tunnels.

6.3.2.2 Effect of tunnel radius

In this section, we investigate the impact of the tunnel radius on electrode performance. We vary tunnel radius from 0 – 40 μm for quadruple thickness, t = 220 μm with tunnel separation, d = 88.4 μm, and a hexagonal arrangement of tunnels. Fig. 6.7 (a) shows the cell voltage curves vs SoC for fourteen tunnel radii varying from 0 – 40 μm at a 6C lithiation rate. It can be noticed that the achievable SoC at the cut-off point increases with increasing tunnel radii. Additionally, on curves where more graphite particles achieve higher utilization, more pronounced steps appear on the cell voltage curves, indicating that the overall lithiation processes are closer to equilibrium processes even though all of them are lithiated at the same 6C rate. This is also displayed with the blue curve in Fig. 6.7 (b). The curve reveals two distinct slopes: an initial rapid increase in achievable SoC, followed by a saturated plateau region. As discussed later, the initial stage signifies the lateral (radial direction to the tunnel) Li salt diffusion in the electrolyte is still limited. This limitation arises because the tunnel cross-sectional area is insufficient to support Li salt in all lateral directions along the tunnel cylinder surfaces. Consequently, reaching the cut-off condition is governed by diffusion in the primary (thickness) direction. Notably, the particle surfaces remain unsaturated (as indicated by bright yellow regions) throughout the entire electrode. In contrast, in the plateau region, the lateral diffusion can cover most of the electrode volume. At this stage, further increases in tunnel radius no longer enhance Li supply. However, as the tunnel radius increases, the tunnel volume increases and the total graphite volume decreases depicted by the red curve in Fig. 6.7 (b). This trade-off implies an optimal tunnel radius where a balance of achieved SoC and graphite volume is achieved. We can identify this optimum in Figs. 6.7 (c) and (d). Cell voltage vs capacity curves for all fourteen radii are presented in Fig. 6.7 (c) and the achievable Li capacity is displayed in Fig. 6.7 (d). The achieved capacity increases initially with an increase in tunnel volume fraction and drops again with any further increase in tunnel volume fraction after reaching the optimal point.

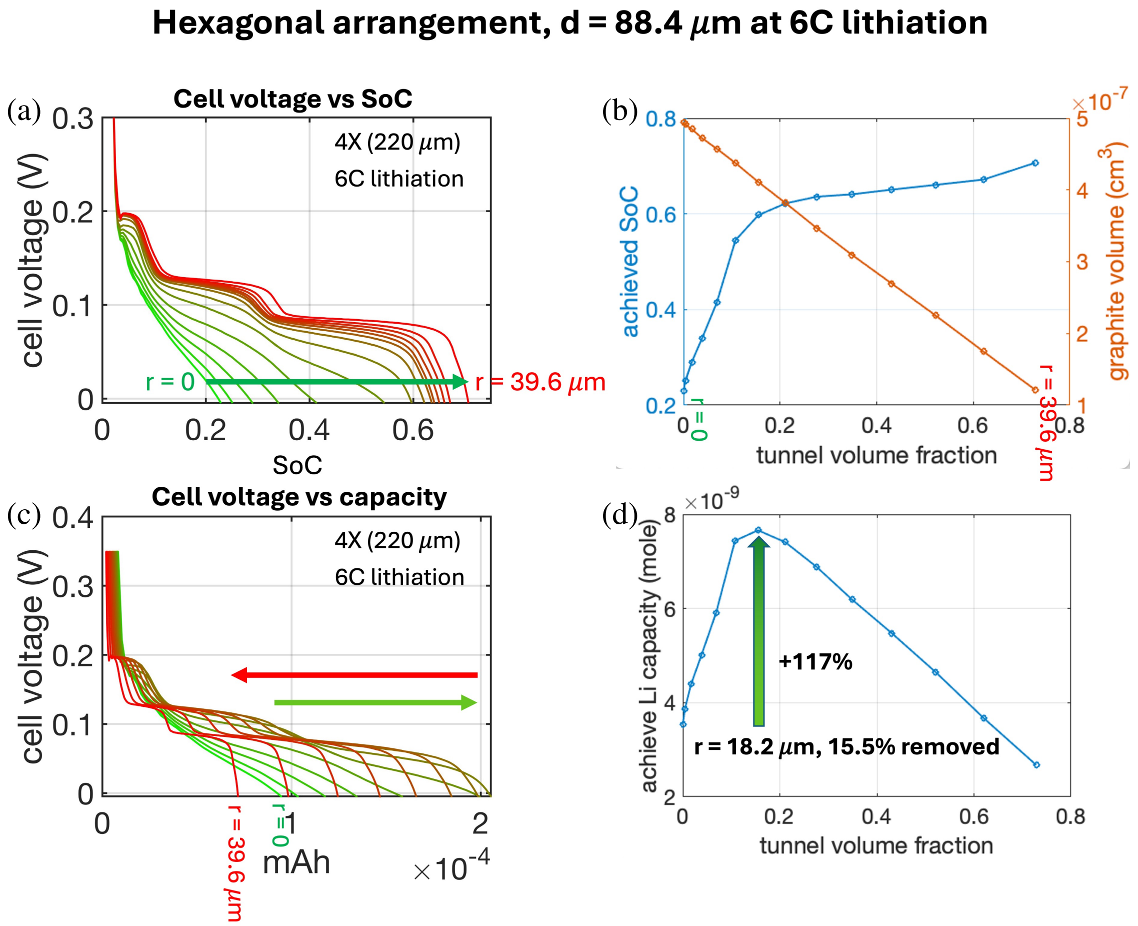

Figure 6.7 (a) Cell voltage curves vs SoC, (b) achieved SoC at cut-off and graphite volume vs tunnel volume fraction, (c) cell voltage vs capacity (mAh), and (d) achieved capacity at cut-off. Hexagonal arrangement in E_II at 6C lithiation with an increasing radius from 0 – 40μm for quadruple thickness (220μm) and a tunnel separation of 88.4μm.

The green curves in Fig. 6.7 (c) correspond to the increasing capacity stage and the red curves correspond to the decreasing capacity stage. For this electrode and a hexagonal arrangement of tunnels, the optimal tunnel radius is identified as, r = $18.2\mu m$, where a 15.5% graphite volume is removed. An outstanding 117% increase in total achievable capacity is observed at this optimal tunnel radius. Li concentration in the electrodes is presented for three different radii, r = $0\mu m$, $18.2\mu m$, and $39.6\mu m$ in Fig. 6.8 (a), (b), and (c) respectively. Fig. 6.8 (a) belongs to the first stage of capacity increase with tunnel volume where a significant volume of the electrode is not utilized before reaching the cut-off voltage due to hindered diffusion of Li ions. It can seen that roughly only 1/4 of the electrode reaches surface saturation at the cut-off point. Fig. 6.8 (b) shows the optimal tunnel radius electrode. At the cut-off point, the entire electrode reaches surface saturation. From this radius onward, all electrodes reach surface saturation at the cut-off point. Lastly, Fig. 6.8 (c) belongs to the last stage where the electrode is efficiently utilized, however, too much volume has been removed for the tunnels for the electrode to demonstrate any significant improvements. In the plateau region, increasing tunnel radius only marginally enhances achievable SoC. This is attributed to the fact that the largest particles cannot be fully lithiated at this C rate. In other words, the radial inward diffusion in particles dominates the lithiation even though lateral Li salt diffusion is sufficient.

We also present the cell voltage curves and cell voltage vs capacity curves for the square arrangement in Fig. 6.9. This arrangement exhibits similar behavior to the hexagonal arrangement with an optimal tunnel radius of 16.5μm. Although these exact quantitative findings only apply to the presented electrodes, the qualitative patterns and behavior extend to any electrode. An optimal tunnel radius that maximizes the achievable capacity exists for all thick electrodes. Tunnels/free pathways can be created in a thick electrode with optimal tunnel radius to attain higher achievable capacity before reaching the cut-off voltage.

6.3.2.3 Effects of thickness

In this section, we analyze the improvements tunnels offer in conjugation with the thickness of electrodes. We keep the tunnel separation, d = 88.4μm, width = 44.2μm, and depth = 76.7μm as constants for these simulations. Four different electrode thicknesses, ~ 55μm, ~ 110μm, ~ 165μm and ~ 220μm referred to as 1X, 2X, 3X, and 4X are studied in this section. The unit cell for a hexagonal arrangement of tunnels shown in Fig. 6.1 is used for all the cases.

Fig. 6.10 (a) shows the achieved state of charge (SoC) with increasing tunnel sizes for all four thicknesses. Achieved SoC refers to the lithium fraction of the electrode filled before reaching

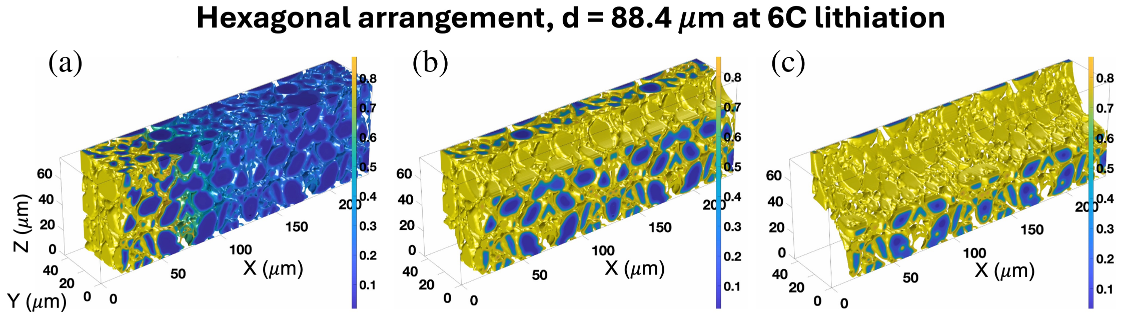

r = 0 μm, 0% | SoC: 0.23; 3.53e-9 mol

r = 18.2 μm, 15.5% | SoC: 0.60; 7.66e-9 mol

r = 39.6 μm, 72.3% | SoC: 0.71; 2.68e-9 mol

Figure 6.8 Li concentration in the electrode with (a) tunnel radius = 0μm and volume = 0%, (b) tunnel radius = 18.2μm and volume = 15.5%, and (c) tunnel radius = 39.6μm and volume = 72.3%. Hexagonal arrangement in E_II at 6C lithiation with an increasing radius for quadruple thickness (220μm) and a tunnel separation of 88.4μm.

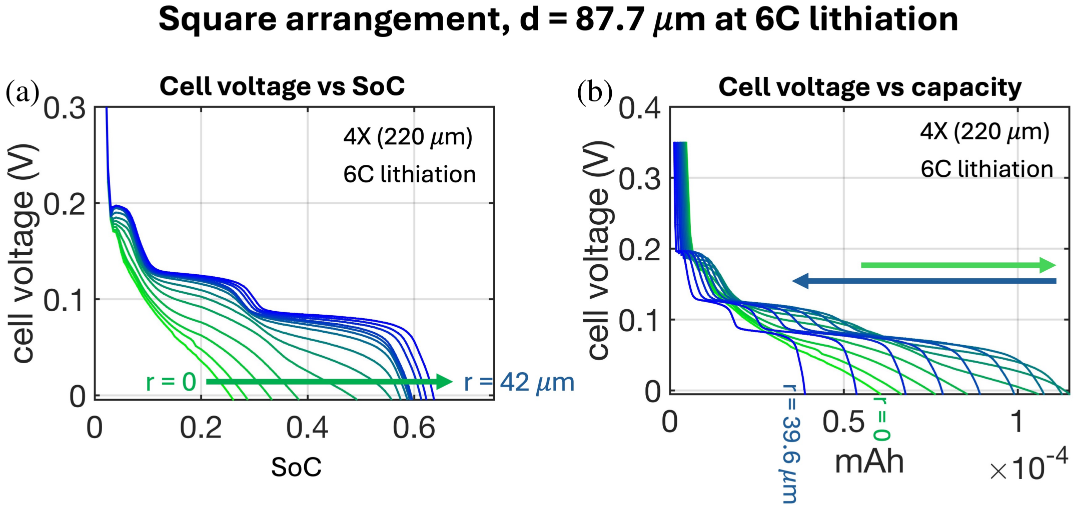

Figure 6.9 (a) Cell voltage curves vs SoC, and (b) cell voltage vs capacity (mAh). Square arrangement in E_II at 6C lithiation with an increasing radius from 0 – 42μm for quadruple thickness (220μm) and a tunnel separation of 87.7μm.

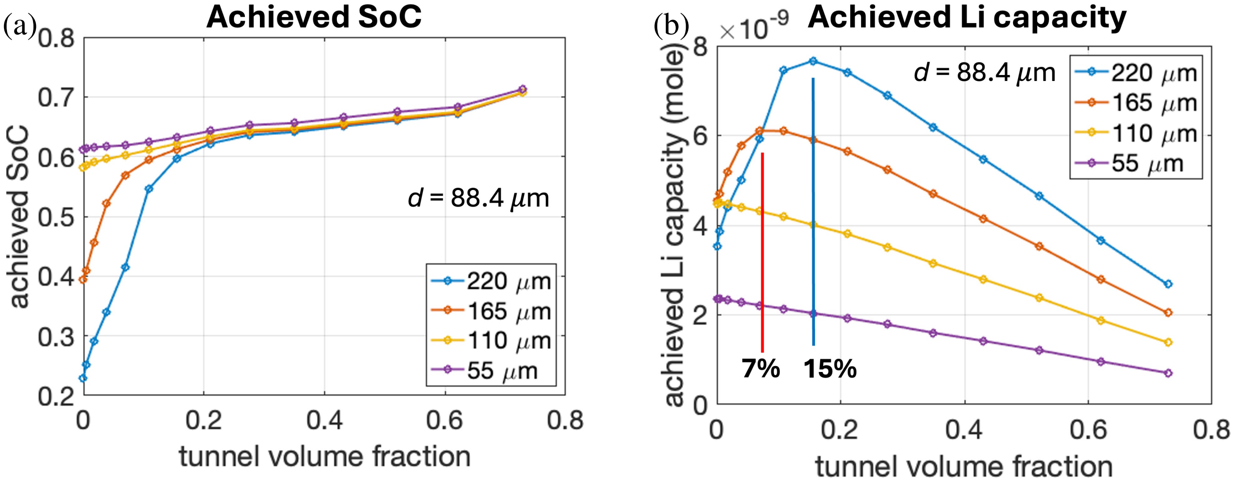

Figure 6.10 (a) Achieved State of Charge (SoC) vs tunnel volume fraction, and (b) achieved capacity vs tunnel volume fraction. Hexagonal arrangement in E_II at 6C lithiation for four thicknesses and a tunnel separation of 88.4μm.

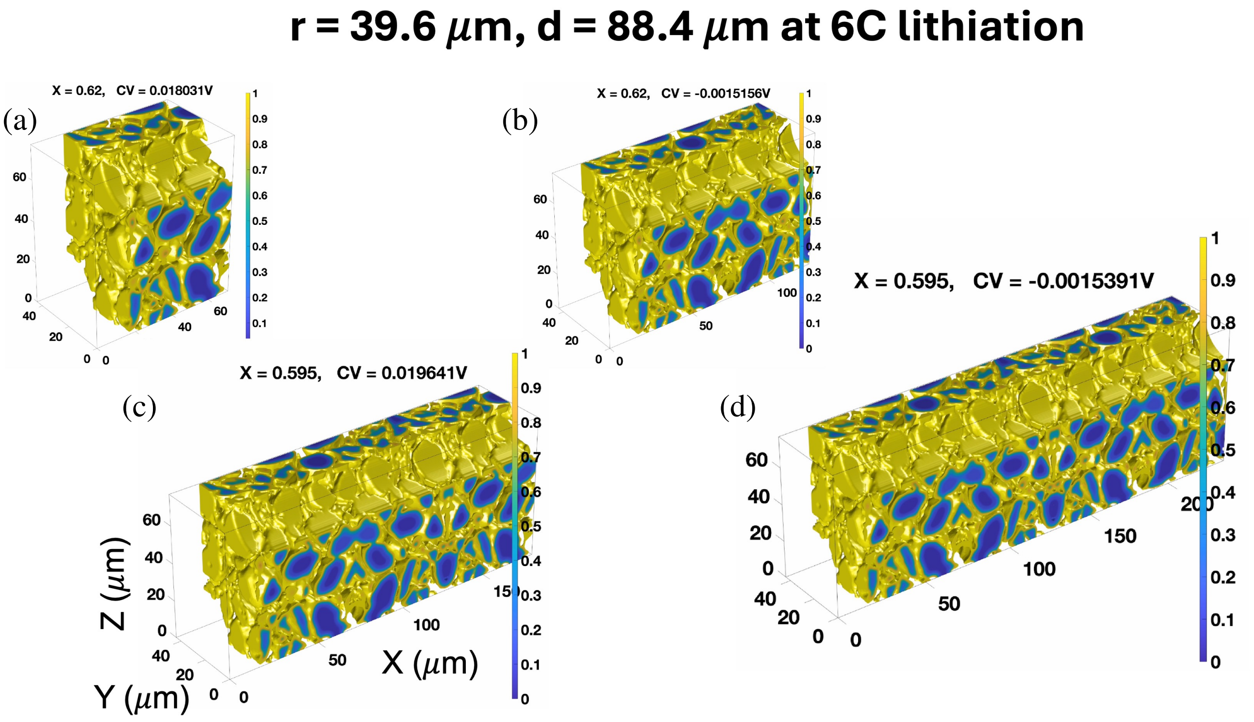

Figure 6.11 Different tunnel thicknesses with hexagonal tunnels and the same tunnel radius, 39.9μm. (a) Single thickness (55μm), (b) Double thickness (110μm), (c) Triple thickness (165μm), and (d) Quadruple thickness (220μm),

the cut-off condition. As in the previous simulations, the cut-off condition is selected as the overcharging condition when the cell voltage reaches below 0V. For 1X (purple curve) and 2X (yellow curve) electrodes, only small improvements can be observed with the introduction of tunnels with the SoC increasing to ~ 0.71 from 0.62 and 0.58 respectively. The 3X and 4X electrodes with no tunnels display a massive dip in performance with 0.39 and 0.24 achievable SoC. In these cases, we see a remarkable increase in SoC with the introduction of tunnels. A steep increase of 50% in SoC is observed in the 3X case while an exceptional increase of 200% is noticed in the 4X case until the tunnel volume grows to approximately 20%. The increase in achievable SoC tapers off significantly after any further enlargement of tunnels even for the 3X and 4X cases. This suggests that even for very thick electrodes, there is an optimal size or radius for tunnels beyond which they provide minimal benefits. The total achievable capacity is also plotted in Fig. 6.10 (b) to further substantiate this claim. As can be seen again, tunnels do not contribute in the 1X and 2X cases, and the highest capacity in these electrodes is attained with no tunnels or very small tunnels. This indicates that Li salt diffusion in the primary diffusion direction is sufficient to penetrate electrodes of these thicknesses. Perfoliation will simply decrease total achievable capacity. Optimal points can be recognized for 3X and 4X electrodes at ~ 7% and ~ 15% tunnel volume with a capacity increase of 30% for 3X and an exceptional 117% increase for 4X. Compared to the original single thickness with no tunnels case, the improvement in achievable capacity is even more remarkable, ~ 160% increase for the 3X case and ~ 230% increase for the 4X case. Once the effects of tunnel enhancement saturate i.e. when the "affected" region of the tunnels begins to overlap and lateral diffusion in the electrolyte eases, particle sizes become the limiting factor. This is because diffusion into the particle is not affected by the introduction of these tunnel/free pathways. We demonstrate the Li concentration profile in the four electrode thicknesses in Fig. 6.11. Evidently, the electrodes are more uniformly lithiated across their thickness compared to no tunnel cases (see Fig. 6.8 (a) for a counter example). Yet some particle cores are still devoid of lithium validating the premise that particle sizes are the constraint to achieving even higher capacity in these electrodes. We conclude that for electrodes with thickness $< 110\mu$m, tunnels do not enhance performance and are therefore a futile investment, but creating thicker electrodes with optimal tunnels can provide high-capacity electrodes.

We concede that only four thicknesses are insufficient to draw concrete conclusions and the exact quantitative optimal tunnel volume and capacity specifically pertains to the electrode. However, we argue that the 4X case is already closing toward the diffusion limit in the electrolyte and the optimal thickness lies somewhere in the range or close to what we explore in our work. Additionally, our study and framework here pave the way for any future studies on specific electrodes and provide a general qualitative idea for optimal tunnels in electrodes.

6.3.2.4 Effect of tunnel separation

In this section, we use our high-throughput strategy to examine the impact of inter-tunnel distance/tunnel separation (d) on electrode performance. Three tunnel separation, d = $60\mu m$, $74.2\mu m$, and $88.4\mu m$ are analyzed here. A varying radius is employed with the three tunnel

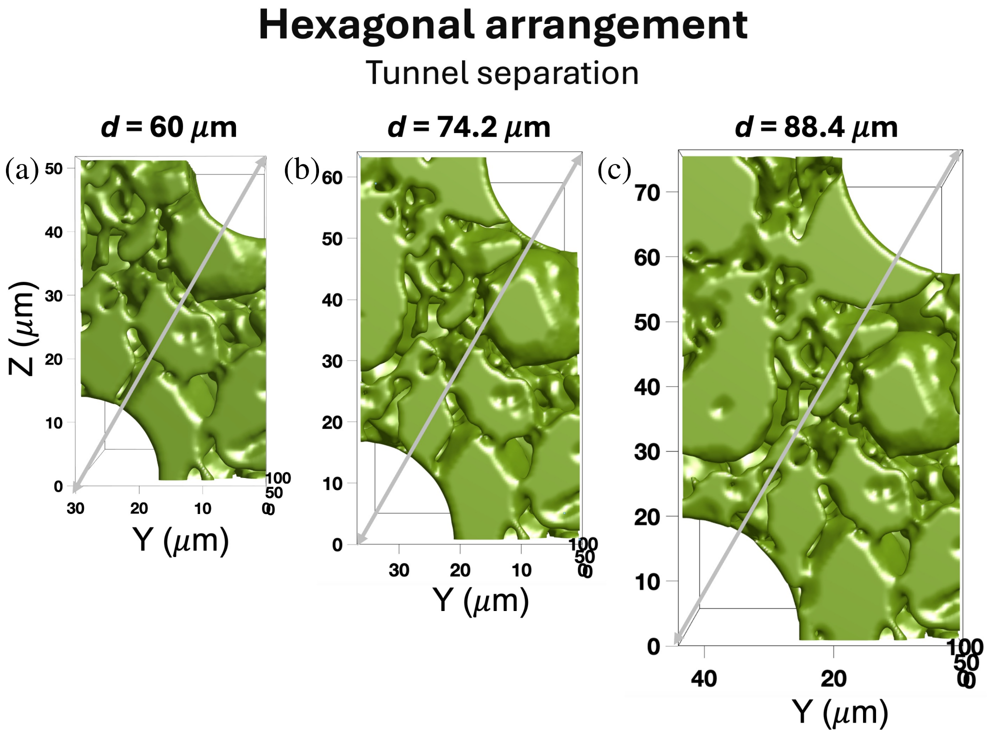

Figure 6.12 Singular units of tunnels of hexagonal arrangement with tunnel separation, d = (a) 60μm, (b) 74.2μm, and (c) 88.4μm.

separations for four thicknesses of electrodes with a hexagonal arrangement of tunnels. The unit cells of the three cases are displayed in Fig. 6.12. To generate electrodes with these three tunnel separations while maintaining a hexagonal arrangement, different widths and depths are used to form the unit cells. The cross-sections of the electrode are $29.7\mu m \times 52\mu m$ for d = $60\mu m$ in Fig. 6.12 (a), $37\mu m \times 64.4\mu m$ for d = $74.2\mu m$ in Fig. 6.12 (b), and $44.2\mu m \times 76.7\mu m$ for d = $88.4\mu m$ in Fig. 6.12 (c).

Since the volume of each of these unit cells differs, we present normalized achievable capacity instead of total achievable capacity for all 12 cases (three tunnel separations for four thicknesses) in Fig. 6.13. The achievable capacities for any electrode with a tunnel are normalized with the achievable capacity for that electrode with no tunnel to calculate the normalized achievable capacity displayed here. The capacities show similar behavior for the three tunnel separations for any electrode thickness. Once again, any considerable impact of tunnels is only observed in electrode thickness > $\sim$ 110μm (the red and the blue curves), i.e., diffusion in the primary direction is sufficient to penetrate electrodes of these thicknesses. As the tunnel separation decreases, the optimal tunnel radius decreases, and the highest achievable capacity increases albeit only marginally. We believe that an empirical pattern can be identified between the tunnel separations, d, and optimal

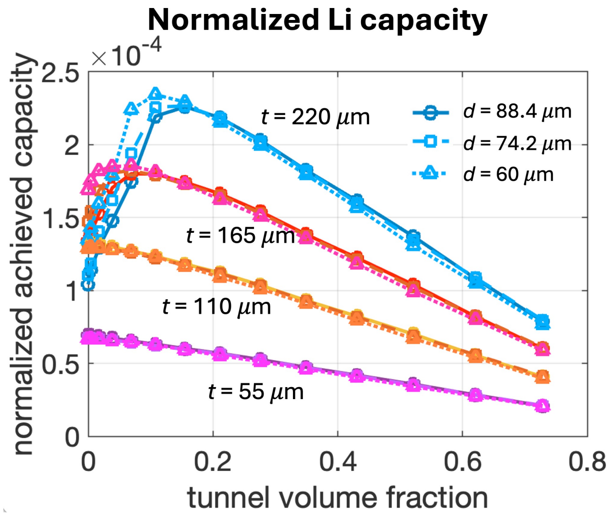

Figure 6.13 Normalized Li capacity for three tunnel separations, d = $60\mu m$, $74.2\mu m$, and $88.4\mu m$ for four different thicknesses of the electrode, 55μm, 110μm, 165μm and 220μm.

tunnel radius, r, and thus a new factor d/r can be used to generate tunnels for any new electrode microstructure. However, recognizing any such pattern will require more data collection for other tunnel separations. The following hypothesis is proposed: as the tunnel separation decreases, the tunnel radius for optimal achievable capacity decreases. Eventually, the electrode reaches a uniform low porosity configuration. However, such low-porosity electrodes may lack mechanical strength. Thus, a balance between electrochemical performance and mechanical strength will need to be considered, which is beyond the scope of the current work.

In summary, a combination of optimal tunnel radius, r, and correspondingly optimal tunnel separation, d, for thick electrodes can provide significantly higher capacity before reaching the cut-off voltage i.e. the overcharging condition.

6.4 Conclusions

Tunnels have demonstrated improvement, particularly for thick electrodes (greater than approximately 110 μm), albeit with a trade-off between higher utilization and loss in volume. There is an opportunity for optimization in the arrangement (including orientation and tunnel separation), and the size of tunnels impacting achievable utilization and total capacity before the onset of plating. A systematic study of tunnels has been conducted, comparing hexagonal versus square arrangements and exploring the effects of increasing electrode thickness, tunnel radius, and tunnel separation. It has been observed that very large tunnels do not significantly improve achievable capacity due to the immense loss of active material. At the same time, higher utilization is achieved with larger tunnels, reaching a maximum total capacity at a tunnel coverage of approximately 10-20 % in the electrodes studied here. The hexagonal arrangement of tunnels provides better coverage and thus higher achievable capacity. An optimal combination of tunnel radius and tunnel separation exists for all electrodes and can be identified through our high-throughput studies. Additionally, identifying patterns for optimal tunnel radius and optimal tunnel separation are under investigation, along with exploring different tunnel shapes.

CHAPTER 7

THREE-DIMENSIONAL ELECTROCHEMICAL SIMULATIONS IN A FULL CELL

7.1 Introduction

Throughout this work, we have primarily focused on half-cell (single electrode) simulations with the assumption of a lithium metal counter electrode on the other side of the cell. While these simulations offer great insights into electrode behavior, it is imperative to incorporate both cathode and anode in a combined cell for a more comprehensive understanding of the working of a practical Li-ion battery. In this chapter, we showcase an extension to our developed framework capable of simultaneously simulating both cathode and anode. We leverage the microstructures detailed in chapters 3 and 4 to model NMC as the cathode and graphite as the anode, respectively. In the previous chapters, we solved the governing electrochemical equations defining diffusion in electrode and electrolyte, current continuity in electrode and electrolyte, and faradaic reaction at the particle-electrolyte interfaces. In a full-cell setup, we simulate the two electrodes and the electrolyte simultaneously, thus requiring additional equations in the solver. The full-cell solver is detailed in the next section. As in the previous chapters, the governing equations are reformulated with SBM. A notable difference here is that the potential in the electrolyte has no-flux boundary conditions on two sides (where the current collectors are) in contrast to the half-cells where the no-flux boundary condition was present only on one side. In fact, the internal boundary conditions imposed on the cathode and anode surfaces for the electrolyte potential are both Neumann conditions. Normally, a domain subject to only Neumann conditions is a numerically underdetermined problem with no unique solution. Remarkably, the simulations are still stable and converge to a solution. This can be explained by the interdependence between the electrolyte potential solver and the two electrode potential solvers with Dirichlet boundary conditions (near the current collectors). We present 6C simulations of the full-cell acting to demonstrate and validate the modified framework.

7.2 Model Formulation

7.2.1 Full-cell modeling

The governing equations presented and utilized in the previous chapters describe a half-cell containing a single electrode and an electrolyte. In contrast, a full-cell simulation involves two electrodes (NMC and graphite) interacting with the electrolyte. We once again leverage the smoothed boundary method (SBM) to reformulate the governing equations allowing the use of non-conformal meshes in complex geometries. Three domain parameters are employed to define the three different regions in the cell; ψ_c for the cathode, ψ_a for the anode, and ψ_e for the electrolyte. ψ_e can be calculated as $\psi_e = 1 - (\psi_c + \psi_a)$. Additional equations and boundary conditions required in a full-cell simulation are presented here.

Cathode:

Similar to Chapter 3 Eq. (2.12), the Li fraction in NMC cathode is described by Fick's diffusion equation —

$$\frac{\partial X_c}{\partial t} = \frac{1}{\psi_c}\nabla \cdot \left(\psi D_c \nabla X_c\right) + \frac{|\nabla \psi_c|_{ce}}{\psi_c}\frac{r_{xn,ce}}{\rho_c}. \tag{7.1}$$

Here, the subscripts 'c' and 'ce' denote cathode particles and cathode particle-electrolyte interface respectively. Similar to Eq. 2.14, the electropotential in NMC is defined by

$$\nabla \cdot (\psi_c \kappa_c \nabla \phi_c) - |\nabla \psi_c|_{ce} z_- F r_{xn,ce} = 0. \tag{7.2}$$

The faradaic reaction on the cathode particles, similar to Chapter 2, is described by the Butler-Volmer equation —

$$r_{xn,ce} = \frac{i_0^c}{z_+ F}\left[\exp\left(\frac{-\alpha z_+ F}{RT}\eta_c\right) - \exp\left(\frac{(1-\alpha) z_+ F}{RT}\eta_c\right)\right] \tag{7.3}$$

where $\eta_c = [\phi]_e^c - \phi_{eq}^c$ is the overpotential on NMC cathode particle surfaces.

Anode:

For graphite anode, we utilize the formulation shown in Chapter 4, where the Cahn-Hilliard equation governs the diffusion in graphite particles, similar to Eq. (4.6) —

$$\frac{\partial X_a}{\partial t} = \frac{1}{\psi_a}\nabla \cdot \left[\psi_a M_a \nabla \left(\mu_b^a - \nabla \cdot \varepsilon \nabla X_a\right)\right] + \frac{|\nabla \psi_a|_{ae}}{\psi_a}\frac{r_{xn,ae}}{\rho_a}. \tag{7.4}$$

where $\mu_b^a = \partial G_a(X_a)/\partial X_a$. Here, the subscripts 'a' and 'ae' denote anode particles and anode particle-electrolyte interfaces. Similar to Eq. (2.14),the electropotential in the anode is given by

$$\nabla \cdot (\psi_a \kappa_a \nabla \phi_a) - |\nabla \psi_a|_{ae} z_- F r_{xn,ae} = 0. \tag{7.5}$$

The faradaic reaction on the anode particles is expressed using the Butler-Volmer equation, similar to Eq. (2.7)

$$r_{xn,ae} = \frac{i_0^a}{z_+ F}\left[\exp\left(\frac{-\alpha z_+ F}{RT}\eta_a\right) - \exp\left(\frac{(1-\alpha) z_+ F}{RT}\eta_a\right)\right] \tag{7.6}$$

where $\eta_a = [\phi]_e^a - \phi_{eq}^a$ is the overpotential on graphite anode particle surfaces.

Electrolyte:

In this chapter, the modeling of the electrolyte differs from the approaches in Chapters 3 and 4 and is more akin to the approach in Chapter 5 with the hybrid anode, due to the addition of another type of particle surface. To define the ion diffusion in the electrolyte in the full cell, we adjust Eq. (2.18) similar to the modification shown in Chapter 5. A new 'source term' is added to the right-hand side of Eq. (2.18) to incorporate the reaction fluxes at both the cathode and anode particle-electrolyte interfaces. The modified equation is shown here:

$$\frac{\partial C_e}{\partial t} = \frac{1}{\psi_e}\nabla \cdot (\psi_e D_e \nabla C_e) + \frac{\left(|\nabla \psi_e|_{ce} r_{xn,ce} + |\nabla \psi_e|_{ae} r_{xn,ae}\right)}{\psi_e}\frac{t_-}{\nu_+} - \frac{\mathbf{i_e} \cdot \nabla t_+}{z_+ \nu_+ F}, \tag{7.7}$$

The method to identify different interfaces is given in Chapter 5. Similarly, to define the current continuity in the electrolyte, we update Eq. (2.20) to account for the additional flux:

$$\begin{aligned} \nabla \cdot \left[\psi_e \left(z_+ m_+ - z_- m_-\right) F C_e \nabla \phi_e\right] + \left(|\nabla \psi_e|_{ce} r_{xn,ce} + |\nabla \psi_e|_{ae} r_{xn,ae}\right)\frac{1}{\nu_+} = \\ \nabla \cdot \left[\psi_e \left(D_- - D_+\right) \nabla C_e\right], \end{aligned} \tag{7.8}$$

These modifications account for the complexities of ion transport and current flow within the electrolyte due to the presence of both cathode and anode particles in a full-cell simulation.

Boundary conditions:

Eq. (7.2) for the cathode is subject to a Dirichlet boundary condition, $\phi_{c|cc}$, at the cathode current collector (the computational boundary box, $x = 113.75\mu$m), displayed as the right boundary in Fig. 7.1 (a) and (b), and an internal boundary condition $r_{xn,ce}$. Similarly, Eq. (7.5) for the anode is subject to a Dirichlet boundary condition, $\phi_{a|ac}$, at the anode current collector (the computational boundary box, $x = 0\mu$m), displayed as the left boundary in Fig. 7.1 (a) and (b); and an internal boundary condition, $r_{xn,ae}$. Eq. (7.8) for the electrolyte contains two internal boundary conditions, $r_{xn,ce}$ and $r_{xn,ae}$. No flux boundary conditions are applied to Eqs. (7.1), (7.4), and (7.7).

Solver:

Eqs. (7.1) and (7.4) are solved to obtain the Li fractions in NMC and graphite, respectively, using the forward Euler explicit scheme. Additionally, Eq. (7.7) is solved for ion concentration in the electrolyte employing an Euler implicit scheme. As before, an implicit scheme is chosen for the electrolyte solver because of the large difference in diffusivity values between the electrolyte and the electrodes. Within each time step, the three electropotentials are computed in an internal iterative

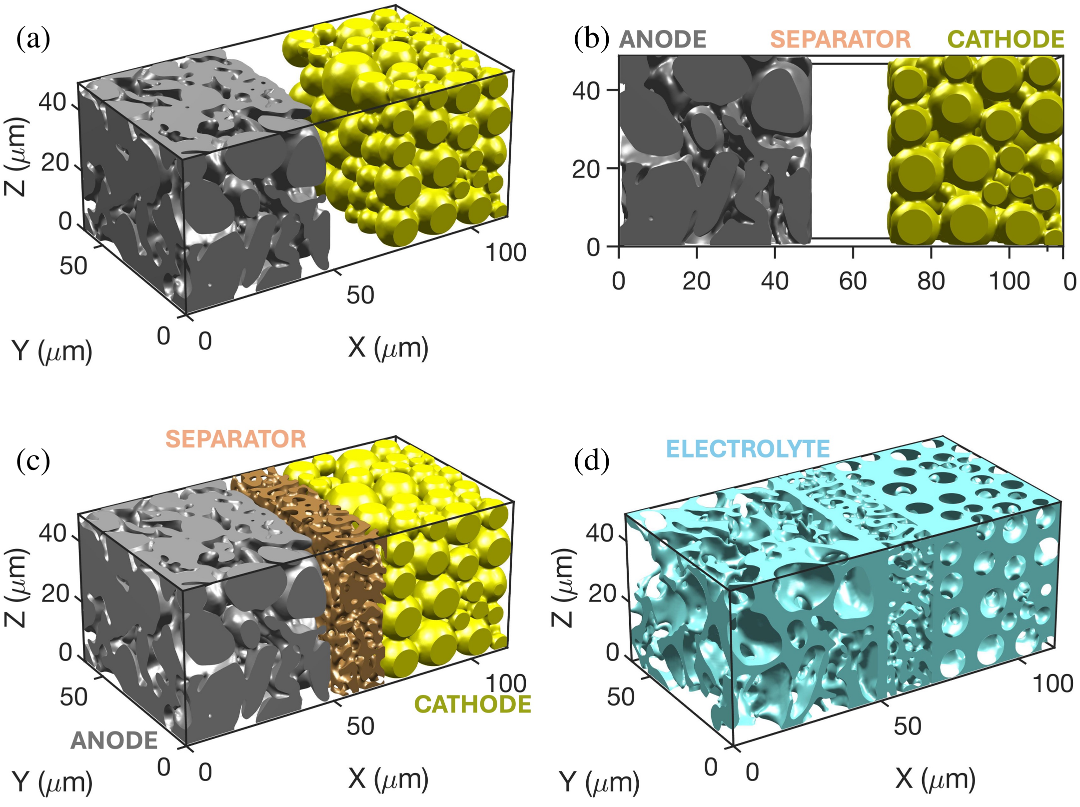

Figure 7.1 (a) Full-cell microstructure without a separator; (b) Side-view of full-cell highlighting the anode, the cathode, and separator regions. The empty spaces and pores in (a) and (b) are filled with the electrolyte; (c) Full-cell microstructure with a synthetic separator; and (d) The electrolyte in a full-cell.

loop from Eqs. (7.2), (7.3), (7.5), (7.6), and (7.8) until a numerical equilibrium is reached where the changes in these potentials become negligible. Once numerical equilibrium is achieved, the two reaction currents, $r_{xn,ce}$ and $r_{xn,ae}$ are used to calculate the total current on both cathode and anode, respectively. The simulation progresses to the next time step only if the total currents on both electrodes match the target current within a small tolerance (around 0.2%). If this criterion is not met, an iterative adjustment process is initiated. In cases where the total currents deviate from the target, the boundary conditions for the electropotentials at the current collectors, $\phi_{a|ac}$ and $\phi_{c|cc}$, are adjusted proportionally to difference in the total currents from the target current. The electropotentials, ϕ_a and ϕ_c, in both cathode and anode are subsequently adjusted to match the changes in the boundary conditions. Following these adjustments, the five fields (three electropotentials and two reaction currents) in the internal loop are relaxed until a new numerical equilibrium is attained. This process of adjusting boundary conditions and re-solving the inner loop continues until the total currents on both electrodes converge to the target current. Note that the target current is determined based on the chosen C-rate for the cathode. Once convergence is achieved, the simulation proceeds to the next time step. In the next time step, Eqs. (7.1), (7.4), and (7.7) are solved using the new updated values for $r_{xn,ce}$ and $r_{xn,ae}$. An illustration of the iterative process is provided in Fig. 7.2.

7.2.2 Simulation setup - microstructures and material parameters

The microstructure setup for the full-cell simulations is shown in Fig. 7.1. The graphite anode is situated on the left with gray color particles obtained from Ref. [99], while the NMC cathode is located on the right with yellow color particles generated using the Discrete Element Method (DEM). Two scenarios for the separator are tested. In Fig. 7.1 (a), the separator is empty and is assumed to be filled with the electrolyte, while in Fig. 7.1 (c), a synthetic bi-continuous separator microstructure generated using a Cahn-Hilliard phase separation is utilized. In both cases, the pores and empty spaces are filled with the electrolyte as shown in Fig. 7.1 (d).

A region of $48.75\mu m \times 61.75\mu m \times 48.75\mu m$ is used for both the cathode and the anode in the full-cell simulation. The separator region is chosen to be $16.25\mu m$. The grid size (dx) used for these simulations is $0.325\mu m$ based on the voxel values for the graphite microstructure. The raw data for the microstructure is smoothed to avoid any isolated voids.

NMC material parameters are the same as in Chapter 3. Graphite material parameters are the same as in Chapters 4, 5, and 6. Similar to previous chapters, $LiPF_6$ is the choice of electrolyte in this chapter. Electrolyte properties are also same as in the previous chapters.

7.3 Results and Discussion

As our focus throughout this work has been fast charging, we present 6C charge and discharge simulations of the presented full-cell microstructures. Fig. 7.3 demonstrates Li concentration in both the electrodes during 6C charge and discharge cycles. Figs. 7.3 (a), (b), and (c) correspond to a discharge cycle while (d), (e), and (f) represent a charge cycle at 6C. Note that the simulations

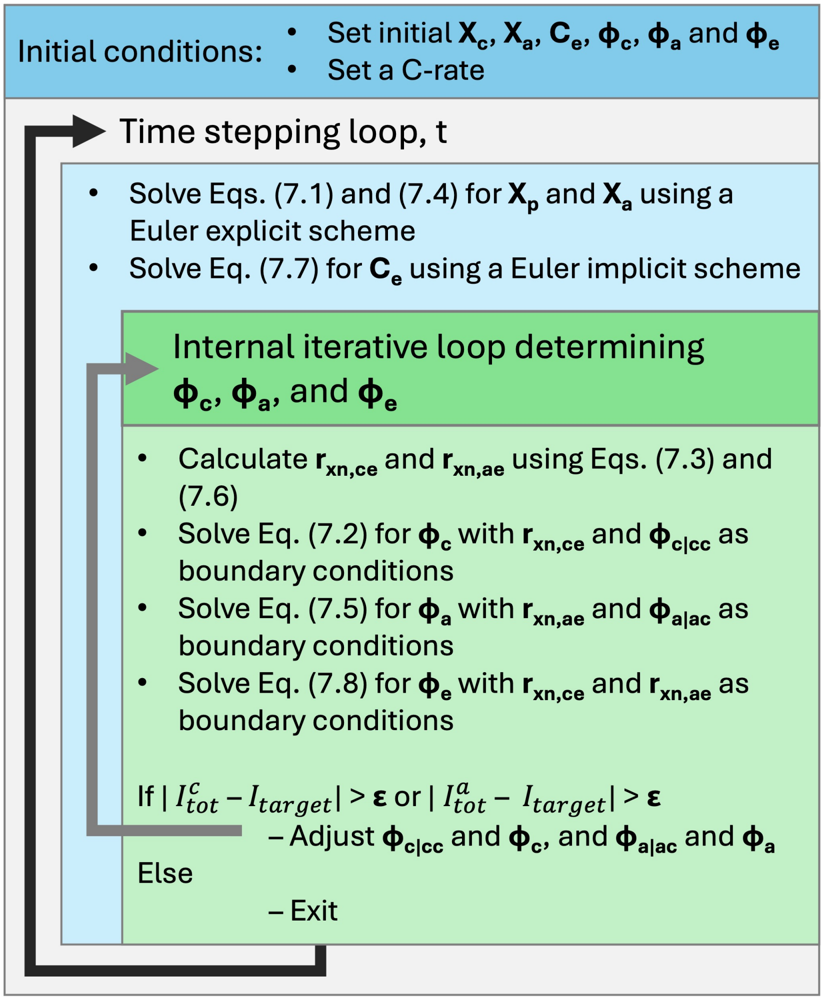

Figure 7.2 Updated flowchart of simulation scheme for solving the coupled governing equations in a full-cell.

for these demonstrations use a 6C rate based on the cathode loading. In the future, C-rate based on anode can also be utilized seamlessly in our full-cell framework. Delithiation of graphite can easily be observed in the discharge cycle from Figs. 7.3 (a), (b), and (c). The four phases can also

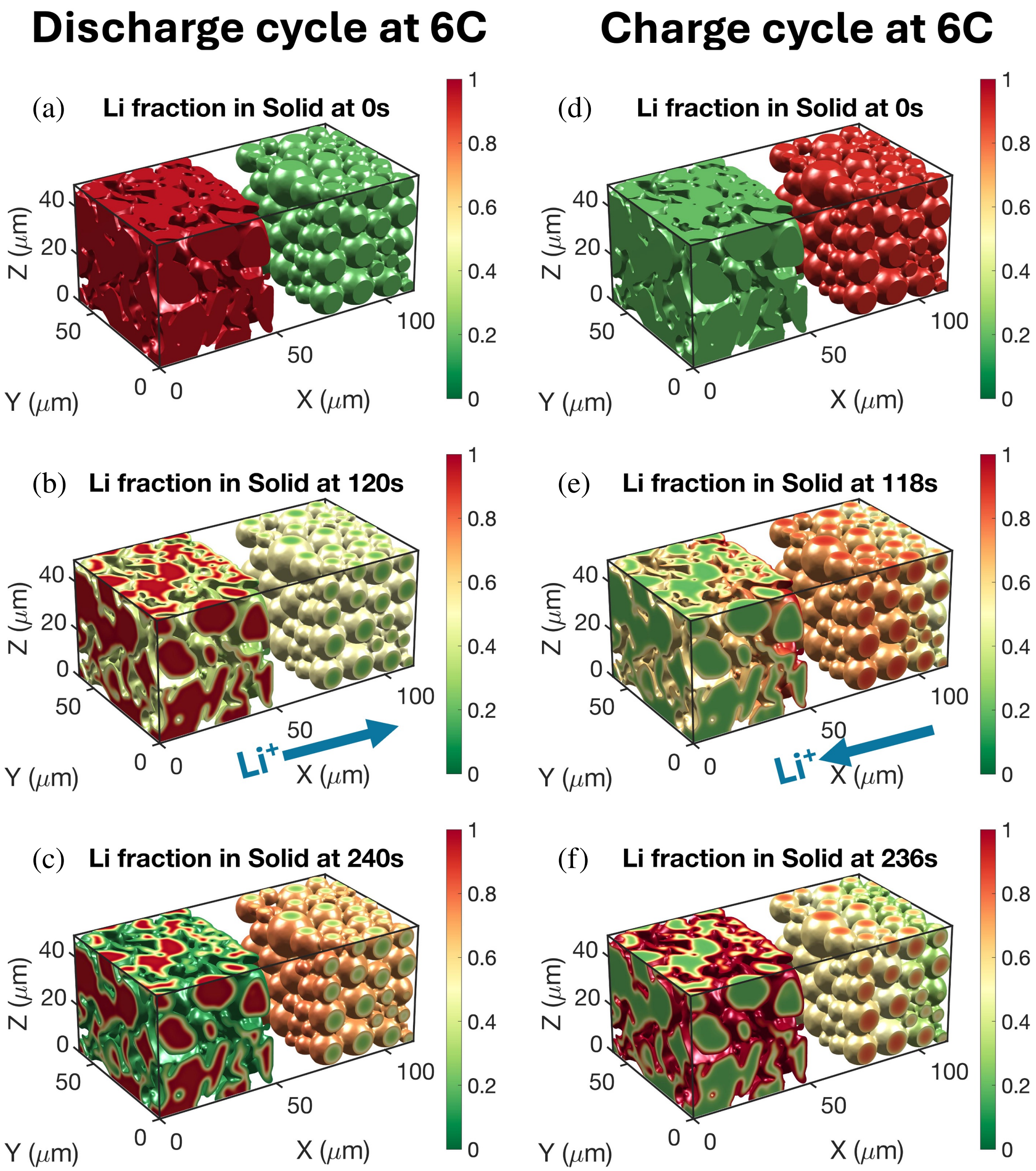

Figure 7.3 Li concentration in the electrodes for a discharge cycle at a 6C cathode rate (a) at 0s, (b) at 120s, and (c) at 240s; Li concentration in the electrodes for a charge cycle at a 6C cathode rate (a) at 0s, (b) at 118s, and (c) at 236s. The blue arrows highlight the direction of lithium movement during that cycle.

be noticed in graphite during both delithiation and lithiation as in Chapter 4. During the discharge cycle, the surfaces of graphite particles get highly delithiated while the core remains relatively full with Li due to this phase behavior. In contrast, NMC lithiation during the discharge cycle leads to a more uniform insertion as NMC is treated as a Li solution in our framework. Similar observations can be made during the charge cycle where graphite is lithiated from the Li coming from NMC. Phase behavior of graphite leads to the graphite particle surfaces being full while the core remains relatively empty. The region close to its current collector at $x = 0$ is filled slower and emptier than the graphite closer to the separator.

Fig. 7.4 (a), (b), and (c) shows electrostatic potential across the two electrodes for a charge cycle at a 6C cathode rate. A small gradient is observed along the thickness of the electrodes, similar to Chapters 3 and 4. Fig. 7.4 (d) demonstrates the overpotential on the two electrodes during the charge cycle. Following ideas from Chapters 4 and 5, we can identify the points of negative overpotential in the graphite anode, thus allowing us to identify the location and time of the theoretical onset of plating. As in Chapters 4 and 5, a higher negative overpotential is observed near

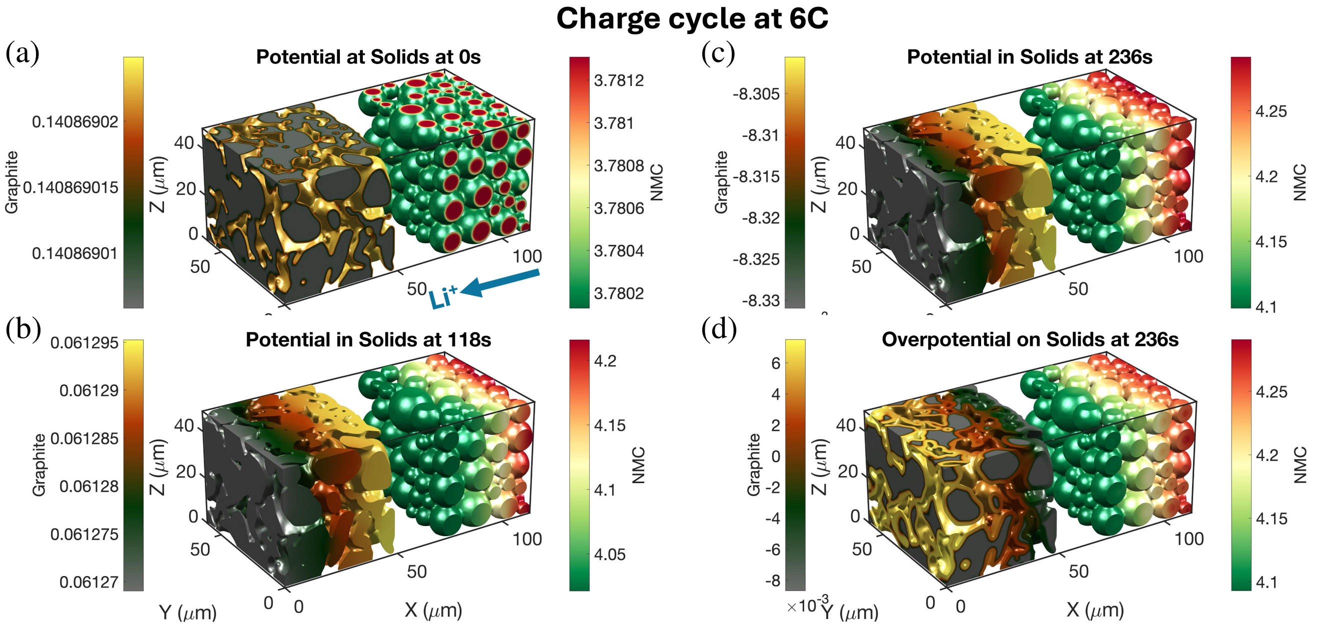

Figure 7.4 Electrostatic potential in the electrodes for a charge cycle at a 6C cathode rate (a) at 0s, (b) at 118s, (c) at 236s; and (d) Overpotential on the electrodes at 236s. The blue arrow highlights the direction of lithium movement during the charge cycle.

the separator compared to the current collector. This identification can be helpful with electrode design.

Fig. 7.5 illustrates concentrations in the electrolyte for both discharge and charge cycles at a 6C cathode rate. Concentration gradients across the whole length can be observed in the cell. Additionally Fig. 7.6 shows electrostatic potential in the electrolyte. Initial ion concentrations in the electrolyte are chosen to be 1M uniformly.

Due to the time dependence of electrolyte concentration, C_e, a no-flux boundary condition is deemed appropriate. However, solving for electrolyte potential, ϕ_e presents challenges as two-sided no-flux boundary conditions can be numerically unstable. Through the use of internal loops for convergence, a numerical equilibrium is achieved, with cathode potential, ϕ_c, and anode potential, ϕ_a having Dirichlet boundary conditions and being indirectly linked to electrolyte potential, ϕ_e through reaction fluxes on the anode, $r_{xn,ae}$, and cathode, $r_{xn,ce}$. This approach stabilizes the solution

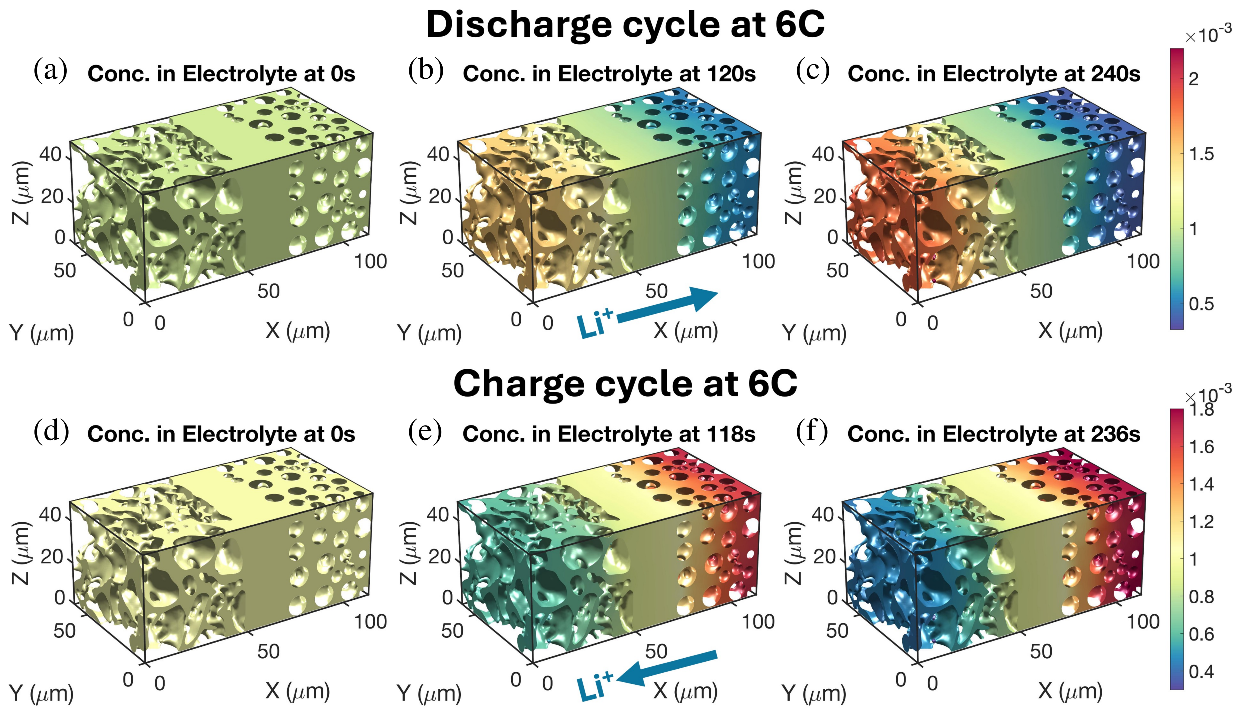

Figure 7.5 Ion concentration in the electrolyte for a discharge cycle at a 6C cathode rate (a) at 0s, (b) at 120s, (c) at 240s; Li concentration in the electrodes for a charge cycle at a 6C cathode rate (a) at 0s, (b) at 118s, and (c) at 236s. The blue arrows highlight the direction of lithium movement during that cycle.

for ϕ_e in our simulations.

Figs. 7.7(a) displays the simulated cell voltage curve for a 6C discharge cycle without a separator as the blue curve. The initial Li fraction in the cathode is chosen to be 0.2 and increases until the termination criterion is reached. Unlike the simulated CV curve for graphite anode from Chapters 4, 5, and 6, this simulated cell voltage curve does not show any kinks and more resembles the

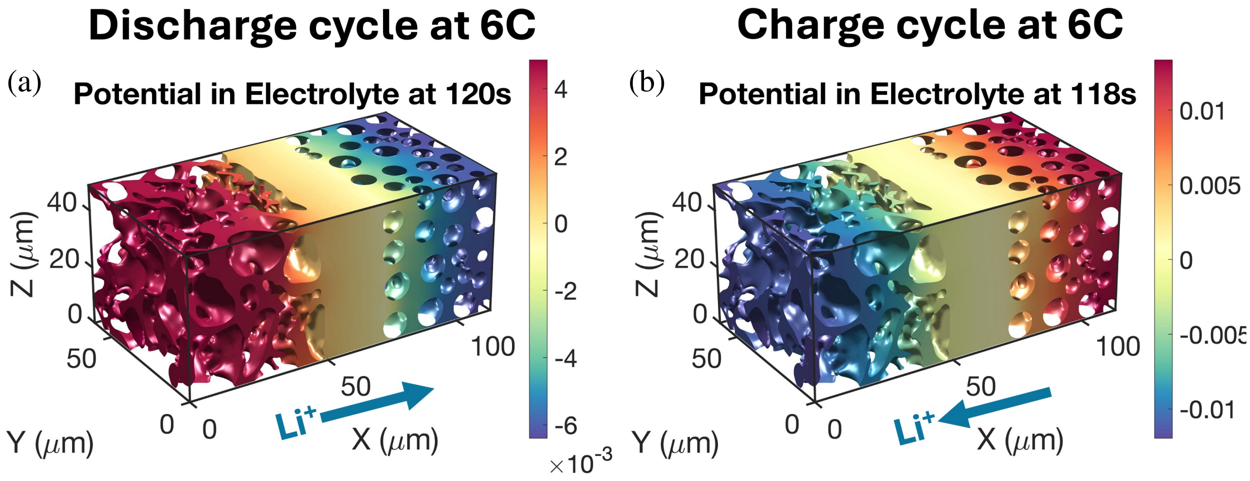

Figure 7.6 Electrostatic potential in the electrolyte at a 6C cathode rate (a) for a discharge cycle at 120s, and (b) for a charge cycle at 118s. The blue arrows highlight the direction of lithium movement during that cycle.

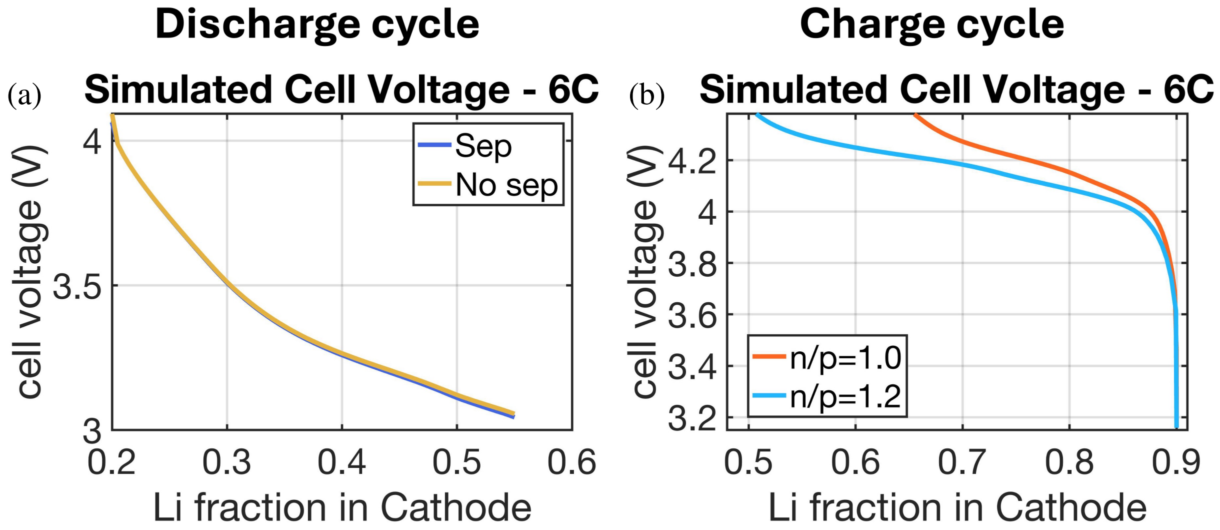

Figure 7.7 Simulated cell voltage curves at 6C cathode for full-cell for (a) a discharge cycle with and without separator, and (b) a charge cycle with two n/p ratios.

NMC cathode curves from Chapter 3. As the potential drop for NMC cathode at equilibrium is significantly higher (~1.8V from $X = 0.2$ to 1.0) than the potential change for graphite anode (~0.6V from $X = 0.0$ to 1.0), the CV curve for the full-cell is dominated by Li solution behavior of NMC.

Additionally, Fig. 7.7(b) compares the simulated cell voltage curves for n/p ratios of 1.0 and 1.2 for a 6C charge cycle. For these simulations, an initial Li fraction of 0.9 is selected for the cathode and a constant 6C cathode current is maintained until the termination criterion is achieved. A n/p ratio of 1.2 shows a higher achievable DoD due to more efficient lithiation of graphite during the charging process as there is less lithium per unit volume diffusing in the graphite anode.

Fig. 7.7(a) also compares the simulated CV curve for the two full cells displayed in Fig. 7.1, one without the separator and one with the separator for a 6C discharge cycle. It can be observed that the introduction of the separator did not lead to any significant changes and only marginally shifted the CV curve. However, a noticeable change is detected in the ion concentration in the electrolyte within the separator region. Fig. 7.8 illustrates the ion concentration in the electrolyte for the two cases. To elucidate the deviation from the no separator case Fig. 7.9(a) displays a 2D cross-section line plot of the ion concentration in the electrolyte in the two cases. Notably, introducing the

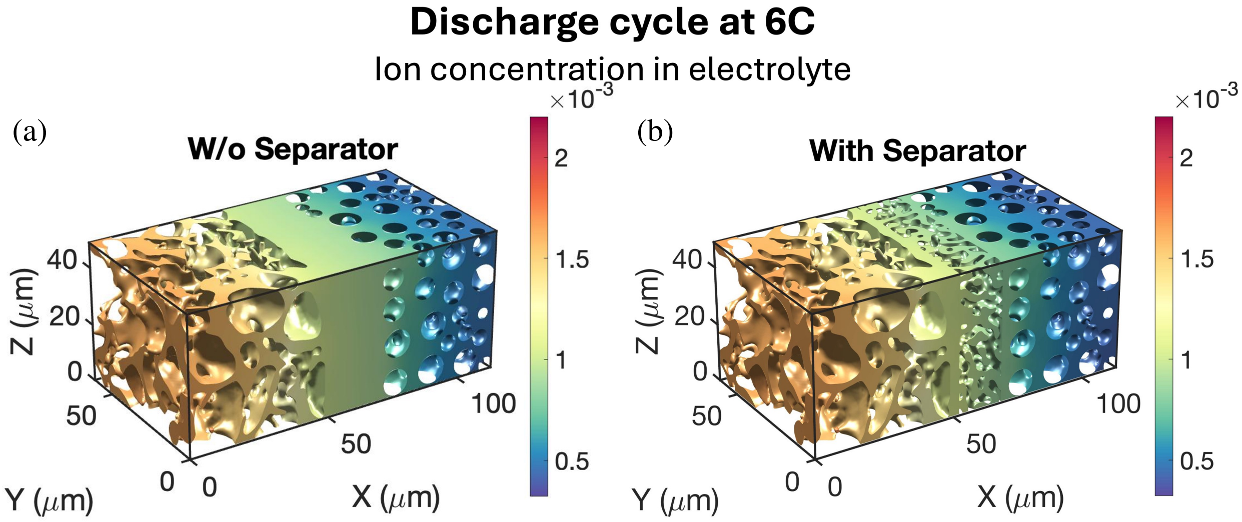

Figure 7.8 Ion concentration in the electrolyte (a) no separator, (b) with a separator.

separator induces a higher gradient for the ion concentration in the separator region due to the new tortuous path generated for the electrolyte. A 6C cycle on this microstructure did not provide sufficient time for the effect to propagate to the end of the electrodes, resulting in only a minor impact on the overall cell voltage curve. Nevertheless, these simulations serve as a demonstration of the adaptability of the full-cell framework.

7.4 Conclusion

This chapter demonstrates an additional framework using the smoothed boundary method to simulate electrochemical processes in a full-cell simulation. By combining a cathode (NMC) and graphite anode, the model incorporates a more realistic representation of a cell, enabling the exploration of three domain parameters with six fields and two reaction fluxes. Numerical stability is achieved in our solver despite the implementation of two no-flux boundary conditions on the electrolyte potential due to its integration with the electrode potential solvers through reaction fluxes. The capabilities of the developed full-cell framework are presented through simulations of charge and discharge cycles at a 6C lithiation rate. The role of the separator is also highlighted

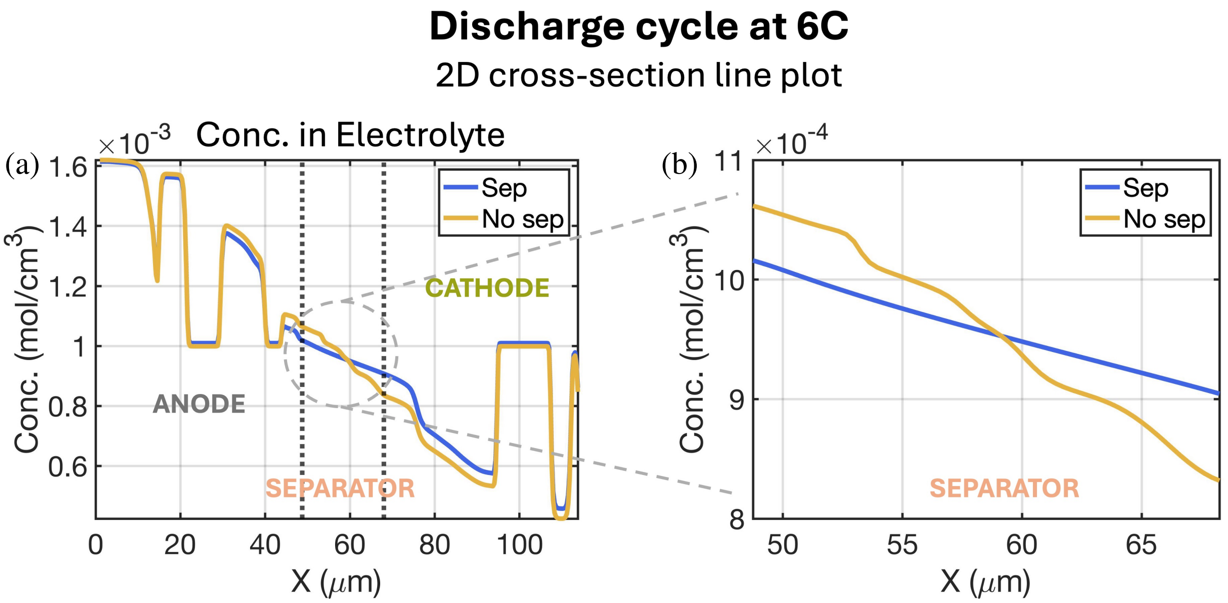

Figure 7.9 (a) Two-dimensional cross-section line plot of ion concentration in the electrolyte highlighting the gradient induced by the introduction of the separator, (b) Zoomed-in version of the separator region.

using two different full-cell setups, further showcasing the model's adaptability. The presented full-cell model demonstrates its potential for advancing battery design.

CHAPTER 8

SUMMARY, PROSPECTS AND FUTURE WORK

8.1 Summary

Lithium-ion batteries do and will play a pivotal role in the energy sector by reducing our reliance on fossil fuels as a society. They are already ubiquitous in electronic devices and electric vehicles. Still, major areas of improvement include higher safety, even further increasing energy density, and reducing costs. Gaining insights into microstructure-level phenomena inside a lithium-ion battery is essential to designing batteries and electrodes to achieve these goals. Mathematical modeling and computer simulations provide an approach to understanding and visualizing such microstructure-level phenomena. Governing equations defining the several simultaneous processes occurring in a battery are well-known and are primarily simultaneous differential equations. Various numerical methods like Finite Different Method (FDM), Finite Element Method (FEM), etc. are usually implemented to solve these equations.

This dissertation introduces a new framework employing a diffuse-interface method, the Smoothed Boundary Method (SBM), in conjunction with a mesh refinement method, Adaptive Mesh Refinement (AMR) for electrochemical simulations. SBM allows for the use of a uniform grid mesh instead of a conformal mesh which is typically utilized in traditional numerical solvers modeling the complex electrode microstructures. Thus, reducing computational burden and time for microstructure-level electrochemical simulations. A diffuse interface defined by a domain parameter, ψ enables the use of a uniform grid for the complex and convoluted microstructures. This domain parameter is used to modify the governing equations in SBM. However, as a consequence of using the diffuse interface, solving these SBM reformulated electrochemical governing equations can incur some inaccuracies in the simulation results. Modifying to a finer mesh can negate and reduce any such inaccuracies. However, a finer mesh will significantly increase the computation burden of the electrochemical simulations, thus nullifying the improvements offered by SBM. A compromise between the two scenarios can work well in which a finer mesh is utilized only near the diffuse interface while still using a regular mesh in bulk. AMR is a technique that fulfills this requirement of varying grid sizes across the entire domain. When combined with SBM can give highly accurate simulation results without any considerable increase in the computational burden. In this work, the framework of SBM+AMR is combined with finite difference numerical schemes to simulate the electrochemical behavior.

The framework is tested and validated on an NMC-333 cathode, a common cathode in contemporary batteries. Synthetic spherical microstructures are computationally generated using the Discrete Element Method (DEM) for these simulations. Comparisons with sharp-interface solutions in 1-D and COMSOL solutions on a 3-D sphere confirm the accuracy of our method. The framework's versatility is realized by presenting charge-discharge cycling, cyclic voltammetry, thermal, and mechanical simulations. The following majority of the dissertation focuses on studying graphite anodes. Phase transformations and the onset of plating in the graphite anode are identified in 3-D microstructures. Two different approaches are explored to mitigate and delay the onset of plating in the graphite anode. The first approach is a thermodynamic one, using a hybrid anode where hard carbon particles are mixed with graphite particles creating a buffer for lithium insertion instead of deposition on the graphite surface, thus delaying the onset of plating in the electrode. The second approach is kinetic in which new pathways/tunnels are artificially created in the electrode allowing easier diffusive channels for more efficient electrode usage, consequently achieving higher capacity before reaching the overcharging conditions. Various configurations and parameters are studied for both approaches through 3-D microstructure electrochemical simulation. The dissertation culminates with an introduction and presentation of the extension of our framework to full-cell simulations.

8.2 Other prospects

The developed framework is employed by Danqi et. al in Refs. [58, 140] for electrochemical impedance spectroscopy (EIS) simulations. EIS is a commonly used technique to measure the electric properties of a material and characterize the behavior of an electrochemical system. An alternating current (AC) signal probes the electrochemical system and measures its current response. The impedance spectra calculated from the response over a range of frequencies provide insights into the electrochemical behavior of the system.

Ref. [58] employs our framework with multiple sinusoidal voltage loadings to capture the underlying relations between the obtained macroscopic properties and electrode microstructures of the NMC-333 cathode. The provided framework facilitates the examination of how various properties influence EIS curves. Fig. 8.1 briefly illustrates some of the simulation results presented in the paper. Fig. 8.1 (c) contrasts EIS curves for two different geometries displayed in Figs. 8.1 (a) and (b) as Geo-1 and Geo-2, respectively. Both geometries are generated with a radius distribution having the same mean radius of 5.8μm and a similar porosity of ~ 0.72. The primary difference between the two geometries is the variance of the distribution around the mean, leading to different

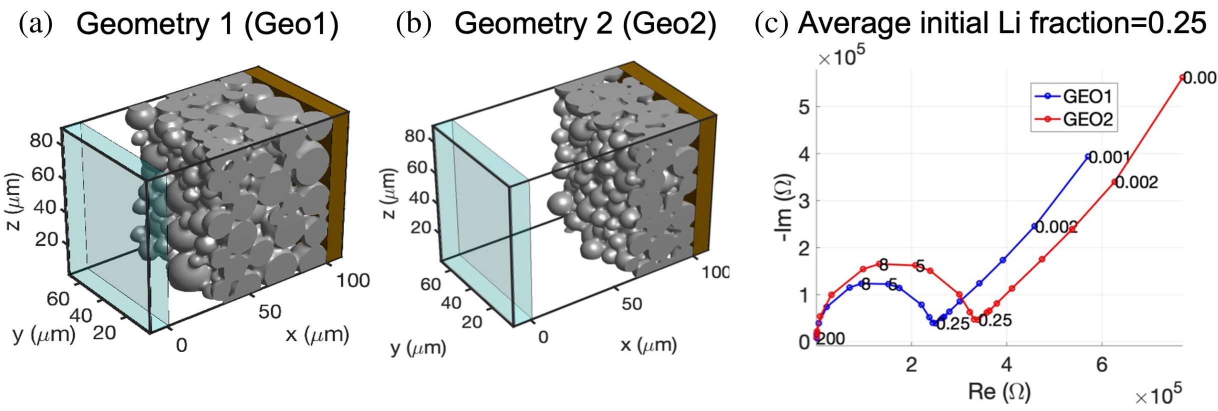
(a) Geometry 1 (Geo1) (b) Geometry 2 (Geo2) (c) Average initial Li fraction=0.25

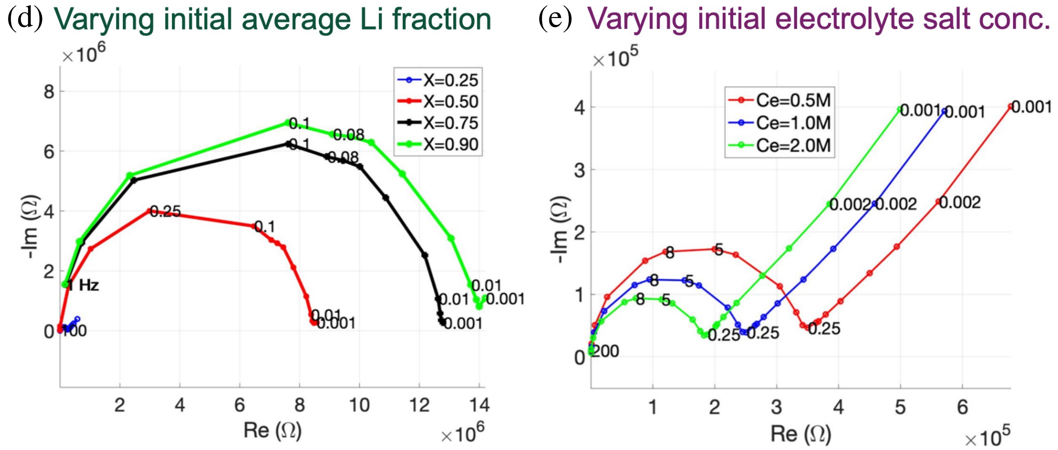
(d) Varying initial average Li fraction (e) Varying initial electrolyte salt conc.

Figure 8.1 (a) Configuration of the virtual cell for Geo-1, (b) configuration of the virtual cell for Geo-2, (c) Nyquist plot of simulated EIS curves of Geo-1 and Geo-2 electrodes with average initial Li fraction = 0.25, (d) Nyquist plot of simulated EIS curves with initial Li fractions equal to 0.25, 0.50, 0.75, and 0.90 in the NMC electrode, and (e) Nyquist plot of simulated EIS curves for initial salt concentrations = 0.5M, 1.0M, and 2.0M in the electrolyte. Figures obtained from [58].

particle surface areas and surface area-to-volume ratios, 68,061 μm^2 and 0.22 μm^{-1} for Geo-1 and 49,151 μm^2 and 0.28 μm^{-1} for Geo-2, respectively. The two simulations are initialized with the same Li fraction of 0.25, resulting in the same exchange current density. As can be noticed from Fig. 8.1 (c), the two geometries produce largely different Nyquist plots and significantly different charge transfer resistances, $2.60 \times 10^5 \Omega$ for Geo-1 and $3.45 \times 10^5 \Omega$ for Geo-2 calculated as twice the radius of the semi-circle. The ratio of the two resistances, $R_{c,Geo-2}/R_{c,Geo-1}$ = 1.33 is found to be consistent with the inverse of the two electrode surface areas, A_{Geo-1}/A_{Geo-2} = 1.38. Additionally, Fig. 8.1 (d) shows four Nyquist plots of simulations with different initial average Li fractions, X_p = 0.25, 0.50, 0.75, and 0.90 for the microstructure Geo-1. Based on these Li fractions and the corresponding electropotential boundary conditions, the four different exchange current densities, i_0 are calculated to be 1.448×10^{-1}, 4.079×10^{-3}, 2.685×10^{-3}, and 2.495×10^{-3} mA/cm^2 respectively. These i_0 values can be substituted in the relation, $R_{ct} = RT/zFi_0$, to determine charge transfer resistances (R_{ct}). Using this relation, the ratios of R_{ct}'s for the four Li fractions are found to be 1:35:53:58, respectively, which are consistent with the values determined from the Nyquist plots in Fig. 8.1 (d). The exact computed R_{ct} values from the Fig. 8.1 (d) are 0.26×10^6, 8.50×10^6, 12.80×10^6, and 14.20×10^6 Ω. Finally, the authors demonstrate the effect of varying initial electrolyte salt concentration, C_e, from 0.5M to 1.0M to 2.0M. The changes in the salt concentrations induce changes to ambipolar and ionic diffusivities. The Nyquist plot for the three EIS simulations can be found in Fig. 8.1 (e). As the C_e increases, the radius of the semi-circle decreases, indicating an increase in the reaction rate with C_e. Each frequency is positioned similarly across all three concentrations, thus implying that the double-layer capacitance has a negligible impact on the EIS behavior for this concentration range. The Warburg impedances (the linear part of the curves) are also approximately the same across the three concentrations, with a shift to the right. This similarity signifies that the Li diffusion in the electrode particles is the limiting factor for the diffusional impedance. As the Li diffusivity in the electrolyte is approximately six orders of magnitude larger than in the particle, the variation of salt diffusivity due to C_e has an insignificant effect on the Warburg impedance, largely corresponding to relatively lower frequency loadings.

Salt concentration, C_e, tends to reach an equilibrium easier for these low-frequency loadings.

Ref. [140] extends the EIS simulation studies to graphite anodes. Fig. 8.2 briefly presents a few findings from Ref. [140]. In contrast to NMC, graphite electrode undergoes phase transitions when lithiated or delithiated. As discussed in detail in Chapters 4, 5, and 6, graphite exhibits four phases labeled as 1', 3, 2, and 1 in our work illustrated in Fig. 4.1. These phase transitions cause interesting behavior in EIS simulations. Fig. 8.2 (a) displays simulated EIS curves for the four uniform and stable single-phases in a lithiated graphite anode. The different EIS curves result in four different charge transfer resistances, all consistent with total theoretical charge transfer resistances calculated using $R_{ct} = RT/zFi_0$. Next, the EIS responses for multi-phase morphologies are contrasted with uniform single-phase morphologies and each other. Note that, a core-shell concentration distribution is observed for lithium in the electrodes. Fig. 8.2 (c) compares Nyquist

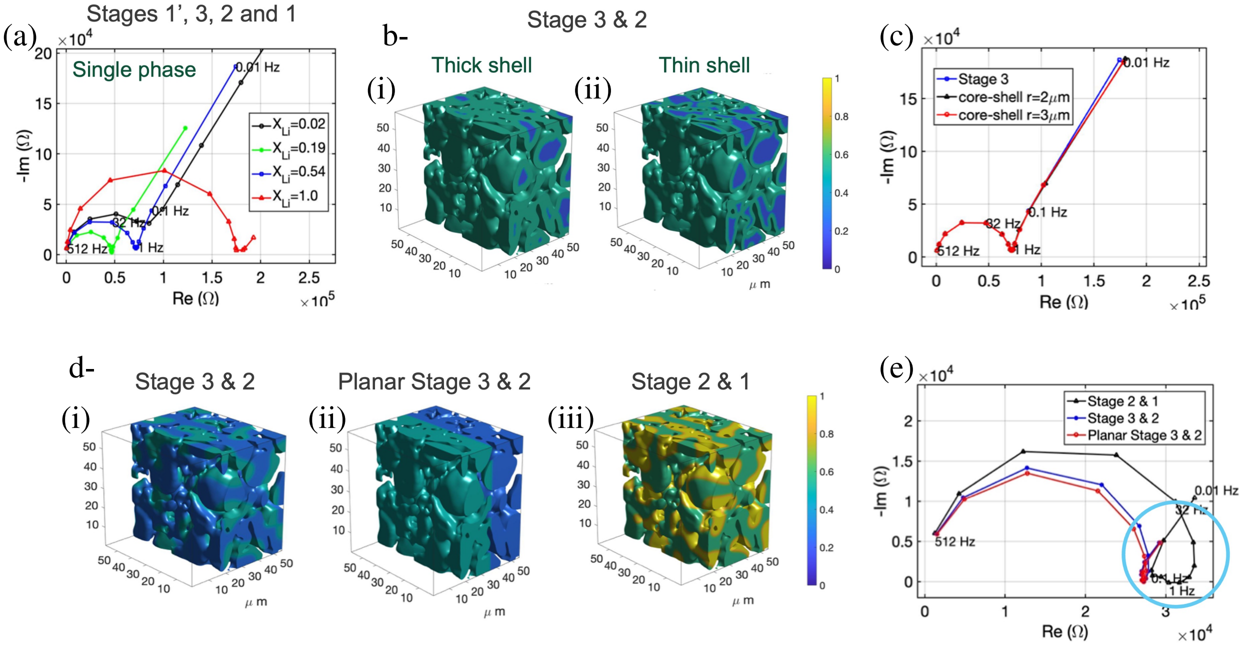

Figure 8.2 (a) Simulated EIS curves for single-phase stages 1', 3, 2, and 1 on the E_II electrode, (b) Stage 3-2 core-shell phase morphologies of a (i) thick shell and (ii) thin shell, (c) Simulated EIS curves for the two core-shell stage 3-2 cases, which are similar to the single-phase stage 2 case, (d) Phase morphologies of (i) stage 3-2 coexistence generated using the Cahn-Hilliard equation, (ii) Planar modification of (i), and (iii) stage 2-1 coexistence generated using the Cahn-Hilliard equation, and (e) Simulated EIS curves for d-(i), (ii), and (iii). The blue circle highlights an inductive loop observed in these phase-separated morphologies. Figures obtained from [140].

plots for single-phase-3 and two different core-shell concentration distributions between phases 3 and 2. The two core shells are illustrated in Figs. 8.2 b-(i) and b-(ii) and differ in the depth of lithium penetration inside the particles leading to a thicker shell in Fig. 8.2 b-(i). The EIS responses for the two core shells overlap almost completely, diverging only slightly from the uniform single-phase-3 in the Warburg impedance region at very low frequencies. Despite the significant differences in average lithium fraction among the three distributions, the near-complete overlap suggests that the EIS response for multi-phase morphologies is stepwise rather than continuous. This implies that the EIS curve remains largely unchanged over a range of Li fractions and shifts suddenly when new phases form in shell layers. In conclusion, if the electrode surface properties remain constant over a range of lithium fractions when probed, it can be assumed that the electrode is undergoing phase transitions. On the contrary, if there is a continuous change in measurements, a solid-solution lithiation can be inferred in the electrode. The authors also presented a study of phase-separated morphologies in graphite which rarely occur naturally in batteries but offer interesting insights nonetheless. Phase-separated or spinodal configurations are generated using the Cahn-Hilliard equation without any surface reactions. One spinodal configuration illustrated in Fig, 8.2 d-(i) has phase-separated stages 3 & 2, and another configuration with phase-separated stages 2 & 1 is shown in Fig, 8.2 d-(iii). Additionally, a planar artificial configuration is generated from (i) where the two stages 3 & 2 are physically separated into two halves of the electrode displayed in Fig. 8.2 d-(ii). The Nyquist plots for these three synthetic configurations are shown in Fig. 8.2 (e). The semi-circle regions corresponding to (i) and (ii) (with stages 3 & 2) in blue and red are almost overlapping. The slight deviation results from the small differences in average exchange current densities (i_0's) caused by the different morphologies. On the other hand, the semi-circle region for (iii) (with stages 2 & 1) in black is substantially larger than the other two, indicating a larger charge transfer resistance, R_{ct}, as the average exchange current density is smaller in this case. More peculiarly, a "loop" is observed in the low-frequency regions for all three morphologies highlighted by the blue circle in Fig. 8.2 (e). This loop, more commonly referred to as an inductive loop, is often associated with EIS measurements involving phase transformations. One potential explanation for these induction loops can be the sudden change in exchange current densities at phase boundaries on particle surfaces. Since the deviation in exchange current density between phases 2 & 1 is greater than that between phases 3 & 2, the induction loop is significantly larger and spans more frequencies for the phases 2 & 1 case.

Presented above are some of the EIS simulation results conducted by Danqi et. al. Interested readers are encouraged to refer to the full articles in Ref. [58] and [140] for additional details. The papers effectively demonstrate the applicability and versatility of the presented framework for exploring and examining EIS behavior.

8.3 Future Work

In the future, the studies and the investigations performed in this dissertation can be extended to full cells for more realistic and accurate quantitative simulation results using the new full-cell framework. More specifically, we can (1) examine the impact of hybrid anodes on full-cell performance and their role in alleviating plating in a full cell, and (2) the effect of tunnels in a full cell can be studied. It is also imperative to analyze tunneling in cathodes alongside the tunnels in the anodes. As introducing these tunnels/pathways affects the total Li flux in/out of the anode, the Li flux for the cathode will also be affected.

Another area where we have made some strides but need to explore more is examining other different anode materials using the developed framework, especially in the hybrid anode setup. We have conducted a few preliminary simulations for hybrid anodes incorporating lithium titanate (LTO), silicon, and silicon oxide anodes with graphite and hard carbon anodes [141–144]. Silicon is a promising anode material as it displays significantly high capacity ($\sim$ 10 times the theoretical capacity of graphite) and is highly abundant and cheap compared to several other anode materials. However, as an anode, it faces considerable volume expansion during lithiation (about $200 - 300\%$) which can lead to structural changes and mechanical degradation over multiple cycles [142, 143]. Creating a hybrid anode with silicon can potentially resolve the volume expansion issue to some extent. Composite particles comprising silicon and hard carbon show promise as high-capacity anode particles with remarkably less volume expansion [144]. These composite particles can be effortlessly simulated using our framework and the simulations can provide deep insights into their construction and benefits. Other cathode materials can be researched as well using the full-cell framework. We conducted rudimentary simulations for lithium cobalt oxide (LCO) [145, 146], lithium iron phosphate (LFP) [147, 148], lithium nickel manganese cobalt-811 (NMC-811) [148, 149], and lithium nickel cobalt aluminum oxide (NCA) [150, 151] cathodes with our single electrode framework. Expanding on that, the detailed performance of these cathodes in a full cell can be easily explored.

Furthermore, investigating the numerical solver and the refinement process can be prudent in improving the simulations using the developed framework. To contrast the computational performance, an implementation of the SBM+AMR equations using the finite element methods (FEM) or the finite volume methods (FVM), rather than the finite difference schemes used in this work, should be examined. Additionally, while the octree refinement is highly effective in our framework, it is not necessarily the most computationally efficient refinement technique for complex 3D microstructures and needs to be compared to alternative refinement techniques such as block or patch refinement [152–157]. Lastly, we concede that our implementation of the framework in FORTRAN is not highly optimized for computational time and speed. In the future, this implementation can be potentially improved by incorporating already existing optimized solvers, libraries, and frameworks.

BIBLIOGRAPHY

[1] M. Aneke and M. Wang. Energy storage technologies and real life applications – a state of the art review. *Applied Energy*, 179:350–377, 2016.

[2] Xing Luo, Jihong Wang, Mark Dooner, and Jonathan Clarke. Overview of current development in electrical energy storage technologies and the application potential in power system operation. *Applied Energy*, 137:511–536, 2015.

[3] Mathew Aneke and Meihong Wang. Energy storage technologies and real life applications – A state of the art review. *Applied Energy*, 179:350–377, October 2016.

[4] Léonard Wagner. Chapter 27 - Overview of Energy Storage Technologies. In Trevor M. Letcher, editor, *Future Energy (Second Edition)*, pages 613–631. Elsevier, Boston, January 2014.

[5] Md Mustafizur Rahman, Abayomi Olufemi Oni, Eskinder Gemechu, and Amit Kumar. Assessment of energy storage technologies: A review. *Energy Conversion and Management*, 223:113295, November 2020.

[6] H. Ibrahim, A. Ilinca, and J. Perron. Energy storage systems—Characteristics and comparisons. *Renewable and Sustainable Energy Reviews*, 12(5):1221–1250, June 2008.

[7] Susan M. Schoenung. Characteristics and Technologies for Long- vs. Short-Term Energy Storage: A Study by the DOE Energy Storage Systems Program. Technical Report SAND2001-0765, Sandia National Lab. (SNL-NM), Albuquerque, NM (United States); Sandia National Lab. (SNL-CA), Livermore, CA (United States), March 2001.

[8] Alexandra Zablocki. Fact Sheet | Energy Storage (2019) | White Papers | EESI.

[9] Hanif SedighNejad, Tariq Iqbal, and John Quaicoe. Compressed Air Energy Storage System Control and Performance Assessment Using Energy Harvested Index. *Electronics*, 3(1):1–21, March 2014. Number: 1 Publisher: Multidisciplinary Digital Publishing Institute.

[10] Arumugam Manthiram. An outlook on lithium ion battery technology. *ACS Central Science*, 3:1063–1069, 2017.

[11] John B. Goodenough and Kyu-Sung Park. The Li-Ion Rechargeable Battery: A Perspective. *Journal of the American Chemical Society*, 135(4):1167–1176, January 2013. Publisher: American Chemical Society.

[12] M. Armand and J. Tarascon. Building better batteries. *Nature*, 451:652–657, 2008.

[13] Manuel Weiss, Raffael Ruess, Johannes Kasnatscheew, Yehonatan Levartovsky, Natasha Ronith Levy, Philip Minnmann, Lukas Stolz, Thomas Waldmann, Margret Wohlfahrt-Mehrens, Doron Aurbach, Martin Winter, Yair Ein-Eli, and Jürgen Janek. Fast Charging of Lithium-Ion Batteries: A Review of Materials Aspects. *Advanced Energy Materials*, 11(33):2101126, 2021.

[14] Taehoon Kim, Wentao Song, Dae-Yong Son, Luis K. Ono, and Yabing Qi. Lithium-ion batteries: outlook on present, future, and hybridized technologies. *Journal of Materials Chemistry A*, 7(7):2942–2964, 2019.

[15] Anna Tomaszewska, Zhengyu Chu, Xuning Feng, Simon O'Kane, Xinhua Liu, Jingyi Chen, Chenzhen Ji, Elizabeth Endler, Ruihe Li, Lishuo Liu, Yalun Li, Siqi Zheng, Sebastian Vetterlein, Ming Gao, Jiuyu Du, Michael Parkes, Minggao Ouyang, Monica Marinescu, Gregory Offer, and Billy Wu. Lithium-ion battery fast charging: A review. *eTransportation*, 1:100011, August 2019.

[16] Xinghui Zhang, Zhao Li, Lingai Luo, Yilin Fan, and Zhengyu Du. A review on thermal management of lithium-ion batteries for electric vehicles. *Energy*, 238:121652, January 2022.

[17] Da Deng. Li-ion batteries: basics, progress, and challenges. *Energy Science & Engineering*, 3(5):385–418, 2015.

[18] Dhrupad Parikh, Tommiejean Christensen, Chien-Te Hsieh, and Jianlin Li. Elucidation of Separator Effect on Energy Density of Li-Ion Batteries. *Journal of The Electrochemical Society*, 166(14):A3377, October 2019. Publisher: IOP Publishing.

[19] Dhrupad Parikh, Tommiejean Christensen, and Jianlin Li. Correlating the influence of porosity, tortuosity, and mass loading on the energy density of $LiNi_{0.6}Mn_{0.2}Co_{0.2}O_2$ cathodes under extreme fast charging (XFC) conditions. *Journal of Power Sources*, 474:228601, October 2020.

[20] Arumugam Manthiram. A reflection on lithium-ion battery cathode chemistry. *Nature Communications*, 11(1):1550, March 2020. Number: 1 Publisher: Nature Publishing Group.

[21] Hui Cheng, Joseph G. Shapter, Yongying Li, and Guo Gao. Recent progress of advanced anode materials of lithium-ion batteries. *Journal of Energy Chemistry*, 57:451–468, June 2021.

[22] Ying Ma. Computer Simulation of Cathode Materials for Lithium Ion and Lithium Batteries: A Review. *ENERGY & ENVIRONMENTAL MATERIALS*, 1(3):148–173, 2018.

[23] Ulrike Krewer, Fridolin Röder, Eranda Harinath, Richard D. Braatz, Benjamin Bedürftig, and Rolf Findeisen. Review—Dynamic Models of Li-Ion Batteries for Diagnosis and Operation: A Review and Perspective. *Journal of The Electrochemical Society*, 165(16):A3656, November 2018. Publisher: IOP Publishing.

[24] Affan Malik and Hui-Chia Yu. Complex Electrode Microstructure Simulations using a Smoothed Boundary Method with Adaptive Mesh Refinement. *Journal of The Electrochemical Society*, 169(7):070527, Jul 2022.

[25] Bor Yann Liaw, Ganesan Nagasubramanian, Rudolph G. Jungst, and Daniel H. Doughty. Modeling of lithium ion cells – a simple equivalent-circuit model approach. *Solid State Ionics*, 175:835–839, 2004.

[26] M. Ecker. *Lithium Plating in Lithium-Ion batteries: An experimental and simulation approach*. Shaker Verlag, 2016.

[27] Y. Hu, S. Yurkovich, Y. Guezennec, and B. J. Yurkovich. A technique for dynamic battery model identification in automotive applications using linear parameter varying structures. *Control Engineering Practice*, 17:1190–1201, 2009.

[28] Seyed Mohammad Rezvanizaniani, Zongchang Liu, Yan Chen, and Jay Lee. Review and recent advances in battery health monitoring and prognostics technologies for electric vehicle (EV) safety and mobility. *Journal of Power Sources*, 256:110–124, 2014.

[29] Mehmet Ugras Cuma and Tahsin Koroglu. A comprehensive review on estimation strategies used in hybrid and battery electric vehicles. *Renewable and Sustainable Energy Reviews*, 42:517–531, 2015.

[30] Gae-won You, Sangdo Park, and Dukjin Oh. Real-time state-of-health estimation for electric vehicle batteries: A data-driven approach. *Applied Energy*, 176:92–103, 2016.

[31] Pritpal Singh, Ramana Vinjamuri, Xiquan Wang, and David Reisner. Design and implementation of a fuzzy logic-based state-of-charge meter for Li-ion batteries used in portable defibrillators. *Journal of Power Sources*, 162:829–836, 2006.

[32] J. Newman and W. Tiedemann. Porous-electrode theory with battery application. *AIChE Journal*, 21:25–41, 1975.

[33] M. Doyle, T.F. Fuller, and J. Newman. Modeling of galvanostatic charge and discharge of the lithium/polymer/insertion cell. *Journal of The Electrochemical Society*, 140:1526, 1993.

[34] T R Ferguson and M Z Bazant. Nonequilibrium Thermodynamics of Porous Electrodes. *Journal of The Electrochemical Society*, 159(12):A1967 – A1985, 01 2012.

[35] Andrew M. Colclasure, Kandler A. Smith, and Robert J. Kee. Modeling detailed chemistry and transport for solid-electrolyte-interface (SEI) films in Li–ion batteries. *Electrochimica Acta*, 58:33–43, 2011.

[36] Y.-H. Chen, C.-W. Wang, X. Zhang, and A.M. Sastry. Porous cathode optimization for lithium cells: Ionic and electronic conductivity, capacity, and selection of materials. *Journal of Power Sources*, 195:2851–2862, 2010.

[37] A F Bower and P R Guduru. A simple finite element model of diffusion, finite deformation, plasticity and fracture in lithium ion insertion electrode materials. *Modelling and Simulation in Materials Science and Engineering*, 20:045004, 2012.

[38] S J Cooper, D S Eastwood, J Gelb, G Damblanc, D J L Brett, R S Bradley, P J Withers, P D Lee, A J Marquis, N P Brandon, and P R Shearing. Image based modelling of microstructural heterogeneity in $LiFePO_4$ electrodes for Li-ion batteries. *Journal of Power Sources*, 247(c):1033 – 1039, 02 2014.

[39] Bo Yan, Cheolwoong Lim, Leilei Yin, and Likun Zhu. Three dimensional simulation of galvanostatic discharge of $LiCoO_2$ cathode based on X-ray nano-CT images. *Journal of The Electrochemical Society*, 159(10):A1604–A1614, 2012.

[40] Samuel J. Cooper, Antonio Bertei, Donal P. Finegan, and Nigel P. Brandon. Simulated impedance of diffusion in porous media. *Electrochimica Acta*, 251:681–689, 2017.

[41] Andreas H. Wiedemann, Graham M. Goldin, Scott A. Barnett, Huayang Zhu, and Robert J. Kee. Effects of three-dimensional cathode microstructure on the performance of lithium-ion battery cathodes. *Journal of The Electrochemical Society*, 88:580–588, 2013.

[42] Mehdi Chouchane, Emiliano N Primo, and Alejandro A Franco. Mesoscale effects in the extraction of the solid-state lithium diffusion coefficient values of battery active materials: Physical insights from 3D modeling. *The Journal of Physical Chemistry Letters*, pages 1 – 6, 03 2020.

[43] Abbos Shodiev, Emiliano N Primo, Mehdi Chouchane, Teo Lombardo, Alain C Ngandjong, Alexis Rucci, and Alejandro A Franco. 4D-resolved physical model for electrochemical impedance spectroscopy of $Li(Ni_{1-x-y}Mn_xCo_y)O_2$-based cathodes in symmetric cells: Consequences in tortuosity calculations. *Journal of Power Sources*, 454:227871, 04 2020.

[44] Hui-Chia Yu, Hsun-Yi Chen, and K. Thornton. Extended smoothed boundary method for solving partial differential equations with general boundary conditions on complex boundaries. *Modelling and Simulation in Materials Science and Engineering*, 20(7):075008, September 2012. Publisher: IOP Publishing.

[45] Bernardo Orvananos, Todd R. Ferguson, Hui-Chia Yu, Martin Z. Bazant, and Katsuyo Thornton. Particle-level modeling of the charge-discharge behavior of nanoparticulate phase-separating Li-ion battery electrodes. *Journal of The Electrochemical Society*, 161:A535–A546, 2014.

[46] Bernardo Orvananos, Rahul Malik, Hui-Chia Yu, Aziz Abdellahi, Clare P Grey, Gerbrand Ceder, and Katsuyo Thornton. Architecture Dependence on the Dynamics of Nano-LiFePO4 Electrodes. *Electrochimica Acta*, 137:245 – 257, 08 2014.

[47] Bernardo Orvananos, Hui-Chia Yu, Rahul Malik, Aziz Abdellahi, Clare P. Grey, Gerbrand Ceder, and Katsuyo Thornton. Effect of a size-dependent equilibrium potential on Nano-$LiFePO_4$ particle interactions. *Journal of The Electrochemical Society*, 162:A1718–A1724, 2015.

[48] B Orvananos, H C Yu, A Abdellahi, R Malik, C P Grey, G Ceder, and K Thornton. Kinetics of Nanoparticle Interactions in Battery Electrodes. *Journal of The Electrochemical Society*, 162(6):A965 – A973, 02 2015.

[49] Chohong Min, Frédéric Gibou, and Hector D Ceniceros. A supra-convergent finite difference scheme for the variable coefficient poisson equation on non-graded grids. *J. Comput. Phys.*, 218(1):123–140, October 2006.

[50] Affan Malik, Kent Snyder, Minghong Liu, and Hui-Chia Yu. Phase-field electrochemical simulations of reconstructed graphite electrodes. *Journal of Energy Storage*, 77:109937, January 2024.

[51] M.S. Wittingham. Lithium batteries and cathode materials. *Chemical Reviews*, 104:4271–4302, 2004.

[52] Devin T O'Connor, Michael J Welland, Wing Kam Liu, and Peter W Voorhees. Phase transformation and fracture in single $\mathrm{Li}_x\mathrm{FePO}_4$ cathode particles: a phase-field approach to Li–ion intercalation and fracture. *Modelling and Simulation in Materials Science and Engineering*, 24(3):035020 – 17, 03 2016.

[53] L Hong, L Liang, S Bhattacharyya, W Xing, and L-Q Chen. Anisotropic Li intercalation in a $\mathrm{Li}_x\mathrm{FePO}_4$ nano-particle: a spectral smoothed boundary phase-field model. *Physical Chemistry Chemical Physics*, 18(14):9537 – 9543, 03 2016.

[54] Liang Hong, Linsen Li, Yuchen-Karen Chen-Wiegart, Jiajun Wang, Kai Xiang, Liyang Gan, Wenjie Li, Fei Meng, Fan Wang, Jun Wang, Yet-Ming Chiang, Song Jin, and Ming Tang. Two-dimensional lithium diffusion behavior and probable hybrid phase transformation kinetics in olivine lithium iron phosphate. *Nature Communications*, 8(1):1194, October 2017.

[55] J. Newman and K. E. Thomas-Alyea. *Electrochemical Systems*. Wiley, 2004.

[56] Martin Z Bazant. Theory of Chemical Kinetics and Charge Transfer based on Nonequilibrium Thermodynamics. *Accounts of Chemical Research*, 46(5):1144 – 1160, 05 2013.

[57] Affan Malik, Kent Snyder, Minghong Liu, and Hui-Chia Yu. Electrochemical dynamics in hybrid graphite–carbon electrodes. *MRS Communications*, 2022.

[58] Danqi Qu, Affan Malik, and Hui-Chia Yu. Physics-based simulation of electrochemical impedance spectroscopy of complex electrode microstructures using smoothed boundary method. *Electrochimica Acta*, 2022.

[59] Danqi Qu, Robert Termuhlen, and Hui-Chia Yu. Simulation of electrochemical double layer formation with complex geometries. *Journal of The Electrochemical Society*, 167:140515, 2020.

[60] Han Chen, Chohong Min, and Frédéric Gibou. A supra-convergent finite difference scheme for the poisson and heat equations on irregular domains and non-graded adaptive cartesian grids. *Journal of Scientific Computing*, 31:19–60, 2007.

[61] K. F. C. Yiu, D. M Greaves, S. Cruz, A. Saalehi, and A. G. L. Borthwick. Quadtree grid generation: Information handling, boundary fitting and CFD applications. *Computers & Fluids*, 25:759–769, 1996.

[62] C.-L. Park, P. W. Voorhees, and K. Thornton. Application of the level-set method to the analysis of an evolving microstructure. *Computational Materials Science*, 85:46–58, 2014.

[63] Robert Termuhlen, Kieran Fitzmaurice, and Hui-Chia Yu. Smoothed boundary method for simulating incompressible flow in complex geometries. *Computer Methods in Applied Mechanics and Engineering*, 399:115312, September 2022.

[64] Ruhul Amin and Yet-Ming Chiang. Characterization of electronic and ionic transport in $Li_{1-x}Ni_{0.33}Mn_{0.33}Co_{0.33}O_2$ (NMC333) and $Li_{1-x}Ni_{0.50}Mn_{0.20}Co_{0.30}O_2$ (NMC523) as a function of Li content. *Journal of The Electrochemical Society*, 163:A1512–A1517, 2016.

[65] Lars Ole Valøen and Jan N Reimers. Transport Properties of $LiPF_6$-Based Li-Ion Battery Electrolytes. *Journal of The Electrochemical Society*, 152(5):A882 – 10, 2005.

[66] Naoki Nitta, Feixiang Wu, Jung Tae Lee, and Gleb Yushin. Li-ion battery materials: present and future. *Materials Today*, 18:252–264, 2015.

[67] Ping-Chun Tsai, Bohua Wen, Mark Wolfman, Min-Ju Choe, Menghsuan Sam Pan, Liang Su, Katsuyo Thornton, Jordi Cabana, and Yet-Ming Chiang. Single-particle measurements of electrochemical kinetics in nmc and nca cathodes for Li-ion batteries. *Energy & Environmental Science*, 11:860–871, 2018.

[68] A Bueno-Orovio and V M Perez-Garcia. Spectral smoothed boundary methods: The role of external boundary conditions. *Numerical Methods for Partial Differential Equations*, 22:435–448, 2006.

[69] A Bueno-Orovio, V M Perez-Garcia, and F H Fenton. Spectral methods for partial differential equations in irregular domains: The spectral smoothed boundary method. *SIAM Journal on Scientific Computing*, 28:886–900, 2006.

[70] Stefan Luding. Introduction to discrete element methods. *European Journal of Environmental and Civil Engineering*, 12:785–826, 2008.

[71] Xifei Li, Jian Liu, Mohammad Norouzi Banis, Andrew Lushington, Ruying Li, Mei Cai, and Xueliang Sun. Atomic layer deposition of solid-state electrolyte coated cathode materials with superior highvoltage cycling behavior for lithium ion battery application. *Energy & Environmental Science*, 7:768–778, 2014.

[72] Yang Wang, Justin Roller, and Radenka Maric. Morphology-controlled one-step synthesis of nanostructured $LiNi_{1/3}Mn_{1/3}Co_{1/3}O_2$ electrodes for Li-ion batteries. *ACS Omega*, 3:3966—3973, 2018.

[73] P J Bouwman, B A Boukamp, H J M Bouwmeester, and P H L Notten. Influence of diffusion plane orientation on electrochemical properties of thin film $LiCoO_2$ electrodes. *Journal of The Electrochemical Society*, 149(6):A699–A709, 2002.

[74] Xin-Cun Tang, Lian-Xing Li, Qiong-Lin Lai, Xia-Wei Song, and Li-Hui Jiang. Investigation on diffusion behavior of Li^+ in $LiFePO_4$ by capacity intermittent titration technique (CITT). *Electrochimica Acta*, 54:2329–2334, 2009.

[75] E. M. Gavilán-Arriazu, O. A. Pinto, B. A. López de Mishima, D. E. Barraco, O. A. Oviedo, and E. P. M. Leiva. Kinetic Monte Carlo applied to the electrochemical study of the Li-ion graphite system. *Electrochimica Acta*, 331:135439, January 2020.

[76] D. Werner, A. Loges, D. J. Becker, and T. Wetzel. Thermal conductivity of li-ion batteries and their electrode configurations – a novel combination of modelling and experimental approach. *Journal of Power Sources*, 364:72–83, 2017.

[77] A. Loges, S. Herberger, P. Seegert, and T. Wetzel. A study on specific heat capacities of li-ion cell components and their influence on thermal management. *Journal of Power Sources*, 336:341–350, 2016.

[78] Hui-Chia Yu, Doaa Taha, Travis Thompson, Nathan J Taylor, Andrew Drews, Jeff Sakamoto, and Katsuyo Thornton. Deformation and stresses in solid-state composite battery cathodes. *Journal of Power Sources*, 440:227116, 11 2019.

[79] Rong Xu, Hong Sun, Luize Scalco de Vasconcelos, and Kejie Zhao. Mechanical and structural degradation of $LiNi_x Mn_yCo_zO_2$ cathode in Li-ionbatteries: An experimental study. *Journal of The Electrochemical Society*, 164(13):A3333–A3341, 2017.

[80] Eric Jianfeng Cheng, Kicheol Hong, Nathan John Taylor, Heeman Choe, Jeff Wolfenstine, and Jeff Sakamoto. Mechanical and physical properties of $LiNi_{0.33}Mn_{0.33}Co_{0.33}O_2$ (NMC). *Journal of the European Ceramic Society*, 37(9):3213–3217, 2017.

[81] Yinsheng Guo, Raymond B. Smith, Zhonghua Yu, Dmitri K. Efetov, Junpu Wang, Philip Kim, Martin Z. Bazant, and Louis E. Brus. Li Intercalation into Graphite: Direct Optical Imaging and Cahn–Hilliard Reaction Dynamics. *The Journal of Physical Chemistry Letters*, 7(11):2151–2156, June 2016. Publisher: American Chemical Society.

[82] Stephen J. Harris, Adam Timmons, Daniel R. Baker, and Charles Monroe. Direct in situ measurements of Li transport in Li-ion battery negative electrodes. *Chemical Physics Letters*, 485(4):265–274, January 2010.

[83] Alexander Urban, Dong-Hwa Seo, and Gerbrand Ceder. Computational understanding of Li-ion batteries. *npj Computational Materials*, 2(1):1–13, March 2016. Number: 1 Publisher: Nature Publishing Group.

[84] Alejandro A. Franco. Multiscale modelling and numerical simulation of rechargeable lithium ion batteries: concepts, methods and challenges. *RSC Advances*, 3(32):13027–13058, July 2013. Publisher: The Royal Society of Chemistry.

[85] John W. Cahn and John E. Hilliard. Free Energy of a Nonuniform System. I. Interfacial Free Energy. *The Journal of Chemical Physics*, 28(2):258–267, February 1958. Publisher: American Institute of Physics.

[86] Ming Tang, James F Belak, and Milo R Dorr. Anisotropic Phase Boundary Morphology in Nanoscale Olivine Electrode Particles. *The Journal of Physical Chemistry C*, 115:4922 – 4926, 2011.

[87] Daniel A Cogswell and Martin Z Bazant. Theory of Coherent Nucleation in Phase-Separating Nanoparticles. *Nano Letters*, 13:3036 – 3041, 2013.

[88] Marion Chandesris, Damien Caliste, Didier Jamet, and Pascal Pochet. Thermodynamics and related kinetics of staging in intercalation compounds. *JOURNAL OF PHYSICAL CHEMISTRY C*, 123(38):23711–23720, SEP 26 2019.

[89] Matthieu Rykner and Marion Chandesris. Free energy model for lithium intercalation in graphite: Focusing on the coupling with graphene stacking sequence. *JOURNAL OF PHYSICAL CHEMISTRY C*, 126(12):5457–5472, MAR 31 2022.

[90] Raymond B. Smith, Edwin Khoo, and Martin Z. Bazant. Intercalation kinetics in multiphase-layered materials. *JOURNAL OF PHYSICAL CHEMISTRY C*, 121(23):12505–12523, JUN 15 2017.

[91] Yi Zeng and Martin Z. Bazant. Cahn-Hilliard Reaction Model for Isotropic Li-ion Battery Particles. *MRS Online Proceedings Library*, 1542(1):0201, July 2013.

[92] L. Chen, F. Fan, L. Hong, J. Chen, Y. Z. Ji, S. L. Zhang, T. Zhu, and L. Q. Chen. A Phase-Field Model Coupled with Large Elasto-Plastic Deformation: Application to Lithiated Silicon Electrodes. *Journal of The Electrochemical Society*, 161(11):F3164, October 2014. Publisher: IOP Publishing.

[93] Fangliang Gao and Wei Hong. Phase-field model for the two-phase lithiation of silicon. *Journal of the Mechanics and Physics of Solids*, 94:18–32, September 2016.

[94] Hui-Chia Yu, Feng Wang, Glenn G. Amatucci, and Katsuyo Thornton. A Phase-Field Model and Simulation of Kinetically Asymmetric Ternary Conversion-Reconversion Transformation in Battery Electrodes. *Journal of Phase Equilibria and Diffusion*, 37(1):86–99, February 2016.

[95] Yudi Kuang, Chaoji Chen, Dylan Kirsch, and Liangbing Hu. Thick Electrode Batteries: Principles, Opportunities, and Challenges. *Advanced Energy Materials*, 9(33):1901457, September 2019.

[96] Junsheng Zheng, Guangguang Xing, Liming Jin, Yanyan Lu, Nan Qin, Shansong Gao, and Jim P. Zheng. Strategies and Challenge of Thick Electrodes for Energy Storage: A Review. *Batteries*, 9(3):151, March 2023. Number: 3 Publisher: Multidisciplinary Digital Publishing Institute.

[97] Moses Ender, Jochen Joos, André Weber, and Ellen Ivers-Tiffée. Anode microstructures from high-energy and high-power lithium-ion cylindrical cells obtained by X-ray nano-tomography. *Journal of Power Sources*, 269(c):912 – 919, 12 2014.

[98] Simon Müller, Jens Eller, Martin Ebner, Chris Burns, Jeff Dahn, and Vanessa Wood. Quantifying Inhomogeneity of Lithium Ion Battery Electrodes and Its Influence on Electrochemical Performance. *Journal of The Electrochemical Society*, 165(2):A339, January 2018. Publisher: IOP Publishing.

[99] Simon Müller. X-ray tomography data of four commercial lithium ion battery graphite electrodes: Research data supporting “quantifying inhomogeneity of lithium ion battery electrodes and its influence on electrochemical performance”. https://www.research-collection.ethz.ch/handle/20.500.11850/224851, 2018.

[100] Lukas Pfaffmann, Claudia Birkenmaier, Marcus Müller, Werner Bauer, Tim Mitsch, Julian Feinauer, Yvonne Krämer, Frieder Scheiba, Andreas Hintennach, Thomas Schleid, Volker Schmidt, and Helmut Ehrenberg. Investigation of the electrochemically active surface area and lithium diffusion in graphite anodes by a novel OsO_4 staining method. *Journal of Power Sources*, 307(C):762 – 771, 03 2016.

[101] Rachid Yazami, Audrey Martinent, and Yvan Reynier. Some thermodynamics and kinetics aspects of the graphite-lithium negative electrode for lithium-ionbatteries. In Igor V. Barsukov, Christopher S. Johnson, Joseph E. Doninger, and Vyacheslav Z. Barsukov, editors, *New Carbon Based Materials for Electrochemical Energy Storage Systems: Batteries, Supercapacitors and Fuel Cells*, NATO Science Series II: Mathematics, Physics and Chemistry, pages 245–258, Dordrecht, 2006. Springer Netherlands.

[102] Kristin Persson, Vijay A. Sethuraman, Laurence J. Hardwick, Yoyo Hinuma, Ying Shirley Meng, Anton van der Ven, Venkat Srinivasan, Robert Kostecki, and Gerbrand Ceder. Lithium Diffusion in Graphitic Carbon. *The Journal of Physical Chemistry Letters*, 1(8):1176–1180, April 2010. Publisher: American Chemical Society.

[103] Hua-Jun Guo, Xin-Hai Li, Xin-Ming Zhang, Hong-Qiang Wang, Zhi-Xing Wang, and Wen-Jie Peng. Diffusion coefficient of lithium in artificial graphite, mesocarbon microbeads, and disordered carbon. *New Carbon Materials*, 22(1):7 – 10, 2007-03.

[104] Xiao-Guang Yang, Yongjun Leng, Guangsheng Zhang, Shanhai Ge, and Chao-Yang Wang. Modeling of lithium plating induced aging of lithium-ion batteries: Transition from linear to nonlinear aging. *Journal of Power Sources*, 360:28 – 40, 08 2017.

[105] Robert Termuhlen, Xanthippi Chatzistavrou, Jason D Nicholas, and Hui-Chia Yu. Three-dimensional phase field sintering simulations accounting for the rigid-body motion of individual grains. *Computational Materials Science*, 186:109963, 08 2020.

[106] Timo Danner, Madhav Singh, Simon Hein, Jörg Kaiser, Horst Hahn, and Arnulf Latz. Thick electrodes for Li-ion batteries: A model based analysis. *Journal of Power Sources*, 334:191–201, December 2016.

[107] Kuan-Hung Chen, Min Ji Namkoong, Vishwas Goel, Chenglin Yang, Saeed Kazemiabnavi, S. M. Mortuza, Eric Kazyak, Jyoti Mazumder, Katsuyo Thornton, Jeff Sakamoto, and Neil P. Dasgupta. Efficient fast-charging of lithium-ion batteries enabled by laser-patterned three-dimensional graphite anode architectures. *Journal of Power Sources*, 471:228475, September 2020.

[108] Vittorio De Lauri, Lukas Krumbein, Simon Hein, Benedikt Prifling, Volker Schmidt, Timo Danner, and Arnulf Latz. Beneficial effects of three-dimensional structured electrodes for the fast charging of lithium-ion batteries. *ACS APPLIED ENERGY MATERIALS*, 4(12):13847–13859, DEC 27 2021.

[109] Tao Gao, Yu Han, Dimitrios Fraggedakis, Supratim Das, Tingtao Zhou, Che-Ning Yeh, Shengming Xu, William C. Chueh, Ju Li, and Martin Z. Bazant. Interplay of Lithium Intercalation and Plating on a Single Graphite Particle. *Joule*, 5(2):393–414, February 2021.

[110] Juliette Billaud, Florian Bouville, Tommaso Magrini, Claire Villevieille, and André R. Studart. Magnetically aligned graphite electrodes for high-rate performance Li-ion batteries. *Nature Energy*, 1(8):1–6, July 2016. Number: 8 Publisher: Nature Publishing Group.

[111] Dhrupad Parikh and Jianlin Li. Bilayer hybrid graphite anodes via freeze tape casting for extreme fast charging applications. *Carbon*, 196:525–531, 2022.

[112] Zhijia Du. Understanding limiting factors in thick electrode performance as applied to high energy density Li-ion batteries. *Journal of Applied Electrochemistry*, 47(3):405 – 415, 03 2017.

[113] Jingyi Wu, Xiao Zhang, Zhengyu Ju, Lei Wang, Zeyu Hui, Karthik Mayilvahanan, Kenneth J. Takeuchi, Amy C. Marschilok, Alan C. West, Esther S. Takeuchi, and Guihua Yu. From Fundamental Understanding to Engineering Design of High-Performance Thick Electrodes for Scalable Energy-Storage Systems. *Advanced Materials*, 33(26):e2101275, 2021.

[114] Andrew M. Colclasure, Alison R. Dunlop, Stephen E. Trask, Bryant J. Polzin, Andrew N. Jansen, and Kandler Smith. Requirements for Enabling Extreme Fast Charging of High Energy Density Li-Ion Cells while Avoiding Lithium Plating. *Journal of The Electrochemical Society*, 166(8):A1412, April 2019. Publisher: IOP Publishing.

[115] Thomas Waldmann, Björn-Ingo Hogg, and Margret Wohlfahrt-Mehrens. Li plating as unwanted side reaction in commercial Li-ion cells – A review. *Journal of Power Sources*, 384:107–124, April 2018.

[116] David E. Brown, Eric J. McShane, Zachary M. Konz, Kristian B. Knudsen, and Bryan D. McCloskey. Detecting onset of lithium plating during fast charging of Li-ion batteries using operando electrochemical impedance spectroscopy. *Cell Reports Physical Science*, 2(10):100589, October 2021.

[117] Eric J. McShane, Andrew M. Colclasure, David E. Brown, Zachary M. Konz, Kandler Smith, and Bryan D. McCloskey. Quantification of Inactive Lithium and Solid–Electrolyte Interphase Species on Graphite Electrodes after Fast Charging. *ACS Energy Letters*, 5(6):2045–2051, June 2020. Publisher: American Chemical Society.

[118] Katsunori Yanagida, Atsushi Yanai, Yoshinori Kida, Atsuhiro Funahashi, Toshiyuki Nohma, and Ikuo Yonezu. Carbon Hybrids Graphite-Hard Carbon and Graphite-Coke as Negative Electrode Materials for Lithium Secondary Batteries Charge/Discharge Characteristics. *Journal of The Electrochemical Society*, 149(7):A804, May 2002. Publisher: IOP Publishing.

[119] Richard Schmuch, Ralf Wagner, Gerhard Hörpel, Tobias Placke, and Martin Winter. Performance and cost of materials for lithium-based rechargeable automotive batteries. *Nature Energy*, 3(4):267–278, April 2018. Publisher: Nature Publishing Group.

[120] Chuanzhang Ge, Zhenghua Fan, Jie Zhang, Yongmin Qiao, Jianming Wang, and Licheng Ling. Novel hard carbon/graphite composites synthesized by a facile in situ anchoring method as high-performance anodes for lithium-ion batteries. *RSC Advances*, 8(60):34682–34689, October 2018. Publisher: The Royal Society of Chemistry.

[121] Young-Geun Lim, Jung Woo Park, Min-Sik Park, Dongjin Byun, Ji-Sang Yu, Yong Nam Jo, and Young-Jun Kim. Hard Carbon-coated Natural Graphite Electrodes for High-Energy and Power Lithium-Ion Capacitors. *Bulletin of the Korean Chemical Society*, 36(1):150–155, 2015.

[122] Kyung-Jin Kim, Taek-Soo Lee, Hyung-Giun Kim, Sung-Hwan Lim, and Sung-Man Lee. A hard carbon/microcrystalline graphite/carbon composite with a core-shell structure as novel anode materials for lithium-ion batteries. *Electrochimica Acta*, 135:27–34, July 2014.

[123] Kuan-Hung Chen, Vishwas Goel, Min Ji Namkoong, Markus Wied, Simon Müller, Vanessa Wood, Jeff Sakamoto, Katsuyo Thornton, and Neil P. Dasgupta. Enabling 6C Fast Charging of Li-Ion Batteries with Graphite/Hard Carbon Hybrid Anodes. *Advanced Energy Materials*, 11(5):2003336, 2021.

[124] Edward Buiel and J. R Dahn. Li-insertion in hard carbon anode materials for Li-ion batteries. *Electrochimica Acta*, 45(1):121–130, September 1999.

[125] D. A. Stevens and J. R. Dahn. The Mechanisms of Lithium and Sodium Insertion in Carbon Materials. *Journal of The Electrochemical Society*, 148(8):A803, June 2001. Publisher: IOP Publishing.

[126] E. Irisarri, A. Ponrouch, and M. R. Palacin. Review—Hard Carbon Negative Electrode Materials for Sodium-Ion Batteries. *Journal of The Electrochemical Society*, 162(14):A2476–A2482, 2015.

[127] Hui-Chia Yu, Stuart B Adler, Scott A Barnett, and K Thornton. Simulation of the diffusional impedance and application to the characterization of electrodes with complex microstructures. *Electrochimica Acta*, 354:136534, 09 2020.

[128] S Dargaville and T W Farrell. A comparison of mathematical models for phase-change in high-rate $LiFePO_4$ cathodes. *Electrochimica Acta*, 111:474 – 490, 11 2013.

[129] S Dargaville and T W Farrell. The persistence of phase-separation in LiFePO4 with two-dimensional Li+ transport: The Cahn–Hilliard-reaction equation and the role of defects. *Electrochimica Acta*, 94:143 – 158, 04 2013.

[130] Srivatsan Hulikal, Chun-Hao Chen, Eric Chason, and Allan Bower. Experimental Calibration of a Cahn-Hilliard Phase-Field Model for Phase Transformations in Li-Sn Electrodes. *Journal of The Electrochemical Society*, 163(13):A2647 – A2659, 09 2016.

[131] Wolfgang Dreyer, Janko Jamnik, Clemens Guhlke, Robert Huth, Jože Moškon, and Miran Gaberšček. The thermodynamic origin of hysteresis in insertion batteries. *Nature Materials*, 9(5):448 – 453, 04 2010.

[132] Chang-Jun Bae, Can K Erdonmez, John W Halloran, and Yet-Ming Chiang. Design of Battery Electrodes with Dual-Scale Porosity to Minimize Tortuosity and Maximize Performance. *Advanced Materials*, 25(9):1254 – 1258, 12 2012.

[133] Jan B. Habedank, Joseph Endres, Patrick Schmitz, Michael F. Zaeh, and Heinz P. Huber. Femtosecond laser structuring of graphite anodes for improved lithium-ion batteries: Ablation characteristics and process design. *Journal of Laser Applications*, 30(3):032205, August 2018. Publisher: Laser Institute of America.

[134] Nathan Dunlap, Dana B. Sulas-Kern, Peter J. Weddle, Francois Usseglio-Viretta, Patrick Walker, Paul Todd, David Boone, Andrew M. Colclasure, Kandler Smith, Bertrand J. Tremolet de Villers, and Donal P. Finegan. Laser ablation for structuring Li-ion electrodes for fast charging and its impact on material properties, rate capability, Li plating, and wetting. *Journal of Power Sources*, 537:231464, July 2022.

[135] Vishwas Goel, Kuan-Hung Chen, Neil P. Dasgupta, and Katsuyo Thornton. Optimization of laser-patterned electrode architectures for fast charging of Li-ion batteries using simulations parameterized by machine learning. *ENERGY STORAGE MATERIALS*, 57:44–58, MAR 2023.

[136] Dane Morgan, Gerbrand Ceder, and Stefano Curtarolo. High-throughput and data mining with ab initio methods. *Measurement Science and Technology*, 16(1):296, December 2004.

[137] Anubhav Jain, Geoffroy Hautier, Charles J. Moore, Shyue Ping Ong, Christopher C. Fischer, Tim Mueller, Kristin A. Persson, and Gerbrand Ceder. A high-throughput infrastructure for density functional theory calculations. *Computational Materials Science*, 50(8):2295–2310, June 2011.

[138] Shyue Ping Ong. Accelerating materials science with high-throughput computations and machine learning. *Computational Materials Science*, 161:143–150, April 2019.

[139] Dingguo Xu, Qiao Zhang, Xiangyu Huo, Yitong Wang, and Mingli Yang. Advances in data-assisted high-throughput computations for material design. *Materials Genome Engineering Advances*, 1(1):e11, 2023.

[140] Danqi Qu and Hui-Chia Yu. Multiphysics Electrochemical Impedance Simulations of Complex Multiphase Graphite Electrodes. *ACS Applied Energy Materials*, 6(6):3468–3485, March 2023. Publisher: American Chemical Society.

[141] Hao Zhang, Yang Yang, Hong Xu, Li Wang, Xia Lu, and Xiangming He. LiTiO spinel anode: Fundamentals and advances in rechargeable batteries. *InfoMat*, 4(4):e12228, 2022.

[142] Guanjia Zhu, Wei Luo, Lianjun Wang, Wan Jiang, and Jianping Yang. Silicon: toward eco-friendly reduction techniques for lithium-ion battery applications. *Journal of Materials Chemistry A*, 7(43):24715–24737, 2019.

[143] Jingxing Wu, Yinliang Cao, Haimin Zhao, Jianfeng Mao, and Zaiping Guo. The critical role of carbon in marrying silicon and graphite anodes for high-energy lithium-ion batteries. *Carbon Energy*, 1(1):57–76, 2019.

[144] Hyun Jung Kwon, Jang-Yeon Hwang, Hyeon-Ji Shin, Min-Gi Jeong, Kyung Yoon Chung, Yang-Kook Sun, and Hun-Gi Jung. Nano/Microstructured Silicon–Carbon Hybrid Composite Particles Fabricated with Corn Starch Biowaste as Anode Materials for Li-Ion Batteries. *Nano Letters*, 20(1):625–635, January 2020. Publisher: American Chemical Society.

[145] Sujith Kalluri, Moonsu Yoon, Minki Jo, Suhyeon Park, Seungjun Myeong, Junhyeok Kim, Shi Xue Dou, Zaiping Guo, and Jaephil Cho. Surface Engineering Strategies of Layered $LiCoO_2$ Cathode Material to Realize High-Energy and High-Voltage Li-Ion Cells. *Advanced Energy Materials*, 7(1):1601507, 2017.

[146] Si-Dong Zhang, Mu-Yao Qi, Si-Jie Guo, Yong-Gang Sun, Xin-Xin Tan, Pei-Zhong Ma, Jin-Yang Li, Rong-Zhong Yuan, An-Min Cao, and Li-Jun Wan. Advancing to 4.6 V Review and Prospect in Developing High-Energy-Density $LiCoO_2$ Cathode for Lithium-Ion Batteries. *Small Methods*, 6(5):2200148, 2022.

[147] Zishan Ahsan, Bo Ding, Zhenfei Cai, Cuie Wen, Weidong Yang, Yangzhou Ma, Shihong Zhang, Guangsheng Song, and Muhammad Sufyan Javed. Recent Progress in Capacity Enhancement of $LiFePO_4$ Cathode for Li-Ion Batteries. *Journal of Electrochemical Energy Conversion and Storage*, 18(010801), June 2020.

[148] S. El Moutchou, H. Aziam, M. Mansori, and I. Saadoune. Thermal stability of Lithium-ion batteries: Case study of NMC811 and LFP cathode materials. *Materials Today: Proceedings*, 51:A1–A7, January 2022.

[149] Katharina Märker, Philip J. Reeves, Chao Xu, Kent J. Griffith, and Clare P. Grey. Evolution of Structure and Lithium Dynamics in $LiNi_{0.8}Mn_{0.1}Co_{0.1}O_2$ (NMC811) Cathodes during Electrochemical Cycling. *Chemistry of Materials*, 31(7):2545–2554, April 2019. Publisher: American Chemical Society.

[150] Hoon-Hee Ryu, Nam-Yung Park, Jeong Hyun Seo, Young-Sang Yu, Monika Sharma, Robert Mücke, Payam Kaghazchi, Chong S. Yoon, and Yang-Kook Sun. A highly stabilized Ni-rich NCA cathode for high-energy lithium-ion batteries. *Materials Today*, 36:73–82, June 2020.

[151] Agus Purwanto, Cornelius Satria Yudha, U. Ubaidillah, Hendri Widiyandari, Takashi Ogi, and Hery Haerudin. NCA cathode material: synthesis methods and performance enhancement efforts. *Materials Research Express*, 5(12):122001, September 2018. Publisher: IOP Publishing.

[152] M. R. Pivello, M. M. Villar, R. Serfaty, A. M. Roma, and A. Silveira-Neto. A fully adaptive front tracking method for the simulation of two phase flows. *International Journal of Multiphase Flow*, 58:72–82, January 2014.

[153] M. J. Berger and P. Colella. Local adaptive mesh refinement for shock hydrodynamics. *Journal of Computational Physics*, 82(1):64–84, May 1989.

[154] Louis H. Howell and John B. Bell. An Adaptive Mesh Projection Method for Viscous Incompressible Flow. *SIAM Journal on Scientific Computing*, 18(4):996–1013, July 1997. Publisher: Society for Industrial and Applied Mathematics.

[155] Boyce E. Griffith, Richard D. Hornung, David M. McQueen, and Charles S. Peskin. An adaptive, formally second order accurate version of the immersed boundary method. *Journal of Computational Physics*, 223(1):10–49, April 2007.

[156] R. M. J. Kramer, C. Pantano, and D. I. Pullin. Nondissipative and energy-stable high-order finite-difference interface schemes for 2-D patch-refined grids. *Journal of Computational Physics*, 228(14):5280–5297, August 2009.

[157] Koji Nishiguchi, Rahul Bale, Shigenobu Okazawa, and Makoto Tsubokura. Full Eulerian deformable solid-fluid interaction scheme based on building-cube method for large-scale parallel computing. *International Journal for Numerical Methods in Engineering*, 117(2):221–248, 2019.

[158] Caihao Weng, Jing Sun, and Huei Peng. A unified open-circuit-voltage model of lithium-ion batteries for state-of-charge estimation and state-of-health monitoring. *Journal of Power Sources*, 258(C):228 – 237, 07 2014.

APPENDIX A

EXAMPLE OF FDM STENCIL DERIVATION

Here, we use the Taylor series to derive the FDM stencil for a west-facing T-junction based on the examples in Ref. [49, 60]. The node-neighbor configuration is shown in Fig. A.1. In the east direction, we can write

$$u_E = u_C + s_E u_x + \frac{s_E^2}{2} u_{xx} + \cdots , \tag{A.1}$$

where the subscripts x and xx indicate derivative. In the west direction, we can write

$$u_{NW} = u_C - s_W u_x + s_N u_y + \frac{s_W^2}{2} u_{xx} + \frac{s_N^2}{2} u_{yy} - s_W s_N u_{xy} + \cdots \tag{A.2}$$

and

$$u_{SW} = u_C - s_W u_x - s_S u_y + \frac{s_W^2}{2} u_{xx} + \frac{s_S^2}{2} u_{yy} + s_W s_S u_{xy} + \cdots . \tag{A.3}$$

Eq. (A.2) $\times s_S$ + Eq. (A.3) $\times s_N$ eliminates the u_y terms, and ignoring higher order terms gives

$$\frac{1}{s_S + s_N} \left[s_S \left(u_C - u_{NW} \right) + s_N \left(u_C - u_{SW} \right) \right] = s_W u_x - \frac{s_W^2}{2} u_{xx} - \frac{s_S s_N}{2} u_{yy} \tag{A.4}$$

which can be organized to

$$u_C - u_W = s_W u_x - \frac{s_W^2}{2} u_{xx} - \frac{s_S s_N}{2} u_{yy} \tag{A.5}$$

where $u_W = \left(s_S / \left(s_S + s_N \right) \right) u_{NW} + \left(s_N / \left(s_S + s_N \right) \right) u_{SW}$ can be viewed as the u value on the virtual west neighbor (the green circle in Fig. A.1). To eliminate u_x terms, we use Eq. (A.1) $\times s_W$ − Eq. (A.5) $\times s_E$ to obtain

$$s_W \left(u_E - u_C \right) - s_E \left(u_C - u_W \right) = \frac{s_W s_E \left(s_W + s_E \right)}{2} u_{xx} + \frac{s_E s_S s_N}{2} u_{yy} \tag{A.6}$$

which is organized to

$$u_{xx} = \frac{2}{s_W + s_E} \left(\frac{u_E - u_C}{s_E} - \frac{u_C - u_W}{s_W} \right) - \frac{s_S s_N}{s_W \left(s_W + s_E \right)} u_{yy}. \tag{A.7}$$

In the y-direction

$$u_N = u_C + s_N u_y + \frac{s_N^2}{2} u_{yy} + \cdots \tag{A.8}$$

$$u_S = u_C - s_S u_y + \frac{s_S^2}{2} u_{yy} + \cdots . \tag{A.9}$$

Eq. (A.8) $\times s_S$ − Eq. (A.9) $\times s_N$ eliminates the u_y terms. Ignoring the higher-order terms and performing some algebraic operations gives

$$u_{yy} = \frac{2}{s_S + s_N} \left(\frac{u_N - u_C}{s_N} - \frac{u_C - u_S}{s_S} \right). \tag{A.10}$$

Similarly, in the z-direction

$$u_T = u_C + s_T u_z + \frac{s_T^2}{2} u_{zz} + \cdots \tag{A.11}$$

$$u_B = u_C - s_B u_z + \frac{s_B^2}{2} u_{zz} + \cdots \tag{A.12}$$

Eq. (A.11) $\times s_B$ − Eq. (A.12) $\times s_T$ eliminates the u_z terms. Ignoring higher-order terms and performing algebraic operations again gives

$$u_{zz} = \frac{2}{s_B + s_T} \left(\frac{u_T - u_C}{s_T} - \frac{u_C - u_B}{s_B} \right). \tag{A.13}$$

The Laplace operator is written as

$$\nabla^2 u = u_{xx} + u_{yy} + u_{zz}. \tag{A.14}$$

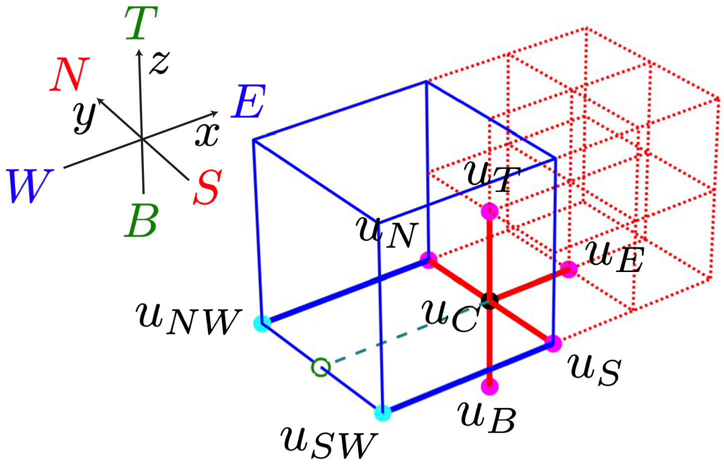

Figure A.1 Illustration of node configuration of a west-facing T-junction.

Combining Eqs. (A.6), (A.10), and (A.13), we obtain

$$\begin{aligned}\nabla^2 u =& \frac{2}{s_W + s_E}\left(\frac{u_E - u_C}{s_E} - \frac{u_C - u_W}{s_W}\right) + \\ & \frac{2}{s_S + s_N}\left(\frac{u_N - u_C}{s_N} - \frac{u_C - u_S}{s_S}\right)\left(1 - \frac{s_S s_N}{s_W(s_W + s_E)}\right) + \\ & \frac{2}{s_B + s_T}\left(\frac{u_T - u_C}{s_T} - \frac{u_C - u_B}{s_B}\right),\end{aligned} \tag{A.15}$$

which contains a nonzero correction factor

$$\beta_{12} = \frac{s_S s_N}{s_W(s_W + s_E)} \tag{A.16}$$

for a west-facing T-junction on the x-y plane. The first subscript, '1', indicates that it is a T-junction along the x-axis, and the two subscripts, '12', indicate that this T-junction is on the x-y plane. Performing the derivations for T-junctions and face-centered junctions in all three axial directions and summarizing the results will give the general form of FDM Laplace stencils with all correction factors similar to Eq. (2.21).

As in Refs. [49,60], for a Laplace operator with variable coefficient, $\nabla \cdot (\psi \nabla u)$, we start with the second derivative in the x-direction:

$$\begin{aligned}(\psi u_x)_x =& \frac{2}{s_W + s_E}\left(\frac{\psi_E + \psi_C}{2} \cdot \frac{u_E - u_C}{s_E} - \frac{s_S D_{NW} + s_N D_{SW}}{s_S + S_N}\right) \\ & + \frac{s_S s_N}{s_W(s_W + s_E)}(\psi u_y)_y,\end{aligned} \tag{A.17}$$

with the assumption of

$$D_{NW} = \frac{\psi_C + \psi_{NW}}{2} \cdot \frac{u_C - u_{NW}}{s_W} \text{ and } D_{SW} = \frac{\psi_C + \psi_{SW}}{2} \cdot \frac{u_C - u_{SW}}{s_W}. \tag{A.18}$$

Following similar earlier algebraic derivations, one can obtain Eq. (2.21). The correction factor, α_{ij}, for the first derivatives in Eq. (2.23) can also be derived from the Taylor series similarly.

APPENDIX B

PARAMETERIZATION OF MATERIAL PROPERTIES

Based on the values corresponding to the green circles in Fig. 3.1(a), Li diffusivity in NMC crystals in terms of Li fraction was fitted using Matlab® curve-fit function as

$$D_{Li} = (0.0277 - 0.0840X + 0.1003X^2) \times 10^{-8} \ \text{cm}^2/\text{s}, \tag{B.1}$$

which is shown as the red curve in Fig. 3.1(a). Here X is the same quantity as X_p in the main text. This curve indicates a low Li diffusivity when $X \sim 0.5$, commonly observed in layered transition metal oxide cathode materials, reflecting the Li ordering in those host crystals. Similarly, the electric conductivity of NMC as a function of Li fraction was fitted based on the green circles in Fig. 3.1(b) as

$$\kappa = 0.0193 + 0.7045 \tanh(2.399X) - 0.7238 \tanh(2.412X) \ \text{S/cm}, \tag{B.2}$$

which is shown as the red curve in the same figure. At a high Li fraction, the valence electrons move toward Li centers. Ionic bonding prevails, thus showing a low conductivity. We scaled the concentration-dependent Li salt diffusivity in Ref. [65] such that the values of D_+ and D_- at 1 M are 1.25×10^{-6} cm^2/s and 4.0×10^{-6} cm^2/s, respectively. The D_+ and D_- curves are shown as the green and blue curves in Fig. 3.1(c). The D_e was obtained as

$$D_e = 0.00489 \times \exp(-7.02 - 830C_e + 50000C_e^2) \ \text{cm}^2/\text{s}, \tag{B.3}$$

which is indicated as the red curve in the same figure.

The open-circuit voltage as a function of Li fraction was fitted from the green circles in Fig. 3.1(d) using the suggested function in Ref. [158] as

$$\phi_{OCV} = 1.095X^2 - 8.234 \times 10^{-7} \exp(14.32X) + 4.692 \exp(-0.5389X) \ \text{V}, \tag{B.4}$$

which is shown as the red curve in the same figure. The exchange current density fitted from the green circles in Fig. 3.1(e) is

$$i_0 = 10^{-0.2(X-0.37) - 0.9376 \tanh(8.961X - 3.195) - 1.559} \ \text{mA/cm}^2, \tag{B.5}$$

which is plotted as the red curve in the same figure. All the curve fittings were performed using Matlab$^{®}$ curve-fit function.

APPENDIX C

ADAPTIVE MESH REFINEMENT ON RECONSTRUCTED GRAPHITE MICROSTRUCTURE

For accurate electrochemical simulations, it can be advantageous to directly utilize 3D voxelated data obtained from reconstructed microstructures in SBM simulations [44, 127], with voxel centers serving as the grid points. Our octree AMR code was tested to generate L2 meshes on two X-ray computed tomography reconstructed graphite electrode microstructures [98, 99]. Figures C.1(a) and (b) show the two microstructures: one contains sphere-like particles and the other plate-like particles. The input data comprise $360 \times 220 \times 320 = 25,344,000$ voxels with a voxel edge size of 0.325 μm. Using the refinement criteria of 2.20 and 1.05 for the Lv1 and Lv2 refinement criteria, L2 meshes were generated in approximately 13.75 and 19.25 minutes, respectively. The total numbers of grid points are 303,877,035 and 308,607,135, respectively, approximately 12.2 times the original number. The initial voxelated 3D data can be manipulated easily to create artificial microstructures. For instance, Fig. C.1(c) displays an electrode with a conic tunnel that mimics a laser-ablated tunnel [107], achieved by removing the voxels in the space occupied by the tunnel. The L2 mesh contained 303,823,339 grid points and was generated in about 12.8 minutes. A small region of the grid system is depicted in Fig. C.1(d). Notably, the root-level mesh (voxels) is reasonably fine, suggesting that AMR may not be necessary in this case. Additionally, the total number of grid points can be reduced by coarsening the root-level cells to alleviate the computational burden in simulations. However, such treatment may not significantly decrease the number of grid points since most grid points are associated with L1 and L2 cells. In our tests, the total number of nodes only decreased to $\sim$ 220 million. Therefore, considering computational costs, we recommend employing AMR with SBM either when complex geometries are challenging to discretize with body-conforming meshes, such as in highly porous electrode microstructures, or when the operating conditions of the system are extreme, such as high C rate lithiation/delithiation. If the domain of interest can be easily meshed, conventional sharp-interface approaches will be more cost-effective and efficient computationally.

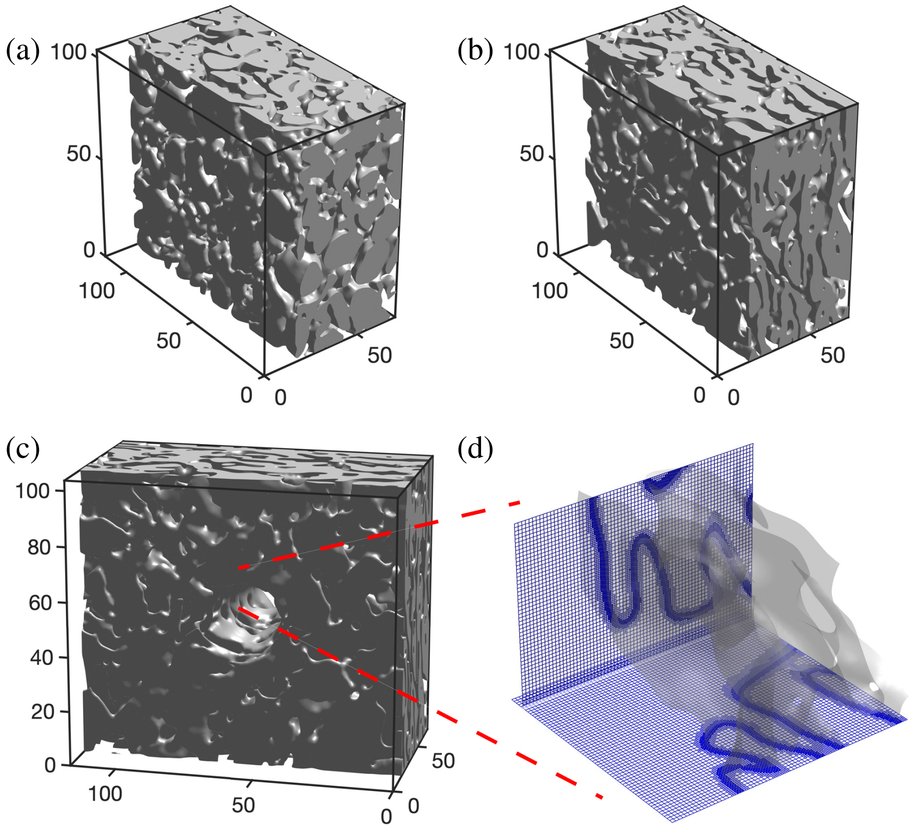

Figure C.1 Reconstructed 3D microstructures: (a) Electrode with large and spherical-like particles (electrode II_a in Ref. [99]), (b) Electrode with plate-like particles (electrode IV in Ref. [99]), (c) Electrode with a conical tunnel at the center to mimic a configuration of laser ablated electrode, and (d) A magnified view of the grid system in (c) to show the L2 octree refinement. The spatial unit is μm.

APPENDIX D

SUPPLEMENTARY INFORMATION TO CHAPTER 5

D.1 Li intake in terms of moles

The volumes of graphite and carbon particles are 1.94×10^5 and 1.92×10^5 μm^3, respectively, in the standard case. Multiplying with Li site densities, the capacity of the graphite particles, that of the hard carbon particles, and the total capacity are 6.053×10^{-9}, 4.358×10^{-9}, and 1.041×10^{-8} mol (or 1.004 mAh), respectively. For a 6C rate of this hybrid electrode, the current is $1.041 \times 10^{-8} \times 96485.3/3600 \times 1000 = 2.790 \times 10^{-4}$ mA. The total capacities of pure graphite and hard carbon electrodes with the same volume as the hybrid one will be 1.204×10^{-8} mol (or 1.162 mAh) and 8.762×10^{-8} mol (or 0.845 mAh). A 6C rate for the pure graphite and hard carbon electrodes will be 3.228×10^{-4} and 2.348×10^{-4} mA, respectively. The cross-section area (y-z plane) of the computational domain is 1.217×10^{-4} cm^2. Thus, the cell current densities at 6C are 2.293, 2.653, and 1.390 mA/cm^2 for the hybrid, pure graphite, and pure carbon electrode, respectively. For the cases of arranging particles according to positions and sizes, the insertion currents are similar to the standard case because graphite and carbon both occupied 50% of the total volume.

D.2 Simulation videos

Videos are provided on Ref. [57] SI web page. The video file names are listed below.

Table D.1 Video file names. Four physical fields in the standard case (random particle arrangement) are provided here. For the remaining cases, only the Li fractions are provided.

	6C	1C
	random arrangement	
Li fraction	LiFrax_Random_6C.mov	LiFrax_Random_1C.mov
salt conc	SaltConc_Random_6C.mov	SaltConc_Random_1C.mp4
electrode potential	ElectrodePoten_Random_6C.mov	ElectrodePoten_Random_1C.mp4
electrolyte potential	ElectrolytePoten_Random_6C.mov	ElectrolytePoten_Random_1C.mov
	small graphite particles	
Li fraction	LiFrax_SmlGrap_6C.mov	LiFrax_SmlGrap_1C.mp4
	small carbon particles	
Li fraction	LiFrax_SmlCarb_6C.mov	LiFrax_SmlCarb_1C.mp4
	graphite particles in the front	
Li fraction	LiFrax_GrapFront_6C.mov	LiFrax_GrapFront_1C.mp4
	carbon particles in the front	
Li fraction	LiFrax_CarbFront_6C.mov	LiFrax_CarbFront_1C.mp4
	high carbon i_0	
Li fraction	LiFrax_highCarbI0_6C.mov	LiFrax_highCarbI0_1C.mp4
	low carbon D_c	
Li fraction	LiFrax_LowCarbDif_6C.mov	LiFrax_LowCarbDif_1C.mp4

D.3 Simulations of 1C lithiation

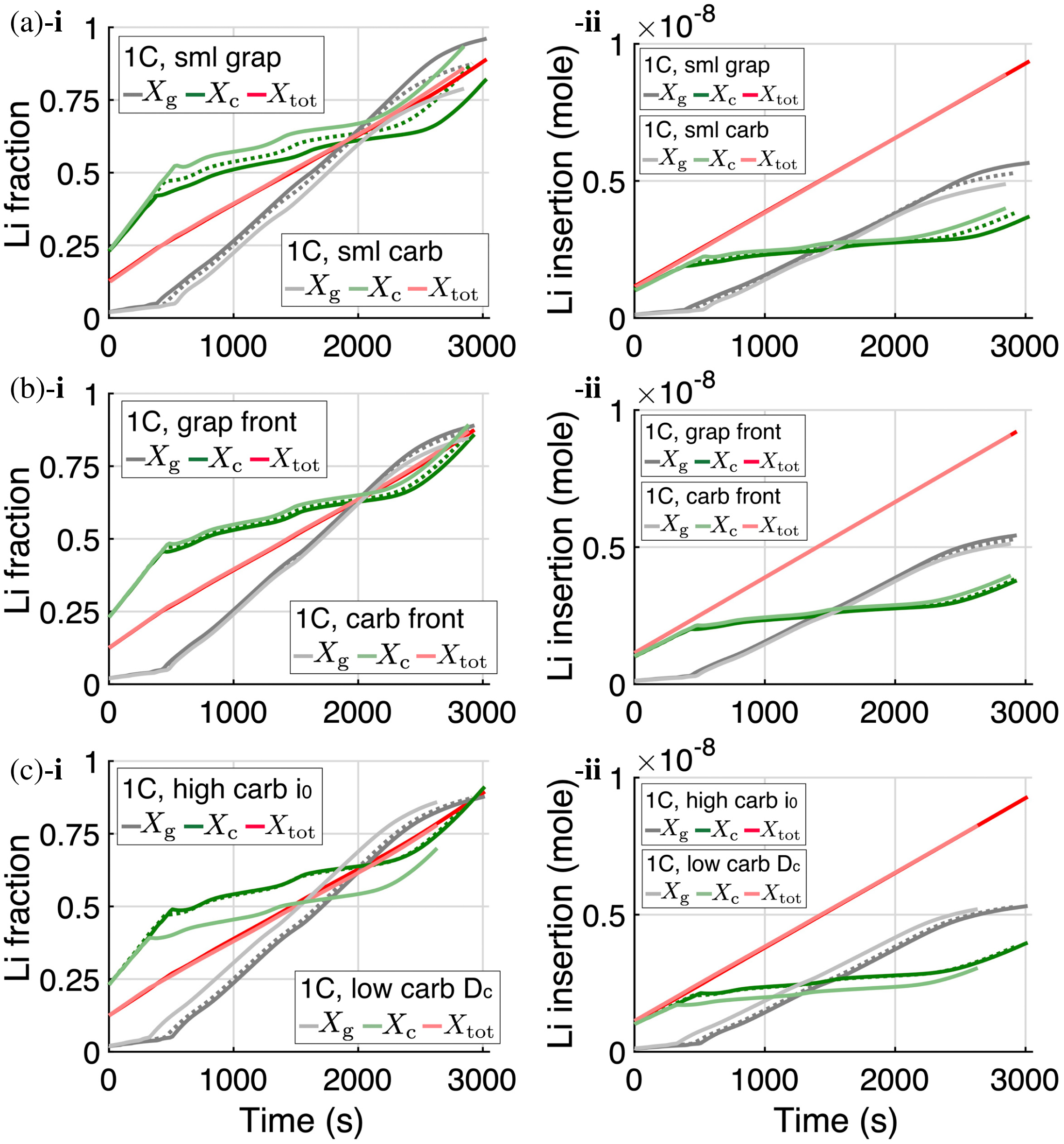

Figure D.3 Simulated Li fraction evolution (column **i**) and accumulated Li intakes (column **ii**) over time at 1C lithiation. (a) Cases of small graphite or small carbon particles. (b) Cases of graphite or carbon in the front region. (c) Cases of high carbon i_0 or low D_c.